UNIVERSITÉ DE GENÈVE
Department of Quantum Matter Physics

FACULTÉ DES SCIENCES
Professeur Dirk van der Marel

Electronic correlations in interacting quantum matter

THÈSE

présentée à la Faculté des Sciences de l'Université de Genève
pour obtenir le grade de docteur ès Sciences, mention Physique

par

Davide Filippo Valentinis
de
Milano (Italy)

Thèse n° ——

GENÈVE
Imprimerie Harder
2017

Ever tried. Ever failed. No matter. Try again. Fail again. Fail better.

Samuel Beckett, from "‘Worstward Ho’" (1983)

Dedication.

Abstract

English version

The subject of this thesis is electronic correlations in quantum matter, particularly in low-dimensional metallic systems at low temperatures. In such conditions, the response of electron liquids to external excitations, like electric fields and electromagnetic waves, is remarkably modified by the presence of correlations: the latter make the response nonlocal in space, meaning that electrons not only react at the coordinate where the local perturbation is applied, but also at other spatial coordinates. This collective behaviour, stemming from microscopic nonlocal correlations, allows us to treat the electron liquid macroscopically as a viscoelastic fluid, in analogy with hydrodynamics and elasticity theory, and to study the collective modes that emerge in the electrically neutral and charged cases. This picture is naturally suitable to study the phenomenology of Fermi liquids, which describes the normally-conducting state of many metals. Employing the viscoelastic approach, we can analyze the collective modes of Fermi liquids and their interaction with electric fields and electromagnetic radiation: depending on the excitation frequency and on the scattering time, the response of the Fermi surface evolves from the one of a viscous fluid to the one of an elastic solid, so that one can trace the phase diagram of such viscoelastic quantum liquid. These phenomena leave observable traces in experiments: for instance, the simultaneous presence of two degenerate electromagnetic modes that interfere coherently inside the material, giving rise to oscillatory patterns in the optical transmission and reflection spectra as a function of frequency, in the same way as anomalous skin effect that shows in the surface impedance. This allows one to probe the finite-momentum response of Fermi liquids with light. The analysis is specialized to low-dimensional systems: in fact, thin metallic films are suitable for transport and optical experiments, and nonlocal correlations are favored by low dimensionality, when the mean free path of electrons becomes greater

than the sample thickness. The conclusion is that Fermi liquids, although well documented, still exhibit new and useful properties when we introduce viscoelastic correlations into the problem. Furthermore, such correlations at low temperature have repercussions on the superconducting phase, when there is one. Indeed, Fermi liquids model the normally conducting phase of many known superconductors, and many well-established theories of superconductivity assume a Fermi liquid as the underlying normal state. In these materials, pairing correlations are modified by low dimensionality by virtue of quantum confinement, which produces quantized subbands and alters both the electronic density of states and the pairing interaction. To observe these effects, one can play with the sample geometry and produce superconducting thin films or interfaces, which are often characterized by a low electron density. In these configurations, of low dimensionality and/or low density, superconducting properties like the critical temperature T_c are significantly altered when the Fermi level approaches any band edge in the bulk, or subband edge in a quantum-confined geometry. We study these band-edge effects using a BCS approach for the pairing interaction, for different dimensionality and multiband configurations. This allows us to describe shape resonances, i.e. the oscillatory evolution of T_c as a function of the confinement parameters like the film thickness. We apply the model to bulk low-density superconductors like doped $SrTiO_3$, thin films, and superconducting heterostructures like $LaAlO_3/SrTiO_3$. We interpret the superconducting dome of $LaAlO_3/SrTiO_3$ as a shape resonance due to quantum confinement on bulk $SrTiO_3$.

Résumé en français

Cette thèse porte sur les corrélations électroniques dans la matière quantique, en particulier dans les systèmes métalliques de basse dimensionalité et à basse température. Dans ces conditions, la réponse du liquide composé par les électrons de conduction aux perturbations est modifiée de manière significative par la présence des corrélations: celles-ci rendent la réponse non-locale dans l'espace, c'est-à-dire que les électrons ne réagissent pas seulement à l'endroit où l'on applique la perturbation, mais aussi dans la région environnante. En raison de ce comportement collectif causé par les corrélations microscopiques non-locales, il est possible de décrire macroscopiquement le liquide d'électrons comme un fluide visco-élastique, en analogie avec la théorie de l'élasticité et l'hydrodynamique. Cette description permet d'étudier les modes collectifs qui émergent dans un fluide neutre ou chargé électriquement. Cette approche peut être appliquée pour comprendre la phénoménologie des liquides de Fermi qui décrivent bien l'état de conduction normal de la majorité des métaux. Grâce à l'approche visco-élastique, on peut analyser les modes collectifs qui existent dans

le liquide de Fermi et leur interaction avec le champ électromagnétique: en fonction de la fréquence d'excitation et du temps de relaxation des électrons, la réponse de la surface de Fermi change et peut ressembler à la réponse d'un fluide visqueux ou à la réponse d'un solide élastique; on peut ainsi tracer le diagramme de phase solide-liquide de ce système quantique visco-élastique. Les phenomènes mentionnés ci-dessus laissent des traces observables dans les expériences: par exemple, l'existence combinée de deux modes électromagnétiques dégénérés qui interfèrent de façon cohérente dans le matériau et qui génèrent des oscillations dans les spectres de transmission et réflexion optique en fonction de la fréquence. Ce mécanisme est similaire à l'"effet de peau anormal" qui se manifeste par la saturation à basse température de l'impédance de surface des métaux. En bref, la description visco-élastique permet d'investiguer grâce à la lumière la réponse diélectrique non-locale et les modes collectifs dans les liquides de Fermi. Les analyses effectuées dans cette thèse sont souvent specialisées à des systèmes de basse dimensionnalité: en fait, les couches minces métalliques sont bien adaptées aux expériences optiques car les corrélations non-locales sont amplifiées par la basse dimensionnalité quand le libre parcours moyen des électrons est plus grand que l'épaisseur de la couche. La conclusion de ces études est que les liquides de Fermi montrent des propriétés nouvelles et potentiellement utiles quand on introduit les corrélations visco-élastiques dans le problème, en plus de leurs autres propriétés déjà largement documentées. De plus, ces corrélations ont un impact non-negligeable à basse température sur la phase supraconductrice, quand cette dernière existe dans le matériau. En fait, les liquides de Fermi modélisent l'état de conduction électrique normale des supraconducteurs conventionnels et plusieurs théories bien établies de la supraconductivité supposent que l'état normal est un liquide de Fermi. Dans ces matériaux, les corrélations sont modifiées par la basse dimensionnalité en raison du confinement quantique; ce dernier produit des sous-bandes quantifiées et change la densité d'états électroniques ainsi que l'interaction de couplage. Afin d'observer ces effets, on peut manipuler la géometrie des échantillons en fabriquant des couches minces supraconductrices ou des interfaces, lequelles sont souvent caractérisées par une basse densité électronique. Dans ces configurations, c'est-à-dire basse dimension et basse densité, les propriétés supraconductrices comme la température critique T_c sont altérées de manière significative quand le niveau de Fermi approche le fond d'une sous-bande. Pour cette raison, on étudie dans cette thèse les effets liés à la proximité d'un fond de bande électronique sur l'état supraconducteur en utilisant une approche BCS pour l'interaction de couplage, en présence de plusieurs bandes et en dimension deux et trois. Cette étude permet de décrire les "résonances de forme" caractérisées par une évolution oscillatoire de T_c en fonction des paramètres de confinement, comme l'épaisseur d'une couche mince. On applique ce

modèle aux supraconducteurs 3D de basse densité comme le titanate de strontium ($SrTiO_3$) dopé, aux couches minces et aux interfaces supraconductrices comme $LaAlO_3/SrTiO_3$. On interprète le dôme supraconducteur de l'interface $LaAlO_3/SrTiO_3$ comme une résonance de forme provoquée par le confinement quantique qui agit sur $SrTiO_3$.

Contents

Chapter 1

Electronic correlations in metals

1.1 Introduction

Many-body systems, composed of a macroscopic ensemble of mutually interacting particles, can show very different physical properties with respect to their individual microscopic constituents. Such emergent properties result from correlations among particles: the evolution of one body in space and time influences the behaviour of all other bodies in the ensemble, and vice versa [1, 2]. A prominent consequence of this dynamics in condensed matter is given by collective excitations, whereby all correlated particles in a macroscopic system react with a coordinated evolution in space and time, either spontaneously or in response to an external perturbation of appropriate frequency and momentum. This produces wavelike, self-sustained oscillatory patterns in the system that are named *collective modes*. Classic examples of collective modes are mechanical waves in a rope that is transversally shaken and fixed at one boundary, or waves on the surface of a fluid that is excited by a transversal force at one spatial coordinate. Quantum systems possess collective modes as well, like vibrational excitations of a crystalline lattice, i.e. phonons [3]. The same conclusion applies to the liquid formed by nearly-free conduction electrons in metallic solids.

For an electron liquid, the dispersion relations of density-density collective excitations in the presence of weak correlations are known [4–6], and can be obtained through different techniques, all similar to each other and successively proposed in the literature. The common foundational assumption of most of these techniques is that, when the correlation energy is much smaller than the characteristic kinetic energy of individual electrons, we can treat the latter as nearly free particles; then, correlation effects amount only to the renormalization of quasiparticle properties like effective mass and relaxation time.

Among the different electronic systems that can exist in nature, Fermi liquids offer an exemplary case to study such collective excitations, as their low-energy physics can be described by nearly-independent quasiparticles according to Landau phenomenology; such possibility permits to treat an intrinsically correlated system with the same methods that have been originally developed for independent particles [7, 8]. Since electron liquids are electrically charged, collective modes can be induced in such liquids by applying a space- and time-dependent electric field. The liquid responds to the electric field, for instance with a perturbation in the local electron density and/or by creating electric currents in the system. We first consider the density response in many-body theory. From the perspective of many-body correlation functions, the density collective excitations in an interacting system can be analyzed through the density-density correlation function $C_{\hat{n}(\vec{q},t)\hat{n}(-\vec{q},0)} = \langle \hat{n}(\vec{q},t)\hat{n}(-\vec{q},0)\rangle$, which describes the correlation of the density operator $\hat{n}(\vec{q},t)$ at momentum $\hbar\vec{q}$ and time t, once we let it evolve from time 0. From linear response theory, the density-density correlation function is linked to the charge susceptibility of the system $\chi_{\hat{n}\hat{n}}(\vec{q},t) = -i\theta(t)\langle[\hat{n}(\vec{q},t),\hat{n}(-\vec{q},0)]\rangle$, that is the response to an applied electric field [1, 2]. The correspondent Fourier transform in frequency space is $\chi_{\hat{n}\hat{n}}(\vec{q},\omega)$. We write the Dyson equation for the latter,

$$-\frac{1}{\chi_{\hat{n}\hat{n}}(\vec{q},\omega)} = \frac{1}{\Pi_{\hat{n}\hat{n}}(\vec{q},\omega)} + V_{int}(\vec{q}) \tag{1.1}$$

where the interaction potential is $V_{int}(\vec{q})$ and $\Pi_{\hat{n}\hat{n}}(\vec{q},\omega)$ is the many-body polarization, which indeed describes the polarization of the system in response to the perturbation $V_{int}(\vec{q})$ and sums all irreducible diagrams which screen the bare interaction [1, 2, 9].

Equation (1.1) can be solved formally for the susceptibility $\chi_{\hat{n}\hat{n}}(\vec{q},\omega)$, giving

$$\chi_{\hat{n}\hat{n}}(\vec{q},\omega) = \frac{-\Pi_{\hat{n}\hat{n}}(\vec{q},\omega)}{1 + \frac{V_{int}(\vec{q})}{\mathscr{V}}\Pi_{\hat{n}\hat{n}}(\vec{q},\omega)} \tag{1.2}$$

The graphical representation corresponding to the Dyson equation (1.2), in the case of the density susceptibility $\chi_{\hat{n}\hat{n}}(\vec{q},\omega)$, is

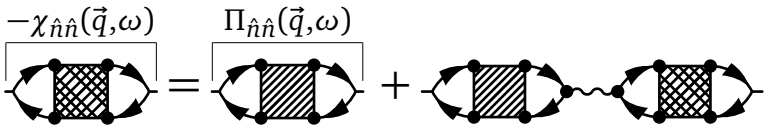

The stable collective excitations of density for the interacting system are given by the

poles of the susceptibility $\chi_{\hat{n}\hat{n}}(\vec{q},\omega)$ in equation (1.2), for which the polarization response is not damped, $Im\{\Pi_{\hat{n}\hat{n}}(\vec{q},\omega)\}=0$. Indeed, we have

$$\chi_{\hat{n}\hat{n}}(\vec{q},\omega)\to\infty \;:\; 1+V_{int}(\vec{q})\Pi_{\hat{n}\hat{n}}(\vec{q},\omega)=0 \qquad (1.3)$$
$$Im\{\Pi_{\hat{n}\hat{n}}(\vec{q},\omega)\}=0$$

In general, there are various kinds of solutions for equation (1.3): sound waves, of dispersion $\omega_\lambda(\vec{q})=v_\lambda q$, with v_λ sound velocity for the branch λ; power-law waves, with dispersion $\omega_\lambda(\vec{q})=\beta q^\alpha$, with $\{\alpha,\beta\}\in\mathbb{R}$; plasmons, of dispersion $\omega_\lambda(\vec{q})=\omega_0+\alpha q^2+o(q^3)$, $\alpha\in\mathbb{R}$, for long-ranged interaction $V_{int}(\vec{q})$; Charge Density Waves (CDW), of static $\omega=0$ and periodic $q\neq 0$ character. In this chapter, we will concentrate on the first three kinds of solutions to equation (1.3), namely sound, other power-law waves, and plasmons.

The results to be shortly derived will be mainly applied to Fermi liquids, for which the dispersion of sound-like excitations has been calculated in detail, and experimentally observed, for example in liquid helium [10, 11]. The inclusion of electronic correlations complicates the problem, and exact general treatments are still lacking; therefore, multiple complementary approaches have been developed, to account for correlation effects in specific regimes of momentum and frequency. Among these approaches, the hydrodynamic perspective offers analytical solutions to the density-density and current-current correlation functions, whenever we can treat the electronic ensemble as a fluid [12]; this simplicity of the formalism and its predictive power make the hydrodynamic approach appealing for correlations phenomenology, and its validity for vanishing wave vector $q\to 0^+$ makes it suitable for optics experiments, that probe this realm around zero wave vector [4, 5, 13]. Having a sound-like mode is in fact a quite general property of condensed matter systems: this occurs each time the hamiltonian has a continuous symmetry (e.g. the translation symmetry), which is spontaneously broken by elementary excitations; such symmetry breaking generates low-energy collective modes (so called Goldstone modes) [14]. We can distinguish two categories of sound-like excitations, depending on the nature of the mechanism that causes the perturbation:

- Normal sound: wave of linear dispersion, originating from pressure gradients on the particle density;
- Zero sound: wave of linear dispersion, stemming from direct short-range interactions between quasiparticles.

As such, zero sound (also called isothermal first sound [15]) can propagate even at zero temperature, depending only on short-range quasiparticle interactions that persist even

in the absence of collisions: this is the very origin of the term "zero sound". On the other hand, normal sound results from pressure gradients and can only exist in the presence of collisions. Sound-like excitations possess a real dispersion relation, with self-sustained propagation, when the collision time among quasiparticles τ_c is sufficiently long compared to the excitation frequency ω, according to $\omega\tau_c \to +\infty$; this is the regime where zero sound propagates. In the opposite collisional regime $\omega\tau_c \ll 1$ the mechanism for sound is governed by collisions in local equilibrium, and the crossover to normal sound develops. Notably, the inclusions of correlations, that introduce spatial nonlocality in the linear response, originate additional propagation modes with respect to the uncorrelated situation, as described in multiple references [12, 16, 17]; in this chapter, we will see how additional propagation modes for electromagnetic radiation appear in electron liquids characterized by a nonlocal response.

1.2 Sound collective excitations in random phase approximation

We first recall the theoretical foundations of the density excitation spectrum in the random phase approximation (RPA), which will serve as a comparison with later sections. In RPA, we take a simple particle-hole bubble as the approximation for the true polarization $\Pi_{\hat{n}\hat{n}}(\vec{q},\omega)$; this means that we can excite particle-hole pairs, but the particle and hole remain mutually independent. In turn, the independence of the particle and the hole in a loop allows to describe such processes through the retarded density-density correlation function, or charge susceptibility $\chi^0_{\hat{n}\hat{n}}(\vec{q},\omega)$, for independent fermions,

$$\chi^0_{\hat{n}\hat{n}}(\vec{q},\omega) = \sum_{\vec{k},\sigma} \frac{f_{FD}(\xi_{\vec{k}}) - f_{FD}(\xi_{\vec{k}+\vec{q}})}{\omega + \xi_{\vec{k}} - \xi_{\vec{k}+\vec{q}}} \tag{1.4}$$

Here, $f_{FD}(\xi_{\vec{k}})$ is the Fermi-Dirac distribution for fermions with dispersion $\xi_{\vec{k}} = E_{\vec{k}} - \mu$, and μ is the chemical potential. Furthermore, in a free-particle system with dispersion $E_{\vec{k}} = \frac{\hbar^2 k^2}{2m}$, the momentum sum in equation (1.4) can be performed analytically at zero temperature. Then, the polarization $\Pi_{\hat{n}\hat{n}}(\vec{q},\omega)$ in RPA is

$$\Pi_{\hat{n}\hat{n}}(\vec{q},\omega) = -\chi^0_{\hat{n}\hat{n}}(\vec{q},\omega) \tag{1.5}$$

In diagrammatic representation, this corresponds to

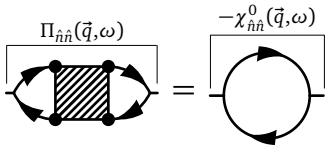

Inserting expression (1.5) in the Dyson equation (1.2), we find the RPA charge susceptibility

$$\chi^{RPA}_{\hat{n}\hat{n}}(\vec{q},\omega) = \frac{\chi^0_{\hat{n}\hat{n}}(\vec{q},\omega)}{1 - V_{int}(\vec{q})\chi^0_{\hat{n}\hat{n}}(\vec{q},\omega)} \tag{1.6}$$

From equation (1.6), we see that the RPA takes into account correlations due to particle-hole loops, with the particle and the hole that propagate freely between creation and recombination, while the renormalization of the particle and hole propagators, and vertex corrections, are both neglected. Therefore, the RPA sums over an infinite number of particle-hole loops connected by the interaction $V_{int}(\vec{q})$. Physically, the random phase approximation is expected to be more accurate for a gas of nearly-independent fermions at high density: in fact, in the high-density limit the kinetic energy becomes the dominant energy scale in the interacting electron gas with respect to electron-electron interactions; then, it is more probable for the excited electron-hole pairs to simply recombine after free propagation instead of interacting with the rest of the Fermi sea. Based on expression (1.6), we can draw the famous graph representing the density excitations of the interacting homogeneous fermion gas [2, 5, 6, 14]; this graph is reported in figure 1.1. In RPA, the dispersion of the principal density collective modes can be calculated analytically [2, 6, 9] for a given interaction potential $V_{int}(\vec{q})$. In order to perform the calculation, first we have to know the bare susceptibility $\chi^0_{\hat{n}\hat{n}}(\vec{q},\omega)$, which is (1.4) for free fermions in three dimensions and at zero temperature. One proceeds by defining a spherical coordinate system where one axis lies along $\vec{q}$, with $\vec{k}$ forming an angle θ with respect to $\vec{q}$. Then, one transforms the sum over $\vec{k}$ in equation (1.4) in an integral according to $\sum_{\vec{k}} \to \frac{1}{(2\pi)^3}\int d\vec{k}$, and introduces the Fermi-level density of states $N_0^{el}(0) = \frac{mk_F}{\pi^2\hbar^2}$ per unit volume for the homogeneous electron gas in 3 dimensions. The Fermi functions in equation (1.4) restrict the integration to $k < k_F$, where $k_F = \left(3\pi^2 n\right)^{\frac{1}{3}}$ is the Fermi wave vector. Finally, it is convenient to define adimensional variables of momentum and frequency according to $x = \frac{q}{2k_F}$ and $z = \frac{2m\omega}{\hbar^2 q^2}$. After integration, the imaginary part of the bare susceptibility (1.4) is

$$Im\left\{\chi^0_{\hat{n}\hat{n}}(\vec{q},\omega)\right\} = -\frac{\pi N_0^{el}(0)}{8x}\left[\max\left\{0, 1-x^2(z-1)^2\right\} - \max\left\{0, 1-x^2(z+1)^2\right\}\right] \tag{1.7}$$

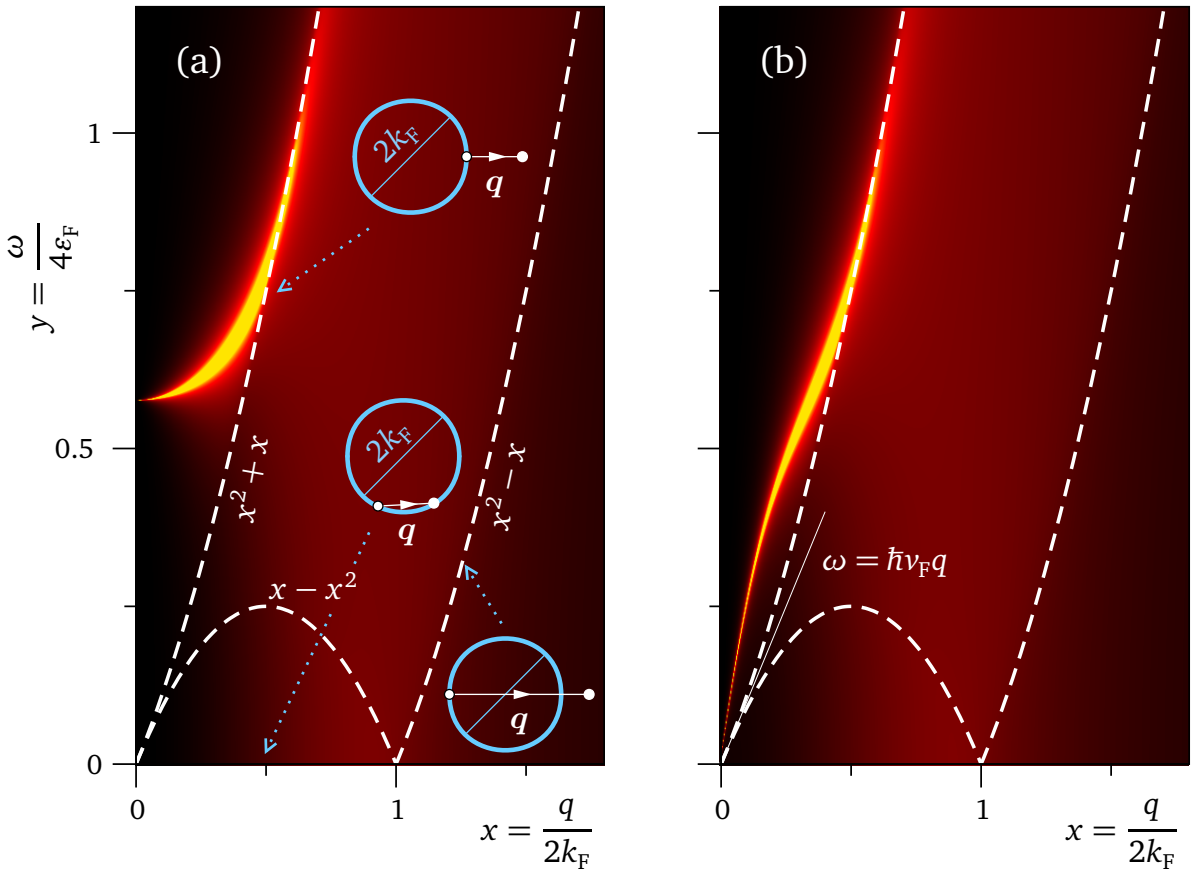

Figure 1.1: Density excitation spectrum in the 3D homogeneous fermion gas for (a) long-range and (b) short-range interaction. The color scale represents the value of $\chi^{RPA}_{\hat{n}\hat{n}}(\vec{q},\omega)$, and shows the plasmon in (a) and the zero sound in (b) as bright lines. Typical particle-hole excitations are sketched in (a). From reference [2].

which is an odd function of frequency ω. The real part of $\chi^0_{\hat{n}\hat{n}}(\vec{q},\omega)$ results

$$Re\left\{\chi^0_{\hat{n}\hat{n}}(\vec{q},\omega)\right\} = \frac{N_0^{el}(0)}{4x}\left\{x(z-1)+\frac{1}{2}\left[1-x^2(z-1)^2\right]\ln\left|\frac{1+x(z-1)}{1-x(z-1)}\right|\right\} - \frac{N_0^{el}(0)}{4x}\left\{x(z+1)+\frac{1}{2}\left[1-x^2(z+1)^2\right]\ln\left|\frac{1+x(z+1)}{1-x(z+1)}\right|\right\} \quad (1.8)$$

The static limit $\omega \to 0$ of equation (1.8) gives the Lindhard function for dielectric screening [1,3], while in the static long-wavelength limit the free-fermion susceptibility is $\chi^0_{\hat{n}\hat{n}}(0,0) = -N_0^{el}(0)$ [2,3]. For a given interaction potential $V_{int}(\vec{q})$, it is sufficient to insert the bare susceptibility $\chi^0_{\hat{n}\hat{n}}(\vec{q},\omega)$ in equation (1.6) to obtain the total RPA susceptibility $\chi^{RPA}_{\hat{n}\hat{n}}(\vec{q},\omega)$. We first focus on the sound excitations $\omega(\vec{q}) = v_S q$, with v_S sound velocity. These excitations exist provided that the interaction is short-ranged. The unrenormalized polarization equals minus the density susceptibility, according to equation (1.5); for long wavelength $q \to 0$, and seeking solutions of the kind $\omega(q) \propto q$, the particle-hole loop contributions can be explicitly evaluated, giving [2,5,6]

$$\underbrace{lim}_{\omega \propto q \to 0} \chi^0_{\hat{n}\hat{n}}(\vec{q},\omega) = -N_0^{el}(0)\left(1-\frac{\zeta}{2}\ln\left|\frac{1+\zeta}{1-\zeta}\right|\right) \quad (1.9)$$

where $\zeta = \frac{v_S}{v_F} = \frac{\hbar q}{m v_F}$,and $v_F = \frac{\hbar k_F}{m} = \frac{\hbar}{m}\left(3\pi^2 n\right)^{\frac{1}{3}}$ Fermi velocity. As derived, (1.9) is valid for free fermions at temperature $T = 0$. Notice that, by only focusing on the long-wavelength limit $q \to 0$ for the interaction $V_{int}(0) = \lim_{q\to 0} V_{int}(\vec{q})$, we assume that the interaction is local, that is, we are neglecting nonlocal effects in the density response. According to the criterion (1.3), the sound collective excitations for the susceptibility (1.9) satisfy the dispersion relation

$$-1+\frac{\zeta}{2}\ln\left|\frac{1+\zeta}{1-\zeta}\right| = \frac{1}{V_{int}(0)N_0^{el}(0)} \quad (1.10)$$

Solving this equation for ζ, we find the sound velocity $v_{S,RPA} = \zeta v_F$. On the graphical representation in figure 1.2, we see that there are always two solutions, one with $\zeta < 1$, and one with $\zeta > 1$. The first solution implies $v_{S,RPA} < v_F$, and corresponds to a damped sound. Indeed, this collective excitation is not self-sustained: if $\zeta < 1$, the line $y = \zeta x$ in figure (1.1) lies within the region where $Im\{\Pi_{\hat{n}\hat{n}}(\vec{q},\omega)\} \neq 0$, meaning that the excitation is not stable, but Landau-damped - see also section 1.5.3. On the contrary, the solution with $v_{S,RPA} > v_F$ corresponds to a propagating sound mode, as we see graphically in figure (1.1), panel (b). In the limit of vanishing interactions, the velocity of this sound approaches the Fermi velocity v_F. The physical nature of the sound-like solution of equation (1.10) is

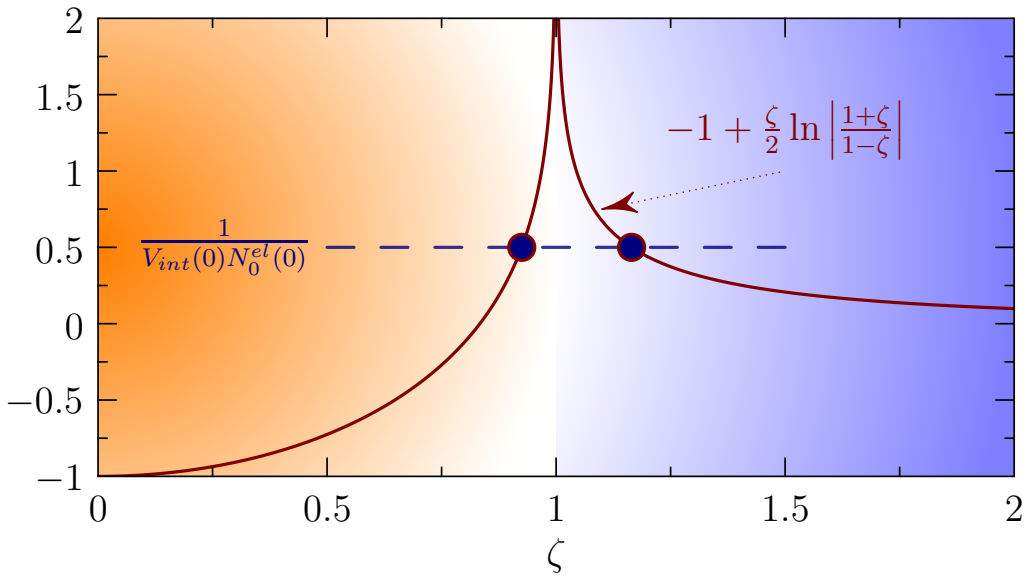

Figure 1.2: Graphical representation of the sound wave solutions (1.10) for the RPA density-density susceptibility [2]. The orange and light blue shaded areas represent the regions of Landau-damped zero sound and propagating zero sound, respectively.

different from the one of normal sound. In the latter case, oscillations of particle density away from thermodynamic equilibrium cause mechanical pressure gradients in the system, which constitute the driving force for the collective excitation. This means that particles have to collide with each other at a sufficient rate $\frac{1}{\tau_c} > 0$, in order to transfer the excitation energy and momentum through the ensemble and propagate the collective mode. In other words, in the time interval between two density oscillations, local thermodynamic equilibrium must be restored for a normal sound to propagate. As the density oscillation rate is set by the excitation frequency ω, this means that the typical collision time τ_c has to be short compared to ω, i.e. $\omega\tau_c < 1$. For an ordinary Fermi liquid, τ_c typically increases like $\frac{1}{T^2}$ with decreasing temperature T, so that the collisional regime $\omega\tau_c < 1$ is no longer satisfied as $T \to 0$: that is why ordinary sound disappears at low temperature. On the other hand, the solution of equation (1.10) is not generated by mechanical pressure gradients like normal sound. Instead, the driving force for this collisionless sound is the direct interaction between particles. Not depending on collisions, this mode can propagate down to zero temperature, where we reach $\omega\tau_c \to +\infty$: this is why such excitation is called zero sound. Hence, equation (1.10) describes the transition from damped zero sound to propagating zero sound by increasing the particle velocity $\frac{v_S}{v_F}$.

The sound-like waves (1.9) in standard RPA do not distinguish between longitudinal and transverse excitations, in the long-wavelength limit $q \to 0$. In order to distinguish

different spatial polarizations of collective modes, we have to move away from the $q \to 0$ limit: in other words, we must have some information on the magnitude and the direction of the excitation wave vector $\vec{q}$, with respect to the mode propagation wave vector $\vec{k}$. In these conditions, the longitudinal and transverse responses show their differences, and we can have multiple oscillation modes of longitudinal or transverse character for the same electronic system. We will later focus on longitudinal and transverse RPA sound-like modes, and we will later apply the same arguments to electrically charged Fermi liquids. Another kind of density-density collective mode that can be analyzed in RPA is the plasmon. This corresponds to a dispersion $\omega(\vec{q}) = \omega_0 + \alpha q^2 + o(q^3),\ \alpha \in \mathbb{R}$, which is admitted for long-ranged interaction $V_{int}(\vec{q})$ such that $V_{int}(0)\chi^{RPA}_{\hat{n}\hat{n}}(0,\omega) \neq 0$ with $\omega > 0$. Expanding equation (1.3) with the RPA polarization (1.5) for $\frac{q}{\omega} \to 0,\ \omega > 0$ at first order in 3 dimensions, we obtain

$$\omega^2 = (\omega_p)^2 \left[\frac{1}{2} + \frac{1}{2}\sqrt{1 + \frac{12}{5}\frac{(v_F)^2}{(\omega_p)^2}q^2} \right] \tag{1.11}$$

where $\omega_p = \sqrt{\frac{ne^2}{m\epsilon_0}}$. Therefore, equation (1.11) becomes ω_p at $q = 0$, and shows the quadratic dispersion $\omega_{plasmon}(\vec{q}) = \omega_p + \frac{3(v_F)^2}{10\omega_p}q^2 + O(q^3)$ at second order in momentum $\vec{q}$. All in all, the RPA is a good way to describe density-density excitations in simple metals, when correlation effects are weak. For example, the quadratic plasmon dispersion has been observed and found experimentally in good agreement with RPA, for Na, Mg, Al, and Si [2]. However, there are cases where some deviations with respect to RPA are visible, even for metals such as K, Rb, and Cs [18]; typically, these cases exhibit stronger correlation effects, which cannot be entirely captured by the single electron-hole excitations of RPA [6, 19]. In fact, as previously mentioned, the random phase approximation neglects both the renormalization of the quasiparticle-quasihole propagator and vertex corrections: for example, the exchange hole for quasiparticles possessing the same spin, due to the Pauli exclusion principle [6]. As described in multiple references [6], going beyond RPA is not a straightforward task, and an exact solution is still lacking.

1.3 Theoretical toolbox for radiation-matter interaction

1.3.1 The dielectric function and linear response

The dielectric function $\epsilon(\vec{q}, \omega)$ provides the traditional grounding for calculating the optical properties of materials, and specifically metals. The physical reason for this is that $\epsilon(\vec{q}, \omega)$

represents the screening reaction of the material to external electric fields, which renormalizes the latter fields; in the language of many-body theory, this is naturally connected to the many-body polarization of the medium, entering into the susceptibility (1.1). We will comment more on the many-body aspects of screening in the next section 1.3.2, while here we rapidly review the most relevant aspects of classical macroscopic properties of dielectrics, for what concerns this work.

In linear and isotropic media, the macroscopic electric and displacement fields, $\vec{E}(\vec{r},t)$ and $\vec{D}(\vec{r},t)$, are colinear. In this case, the two fields are related via the dielectric function $\epsilon(\vec{r}-\vec{r}^{'},t-t^{'})$: in real space of coordinates $\vec{r}$ and time t, and for a translation-invariant response in space and time, we have

$$\vec{D}(\vec{r},t)=\int d\vec{r}^{'}\int dt^{'}\epsilon(\vec{r}-\vec{r}^{'},t-t^{'})\vec{E}(\vec{r}^{'},t^{'}) \tag{1.12}$$

which, in reciprocal space of momenta $\vec{q}$ and frequency ω, becomes

$$\vec{D}(\vec{q},\omega)=\epsilon(\vec{q},\omega)\vec{E}(\vec{q},\omega) \tag{1.13}$$

We notice that the real-space form (1.12) highlights a fundamental property of dielectric response: the latter is *nonlocal in space* and *retarded in time*, in general: the field at coordinates $\{\vec{r},t\}$ is not only determined by the excitation at the same coordinates $\{\vec{r},t\}$, but it is also influenced by the excitation at other coordinates $\left\{\vec{r}^{'},t^{'}\right\}$. This happens because the material response function, which is the dielectric function in equation (1.12) is spatially nonlocal and retarded in time. In the same way as the electric displacement field in equation (1.12), this holds for the current response through Ohm's law

$$\vec{J}(\vec{r},t)=\int d\vec{r}^{'}\int dt^{'}\sigma(\vec{r}-\vec{r}^{'},t-t^{'})\vec{E}(\vec{r}^{'},t^{'}), \tag{1.14}$$

where $\sigma(\vec{r}-\vec{r}^{'},t-t^{'})$ is the conductivity [1, 4, 5], or in Fourier space of momenta and frequency

$$\vec{J}(\vec{q},\omega)=\sigma(\vec{q},\omega)\vec{E}(\vec{q},\omega). \tag{1.15}$$

Let us focus on spatial nonlocality of the response: applying an excitation at $\vec{r}^{'}$ produces a response at $\vec{r}^{'}$ but also at other points $\vec{r}$. However, one often simplifies the analysis of transport and optical experiments by assuming a local response: this means that the response function does not depend on the distance $\vec{r}-\vec{r}^{'}$, which corresponds to neglecting the momentum dependence through the limit $q\to 0$. Indeed, if $\epsilon(\vec{r}-\vec{r}^{'},t)$ does not depend

on $\vec{r}-\vec{r}'$, its Fourier transform (1.15) is $\epsilon(\vec{q},\omega) \propto \delta(q)$. In reality, the response depends on spatial distance: in this case, taking the limit $q \to 0$ means taking the spatial average of the $\vec{r}-\vec{r}'$-dependent response function. This is what optical experiments commonly do, since electromagnetic radiation probes the limit $q \to 0$ of the material response [1, 4, 5]. Nevertheless, we have seen throughout this chapter that we cannot operate this limit in particular instances, like for metals at low temperatures. We will see that, in the latter situation, one is able to probe finite-momentum physics with electromagnetic radiation, because of the nonlocality of the material response

It is convenient to separate the fields in two components, one parallel and the other normal to the wave-vector $\vec{q}$, also named longitudinal and transverse respectively: $\vec{E}(\vec{q},\omega) = \vec{E}_{\parallel}(\vec{q},\omega) + \vec{E}_{\perp}(\vec{q},\omega)$ with $\vec{q}\cdot\vec{E}_{\parallel}(\vec{q},\omega) = qE_{\parallel}(\vec{q},\omega)$ and $\vec{q}\cdot\vec{E}_{\perp}(\vec{q},\omega) = 0$, and similarly for $\vec{D}(\vec{q},\omega)$. Likewise, the dielectric function is split in longitudinal and transverse components $\epsilon_L(\vec{q},\omega)$ and $\epsilon_T(\vec{q},\omega)$, so that

$$\vec{D}_{\parallel}(\vec{q},\omega) = \epsilon_L(\vec{q},\omega)\vec{E}_{\parallel}(\vec{q},\omega) \tag{1.16a}$$

$$\vec{D}_{\perp}(\vec{q},\omega) = \epsilon_T(\vec{q},\omega)\vec{E}_{\perp}(\vec{q},\omega) \tag{1.16b}$$

In the longitudinal channel, the sources of $\vec{D}_{\parallel}(\vec{q},\omega)$ and $\vec{E}_{\parallel}(\vec{q},\omega)$ are the "free" portion and the total charge density $\rho = en$, respectively [5]: physically, this means that $\vec{D}_{\parallel}$ considers the net dielectric response taking into account the medium polarization, i.e. how the electron density in the material reacts to a longitudinal electric field with $\epsilon_L(\vec{q},\omega)$. Likewise, in the transverse channel $\vec{D}_{\perp}$ takes into account the dielectric response $\epsilon_T(\vec{q},\omega)$ of the material in the perpendicular direction with respect to the wave vector $\vec{q}$. Since electromagnetic waves are transversally polarized, $\epsilon_T(\vec{q},\omega)$ is the quantity involved in the study of radiation-matter interaction.

1.3.2 The photon propagator

The dielectric polarization of a material, in response to interactions with incident electromagnetic radiation, can also be analyzed from a complementary viewpoint with respect to the dielectric function formalism of section 1.3.1: rather than describing the material dielectric polarization and screening with $\epsilon(\vec{q},\omega)$ in reaction to the electromagnetic field of the incoming wave, we can equivalently describe with a vector potential $\vec{A}_T(\vec{q},\omega)$ how the propagation of the electromagnetic radiation is affected when the wave enters the material. The latter perspective, utilized in quantum electrodynamics, requires the calculation of the transverse photon propagator.

As a matter of principle, one has to distinguish the longitudinal and transverse responses of the medium. The magnetic field $\vec{B}(\vec{q},\omega)$ and propagating photons are purely transverse; the transverse part of the vector potential $\vec{A}_T(\vec{q},\omega)$ is gauge-invariant, whereas the longitudinal component transforms like $\vec{A}_L^{'}(\vec{q},\omega)=\vec{A}_L(\vec{q},\omega)+\nabla\Xi$ under the gauge transformation Ξ and is not physical. Therefore, everything that is measured by propagating light is in the transverse sector, while the static electric screening and the electron-loss-density spectra are exclusively longitudinal and couple to the charge density [5, 17]. The macroscopic field $\vec{A}(\vec{q},\omega)$ is generated microscopically by the propagation of photons, the quanta of electromagnetic radiation. In order to see this, one quantizes the electromagnetic field into optical modes whose state α is specified by wave vector $\vec{q}$, frequency ω and polarization $\vec{u}$, in analogy with the quantization of the harmonic oscillator [17, 20]. Hence, photons are destroyed and created according to the annihilation and creation operators $\left\{\hat{A}_\alpha,\hat{A}_\alpha^\dagger\right\}$. One can also consider photons in the basis of space coordinates $\vec{r}$ and time t through the usual Fourier transforms. In the thermodynamic limit, we retrieve the classical electromagnetic fields from the microscopic description of photons. Many-body theory can effectively describe the interaction of such ensemble of photons with the surrounding matter. In metals, the radiation propagates inside the material and excites interaction processes with the electron liquid, so that, by propagating a photon at point $\vec{r}$ and at time 0 and measuring it at point $\vec{r}^{\,'}$ and time τ, we can infer its interactions with the medium. This is the physical concept of the photon propagator. We assume again a translationally-invariant response, which leads to

$$\mathscr{A}_{\alpha\beta}(\vec{r}-\vec{r}^{\,'},\tau)=-\left\langle \hat{T}_\tau \hat{A}_\alpha(\tau)(\vec{r})\hat{A}_\beta^\dagger(0)(\vec{r}^{\,'})\right\rangle \tag{1.17}$$

The photon operators obey the same gauge invariance as the corresponding macroscopic fields, so we can decompose equation (1.17) into its longitudinal and transverse components, with the latter that enters into the electromagnetic transverse response. In the domain of momenta and frequency, the transverse photon propagator becomes

$$\mathscr{A}_T(\vec{q},\omega)=\frac{1}{\epsilon_0(\omega^2-c^2q^2)+\Pi_{\vec{j}\vec{j}}(\vec{q},\omega)} \tag{1.18}$$

where $\Pi_{\vec{j}\vec{j}}(\vec{q},\omega)$ is the transverse (current) many-body polarization of the medium, which contains the information about the interaction processes of photons with the material. In fact, the correlated electron system responds to the propagation of electromagnetic radiation; this affects the optical properties. Equation (1.18) directly stems from the Dyson equation of the photon propagator [21], in the same way as equation (1.1) for the density susceptibility. In the present case, it describes the interacting photon propagator due to the material response. The correspondence with the macroscopic electromagnetic

fields is always preserved: choosing the radiation gauge in which the scalar potential $\phi_\sigma = 0$ [5,21], the photon propagator satisfies the wave equation, consistently with the macroscopic Maxwell equations. From equation (1.18), one obtains the relation between the microscopic many-body polarization and the macroscopic dielectric function. For a homogeneous and isotropic body and in Fourier space of momenta and frequency, this relation reads

$$\Pi_{jj}(\vec{q},\omega) = \epsilon_0 \left[\epsilon_T(\vec{q},\omega) - 1\right] \omega^2 \tag{1.19}$$

Therefore, the dielectric function can be obtained in terms of the transverse many-body polarization as

$$\epsilon_T(\vec{q},\omega) = 1 + \frac{\Pi_{jj}(\vec{q},\omega)}{\epsilon_0 \omega^2} \tag{1.20}$$

The dielectric function (1.20) is manifestly nonlocal, depending on q as well as on ω. This way, inserting equation (1.20) into the definition (1.18), the photon propagator can be written in an equivalent form

$$\mathscr{A}_T(\vec{q},\omega) = \frac{1}{\epsilon_0} \frac{1}{\epsilon_T(\vec{q},\omega)\omega^2 - q^2 c^2} \tag{1.21}$$

A pole in the photon propagator (1.21) signals the emergence of a transverse collective mode for the light-matter system, in the same way as the divergence of the many-body susceptibility (1.2) in section 1.1 indicates the propagation of a density-density collective mode. In turn, a stable pole in equation (1.21) implies that there is no imaginary part, $Im\left\{\epsilon_T(\vec{q},\omega)\omega^2 - q^2c^2\right\} = 0$, i.e. the polarization response is not damped. Analogously, for the photon propagator we have $Im\left\{\mathscr{A}_T(\vec{q},\omega)\right\} \to \infty$: this is the same general principle for propagating collective modes as for the density susceptibility (1.2) in section 1.1. When the polarization response of the system is not damped, i.e. $Im\left\{\epsilon_T(\vec{q},\omega)\right\} = 0$, the photon propagator becomes real, i.e. $Im\left\{\mathscr{A}_T(\vec{q},\omega)\right\} = 0 \forall \left\{\vec{q},\omega\right\}$. In this case, a collective mode simply corresponds to the divergence of the real photon propagator, $|\mathscr{A}_T(\vec{q},\omega)| \to +\infty$.

1.4 Nonlocal density and current responses

The standard RPA formalism of section 1.2 allows us to describe density excitations in the local limit $q \to 0$, which are sound waves. However, as sketched in the previous section 1.3, many physical properties of correlated electronic systems depend on spatially nonlocal response functions: the state of one electron at position $\vec{r}$ influences the state of another electron at position $\vec{r}' \neq \vec{r}$, which translates into a $\vec{q}$ dependence of the response in reciprocal space [6,22,23]. Notice that this happens even if the excitation potential is completely local,

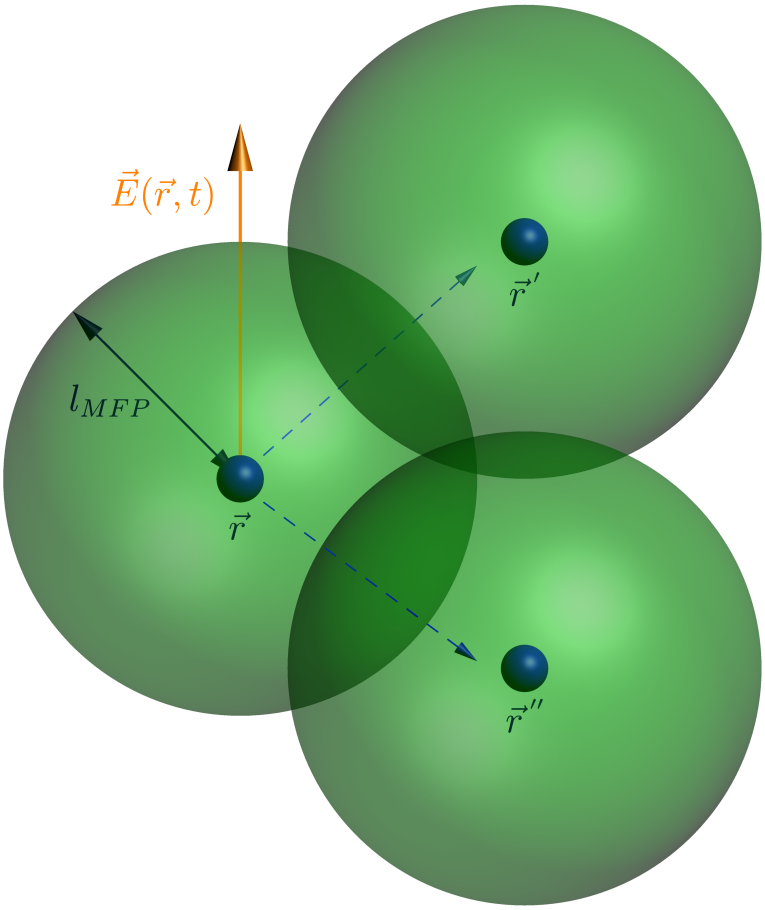

Figure 1.3: Schematic representation of nonlocal response of an electron liquid to an electric field $\vec{E}(\vec{r},t)$: in real space, electrons - depicted as blue particles - are mutually coherent up to a distance equal to the mean free path $l_{MFP} = v_F \tau_c$; this coherence volume is represented as green spheres. Mutually coherent electrons give rise to a nonlocal response, whereby by exciting locally one electron at coordinate $\vec{r}$, also other electrons respond at different coordinates $\vec{r}'$ and $\vec{r}''$ within the coherence volumes set by l_{MFP}.

$\lim_{q\to 0} V_{int}(\vec{q})$, because the nonlocality emerges anyway from the q-dependent response function like the dielectric function (1.15). As we will see in this section, the typical spatial distance over which electrons respond coherently, and therefore influence each other nonlocally, is the mean free path $l_{MFP} = v_F \tau_c$, with $\tau_c \in \mathbb{R}^+$ an interaction-dependent relaxation time. At distances beyond l_{MFP}, electrons lose coherence and their behaviour becomes diffusive: hence, the mean free path sets the length scale above which the response function of electrons is governed by diffusion. This picture is schematically illustrated by figure 1.3. In ordinary metals, l_{MFP} can increase by some orders of magnitude at cryogenic temperatures, due to the increase of the relaxation time [3]: for this reason, the results of this section are relevant for low-temperature metallic systems. When the electronic density

$n(\vec{r},t)$ is redistributed in the system by nonlocal perturbations, giving rise to electron diffusion at distances beyond l_{MFP}, this behaviour is dissipative [22, 23]: in fact, the change of the local density field causes local relaxation among quasiparticles with energy dissipation. By the fluctuation-dissipation theorem [14], a change in density in response to an excitation potential $V_{int}(\vec{q})$ is given by the density susceptibility (1.2). Here we evaluate the corrections to the results of the previous section 1.2, when nonlocal correlations are not negligible. There are many momentum-dependent interaction processes that could give rise to nonlocality in the density response. How can we distinguish the most relevant processes in electron liquids? We still retain the quasiparticle picture by which the low-energy elementary excitations are electron-hole excitations. In the next section 1.4.1, we will see that a first-order effect of a short-ranged interaction $V_{int}(\vec{q})|_{q\to 0}$ is to generate a self-energy $\Sigma(\vec{k},\omega)$, the imaginary part of which gives a finite lifetime $\tau_{lf}=\tau_c<+\infty$ for quasiparticle excitations. Physically, since we have an interacting quasielectrons ensemble, the medium react to a density (charge) excitation through a many-body polarization $\Pi_{\hat{n}\hat{n}}(\vec{q},\omega)$. In section 1.2, we considered a single noninteracting electron-hole bubble (1.5) for the polarization, according to RPA. This becomes inaccurate for interacting electrons: the properties of the quasielectron and the quasihole in a bubble are renormalized by the self-energy $\Sigma(\vec{k},\omega)$, due to interactions with the ensemble. This influences the many-body polarization of the medium, i.e. $\Pi_{\hat{n}\hat{n}}(\vec{q},\omega)$, which is now calculated with renormalized propagators [1, 2].

Here, we consider the effect of short-ranged impurity scattering in first Born approximation - see section 1.4.2 - to model the self-energy that we add prior to the RPA resummation. In this approach, the renormalized electron and hole in a bubble are still noninteracting. This approximation holds provided that interactions between the renormalized electron and hole in a bubble are sufficiently weak compared to their energies $\xi_{\vec{k}}$. In this case, we can neglect *vertex corrections*, which represent the sum of all irreducible processes that renormalize the interaction at the vertex of an electron-hole bubble [1, 2, 23]. In this physical picture, the density response of the system to an external $\vec{q}$-dependent excitation is given by an RPA series of nearly-independent electron-hole pairs, renormalized by a long-wavelength potential V_0, e.g. representing impurity scattering. The polarization bubble of quasielectrons at k_F naturally depends on momentum, i.e. it is nonlocal. For $q\to 0^+$, the simultaneous presence of nonlocality and of a finite quasiparticle relaxation time τ_c gives rise to a *diffusive* pole for the solid angle-averaged polarization $\langle\Pi_{\hat{n}\hat{n}}(\vec{q},\omega)\rangle_{ang}$, which depends on the mean free path $l_{MFP}=v_F\tau_c$. In view of the arguments above, we

can write the interacting density susceptibility as

$$\chi_{\hat{n}\hat{n}}(\vec{q},\omega) = \frac{\chi^{I}_{\hat{n}\hat{n}}(\vec{q},\omega)}{1 - V_{int}(\vec{q})\chi^{I}_{\hat{n}\hat{n}}(\vec{q},\omega)} \tag{1.22}$$

where the susceptibility $\chi^{I}_{\hat{n}\hat{n}}(\vec{q},\omega) = -\Pi^{RPA}_{\hat{n}\hat{n}}(\vec{q},\omega)$ takes into account the finite relaxation time τ_c for free propagators, as in section 1.4.1.

In the following sections, we first model the relaxation time τ_c, then we calculate the many-body polarization $\Pi^{RPA}_{\hat{n}\hat{n}}(\vec{q},\omega)$, which will lead us to the RPA dielectric properties of the system.

1.4.1 Single-particle self-energy and lifetime

In RPA, the electron and hole propagators are given by the free particle Green's functions, which are written as $\mathcal{G}^0(\vec{k},\omega) = \frac{1}{\omega - \xi_{\vec{k}}}$ in reciprocal space of momentum and frequency. In the latter expression, $\xi_{\vec{k}} = E_{\vec{k}} - \mu$ are the electron energy eigenvalues $E_{\vec{k}}$ at momentum $\vec{k}$ referred to the chemical potential μ. Being noninteracting, these propagators represent stable excitations of infinite lifetime. However, single-particle excitations do interact with their surroundings in practical condended-matter systems. In general, the interacting propagator acquires a self-energy $\Sigma = \Sigma(\vec{q},\omega)$, which is the result of all the interaction processes experienced by the particle throughout its propagation in the ensemble. [1,2]. Intuitively, one can imagine this as the particle "dragging" a cloud of excitations of the medium, all together forming a quasiparticle with its own velocity, energy, and a finite lifetime $\tau_{lf} < +\infty$ due to the dynamical nature of the cloud. The real part of the self-energy enters into the quasiparticle spectral weight, according to

$$\frac{1}{Z(\vec{k})} = 1 - \left.\frac{\partial Re\left\{\Sigma(\vec{k},\omega)\right\}}{\partial\,\omega}\right|_{\omega=0} \tag{1.23}$$

If we can neglect the momentum dependence $Re\left\{\Sigma(\vec{k},\omega)\right\} \equiv Re\left\{\Sigma(\omega)\right\}$, then the spectral weight represents the effective mass of the quasiparticle according to $\frac{m^*}{m} = \frac{1}{Z(\vec{k})}$.

Similarly, the imaginary part of the self-energy gives a finite quasiparticle lifetime

$$\Gamma(\vec{k},\omega) = -2Z(\vec{k})Im\left\{\Sigma(\vec{k},\omega)\right\} \tag{1.24}$$

$$\tau_{lf}(\vec{k},\omega) = \frac{1}{2\Gamma(\vec{k},\omega)} \tag{1.25}$$

Let us consider the lifetime $\tau_c \equiv \tau_{lf}$ acquired by quasiparticles in an electron liquid

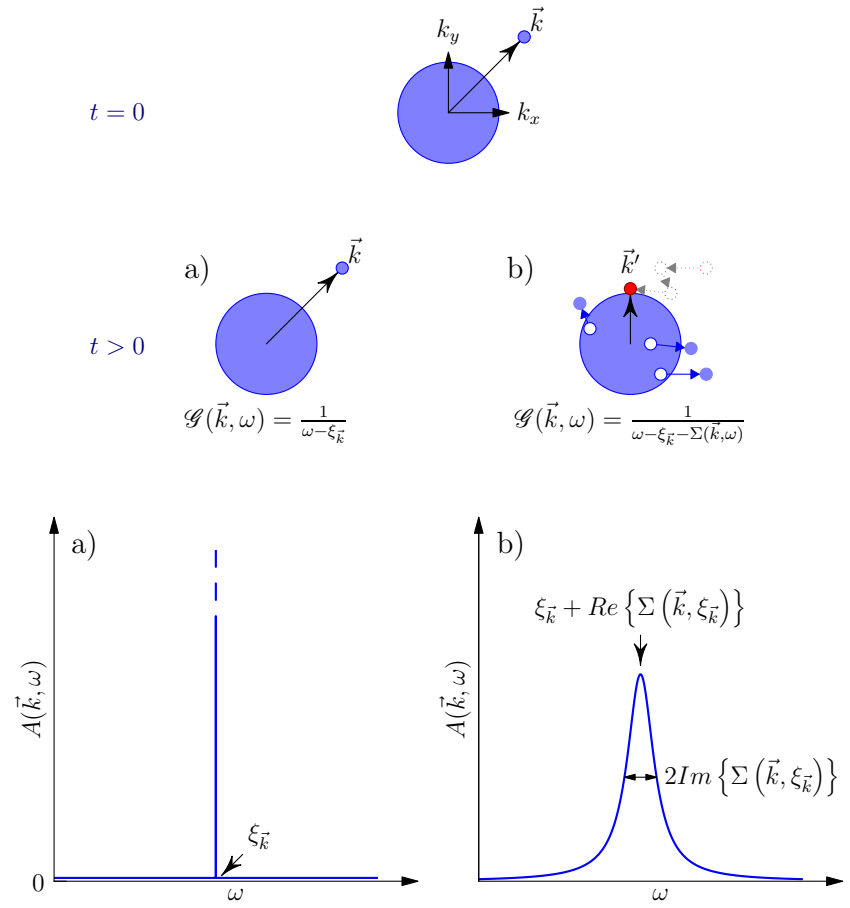

Figure 1.4: Top row: schematic representation of a quasielectron excitation with wave vector $\vec{k}$ outside of the Fermi surface, at time $t = 0$. Middle row: evolution of the quasielectron excitation at time $t > 0$. In the noninteracting case a), the free quasielectron does not have a self-energy, and therefore it is a stable excitation. In the interacting case b), the quasielectron interacts with the Fermi sea, creating other electron-hole excitations and thereby losing momentum and energy: the quasielectron acquires a self-energy $\Sigma(\vec{k},\omega)$, which implies a finite lifetime τ_{lf} and an increased effective mass. Bottom row: spectral function $\vec{A}(\vec{k},\omega) = -\frac{1}{\pi} Im\left\{\mathcal{G}(\vec{k},\omega)\right\}$ [1,9]. In the noninteracting case a), the spectral function is simply a Dirac delta function peaked at the quasielectron energy $\xi_{\vec{k}}$. In case b), interactions broaden the spectral function to a lorentzian centered at the energy to $\xi_{\vec{k}} + Re\left\{\Sigma(\vec{k},\xi_{\vec{k}})\right\}$ and having full width at half maximum $2Im\left\{\Sigma(\vec{k},\xi_{\vec{k}})\right\}$ [1,2].

that interacts with its surroundings (e.g with the crystalline lattice, impurities and so on) through a momentum-dependent potential $V_{int}(\vec{q})$. This can describe the relaxation of quasielectrons at the Fermi surface, i.e. $\vec{k} = \vec{k}_F$. At low excitation energies and temperatures, the dominant source of finite quasiparticle lifetime is impurity scattering [2], which originates the residual resistivity of metals. Let the impurity concentration be n_i, and the correspondent potential be $V_{imp}(\vec{q})$. For many applications, this scattering can be modeled in the first Born approximation (1BA), taking into account the second (two-scattering) term in the self-energy expansion

$\Sigma^{\text{FBA}}(\vec{k},\omega) =$ 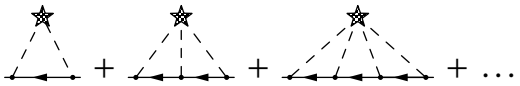 $+ \ldots$

The first term in the series (not shown) gives a constant, which can be reabsorbed into the definition of the chemical potential μ for all practical purposes [23]. The second (1BA) term of the series yields a frequency- and momentum- dependent self-energy $\Sigma^{1BA}(\vec{k},\omega)$, which reads

$$\Sigma^{1BA}(\vec{k},\omega) = \frac{n_i}{\mathcal{V}} \sum_{\vec{q}} \frac{\left|V_{imp}(\vec{q})\right|^2}{\omega - \xi_{\vec{k}-\vec{q}}} \tag{1.26}$$

An analysis of 1BA for impurity scattering in metallic hosts near the Fermi level reveals that, for $\vec{k} \approx \vec{k}_F$, the self-energy is almost constant with ω [2]. Hence, in many practical applications (low energy and momentum close to k_F), one can take into account the effect of impurities by introducing a phenomenological self-energy that is purely imaginary

$$\Sigma^{1BA}(\vec{k},\omega) \approx -i\Gamma, \tag{1.27a}$$

$$\Gamma = 4\pi n_i (V_0)^2 N_0^{el}(0),\ k \approx k_F \tag{1.27b}$$

where $V_0 \equiv \lim_{q\to 0} V_{imp}(\vec{q})$ is the long-wavelength impurity scattering potential, and $N_0^{el}(0)$ is the electron density of states at the Fermi level. The scattering rate (1.27) gives a lifetime $\tau_{lf} = \tau_c = \frac{1}{2\Gamma}$. Hence, quasielectrons at the Fermi surface acquire a lifetime through scattering off the long-wavelength impurity potential V_0. Apart from impurities, the same argument applies to a generic momentum-dependent potential with a well-defined long-wavelength limit $\left|\lim_{q\to 0} V_{int}(\vec{q})\right| < +\infty$. Hence, we introduce a relaxation rate (1.27b) at the poles of the quasiparticle propagator [23], as

$$\mathcal{G}(\vec{k},\omega) = \frac{1}{\omega + i\Gamma sign(\omega) - \xi_{\vec{k}}} \tag{1.28}$$

where $2\Gamma = \frac{1}{\tau_c}$.

1.4.2 Renormalized polarization bubble

Given the interacting propagator (1.28), we can calculate the renormalized electron-hole bubble using the spectral representation of Green's functions [1, 2, 23]. We have

$$\chi^I_{\hat{n}\hat{n}}(\vec{q},\omega) = -\Pi^{RPA}_{\hat{n}\hat{n}}(\vec{q},\omega) = \sum_{\vec{k},\sigma}\int d\epsilon_1 d\epsilon_2 \frac{\Gamma/\pi}{(\epsilon_1-\xi_{\vec{k}})^2+\Gamma^2}\frac{\Gamma/\pi}{(\epsilon_2-\xi_{\vec{k}+\vec{q}})^2+\Gamma^2}\frac{f_{FD}(\epsilon_1)-f_{FD}(\epsilon_2)}{\omega+i0^+ +\epsilon_1-\epsilon_2} \tag{1.29}$$

For long-wavelength excitations, we can expand the $\vec{q}$-dependent portion of the denominator in eq. (1.29) according to $\xi_{\vec{k}+\vec{q}} = \xi_{\vec{k}} + \frac{1}{\hbar}\nabla_{\hbar\vec{k}}\xi_{\vec{k}}\cdot\vec{q} + o(q)^2$. Linearizing the parabolic dispersion $\xi_{\vec{k}} = \frac{\hbar^2k^2}{2m} - \mu$ for $\vec{k}\approx\vec{k}_F$, we have $\frac{1}{\hbar}\nabla_{\vec{k}}\xi_{\vec{k}} \equiv \vec{v}_{\vec{k}} = \frac{\hbar\vec{k}}{m}$, therefore

$$\chi^I_{\hat{n}\hat{n}}(\vec{q},\omega) = \sum_{\vec{k},\sigma}\int d\epsilon_1 d\epsilon_2 \frac{\Gamma/\pi}{(\epsilon_1-\xi_{\vec{k}})^2+\Gamma^2}\frac{\Gamma/\pi}{(\epsilon_2-\xi_{\vec{k}}-\vec{v}_{\vec{k}}\cdot\vec{q})^2+\Gamma^2}\frac{f_{FD}(\epsilon_1)-f_{FD}(\epsilon_2)}{\omega+\epsilon_1-\epsilon_2}$$

We transform the sum over momentum $\vec{k}$ and spin σ into an integral over energies $\xi_{\vec{k}}\equiv\xi$, using the total density of states $N_0^{el}(\epsilon) = \sum_{\vec{k},\sigma}\delta(\epsilon-\xi_{\vec{k}})$. This way, the sum over $\vec{k}$ becomes a double integration over the solid angle element $\frac{d\Omega_a}{4\pi}$ and on surfaces of constant energy ξ. Having in mind electrons at the Fermi surface, we approximate the density of states to the constant $N_0^{el}(0)$ at the Fermi energy. This also fixes the value of the velocity $\vec{v}_{\vec{k}}$ to the Fermi velocity $\vec{v}_F$. Then, we use the property of Lorentian functions $\frac{1}{\pi}\int d\xi \frac{\Gamma^2}{[(\epsilon_1-\xi)^2+\Gamma^2][(\epsilon_2-\vec{v}_F\cdot\vec{q}-\xi)^2+\Gamma^2]} = \frac{2\Gamma}{(\epsilon_1-\epsilon_2+\vec{v}_F\cdot\vec{q})^2+(2\Gamma)^2}$, to obtain

$$\chi^I_{\hat{n}\hat{n}}(\vec{q},\omega) = \frac{2\Gamma N_0^{el}(0)}{\pi}\int d\epsilon d\epsilon_2 \left\langle \frac{1}{(\epsilon+\vec{v}_F\cdot\vec{q})^2+(2\Gamma)^2}\right\rangle_{ang}\frac{f_{FD}(\epsilon_2+\epsilon)-f_{FD}(\epsilon_2)}{\omega+\epsilon+i0^+} \tag{1.30}$$

where $\epsilon=\epsilon_1-\epsilon_2$; the brackets $\langle\cdot\rangle_{ang}$ denote the angular integration over the solid angle, i.e. for a function $F(\vec{q},\omega)$ we have $\langle F(\vec{q},\omega)\rangle_{ang} = \int\frac{d\Omega_a}{4\pi}F(\vec{q},\omega) = \frac{1}{4\pi}\int_0^{2\pi}d\phi\int_0^{\pi}\sin\theta d\theta F(\vec{q},\omega)$, where θ and ϕ are the angles formed by $\vec{q}$ in a reference system where one cartesian axis is along $\vec{v}_F$. We first evaluate the integral over ϵ in equation (1.30), which allows us to

find the imaginary part

$$Im\left\{\chi^I_{\hat{n}\hat{n}}(\vec{q},\omega)\right\} = -2\Gamma N_0^{el}(0)\int d\epsilon_2 \left\langle \frac{1}{(-\omega+\vec{v}_F\cdot\vec{q})^2+(2\Gamma)^2}\right\rangle_{ang}[f_{FD}(\epsilon_2-\omega)-f_{FD}(\epsilon_2)] \tag{1.31}$$

Now we evaluate the integral over ϵ_2, to obtain the imaginary part

$$Im\left\{\chi^I_{\hat{n}\hat{n}}(\vec{q},\omega)\right\} = -\left\langle \frac{2\Gamma N_0^{el}(0)\omega}{(\omega-\vec{v}_F\cdot\vec{q})^2+(2\Gamma)^2}\right\rangle_{ang} \tag{1.32}$$

The corresponding real part of the susceptibility can be calculated from eq. (1.32) using Kramers-Kronig relations, which are valid for causal functions [4, 5]. We have

$$\begin{aligned} Re\left\{\chi^I_{\hat{n}\hat{n}}(\vec{q},\omega)\right\} &= -\frac{1}{\pi}\mathscr{P}\int d\varepsilon \frac{1}{\omega-\varepsilon} Im\left\{\chi^I_{\hat{n}\hat{n}}(\vec{q},\varepsilon)\right\} \\ &= -N_0^{el}(0)\left\langle \frac{(2\Gamma)^2-(\vec{v}_F\cdot\vec{q})(\omega-\vec{v}_F\cdot\vec{q})}{(\omega-\vec{v}_F\cdot\vec{q})^2+(2\Gamma)^2}\right\rangle_{ang} \end{aligned} \tag{1.33}$$

where the symbol $\mathscr{P}\int$ denotes the Cauchy principal value. We add the real (1.33) and imaginary (1.32) parts to find the complex polarization bubble

$$\chi^I_{\hat{n}\hat{n}}(\vec{q},\omega) = N_0^{el}(0)\left\langle \frac{\vec{v}_F\cdot\vec{q}-2i\Gamma}{\omega-\vec{v}_F\cdot\vec{q}+2i\Gamma}\right\rangle_{ang} \tag{1.34}$$

Notice that the result (1.34) is consistent with Kramers-Kronig relations by construction. In the long-wavelength, low-frequency limit we retrieve the standard result $\lim_{\omega\to 0, q\to 0}\chi^I_{\hat{n}\hat{n}}(\vec{q},\omega) = -N_0^{el}(0)$ [1, 2]. Equation (1.34) shows that the presence of a long-wavelength impurity-like potential modifies the density susceptibility with respect to the standard RPA case of section 1.2.

1.4.3 Dielectric properties with nonlocal correlations: density response

Equipped with the renormalized polarization bubble (1.34), we are ready to calculate the RPA susceptibility (1.22) and the associated dielectric function. In RPA, the many-body polarization is just $\Pi^{RPA}_{\hat{n}\hat{n}}(\vec{q},\omega) = -\chi^I_{\hat{n}\hat{n}}(\vec{q},\omega)$ [1, 2, 23]. Hence, we have

$$\Pi^{RPA}_{\hat{n}\hat{n}}(\vec{q},\omega) = -\chi^I_{\hat{n}\hat{n}}(\vec{q},\omega) = -N_0^{el}(0)\left\langle \frac{\vec{v}_F\cdot\vec{q}-2i\Gamma}{\omega-\vec{v}_F\cdot\vec{q}+2i\Gamma}\right\rangle_{ang} \tag{1.35}$$

The polarization (1.35) still has to be integrated over the relative angle between the excitation momentum $\vec{q}$ and the Fermi velocity $\vec{v}_F$. We obtain the average polarization by integrating over the solid angle element $\frac{d\Omega_a}{4\pi}$, which gives

$$\Pi^{RPA}_{\hat{n}\hat{n}}(\vec{q},\omega) = \frac{N_0^{el}(0)}{2}\int_0^{\pi} \sin\theta\, d\theta \frac{v_F q\cos\theta - 2i\Gamma}{\omega - v_F q\cos\theta + 2i\Gamma} \tag{1.36}$$

The angular integration (1.36) can be performed analytically, with the result

$$\Pi^{RPA}_{\hat{n}\hat{n}}(\vec{q},\omega) = N_0^{el}(0)\left\{1 + \frac{\omega}{2v_F q}\ln\left[\frac{\omega + 2i\Gamma - v_F q}{\omega + 2i\Gamma + v_F q}\right]\right\} \tag{1.37}$$

We can compare the RPA susceptibility $\chi^{RPA}_{\hat{n}\hat{n}}(q,\omega) = -Pi_{\hat{n}\hat{n}}(\vec{q},\omega)$ obtained from the angle-averaged polarization (1.37) with the full susceptibility for independent fermions, i.e. equations (1.7) and (1.8). Equation (1.8) has the same logarithmic structure of equation (1.37), however the latter is valid in the limit $\xi_{\vec{k}+\vec{q}} = \xi_{\vec{k}} + \frac{1}{\hbar}\nabla_{\hbar\vec{k}}\xi_{\vec{k}}\cdot\vec{q} + o(q)^2$, and it includes the scattering rate 2Γ. In the case of the nonlocal dielectric response, the interaction potential is the Coulomb repulsion $V_{int}(q) = V_{Coul}(q) = \frac{e^2}{\epsilon_0 q^2}$. We work in the limit $\Gamma \ll \omega$, meaning that scattering occurs at a much lower rate than the excitation frequency. In this limit, we can write the prefactor multiplying the square parenthesis in equation (1.37) as $\frac{\omega}{v_F q} \approx \frac{\omega+2i\Gamma}{v_F q}$. This makes the result a function of $z = \frac{v_F q}{\omega+2i\Gamma}$. Using the latter variable, we have

$$\Pi^{RPA}_{\hat{n}\hat{n}}(\vec{q},\omega) = N_0^{el}(0)\left\{1 + \frac{1}{2z}\ln\left[\frac{1-z}{1+z}\right]\right\} \tag{1.38}$$

Equation (1.38) coincides with the result obtained from the Boltzmann equation approach [5]. We expand this result at fifth order in z with $\frac{1}{2z}\ln\left(\frac{1-z}{1+z}\right) = -1 - \frac{z^2}{3} - \frac{z^4}{5} + o(z^7)$. This expansion is valid for $z \to 0$, which overall sets the validity conditions of our analysis to $v_F q \ll 2\Gamma \ll \omega$. Employing aforementioned expansion in z, equation (1.38) becomes

$$\Pi^{RPA}_{\hat{n}\hat{n}}(\vec{q},\omega) = -\frac{N_0^{el}(0)}{3}z^2\left(1 + \frac{3}{5}z^2\right) = \frac{N_0^{el}(0)}{3}\frac{(v_F)^2q^2}{(2\Gamma - i\omega)^2}\left[1 - \frac{3}{5}\frac{(v_F)^2q^2}{(2\Gamma - i\omega)^2}\right] \tag{1.39}$$

In the limit $v_F q \ll 2\Gamma \ll \omega$, we can rewrite the q-dependent term in equation (1.39) using the series expansion $1 + \frac{3}{5}z^2 \approx \frac{1}{1-\frac{3}{5}z^2}$: $z \to 0$, and we end up with

$$\Pi^{RPA}_{\hat{n}\hat{n}}(\vec{q},\omega) = -\frac{N_0^{el}(0)}{3}\frac{z^2}{1-\frac{3}{5}z^2} = -\frac{N_0^{el}(0)(v_F q)^2}{3(\omega + 2i\Gamma)}\frac{1}{\omega + 2i\Gamma - \frac{3}{5}\frac{(v_F q)^2}{\omega+2i\Gamma}} \tag{1.40}$$

We notice that $\frac{1}{3}N_0^{el}(0)(v_F q)^2 = \frac{n}{m}q^2$ for the 3D density of states $N_0^{el}(0) = \frac{mk_F}{\pi^2\hbar^2}$ and the Fermi wave vector $k_F = (3\pi^2 n)^{\frac{1}{3}}$. Hence, the first nonlocal contribution in equation (1.40) depends on the product $(v_F q)^2$, which we can write in terms of a diffusion constant D_d in d dimensions

$$D_d = \frac{(v_F)^2\tau_c}{d} = \frac{v_F l_{MFP}}{d} \tag{1.41}$$

where we have used equation (1.28) for the collision time τ_c. One can verify that the quantity (1.41) has the dimensions of a diffusion coefficient, and that it corresponds to the classical diffusion constant for electrons characterized by the mean free path $l_{MFP} = v_F\tau_c$ [23]. Physically, this means that electrons are mutually coherent up to a distance r of the order of l_{MFP} due to nonlocal correlations, while electrons diffuse for distances $r > l_{MFP}$: consequently, at first order in momentum we can consider the dielectric response to be spatially coherent, i.e. nonlocal, for $q \geq \frac{1}{l_{MFP}}$. We can directly distinguish two contributions at the denominator of the many-body polarization (1.40): we have the standard pole $1 - i\omega\tau_c$ of the Drude model for conduction [3–5] and a nonlocal correction that depends on $(v_F q)^2$. This is the fundamental result of this section: the first nonlocal correction to the many-body polarization gives rise to electron diffusion, characterized by the coefficient (1.41). On the other hand, we previously argued that density-redistributing nonlocal correlations are dissipative, hence electron diffusion produces *dissipation* [12, 23, 24]. One can interpret the nonlocal term $\frac{D_3 q^2\tau_c}{1-i\omega\tau_c}$ as a frequency-dependent longitudinal *viscoelastic coefficient* for the electron liquid, as we will see in section 1.5: the quantum Boltzmann equation approach tells us that the long-wavelength momentum dependence of the density response in a Fermi liquid depends on the compressibility and the shear modulus of the liquid. This makes sense, since the concept of Fermi liquid applies to weak short-ranged quasiparticle residual interactions, in the same spirit as the regime $V_{int}(q)|_{q\to 0} \to 0^+$ considered in this section. Our final task is to relate the many-body nonlocal polarization (1.39) to the dielectric function $\epsilon(\vec{q},\omega)$. In general, this relation is expressed by [2, 21]

$$[\epsilon(\vec{q},\omega)]^{-1} = 1 + V_{Coul}(q)\chi_{\hat{n}\hat{n}}(\vec{q},\omega) \tag{1.42}$$

For the RPA density susceptibility $\chi^{RPA}_{\hat{n}\hat{n}}(\vec{q},\omega)$, equation (1.42) becomes

$$[\epsilon(\vec{q},\omega)]^{-1} = 1 + V_{Coul}(q)\chi^{RPA}_{\hat{n}\hat{n}}(\vec{q},\omega) \tag{1.43}$$

The Coulomb interaction is spatially isotropic, therefore the dielectric function calculated with equation (1.43) is longitudinal, $\epsilon(\vec{q},\omega) \equiv \epsilon_L(\vec{q},\omega)$ [5]. Using the result (1.5), equation

(1.43) can be rewritten as

$$\epsilon_L(\vec{q},\omega) = 1 + V_{Coul}(q)\Pi^{RPA}_{\hat{n}\hat{n}}(\vec{q},\omega) \tag{1.44}$$

Inserting equation (1.40) into the expression (1.44), we obtain the dielectric function $\epsilon_L(\vec{q},\omega)$. This yields

$$\epsilon_L(\vec{q},\omega) = 1 + V_{Coul}(\vec{q})\Pi^{RPA}_{\hat{n}\hat{n}}(\vec{q},\omega) = 1 - \frac{e^2}{\epsilon_0 q^2}\frac{\frac{n}{m}q^2}{\left(\omega + \frac{i}{\tau_c}\right)}\frac{1}{\omega + \frac{i}{\tau_c} + \frac{3}{5}i\frac{(v_F)^2\tau_c q^2}{1-i\omega\tau_c}} \tag{1.45}$$

Notice that the momentum dependence of the numerator in equation (1.45) is canceled, so the only q-dependent term is the diffusive pole. We recognize the familiar expression for the electron plasma frequency $\omega_p = \sqrt{\frac{ne^2}{m\epsilon_0}}$ [5]. In the high-frequency regime $\omega \gg \frac{1}{\tau_c}$, the local limit $q \to 0$ gives the Drude model [2, 4, 5]. On the other hand, at finite q and for $\omega \gg \frac{1}{\tau_c}$, such that $v_F q \ll \frac{1}{\tau_c} \ll \omega$, we have $\frac{\frac{n}{m}q^2}{\left(\omega+\frac{i}{\tau_c}\right)} \approx \frac{\frac{n}{m}q^2}{\omega}$, so that equation (1.45) becomes

$$\epsilon_L(\vec{q},\omega) = 1 - \frac{(\omega_p)^2}{\omega}\frac{1}{\omega + i(\tau_c)^{-1} + i\frac{3}{5}\frac{(v_F)^2\tau_c q^2}{1-i\omega\tau_c}}. \tag{1.46}$$

Equation (1.46) tells us that long-wavelength nonlocal quasiparticle correlations in the limit $\omega \gg \frac{1}{\tau_c}$ originate a q-dependent correction at the pole of the dielectric function, with respect to the Drude result $\epsilon_D(\omega) = 1 - \frac{\omega_p}{\omega}\frac{1}{\omega + i(\tau_c)^{-1}}$ [4, 5, 12]. The dielectric function (1.46) is longitudinal and stems from the density response of the electron liquid, while the transverse dielectric function $\epsilon_T(\vec{q},\omega)$ stems from the current response of the system; for instance, this models the propagation of electromagnetic radiation inside the material. To analyze such phenomenon, we will dedicate the next section 1.4.4 to the calculation of the current response. We close this section by deriving the longitudinal optical conductivity $\sigma_L(\vec{q},\omega)$ and the associated DC limit $\omega = 0$, based on equation (1.46) [23]. For the optical conductivity we have have [4, 5]

$$\sigma_L(\vec{q},\omega) = -i\omega\epsilon_0[\epsilon(\vec{q},\omega) - 1] = i\omega\epsilon_0\frac{(\omega_p)^2}{\omega}\frac{1}{\omega + i(\tau_c)^{-1} + i\frac{9}{5}\frac{D_3 q^2}{1-i\omega\tau_c}} \tag{1.47}$$

Here we assume to be in the clean limit $\Gamma \to 0^+$, so that the condition $\omega \gg \frac{1}{\tau_c}$ holds down to $\omega \geq 0$. The static limit $\sigma_L(\vec{q},\omega)|_{\omega\to 0^+} = \sigma_L^{DC}(\vec{q})$ separates two different regimes:

$$\sigma_L^{DC}(\vec{q}) = i\epsilon_0(\omega_p)^2 \frac{1}{i(\tau_c)^{-1} + i\frac{9}{5}D_3q^2} = \begin{cases} \frac{ne^2\tau_c}{m} \ : \ \frac{1}{\tau_c} \gg D_3q^2 \\ \frac{ne^2}{m}\frac{1}{\frac{9}{5}D_3q^2} \ : \ \frac{1}{\tau_c} \ll D_3q^2 \end{cases} \tag{1.48}$$

The regime $\frac{1}{\tau_c} \gg D_3q^2$ is the local one, giving the standard Drude conductivity $\frac{ne^2\tau_c}{m}$. On the other hand, in the nonlocal regime $\frac{1}{\tau_c} \ll D_3q^2$ transport is governed by diffusion. Equation (1.48) is one representation of Einstein's relation, by which dissipative transport equals diffusivity [12].

We stress that the expression (1.45) for the longitudinal dielectric function is valid in the limit $v_Fq \ll 2\Gamma \ll \omega$, which translates as $q \ll \frac{1}{l_{MFP}} \ll \frac{\omega}{v_F}$, where $l_{MFP} = v_F\tau_c = \frac{v_F}{2\Gamma}$ is the mean free path at k_F. Physically, this means that we need a long mean free path with respect to the inverse excitation wave vector, such that electrons, that are coherent up to the length scale of l_{MFP}, can react coherently to the excitation and give rise to a nonlocal dielectric response. Furthermore, the condition $q \ll \frac{\omega}{v_F}$ tells us that the response (1.45) is possible only if we are away from the electron-hole Lindhardt continuum $\omega < v_Fq$, otherwise electron-hole excitations destroy the nonlocal response of electrons through Landau damping - see also section 1.5.3.

1.4.4 Nonlocal electromagnetic properties: current response

The density response (1.35) to Coulomb interaction is longitudinal: it physically amounts to moving electrons with an electric potential acting in the same direction. However, experiments can also probe the transverse response of the electron liquid, whereby the liquid reacts in the perpendicular direction $\vec{k}$ with respect to the excitation momentum $\vec{q} \perp \vec{k}$: this is the case of electromagnetic radiation, as the electric $\vec{E}(\vec{q},\omega) \perp \vec{q}$ and magnetic $\vec{B}(\vec{q},\omega) \perp \vec{q}$ fields of an electromagnetic wave are transversally polarized. The energy resulting from the interaction of electrons with an electromagnetic field is $V_t(t) = \int d\vec{r}(-e)J(\vec{r})A(\vec{r},t)$ [2,5], therefore radiation couples to the current operator $\vec{J}(\vec{r},t)$, thus putting electrons in motion - see also section 1.3.2 on the photon propagator. The above arguments are reflected by the fact that the optical conductivity tensor is related to the current-current correlation function $\mathscr{C}_{\vec{J}_\mu\vec{J}_\nu}(\vec{r},\vec{r}',\omega)$ [1,2]. This leads to the Kubo formula for the optical conductivity

tensor

$$\sigma_{T,\mu\nu}(\vec{r},\vec{r}',\omega)=\frac{ie^2}{\omega}\left[\mathscr{C}_{\vec{J}_\mu\vec{J}_\nu}(\vec{r},\vec{r}',i\Omega_n)\Big|_{i\Omega_n\to\omega+i0^+}+\delta_{\mu\nu}\delta(\vec{r}-\vec{r}')\frac{\langle n(\vec{r})\rangle}{m}\right] \tag{1.49}$$

where m is the electron mass, $\langle n(\vec{r})\rangle$ is the local average value of the electron density at coordinate $\vec{r}$, and the indexes $\{\mu,\nu\}=\{x,y,z\}$ run through spatial dimensions. The first term in square brackets comes from the paramagnetic current density components $\vec{J}_\nu(\vec{r})$, while the second term is related to the diamagnetic current density [1,2]. If the system is translationally invariant, the Kubo formula (1.49) assumes a simpler form in reciprocal space of momenta. Formally, we have

$$\sigma_{T,\mu\nu}(\vec{q},\omega)=\frac{ie^2}{\omega}\left[\chi^{\mu\nu}_{\vec{J}\vec{J}}(\vec{q},i\Omega_n)\Big|_{i\Omega_n\to\omega+i0^+}+\delta_{\mu\nu}\frac{n}{m}\right] \tag{1.50}$$

with n as the average particle density. The object $\chi^{\mu\nu}_{\vec{J}\vec{J}}(\vec{q},i\Omega_n)$ appearing in equation (1.50) is the current-current correlation function, or current susceptibility, in momentum space

$$\chi^{\mu\nu}_{\vec{J}\vec{J}}(\vec{q},\tau)=-\left\langle\mathscr{T}_\tau\vec{J}_\mu(\vec{q},\tau)\vec{J}_\nu(-\vec{q},0)\right\rangle, \tag{1.51}$$

which reflects that the conductivity $\sigma_{T,\mu\nu}(\vec{r},\vec{r}',\omega)$ results microscopically from current correlations. The operator $\mathscr{T}_\tau$ in equation (1.51) is the time-ordering operator [1]. The current susceptibility (1.51) can be represented by the following diagram

$\chi^{\mu\nu}_{\vec{J}\vec{J}}(\vec{q},\tau)=-$

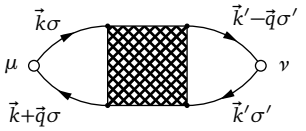

where the two circles are the bare current vertices $\frac{\hbar}{m}\left(k_\alpha+\frac{q_\alpha}{2}\right)$, $\alpha=\{\mu,\nu\}$. The square at the center is nothing other than the many-body polarization of the system, which is $\Pi_{\hat{n}\hat{n}}(\vec{q},\omega)$ for the density response in section 1.4.3, while it is $\Pi_{\vec{J}\vec{J}}(\vec{q},\omega)$ for the transverse current response of section 1.3.1. In the longitudinal channel, the density $\chi_{\hat{n}\hat{n}}(\vec{q},\omega)$ and current $\chi^{\mu\nu}_{\vec{J}\vec{J}}(\vec{q},\omega)$ susceptibilities are related, and one can derive one from the other using the continuity equation for the conservation of particle number, that is a Ward identity [1,2,21]: $\nabla\cdot\vec{J}_L(\vec{r},t)=-\frac{\partial en(\vec{r},t)}{\partial t}$. However, the transverse response is related to transverse current densities $\vec{J}_T$ and it does not couple to the density, since $\nabla\cdot\vec{J}_T=0$ in this case. In the following, we calculate the current susceptibility using directly the Kubo formula (1.50), in a similar way as we have done for the density susceptibility in section 1.4.3. We neglect renormalizations of the current vertices due to vertex corrections; this is an approximation, as momentum-dependent interactions can lead to nontrivial vertex corrections [1]. For the many-body polarization, we take again the impurity-renormalized particle-hole bubble (1.29), and we sum particle-hole bubble contributions in RPA. Inserting

the polarization into the Kubo formula (1.50) and employing the spectral representation of Green's functions, we have

$$\chi^{\mu\nu}_{\vec{J}\vec{J}}(\vec{q},\omega)=\frac{\hbar^2}{m^2}\sum_{\vec{k},\sigma}\Big(k_\mu+\frac{q_\mu}{2}\Big)\Big(k_\nu-\frac{q_\nu}{2}\Big)\int d\epsilon_1 d\epsilon_2\frac{\Gamma/\pi}{(\epsilon_1-\xi_{\vec{k}})^2+\Gamma^2}\frac{\Gamma/\pi}{(\epsilon_2-\xi_{\vec{k}+\vec{q}})^2+\Gamma^2}\frac{f_{FD}(\epsilon_1)-f_{FD}(\epsilon_2)}{i\omega+\epsilon_1-\epsilon_2} \tag{1.52}$$

We consider the diagonal part of the current susceptibility tensor (1.52), which contributes to the optical conductivity in isotropic solids [1,2,5]. Therefore, we define $\chi^{I}_{\vec{J}\vec{J}}(\vec{q},i\Omega_n)=\frac{1}{3}\sum_\alpha\Big[\chi^{\alpha\alpha}_{\vec{J}\vec{J}}(\vec{q},i\Omega_n)\Big]$, with $\alpha=\{x,y,z\}$ for isotropic solids in 3 dimensions. Also, knowing that $\sum_\alpha\big(k_\alpha+\frac{q_\alpha}{2}\big)\big(k_\alpha-\frac{q_\alpha}{2}\big)=k^2-\frac{q^2}{4}$, we have

$$\chi^{I}_{\vec{J}\vec{J}}(\vec{q},\omega)=\frac{\hbar^2}{3m^2}\sum_{\vec{k},\sigma}\left(k^2-\frac{q^2}{4}\right)\int d\epsilon_1 d\epsilon_2\frac{\Gamma/\pi}{(\epsilon_1-\xi_{\vec{k}})^2+\Gamma^2}\frac{\Gamma/\pi}{(\epsilon_2-\xi_{\vec{k}+\vec{q}})^2+\Gamma^2}\frac{f_{FD}(\epsilon_1)-f_{FD}(\epsilon_2)}{i\omega+\epsilon_1-\epsilon_2} \tag{1.53}$$

For long-wavelength excitations, we can expand the $\vec{q}$-dependent portion of the denominator in eq. (1.52) as in section 1.4.3, according to $\xi_{\vec{k}+\vec{q}}=\xi_{\vec{k}}+\frac{1}{\hbar}\nabla_{\hbar\vec{k}}\xi_{\vec{k}}\cdot\vec{q}+o\,(q)^2$. Linearizing the parabolic electron dispersion $\xi_{\vec{k}}=\frac{\hbar^2k^2}{2m}-\mu$ close to k_F, we have $\nabla_{\hbar\vec{k}}\xi_{\vec{k}}\equiv v_{\vec{k}}=\frac{\hbar\vec{k}}{m}$. Also, as in section 1.4.3 we transform the sum over momentum $\vec{k}$ and spin σ into an integral over energies $\xi_{\vec{k}}\equiv\xi$, using the density of states $N_0^{el}(\epsilon)=\sum_{\vec{k},\sigma}\delta(\epsilon-\xi_{\vec{k}})$. This way, the sum over $\vec{k}$ becomes a double integration over the solid angle element $\frac{d\Omega_\alpha}{4\pi}$ and on surfaces of constant energy ξ. Then we approximate $N_0^{el}(\xi)$ to the constant value $N_0^{el}(0)$ at the Fermi energy, and this fixes the value of the velocity $\vec{v}_{\vec{k}}$ to the Fermi velocity $\vec{v}_F$. Then, using $\frac{1}{\pi}\int d\xi\frac{\Gamma^2}{[(\epsilon_1-\xi)^2+\Gamma^2][(\epsilon_2-\vec{v}_F\cdot\vec{q}-\xi)^2+\Gamma^2]}=\frac{2\Gamma}{(\epsilon_1-\epsilon_2+\vec{v}_F\cdot\vec{q})^2+(2\Gamma)^2}$ for Lorentian functions, we achieve

$$\begin{aligned}\chi^{I}_{\vec{J}\vec{J}}(\vec{q},\omega)=\frac{\hbar^2}{3m^2}N_0^{el}(0)\int d\xi\left[\frac{2m}{\hbar^2}(\xi+\mu)-\frac{q^2}{4}\right]\cdot\\ \cdot\int d\epsilon_1 d\epsilon_2\left\langle\frac{(\Gamma/\pi)^2}{[(\epsilon_1-\xi)^2+\Gamma^2][(\epsilon_2-\xi+\vec{v}_F\cdot\vec{q})^2+\Gamma^2]}\right\rangle_{ang}\frac{f_{FD}(\epsilon_1)-f_{FD}(\epsilon_2)}{\omega+\epsilon_1-\epsilon_2}\end{aligned} \tag{1.54}$$

where the angular average $\langle\cdot\rangle_{ang}$ is defined as in section 1.4.3. We see that two separate current vertex terms $\left[\frac{2m}{\hbar^2}(\xi+\mu)-\frac{q^2}{4}\right]$ contribute to the energy ξ integral in equation (1.54). We now evaluate these terms separately. We write

$$\chi^{I}_{\vec{J}\vec{J}}(\vec{q},\omega)=\chi^{\mathscr{A}}_{\vec{J}\vec{J}}(\vec{q},\omega)+\chi^{\mathscr{B}}_{\vec{J}\vec{J}}(\vec{q},\omega) \tag{1.55}$$

$$\begin{aligned}\chi^{\mathscr{A}}_{\vec{J}\vec{J}}(\vec{q},\omega)=\frac{\hbar^2}{3m^2}N_0^{el}(0)\int d\xi\frac{2m(\xi+\mu)}{\hbar^2}\cdot\\ \cdot\int d\epsilon_1 d\epsilon_2\left\langle\frac{(\Gamma/\pi)^2}{[(\epsilon_1-\xi)^2+\Gamma^2][(\epsilon_2-\xi+\vec{v}_F\cdot\vec{q})^2+\Gamma^2]}\right\rangle_{ang}\frac{f_{FD}(\epsilon_1)-f_{FD}(\epsilon_2)}{\omega+\epsilon_1-\epsilon_2}\end{aligned} \tag{1.56}$$

$$\chi^{\mathscr{B}}_{\vec{J}\vec{J}}(\vec{q},\omega) = -\frac{\hbar^2}{3m^2}\frac{q^2}{4}N_0^{el}(0)\cdot$$
$$\int d\xi \int d\epsilon_1 d\epsilon_2 \left\langle \frac{(\Gamma/\pi)^2}{[(\epsilon_1-\xi)^2+\Gamma^2][(\epsilon_2-\xi+\vec{v}_F\cdot\vec{q})^2+\Gamma^2]} \right\rangle_{ang} \frac{f_{FD}(\epsilon_1)-f_{FD}(\epsilon_2)}{\omega+\epsilon_1-\epsilon_2} \quad (1.57)$$

The portion $\frac{2m(\xi+\mu)}{\hbar^2}$ in equation (1.56) is related to the k-dependent part of the current vertex and is a function of energy ξ, which contributes to the optical transport function $\Phi(\xi)$ [25]. With electrons at the Fermi surface in mind, we can approximate the contribution $\frac{2m(\xi+\mu)}{\hbar^2} \approx \frac{2m\mu}{\hbar^2} \equiv \frac{2mE_F}{\hbar^2}$, since the transport function has negligible energy dependence around the Fermi level for common metals [25]; as our calculation is at zero temperature, the chemical potential is equal to the Fermi energy $\mu \equiv E_F$ [3]. Now we have two terms (1.56) and (1.57) that contribute to the current susceptibility, with similar mathematical form apart from a prefactor - $\frac{2mE_F}{\hbar^2}$ and $-\frac{q^2}{4}$ respectively. We evaluate these two terms separately and then we add the result according to equation (1.55); from here, the derivation proceeds in a similar way as for the longitudinal density susceptibility of section 1.4.3. First, we write $\epsilon = \epsilon_1 - \epsilon_2$. Then, we can evaluate the integral over ϵ in equation (1.56). This yields

$$Im\left\{\chi^{\mathscr{A}}_{\vec{J}\vec{J}}(\vec{q},\omega)\right\} = -\frac{4E_F}{3m}N_0^{el}(0)\left\langle \frac{\Gamma\omega}{(-\omega+\vec{v}_F\cdot\vec{q})^2+4\Gamma^2} \right\rangle_{ang} \quad (1.58)$$

We use Kramers-Kronig transformations [5] to calculate the correspondent real part, according to

$$Re\left\{\chi^{\mathscr{A}}_{\vec{J}\vec{J}}(\vec{q},\omega)\right\} = -\frac{1}{\pi}\mathscr{P}\int d\varepsilon \frac{1}{\omega-\varepsilon} Im\left\{\chi^{\mathscr{A}}_{\vec{J}\vec{J}}(\vec{q},\varepsilon)\right\} = \frac{4E_F}{6m}N_0^{el}(0)\left\langle \frac{-4\Gamma^2+\vec{q}\cdot\vec{v}_F(\omega-\vec{q}\cdot\vec{v}_F)}{(-\omega+\vec{v}_F\cdot\vec{q})^2+4\Gamma^2} \right\rangle_{ang} \quad (1.59)$$

Adding equations (1.58) and (1.59) gives

$$\chi^{\mathscr{A}}_{\vec{J}\vec{J}}(\vec{q},\omega) = \frac{4E_F}{3m}N_0^{el}(0)\left\langle -\frac{1}{2}+\frac{\omega}{4i\Gamma+2\omega-2\vec{q}\cdot\vec{v}_F} \right\rangle_{ang} \quad (1.60)$$

The calculation for the portion (1.57) of the current susceptibility proceeds in the exact same manner as for the part (1.56), as the first has only the different prefactor $\frac{q^2}{4}$ instead of $\frac{2mE_F}{\hbar^2}$. The final result is

$$\chi^{\mathscr{B}}_{\vec{J}\vec{J}}(\vec{q},\omega) = \frac{\hbar^2}{3m^2}N_0^{el}(0)\frac{q^2}{4}\left\langle -\frac{1}{2}+\frac{\omega}{4i\Gamma+2\omega-2\vec{q}\cdot\vec{v}_F} \right\rangle_{ang} \quad (1.61)$$

The total q-dependent RPA current susceptibility (1.55) is then

$$\chi^{I}_{\vec{J}\vec{J}}(\vec{q},\omega) = \left(\frac{4E_F}{3m}-\frac{\hbar^2q^2}{6m^2}\right)\frac{N_0^{el}(0)}{2}\left\langle -1+\frac{\omega}{2i\Gamma+\omega-\vec{q}\cdot\vec{v}_F} \right\rangle_{ang} \quad (1.62)$$

Equation (1.62) is the first fundamental result of this section: it tells us how momentum-dependent correlations affect the current susceptibility through the Kubo formula, at RPA level. As for section 1.4.3, we now perform the angular average of the current susceptibility; the resulting angular integrals are analytical and yield the result

$$\chi^{I}_{\vec{J}\vec{J}}(\vec{q},\omega) = N_0^{el}(0)\left(-\frac{2E_F}{3m}+\frac{\hbar^2 q^2}{12m^2}\right)\left\{1+\frac{\omega}{2qv_F}\ln\left[\frac{\omega+2i\Gamma-qv_F}{\omega+2i\Gamma+qv_F}\right]\right\} \tag{1.63}$$

Notice the characteristic RPA logarithmic term in equation (1.63), which appears similarly to equation (1.37) for the density polarization. We are now ready to insert equation (1.63) into the Kubo formula, to calculate the transverse optical conductivity as

$$\sigma_T(\vec{q},\omega) = \frac{ie^2}{\omega}\left[\chi^{I}_{\vec{J}\vec{J}}(q,\omega)+\frac{n}{m}\right] \tag{1.64}$$

We can also calculate the transverse angle-averaged dielectric function, using [4, 5]

$$\epsilon_T(\vec{q},\omega) = 1+\frac{i}{\epsilon_0\omega}\sigma_T(\vec{q},\omega), \tag{1.65}$$

in the same way as for the longitudinal conductivity (1.47). Using the expression for the plasma frequency $\omega_p = \sqrt{\frac{ne^2}{m\epsilon_0}}$, we obtain

$$\epsilon_T(\vec{q},\omega) = 1-\frac{(\omega_p)^2}{\omega^2}+\frac{e^2}{\epsilon_0\omega^2}N_0^{el}(0)\left(\frac{2E_F}{3m}-\frac{\hbar^2q^2}{12m^2}\right)\left\{1+\frac{\omega}{2qv_F}\ln\left[\frac{\omega+2i\Gamma-qv_F}{\omega+2i\Gamma+qv_F}\right]\right\} \tag{1.66}$$

In the limit $q\to 0$, we can employ the series expansion $1+\frac{\omega}{2qv_F}\ln\left[\frac{\omega+2i\Gamma-qv_F}{\omega+2i\Gamma+qv_F}\right] = \frac{2i\Gamma}{2i\Gamma+\omega}+o(q^2)$; this way, we retrieve the Drude dielectric function, as it should be:

$$\epsilon_T(0,\omega) = 1-\frac{(\omega_p)^2}{\omega^2}+\frac{2e^2}{3m\epsilon_0\omega^2}N_0^{el}(0)E_F\frac{2i\Gamma}{2i\Gamma+\omega} = 1-\frac{(\omega_p)^2}{\omega^2}+\frac{ne^2}{m\epsilon_0\omega^2}\frac{2i\Gamma}{2i\Gamma+\omega} =$$
$$1-\frac{(\omega_p)^2}{\omega^2}\left[1-\frac{2i\Gamma}{2i\Gamma+\omega}\right] = 1-\frac{(\omega_p)^2}{\omega(\omega+i/\tau_c)}.$$

On the other hand, in the limit $v_Fq \ll 2\Gamma \ll \omega$, we can expand the logarithmic term in equation (1.66) in Taylor series up to second order for $q\to 0$, similarly to what we have done in section 1.4.3. We have

$$\epsilon_T(\vec{q},\omega) = 1-\frac{(\omega_p)^2}{\omega^2}+\frac{(\omega_p)^2}{\omega^2}\left(1-\frac{\frac{\hbar^2q^2}{4m}}{2E_F}\right)\left[\frac{2i\Gamma}{2i\Gamma+\omega}-\frac{\omega(v_Fq)^2}{3(\omega+2i\Gamma)^3}+o(q^4)\right] \tag{1.67}$$

The vertex term $\frac{\frac{\hbar^2 q^2}{4m}}{2E_F}$ in equation (1.67) is negligible when $\frac{\hbar^2 q^2}{4m} \ll E_F$, which means $q \ll k_F$: in this case, the excitation wave vector is much smaller than the characteristic momentum of the electron distribution, given by k_F. In this regime, equation (1.67) leads to

$$\epsilon_T(\vec{q},\omega) = 1 - \frac{(\omega_p)^2}{\omega^2} + \frac{(\omega_p)^2}{\omega^2}\frac{2i\Gamma}{2i\Gamma+\omega}\left[1 - \frac{\omega(v_F q)^2}{6i\Gamma(\omega+2i\Gamma)^2} + o(q^4)\right] \tag{1.68}$$

If we resum the second-order term $x = \frac{\omega(v_F q)^2}{3i2\Gamma(\omega+2i\Gamma)^2}$ in equation (1.67) using $1-x \approx \frac{1}{1+x}$: $x \to 0$, we obtain

$$\epsilon_T(\vec{q},\omega) = 1 - \frac{(\omega_p)^2}{\omega(\omega+i/\tau_c)}\left[1 + \frac{(v_F q)^2}{3(i/\tau_c+\omega)^2}\right] = 1 - \frac{(\omega_p)^2}{\omega\left[1 + i\omega\tau_c + i\frac{(v_F q)^2\tau_c}{3(1-i\omega\tau_c)}\right]} \tag{1.69}$$

Equation (1.69) is the second main result of this section: we see that, in the long-wavelength limit, the nonlocal correction to the Drude result for the transverse dielectric function comes with a pole at the denominator, of the form $i\frac{(v_F q)^2\tau_c}{1-i\omega\tau_c}$. For this result, the same considerations as for the longitudinal channel (1.46) hold: the nonlocal term $i(v_F q)^2\tau_c$ is dissipative, and therefore it is equivalent to a *viscoelastic coefficient* of the electron liquid. Also, notice that the term crosses over from imaginary (dissipative) behaviour for $\omega\tau_c \ll 1$, to real (elastic shear) behaviour for $\omega\tau_c \gg 1$: this precisely follows the crossover from collisional to collisionless regime of collective modes, that we analyzed in RPA in section 1.2. Also, the same dissipative correction (1.69) to the Drude result can be derived through the semiclassical macroscopic phenomenology, by combining the Maxwell equations of electromagnetism with the linearized Navier-Stokes equation of viscosity [12]. We remind ourselves that the above derivation of the viscoelastic dielectric function relies on the assumptions $v_F q \ll \frac{1}{\tau_c} \ll \omega$ and $q \ll k_F$ - see also section 1.7.2 for the equivalent semiclassical approach; this is an appropriate limit for optical experiments, as the latter probe the electron response for $q \to 0$ [1,5]. Therefore, the results of the present section provide a microscopic grounding to understand the concept of viscosity in electron liquids, originated by nonlocal quasiparticle correlations in the long-wavelength limit.

Up to now, the numerical coefficient that we obtained for the viscosity is $\frac{1}{3}$ according to $i\frac{(v_F q)^2\tau_c}{3(1-i\omega\tau_c)}$ in equation (1.69). This contrasts with the Boltzmann equation result (1.109) for 3-dimensional Fermi liquids, in section 1.5, for which the numerical factor is $\frac{1}{5}$. Such discrepancy has a physical reason: as pointed out in reference [6], when dealing with collective modes one has to consider *shear* deformations of the Fermi surface with shape changes - see figure 1.7 - and not only compressions and dilations of the Fermi sphere with volume changes - see figure 1.6. The calculation of the plasmon dispersion is also

affected, as observed in reference [26]. In other words, the value of k_F can vary in different directions of the Fermi surface under shape changes. On the other hand, in equation (1.54) we fixed the excitation momentum at $\vec{k}_F$ and hence we assumed a single value v_F for the velocity of all reacting electrons, which does not hold under shear deformations of the Fermi surface. We rather have to consider a distribution of velocities $0 < v_{\vec{k}} < v_F$ for electrons that react to the transverse perturbation, and are *still* on the Fermi surface, as done in section 5.4 of reference [5] in the Boltzmann equation approach. This reflects fact that the current susceptibility problem intrinsically depends on the value of the Fermi velocity v_F. In our case, these arguments lead to the susceptibility

$$\chi^I_{\vec{J}\vec{J}}(\vec{q},\vec{k},\omega) = \left(\frac{4E_F}{3m} - \frac{\hbar^2 q^2}{6m^2}\right)\frac{N_0^{el}(0)}{2}\left\langle -1 + \frac{\omega}{2i\Gamma + \omega - \vec{q}\cdot\vec{v}_{\vec{k}}}\right\rangle_{ang} \tag{1.70}$$

where $v_{\vec{k}} \leq v_F$. We can average this susceptibility along constant energy surfaces [5]: one has to average over the solid angle as done for equation (1.63), and also to average with respect to the radial coordinate from 0 to v_F, using $\frac{3}{(v_F)^3}\int_0^{v_F}(v_{\vec{k}})^2 dv_{\vec{k}}\ \chi^I_{\vec{J}\vec{J}}(q,k,\omega)$, where the factor 3 comes from the three spatial dimensions. Then, expanding the result in momentum to order q^2, one obtains

$$\epsilon_T(\vec{q},\omega) = 1 - \frac{(\omega_p)^2}{\omega(\omega + i/\tau_c)}\left[1 + \frac{(v_F q)^2}{5(i/\tau_c + \omega)^2}\right] = 1 - \frac{(\omega_p)^2}{\omega\left[\omega + \frac{i}{\tau_c} + i\frac{(v_F q)^2\tau_c}{5(1-i\omega\tau_c)}\right]} \tag{1.71}$$

Equation (1.71) now has the numerical prefactor $\frac{1}{5}$ for the nonlocal term, in accordance with the Fermi liquid 3-dimensional result for the shear viscoelastic coefficent (1.109); the latter reduces to $i\frac{(v_F q)^2\tau_c}{5(1-i\omega\tau_c)}$ for null Landau parameter F_1. Aforementioned observations highlight the importance of considering correctly shear deformations of the Fermi surface, in response to transverse currents such as the ones generated by an electromagnetic wave inside the material. The Boltzmann equation approach for Fermi liquids naturally distinguishes different kinds of collective modes, of longitudinal and shear character, in terms of microscopic Landau parameters; the latter are used to decompose the angular pattern of the Fermi surface deformation in normal modes, as we will see in the following section. The results will highlight the correspondence with the dielectric and current response derived for the RPA electron liquid, in sections 1.4.3 and 1.4.4.

1.5 Microscopic theory of sound excitations in Fermi liquids

The phenomenology of Fermi liquids was developed by L. D. Landau in 1957-59, refined by successive works, and then widely applied to the physics of metals. The essence of this phenomenology is that a gas of electrically charged interacting particles, like conduction electrons in a solid, can be described by a system of nearly independent entities, named *quasiparticles*. These quasiparticles are approximate excitations of the system at energies $\hbar\omega$ much smaller than the characteristic kinetic energy of the original particles, i.e. the Fermi energy E_F for electrons. This condition, together with the scattering lifetime and the strength of mutual interactions between quasiparticles, ultimately set the limits of applicability of this theoretical framework. The Fermi liquid theory is conceptually fundamental, because it explains why the complicated system of mutually interacting electric charges, like interacting electrons in a metal, can be regarded as a gas of non-interacting quasiparticles. For metals, this can appear counterintuitive, because Coulomb interactions are relatively strong in metallic systems; nevertheless, dielectric screening and generally weak correlations allow to employ a nearly non-interacting gas picture. This simplification provides the theoretical explanation of why all the results that one obtains from the widely used free electron model work so well in modeling transport, optics, photoemission, and other classes of experiments [2]. Furthermore, the quasiparticle concept gives the theoretical foundation of the semiclassical description. The quasiparticle distribution function satisfies a kinetic equation, which may include scattering from one state to another, for example due to impurity scattering. This equation is known as the Landau transport equation, and it is equivalent to the well-known Boltzmann equation from kinetic gas theory. In this description, the interaction potential is allowed to vary in space due to some external perturbation or due to inhomogeneities in the quasiparticle density.

We consider an electronic Fermi sea: electrons occupy states at progressively higher energies, according to their quantum numbers like momentum $\hbar\vec{k}$ and spin $\sigma = \{|\uparrow\rangle, |\downarrow\rangle\}$. In second quantization, we write these eigenstates with the electronic annihilation and creation operators $\left(\hat{c}_{\vec{k},\sigma}, \hat{c}^{\dagger}_{\vec{k},\sigma}\right)$, so that the ground state of this electronic *ensemble* is the product

$$|\mathcal{O}_{FS}\rangle = \prod_{\vec{k},\sigma}^{k<k_F} \hat{c}^{\dagger}_{\vec{k},\sigma} |\mathcal{O}\rangle \tag{1.72}$$

where $|\mathcal{O}\rangle$ is the vacuum and k_F is the Fermi wave vector, defining the Fermi surface; this is

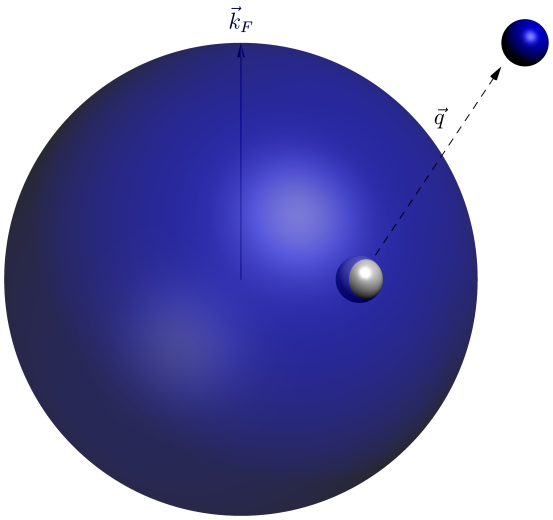

Figure 1.5: A spherical Fermi surface in 3 dimensions for the Fermi sea (1.72). The Fermi wave vector is labeled by $\vec{k}_F$. An example of single-particle excitation for this system is depicted by a little blue sphere, representing a quasielectron promoted above the Fermi level through an excitation of momentum $\vec{q}$; the excitation leaves a quasihole in the Fermi sea, shown by the little white sphere.

fixed by the electron density n and it represents the maximum occupied momentum state in the non-interacting system at temperature $T = 0$ [3]. At low excitation energies $\hbar\omega \ll E_F$, the Pauli exclusion principle and the Coulomb potential essentially prevent all but the electrons in a small momentum shell $k_F - \delta k < k < k_F$, $\delta k \to 0^+$ around the Fermi surface to respond to the excitation. Then, a single electron can be promoted in empty states above the Fermi level, leaving behind a hole in the Fermi sea; however, since all electrons in the system are correlated, properties like the mass and the lifetime of the excited particle are influenced by the presence of all other particles, and therefore they will be different from the ones of independent free electrons. It is customary to say that electrons are *dressed* by many-body correlations with all other charges into *quasielectrons*, which are still single particle excitations resembling free electrons, but with renormalized properties. These single excited entities are the Landau quasiparticles, named quasielectrons and quasiholes. The system (1.72) can be excited by external perturbations through an interaction potential $V_{int} = V_{int}(\vec{q})$, responding to inhomogeneities in particle density n and spin σ excitations: hence, self-sustained periodic motions of the Fermi surface can spontaneously develop, and they constitute the collective modes of the Fermi liquid.

1.5.1 Undamped sound collective modes in Fermi liquids

In order to insert the results of later sections into the theoretical framework of Fermi liquids, we present a detailed derivation of collective excitations for a Fermi liquid, starting from the results of Abrikosov and Khalatnikov of reference [7]. Following Nozières and Pines [22], we first write the microscopic hamiltonian for an electrically charged quasiparticle in the Fermi liquid

$$\hat{H}_{qp}(\vec{r},\vec{p},\sigma) = E_n\left[\vec{p}+e\vec{A}(\vec{r},t),\sigma\right] + \sum_{\vec{p},\sigma,\vec{p}',\sigma'} f_{\vec{p},\sigma,\vec{p}',\sigma'}\delta\mathbb{N}_{\vec{p}',\sigma'}(\vec{r},t) - e\phi_\sigma(\vec{r},t) \tag{1.73}$$

In equation (1.73), we have defined the quasiparticle energy eigenvalues $E_n\left[\vec{p}+e\vec{A}(\vec{r},t),\sigma\right]$, modified by the presence of the vector potential $\vec{A}(\vec{r},t)$, as well as the short-range interaction matrix elements $f_{\vec{p},\sigma,\vec{p}',\sigma'}$ between quasiparticles of momenta $\left\{\vec{p},\vec{p}^{\,'}\right\}$ and spin $\left\{\sigma,\sigma^{'}\right\}$. The quasiparticle velocities are defined from the crystalline momentum $\vec{v}_p = \nabla_p E_n(\vec{p}) = \frac{\vec{p}}{m^*}$. The nonequilibrium distribution function $N_{\vec{p}}(\vec{r},t) = \delta\mathbb{N}_{\vec{p}',\sigma'}(\vec{r},t) + N_0\left(E_n\left[\vec{p}+e\vec{A}(\vec{r},t),\sigma\right]\right)$ contains the departure of the quasiparticle statistics from local equilibrium $N_0\left(E_n\left[\vec{p}+e\vec{A}(\vec{r},t),\sigma\right]\right)$, and can be calculated from particle number conservation and gauge invariance [7, 19]. We also include a scalar potential $\phi_\sigma(\vec{r},t)$.

Equation (1.73) is valid in the regime $k_BT \ll E_F$ and $\hbar\omega \ll E_F$, with $E_F = \frac{\hbar^2(k_F)^2}{2m^*}$ Fermi energy, with quasiparticles of large lifetime $\tau_{\vec{k}} \gg \frac{1}{E_F}$ and a well-defined Fermi surface and relative excitation spectrum. Physically, these conditions signify that thermal agitation and the external perturbation are not so strong to drive quasielectrons completely out of equilibrium, exciting quasiparticles away from the Fermi level and destroying the Fermi surface. From the hamiltonian (1.73), one derives a linearized kinetic equation for quasiparticles of velocity $v_{\vec{k},\sigma}$ on the Fermi surface, which participate to the collective mode thus changing the Fermi-surface distribution. The response to the perturbation depends on the interactions among quasiparticles, which are parameterized by *Landau parameters* $F_l^{S,A}$ - see equation (A.10) - and on the angle θ between the excitation wave vector $\vec{q}$ and the quasiparticle wave vector $\vec{k}$. We report the entire derivation of the kinetic equation in appendix A, while here we only quote the final result. It is

$$\left(qv_{\vec{k},\sigma}\cos\theta-\omega\right)\epsilon_{\vec{k}}(\vec{q},\omega) + qv_{\vec{k},\sigma}\cos\theta\int\frac{d\Omega^{'}}{4\pi}\sum_{l=0}^{+\infty}F_l^{S,A}\wp_l(\cos\theta^{'})\epsilon_{\vec{k}'}(\vec{q},\omega) = 0 \tag{1.74}$$

Given an excitation wave vector $\vec{q}$ and frequency ω, the only unknown parameter left in equation (1.74) is the first-order Fermi-surface distribution change $\epsilon_{\vec{k}}(\vec{q},\omega)$, in response to the perturbation. This distribution change depends on the angular orientation of the

wave vector $\vec{k}$ with respect to the excitation momentum $\vec{q}$. Since we expanded the Landau interaction matrix elements in spherical harmonics, it is convenient to do the same for $\epsilon_{\vec{k}}(\vec{q},\omega)$ as well. Hence, we write [7, 10]

$$\epsilon_{\vec{k}}(\vec{q},\omega) = \sum_{l=0}^{+\infty}\sum_{m=0}^{l}\alpha_l^m(k)\varepsilon_{\theta,\phi} \tag{1.75}$$
$$\varepsilon_{\theta,\phi} = P_l^m(\cos\theta)\cos(m\phi)$$

In the polar coordinates expansion (1.75), $P_l^m(z)$ are the associated Legendre polynomials of $\wp_l(z)$ for a given angular index $l \in \mathbb{N}$ - see appendix A. A displacement of the Fermi surface as a whole, that corresponds to ordinary sound, is described simply by $\varepsilon_{\theta,\phi} \propto \cos\theta$ [7], thus having $m = 0$; on the other hand, for $m = 0$ we can also have an anisotropic distortion of the Fermi surface $\varepsilon_{\theta,\phi}$, with the Fermi surface being extended in the direction of motion as we shall see shortly: this corresponds to zero sound, which propagates at sufficiently high velocities $v > v_F$. A. A. Abrikosov and I. M. Khalatnikov [7] showed that the different values of m define independent motions. For $m = 0$, the solution of equation (1.74) is always a longitudinal wave, passing from collisional ordinary sound to collisionless zero sound, consistently with the discussion in section 1.2 following equation (1.9). The case $m = 1$ implies a transverse oscillation with $\varepsilon_{\theta,\phi} \propto \cos\phi$, and we shall derive the explicit dispersion relations shortly. We notice that the magnitude factor $\alpha_l^m(k)$ drops identically from equation (1.74) because $k = k^{'}$, as only quasiparticles at the chemical potential μ are involved.

Dealing with density-density excitations, we select the symmetric Landau parameters F_l^S.
We start by considering the first harmonic F_0^S only, with $l = m = 0$, so that the distribution function change is $\varepsilon_{\theta,\phi} = P_0^0(\cos\theta) = 1$, and the interaction matrix element is

$$f_{\vec{k},\sigma,\vec{k}',\sigma'} \equiv \frac{2}{N_0^*(0)}F_0^S \tag{1.76}$$

where $N_0^*(0)$ is the renormalized electronic density of states at the Fermi level, obtained by using the effective mass m^*. Inserting equations (1.76) and (1.75) into equation (1.74), we can explicitly find the deviation of the distribution function with respect to global equilibrium

$$\varepsilon_{\theta,\phi}(\vec{q},\omega) = \frac{qv_{\vec{k},\sigma}\cos\theta F_0^S\int\frac{d\Omega^{'}}{4\pi}\epsilon_{\theta'\phi'}(\vec{q},\omega)}{\omega - qv_{\vec{k},\sigma}\cos\theta} = \frac{qv_{\vec{k},\sigma}\cos\theta F_0^S}{\omega - qv_{\vec{k},\sigma}\cos\theta} \tag{1.77}$$

Equation (1.77) demonstrates the earlier statement that, at zero order $l = m = 0$, $\varepsilon_{\theta,\phi} \propto \cos\theta$, with a denominator $\omega - q v_{\vec{k},\sigma} \cos\theta$ that makes the perturbation anisotropic when $\omega > q v_{\vec{k},\sigma} \cos\theta$.

Inserting back the result (1.77) into equation (1.74) with $l = m = 0$ and integrating the angular part $\int \frac{d\Omega'}{4\pi} \varepsilon_{\theta',\phi'}(\vec{q},\omega) = \int_0^{2\pi} d\phi' \int_0^{\pi} d\theta' \frac{\sin\theta'}{4\pi} \frac{q v_{\vec{k}',\sigma'} \cos\theta' F_0^S}{\omega - q v_{\vec{k}',\sigma'} \cos\theta'} = \frac{F_0^S}{2} \left\{ -2 + \frac{\omega \ln\left|\omega + q v_{\vec{k},\sigma}\right|}{q v_{\vec{k},\sigma}} - \frac{\omega \ln\left|\omega - q v_{\vec{k},\sigma}\right|}{q v_{\vec{k},\sigma}} \right\}$, we finally arrive at the dispersion relation [7]

$$-1 + \frac{1}{2} \frac{\omega}{q v_{\vec{k},\sigma}} \ln \left| \frac{1 + \frac{\omega}{q v_{\vec{k},\sigma}}}{1 - \frac{\omega}{q v_{\vec{k},\sigma}}} \right| = \frac{1}{F_0^S} \tag{1.78}$$

We can solve for the longitudinal sound velocity $v_{S,FL} = \frac{\omega}{q}$, recalling that the moving quasiparticles are at the Fermi surface and move at the renormalized Fermi velocity $v_{\vec{k},\sigma} \approx v_F^*$. We obtain

$$-1 + \frac{\zeta}{2} \ln \left| \frac{1 + \zeta}{1 - \zeta} \right| = \frac{1}{F_0^S} \tag{1.79}$$

where $\zeta = \frac{v_{S,FL}}{v_F^*} = \frac{\omega}{q v_F^*}$. Equation (1.79), obtained from the statistical theory of Fermi liquids, has the same form as equation (1.10) in RPA, with the - there unspecified - interaction potential $V_{int}(0) N_0^{el}(0)$ substituted by the appropriate interaction Landau parameter F_0^S for a Fermi liquid. This equivalence stems from the fact that both equations (1.79) and (1.9) are derived for single electron-hole quasiparticle excitations at the Fermi level, which is the cornerstone hypothesis of RPA as well as the foundational assumption of Fermi liquid theory. Also, by retaining only the zero-order interaction matrix elements $l = m = 0$ in (A.10) and (1.75), we pose ourselves in the local limit, where there is no dependence of the interaction matrix elements on the magnitude or the direction of the wave vector $\vec{q}$: the only excitation character that can be developed in this limit is longitudinal, in accordance with the discussion in section 1.2.

Propagating solutions of equation (1.79) exist provided that $\zeta > 1$, while solutions are damped for $\zeta < 1$, in accordance with the discussion after equation (1.9) of RPA. Therefore, collective excitations of the form (1.79) are damped longitudinal ordinary sound in a Fermi liquid when $v < v_F^*$, and are propagating zero sound when $v > v_F^*$: such excitations have the same properties as in standard RPA, apart from the quasiparticle renormalizations at the basis of Landau theory. However, if the only Landau parameter is F_0, the quasiparticle mass and velocities are the same as for free particles, because the mass renormalization $m^* = \left(1 + \frac{F_1^S}{3}\right) m$ depends on the *first* Landau parameter F_1^S. [6,7] The sound velocity from

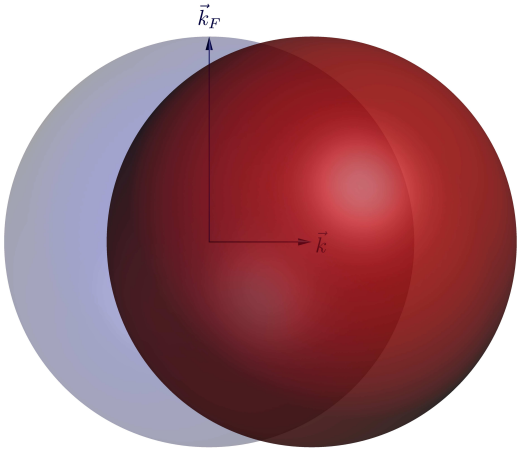

Figure 1.6: Schematic representation of the Fermi surface change due to the isotropic perturbation (1.79) for $v_{S,L} < v_F$: the excitation, associated to the zero-order Landau parameter F_0, is a longitudinal sound, associated to the displacement as a whole of the Fermi surface along the direction $\vec{k}$. The Fermi wave vector is labeled by $\vec{k}_F$.

equation (1.79) results [7]

$$v_{S,FL} = \sqrt{\frac{F_0^S}{3}} v_F \tag{1.80}$$

Now we go one step further and retain also the first Landau parameter F_1^S: the consequence will be that there is a distinction between the longitudinal and transverse channels for sound waves, which is absent if we only consider the zero-order parameter F_0^S. This further step relaxes the hypothesis of an isotropic local interaction: while still in the long-wavelength limit $q \to 0$, F_1^S takes into account the angle θ between the quasiparticle velocity $\vec{v}_{\vec{k},\sigma}$ and the excitation wave vector $\vec{q}$, as well as the angles θ' and ϕ' in 3 dimensions between $\vec{k}$ and $\vec{k}'$. Hence, effects due to the direction $\vec{q}$ are included at first order of interaction. From equation (A.10) at $l = 1$, the interaction matrix elements for the Fermi liquid become

$$f_{\vec{k},\sigma,\vec{k}',\sigma'} \equiv \frac{2}{N_0^*(0)} \left[F_0^S + F_1^S \wp_1(\cos\theta) \right] \tag{1.81}$$

On the other hand, the quasiparticle distribution change contains the first two harmonics $l = \{0,1\}$ and $m = \{0,1\}$, so that the angular portion is $\varepsilon_{\theta,\phi} = P_0^0(\cos\theta) + P_1^0(\cos\theta) + P_1^1(\cos\theta)\cos(\phi) = 1 + \cos\theta - \sin\theta\cos\phi$. To find the dispersion relations in the two independent channels $m = 0$ and $m = 1$, we need to employ the relation between the Legendre polynomials $\wp_l(z)$ and their associated polynomials P_l^m, writing everything in terms of the latter. Then, using equation (1.81) into equation (1.74), we perform similar

calculations as in (1.77) - (1.79), separating the problem into the independent motions $m = 0$ and $m = 1$. The procedure is analogous to the general solution for any order of l, which is sketched in appendix B. The final result is the dispersion relations with F_0^S and F_1^S [7]. In the longitudinal channel $m = 0$, we have

$$-1 + \frac{\zeta}{2} \ln \left| \frac{1+\zeta}{1-\zeta} \right| = \frac{1 + \frac{F_1^S}{3}}{F_0^S + F_0^S \frac{F_1^S}{3} + F_1^S \zeta^2} \tag{1.82}$$

where $\zeta = \frac{v_{S,FL}}{v_F^*} = \frac{\omega}{q v_F^*}$ again. Notice that equation (1.82) reduces to (1.79) in the limit $F_1^S \to 0$, consistently; also, notice the normalization factor $1 + \frac{F_1^S}{3}$ at the numerator, which enters into the mass renormalization of Fermi liquid quasiparticles [7]. In the transverse channel $m = 1$, we obtain

$$-1 + \frac{\zeta}{2} \ln \left| \frac{1+\zeta}{1-\zeta} \right| = \frac{F_1^S - 6}{3F_1^S (\zeta^2 - 1)} \tag{1.83}$$

The collective excitations described by equation (1.83) are transverse sound waves, and they depend on the first Landau parameter F_1^S: as generally mentioned in section 1.1, this kind of excitation corresponds to Landau-damped transverse sound when the dispersion is complex-valued, and it corresponds to propagating transverse zero sound when there are solutions with real wave vector q and frequency ω; therefore, damped transverse zero sound occurs for $F_1^S < 6$, while the transverse sound becomes propagating for $F_1^S > 6$.

Comparing equation (1.79) to the relations (1.82) and (1.83), we realize that the inclusion of F_1^S into the Fermi liquid matrix elements enables us to catch new details of the physics of sound waves: we have two different dispersions for longitudinal and transverse sound-like excitations in the Fermi liquid. Also, the longitudinal sound (1.82) exists independently from F_1^S, but its dispersion is modified if $F_1^S \neq 0$: in the language of hydrodynamics, this means that a pure compressibility stemming from F_0^S does not reproduce the entire sound dispersion if the shear stresses due to F_1^S become important [6]. On the other hand, the transverse sound (1.83) depends entirely on F_1^S, which determines the shear modulus and the shear viscosity of a Fermi liquid: shear stresses are fundamental to describe transverse sound, and we will elaborate more on this point in section 1.7.2.

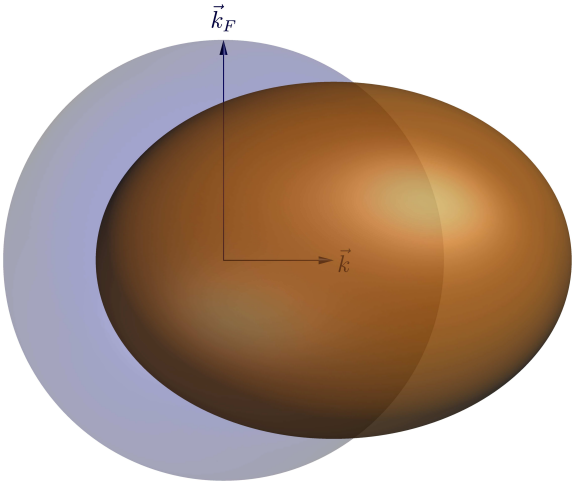

Figure 1.7: Schematic diagram to illustrate the distortion of the Fermi surface during the transition of a transverse zero sound wave, stemming from first Landau paramter $F_1^S \neq 0$, traveling along the direction $\vec{k}$: the Fermi surface is elongated in the direction of motion. The Fermi wave vector is labeled by $\vec{k}_F$.

1.5.2 Collisions in a neutral Fermi liquid: dispersion from liquid helium

The excitation spectrum of an electrically neutral Fermi liquid has been further investigated by M. J. Lea et al. [10], and later by P. R. Roach and J. B. Ketterson [11], with reference to transverse zero sound in liquid helium ^3He. The work of Lea et al. focused on the inclusion of the quasiparticle collision time τ_c: in practice, quasiparticles do not exist indefinitely in time but collide with each other and decay, transferring momentum and energy - see the general discussion after equation (A.1). The product between τ_c and excitation frequency ω determines the thermodynamic regime in which the perturbation takes place: for $\omega\tau_c \ll 1$, within one excitation period ω^{-1} many collisions can occur and the quasiparticles are able to redistribute momentum and energy among themselves, reaching a semiclassical condition of local thermodynamic equilibrium; for $\omega\tau_c \gg 1$, a collisionless regime realizes whereby collisions occur on a timescale much larger than ω^{-1} and quasiparticles respond out of equilibrium. As we already discussed in section 1.2, the collisional regime $\omega\tau_c \ll 1$ is the one for acoustic damped sound, while the collisionless condition $\omega\tau_c \gg 1$ favors propagating zero sound - see discussion after equation (1.10). One is able to write the dispersion relation of sound-like excitations for all $\omega\tau_c$. In order to do so, we have to perform similar calculations as in section 1.5, with the addition of a collisional term in the Boltzmann-like kinetic equation, as included at the right-hand side of equation (A.1). The equation for the collective excitations in the presence of collisions

becomes

$$\left(\vec{q}\cdot\vec{v}_{\vec{k},\sigma}-\omega\right)\epsilon_{\vec{k}}(\vec{q},\omega)+\vec{q}\cdot\vec{v}_{\vec{k},\sigma}\left\{\sum_{\vec{k}',\sigma'}f_{\vec{k},\sigma,\vec{k}',\sigma'}\epsilon_{\vec{k}'}(\vec{q},\omega)\delta\left[E_n(\vec{k}',\sigma')-\mu\right]\right\}=\mathscr{I}\left[\epsilon_{\vec{k}}(\vec{q},\omega)\right] \tag{1.84}$$

where $\mathscr{I}\left[\epsilon_{\vec{k}}(\vec{q},\omega)\right]=F\left\{\left[\frac{\partial\epsilon_{\vec{k}}(\vec{r},t)}{\partial t}\right]_{coll}\right\}$ is the collision integral, equal to the Fourier transform $F\{f(x)\}$ of the right-hand side of equation (A.3); it is $\mathscr{I}\left[\epsilon_{\vec{k}}(\vec{q},\omega)\right]\propto\frac{1}{\tau_c}$ in the relaxation time approximation. This integral is further constrained by particle number, energy and momentum conservation, as it happens in collisions [7, 10]. From this point, proceeding similarly to the calculations of section 1.5, one can extend the dispersion relations to finite collision time.

The work by P. R. Roach and J. B. Ketterson [11] extends the previous results by Lea et al. [10], considering the dispersion relation of the Fermi liquid as a function of the two symmetric Landau parameters F_1^S and F_2^S. This, together with the inclusion of quasiparticle relaxation, generalizes the results with respect to the ones of Abrikosov and Khalatnikov [7], represented by equation (1.83). In the presence of F_1^S, the renormalized Fermi velocity is $v_F^*=\frac{v_F}{1+\frac{F_1}{3}}$. The relation for $F_2^S=0$ in the transverse channel $m=1$ is equivalent to the result by Lea et al., and reads

$$\begin{aligned}&(\xi^2-1)w=\frac{F_1^S-6-9/(-1+i\omega\tau_c)}{3F_1^S-9/(-1+i\omega\tau_c)}\\&\text{where }\ \xi=\frac{i\omega\tau_c-1}{i\tau_c q v_F^*}\ \text{ and }\ w=\frac{1}{2}\xi\ln\left[\frac{\xi+1}{\xi-1}\right]-1\end{aligned} \tag{1.85}$$

The dispersion relation (1.85) describes collective excitations that are linear in q, and therefore they are a kind of sound according to the definition in the introduction 1.1. Defining the complex sound velocity $\tilde{v}_{S,L}=\frac{\omega}{q}$, we can calculate the real and imaginary parts of the ratio $\frac{\tilde{v}_{S,L}}{v_F^*}$, where $v_F^*=\frac{v_F}{1+\frac{F_1^S}{3}}$ is the Fermi velocity renormalized by F_1^S-related quasiparticle interactions. The results for the real and imaginary parts are displayed in figure 1.8 as solid curves, in panels (a) and (b) respectively.

We analyze the collisional regime $\omega\tau_c\ll 1$, where the quasiparticles have time to equilibrate by relaxation between successive oscillations at frequency ω: in this case, we retrieve local thermodynamic equilibrium. The latter implies that quasielectrons respond like semiclassical particles in local equilibrium, in analogy with hydrodynamical flow in a classical fluid; therefore we expect to be able to apply hydrodynamics to the Fermi liquid, characterizing the response with viscoelastic constants obtained from general elasticity

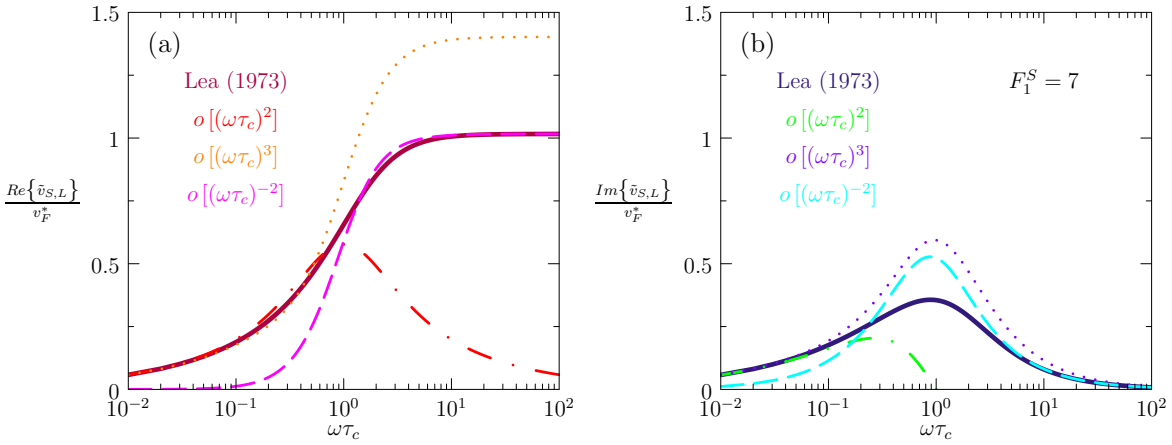

Figure 1.8: The real and imaginary parts of the complex wave velocity $\frac{\tilde{v}_{S,L}}{v_F^*} = \frac{\omega}{kv_F^*}$ as functions of $\omega\tau_c$ for transverse sound in a Fermi liquid, with first Landau parameter $F_1^S = 7$. Panel (a) shows the real part of the sound velocity $Re\left\{\frac{\tilde{v}_{S,L}}{v_F^*}\right\}$, while panel (b) shows the imaginary part $Im\left\{\frac{\tilde{v}_{S,L}}{v_F^*}\right\}$. The solid curves stem from equation (1.85). The dashed-dotted curves result from a series expansion of equation (1.85) to first order in $\omega\tau_c$, and correspond to equation (1.87). The dotted curves stem from a second-order series expansion of equation (1.85) in $\omega\tau_c$, according to equation (1.88). The dashed curves correspond to equation (1.91), which results from a series expansion of equation (1.85) in $\frac{1}{\omega\tau_c}$ at first order.

theory. We will investigate this approach in detail in sections 1.7.2 and 1.7.2.2, while now we concentrate on the explicit form of the sound-like dispersion relations. From the definition (1.85), we can define the sound velocity as $\tilde{v}_{S,L} = \frac{\omega}{q}$ as

$$\xi^2 = \frac{i}{5\omega\tau_c}\left(1 + \frac{F_1^S}{3}\right) = \frac{1}{(v_F^*)^2}\left(\tilde{v}_{S,L} + \frac{i}{\tau_c q}\right)^2 \tag{1.86}$$

In the collisional regime, we have $\xi^2 = \frac{i}{5\omega\tau_c}\left(1 + \frac{F_1^S}{3}\right) \to +\infty \;:\; \omega\tau_c \to 0$ from the definition (1.85), hence we can expand in Taylor series $\frac{1}{2}\xi \ln\left[\frac{\xi+1}{\xi-1}\right] - 1 = \frac{1}{3}(\xi)^2 + \frac{1}{5}(\xi)^4 + o\left\{\xi^6\right\}$. This way, we can solve for the complex sound velocity $\tilde{v}_{S,L}$ at first order in $\omega\tau_c$, with the result

$$\tilde{v}_{S,L} = \sqrt{\frac{i(v_F^*)^2}{5\omega\tau_c}\left(1 + \frac{F_1^S}{3}\right)}\frac{\omega\tau_c}{i + \omega\tau_c} = \sqrt{i\omega\nu(0)}\frac{1}{i + \omega\tau_c} \tag{1.87}$$

Equation (1.87) demonstrates that the transverse collective excitations in the collisional regime for a Fermi liquid are damped sound waves, since the sound velocity has always an imaginary part; the modes, depending on the first Landau parameter F_1^S, have transverse

character [7]. Remarkably, the properties of these excitations can be described in terms of a single parameter $\nu(0) = \frac{1}{5}(v_F)^2\tau_c \frac{1}{1+\frac{F_1^S}{3}}$: this turns out to be the shear viscoelastic coefficient for the Fermi liquid in 3 dimensions at zero frequency, for $F_1^S \neq, 0$ $F_2^S = 0$, consistently with equation (1.114) [6, 12]. The imaginary part of the term $\frac{\sqrt{i\omega\nu(0)}}{i+\omega\tau_c}$ is dissipative, as it gives an imaginary part in the dispersion relation, while the real part is equivalent to an elastic shear term: for $\omega\tau_c \ll 1$, the imaginary part is much bigger than the real part, while increasing the product $\omega\tau_c$ makes the real elastic part increase with a corresponding decrease in the imaginary dissipative part. Therefore, the properties of damped transverse sound excitations in the collisional regime for a Fermi liquid can be described by a shear viscoelastic coefficient: the *ensemble* of quasiparticles behaves like a nonrelaxing fluid in local thermodynamic equilibrium, for $\omega\tau_c \ll 1$. Augmenting $\omega\tau_c$ makes the viscosity diminish, until we pass to the different collisionless regime $\omega\tau \gg 1$ with propagating zero sound. The real and imaginary parts of the sound velocity (1.87) are shown by dash-dotted curves in panels (a) and (b) of figure 1.8, respectively, for first Landau parameter $F_1^S = 7$. Equation (1.87) is asymptotically exact in the limit $\omega\tau_c \to 0$, but it fails qualitatively to reproduce the full transverse sound dispersion (1.85) when $\omega\tau_c \approx 1$. To improve the agreement, we go to second order in the $\omega\tau_c$ expansion of equation (1.85). The result is

$$\tilde{v}_{S,L} = \sqrt{\frac{45 + 2F_1^S + 6i\frac{1+\frac{F_1^S}{3}}{\omega\tau_c}}{30\frac{(i+\omega\tau_c)^2}{(\omega\tau_c)^2}}} \tag{1.88}$$

The real and imaginary parts of equation (1.88) are shown as dotted curves in panels (a) and (b) of figure 1.8, respectively, for $F_1^S = 7$. We see that this second order expansion in $\omega\tau_c$ follows the full numerical solution (1.85) qualitatively, although equation (1.88) becomes inaccurate in the collisionless regime $\omega\tau_c \gg 1$. Physically, this means that for $\omega\tau_c \gg 1$ we cannot describe the Fermi-liquid sound-like excitations as classical waves in a viscoelastic fluid: as mentioned before, the quasiparticles cannot relax and restore local equilibrium in the collisionless regime, thus preventing a hydrodynamic description of their excitations.

Hence, in the opposite collisionless regime, local thermodynamic equilibrium among quasiparticles is destroyed and the hydrodynamic description ceases to be valid. In such conditions, we simply retrieve the transverse zero sound mode without collisions, described by Abrikosov and Khalatnikov in reference [7], and reproduced by equation (1.83). Formally, in the limit $\omega\tau_c \to +\infty$, we have $\xi = \frac{i\omega\tau_c - 1}{i\tau_c q v_F^*} \to v_{S,\infty} = \frac{\omega}{q}$: the velocity of sound becomes a real number, meaning that the excitations are indeed undamped. In this case, the equation

for $v_{S,\infty}$ is [7]

$$-1+\frac{v_{S,\infty}}{2}\ln\left|\frac{1+v_{S,\infty}}{1-v_{S,\infty}}\right|=\frac{F_1^S-6}{3F_1^S\left[(v_{S,\infty})^2-1\right]} \tag{1.89}$$

Equation (1.89) gives the undamped asymptotic limit of the sound velocity $v_{S,\infty}$; it is a trascendental equation, the closed solution of which is not known. However, by noting that $v_{S,\infty}$ increases for growing F_1^S, in the limit $v_{S,\infty}\gg 1$ and $F_1^S\gg 1$ we retrieve

$$v_{S,\infty}=\sqrt{\frac{1}{5}(v_F^*)^2\left(1+\frac{F_1^S}{3}\right)}=\sqrt{\mu_s}\ :\ F_1^S\gg 1 \tag{1.90}$$

where $\mu_s=\frac{1}{5}\frac{(v_F)^2}{1+F_1^S/3}$ is the *shear modulus* of the Fermi liquid, in the presence of first Landau parameter F_1^S [7, 19] - see equation (1.109). Therefore, we can describe the velocity of undamped zero transverse sound for $F_1^S\gg 1$ in terms of a single parameter, corresponding to the shear modulus of the system: from elasticity, this means that physically the Fermi liquid responds like an *elastic solid*. This contrasts the situation in the collisional regime, where the system responded like a viscous fluid as found in equation (1.87). Notice that the relation between the static viscosity and the shear modulus of a Fermi liquid [7, 10, 19], namely $\nu(0)=\mu_s\tau_c$, is obeyed by equations (1.87) and (1.90). For $F_1^S>6$, the transverse zero sound is propagating outside of the continuum of electron-hole quasiparticle excitations, which provide an additional damping source for $F_1^S<6$. For $F_1^S\to 6^+$, the sound velocity $v_{S,\infty}\to v_F^*=\frac{v_F}{1+\frac{F_1^S}{3}}$ - see also the RPA solution in figure 1.2. When $F_1^S\to 6^+$, the effect of electron-hole pair excitations starts to influence the propagating sound velocity $v_{S,\infty}$, which tends to the renormalized Fermi velocity v_F^* and deviates from the shear modulus result $\sqrt{\mu_s}$. This signals that we can treat propagating zero sound with elasticity theory only for sufficiently high $F_1^S\gg 1$, or equivalently $v_{s,\infty}\gg v_F^*$: such condition is consistent with the general conditions to consider the linear response of a Fermi liquid with elasticity, see equations (1.95). The numerical solution of the sound velocity for $\omega\tau_c\to+\infty$ is reported in figure 1.9, together with the asymptotic large-F_1^S limit (1.90). When we start decreasing $\omega\tau_c$ from infinity, collisions will produce damping of transverse zero sound, with a nonvanishing imaginary part, even in the propagating condition For $F_1^S>6$. We can

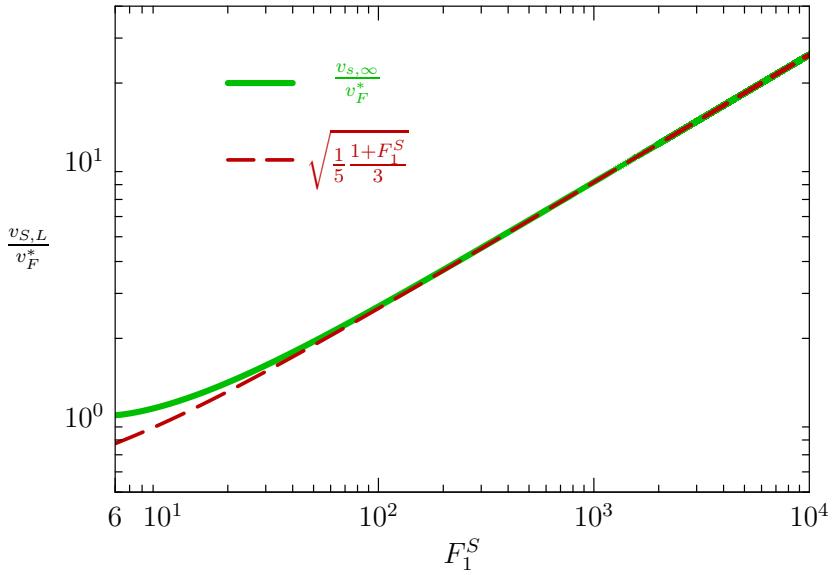

Figure 1.9: Propagating zero sound velocity $\frac{\tilde{v}_{S,L}}{v_F^*} = \frac{\omega}{kv_F^*}$ in the collisionless regime $\omega\tau_c \to +\infty$ for a Fermi liquid, as a function of first Landau parameter $F_1^S > 6$. The full curve is the numerical solution of equation (1.89) and the dashed line is the shear modulus expression (1.90). The results show that the Fermi liquid in the collisionless limit responds to sound-like excitations as an *elastic solid*, for strong quasiparticle interactions $F_1^S \gg 1$.

analyze how this occurs by expanding equation (1.85) at first order in $\frac{1}{\omega\tau_c}$. We obtain

$$\tilde{v}_{S,L} = \frac{\omega\tau_c}{i+\omega\tau_c p_2}\frac{\frac{i-2\omega\tau_c+\frac{F_1^S}{3}(i+\omega\tau_c)}{3i+F_1^S(i+\omega\tau_c)} - p_1 + p_2\tilde{v}_{S,\infty}}{(i+\omega\tau_c)p_2} \tag{1.91}$$

$$p_1 = 1-(\tilde{v}_{S,\infty})^2 - \frac{\tilde{v}_{S,\infty}}{2}\ln\left(\frac{1+\tilde{v}_{S,\infty}}{-1+\tilde{v}_{S,\infty}}\right) + \frac{(\tilde{v}_{S,\infty})^3}{2}\ln\left(\frac{1+\tilde{v}_{S,\infty}}{-1+\tilde{v}_{S,\infty}}\right)$$

$$p_2 = \frac{3}{2}\left[(\tilde{v}_{S,\infty})^2\ln\left(\frac{1+\tilde{v}_{S,\infty}}{-1+\tilde{v}_{S,\infty}}\right) - 2\tilde{v}_{S,\infty} - \ln\left(\frac{1+\tilde{v}_{S,\infty}}{-1+\tilde{v}_{S,\infty}}\right)\right]$$

where $\tilde{v}_{S,\infty} = \frac{v_{S,\infty}}{v_F^*}$. The real and imaginary parts of equation (1.91) are shown as dashed curves in panels (a) and (b) of figure 1.8, respectively, for $F_1^S = 7$. Due to collisions, the zero sound velocity (1.91) has a small imaginary part even for $F_1^S > 6$ when zero sound becomes propagating, unlike the $\omega\tau_c \to +\infty$ limit (1.89). The real part is always $Re\left\{\tilde{v}_{S,L}\right\} > v_F^*$, demonstrating that zero sound exists above the quasiparticle Fermi velocity v_F^*, consistently with the RPA solution in figure 1.2. For $F_1^S < 6$, transverse zero sound is not propagating but damped: the dispersion acquires an imaginary part from $\sqrt{\frac{F_1^S-6}{3F_1^S}}$ for $F_1^S < 6$. This physically results from the Lindhardt continuum of electron-hole incoherent quasiparticle excitations, which destroy the coherent propagation of collective modes - see

figure 1.1 and section 1.5.3.

Apart from equation (1.86), slightly different descriptions have been proposed in the literature. Another derivation of the dispersion for transverse sound has been performed by Litovitz and Davis [10,27], using a single relaxation time approximation for a classical viscoelastic fluid. We also mention an analogous result that was given by Bolton [10,28] for the dispersion of transverse zero sound in Fermi liquids

$$q^2(v_F\tau_c)^2 = \frac{-\omega\tau_c(1-i\omega\tau_c)^2}{\frac{i}{5}\left(1+\frac{F_1^S}{3}\right)+\omega\tau_c} \tag{1.92}$$

Equation (1.92) reproduces qualitatively the transverse sound dispersion throughout the crossover from collisional to collisionless regime, for $F_1^S \approx 6$, and with an overall better accuracy with respect to the asymptotic limits (1.88) and (1.91). However, for smaller $F_1^S \ll 6$ or larger $F_1 \gg 6$, the relation (1.92) loses accuracy, even qualitatively for large $F_1^S \gg 6$.

Another example of parameterization of the Fermi liquid transverse sound dispersion (1.85) is the one of reference [12], the purpose of which is similar to the solution (1.92): obtaining a parametrization by which we can calculate $q(\omega)$ directly with reasonable accuracy, in the entire crossover from collisional to collisionless regime. By considering a dispersion of the form $q^2 \propto \frac{i\omega\tau_c}{1+\frac{F_1^S}{3}}(1-i\alpha\omega\tau_c)$, $\alpha \in \mathbb{R}$ with appropriate numerical factors to approximate equation (1.85), one obtains the following expression [12] which can be used in the full frequency range:

$$(ql_{MFP})^2 = \frac{i\omega\tau_{\vec{k}}}{5(1+F_1^S/3)}\left(1-i\frac{7\sqrt{F_1}}{32}\omega\tau_{\vec{k}}\right) \tag{1.93}$$

where $v_F\tau_{\vec{k}} = l_{MFP}$ is the mean-free path. From equation (1.93), we obtain

$$\tilde{v}_{S,L} = \sqrt{\frac{-i\omega\tau_{\vec{k}}}{5\left(1+\frac{F_1^S}{3}\right)\left(1-i\frac{7\sqrt{F_1}}{32}\omega\tau_{\vec{k}}\right)}} \tag{1.94}$$

The parameterization (1.94) is most accurate with respect to the numerical dispersion (1.85) for first Landau parameter $F_1^S \approx (5 \div 10)$. The comparison between the ratios $\frac{\tilde{v}_{S,L}}{v_F^*}$ calculated through the full numerical solution (1.85) and the parameterization (1.94) is shown in figure 1.10 for $F_1^S = 7$.

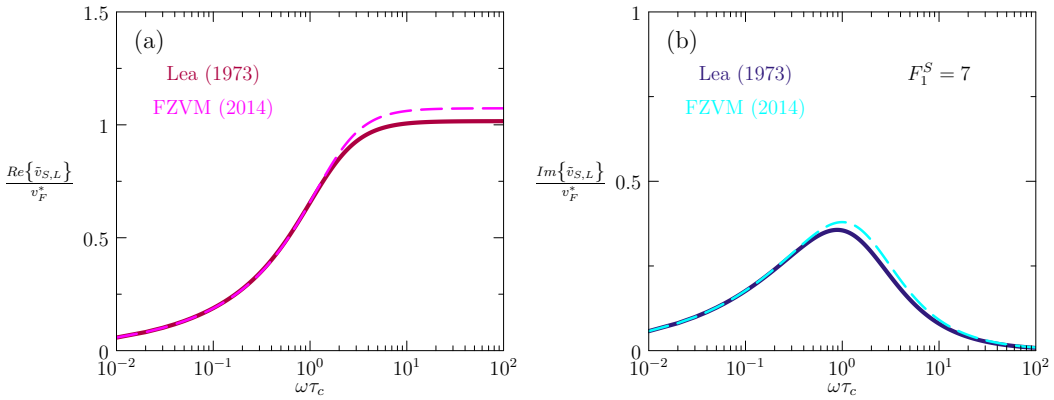

Figure 1.10: The real and imaginary parts of the complex wave velocity $\frac{\tilde{v}_{S,L}}{v_F^*} = \frac{\omega}{kv_F^*}$ as functions of $\omega\tau_c$ for transverse sound in a Fermi liquid, with first Landau parameter $F_1^S = 7$. Panel (a) shows the real part of the sound velocity $Re\left\{\frac{\tilde{v}_{S,L}}{v_F^*}\right\}$, while panel (b) shows the imaginary part $Im\left\{\frac{\tilde{v}_{S,L}}{v_F^*}\right\}$. The solid curves result from equation (1.85), while the dashed curves are calculated from the parameterization (1.94).

1.5.3 Landau damping

Apart from quasiparticle relaxation in time τ_c, collective modes in the system are damped also by single quasiparticle excitations: when the energy $\hbar\omega$ and the momentum $\vec{q}$ of an excitation, acting on the state $\{\vec{k}, \sigma\}$, correspond to an available state $\{\vec{k}', \sigma'\}$, the involved quasielectron makes the transition to the empty level by leaving a quasihole in the initial state. Given the equivalence of the low-energy single-particle excitations in a Fermi liquid with the RPA solution, these single-particle excitations are nearly-independent electron-hole pairs [6]. Such electron-hole pairs are detrimental to the propagation of collective modes, since they damp and ultimately destroy the coordinated motion of the quasiparticles participating in the collective excitations, by randomly exciting quasielectrons out of the oscillation pattern of the given collective mode. With reference to the RPA excitation spectrum in figure 1.1, we can describe the region affected by Landau damping using the variables $x = \frac{q}{2k_F}$ and $y = \frac{\hbar\omega}{4E_F}$. The region of the (x, y) plane where particle-hole excitations do exist corresponds to the region where the susceptibility is damped by an imaginary part, that is $Im\left\{\chi^0_{\hat{n}\hat{n}}(\vec{q}, \omega)\right\}$ in RPA. From equation (1.7), one can deduce the presence of Landau damping when $y < x - x^2$, as well as in he region $x^2 - x < y < x^2 + x$: the latter boundaries represent the minimal electron-hole excitation energy with a momentum larger than $2k_F$, and the maximum energy attainable with a momentum x, respectively [2]. At low frequency, one can approximate the region of Landau damping with $\omega \approx v_F q$ $\omega \to 0^+, q \to 0^+$. In a Fermi liquid, the dispersion relation $\{\vec{q}, \omega\}$ of the sound-like

mode depends on the magnitude of the residual quasiparticle interactions, characterized by the Landau parameters (A.8); therefore, the Landau parameters determine whether the collective mode dispersion falls into a region $\{\vec{q}, \omega\}$ where the excitations are damped by particle-hole pairs, inside the particle-hole continuum. In principle, the dispersion relation calculated from equation (1.85) has been verified in the context of liquid helium, which is an archetype Fermi liquid; therefore, one tends to assume that such dispersion is still valid for electrically neutral fermions in solids, whenever the Landau phenomenology of Fermi liquids applies. For other types of condensed matter, like in the quantum critical case, the dispersion relations are drastically different even in the absence of electric charge.

1.6 Quantum critical state

Although the Fermi liquid state is ubiquitous in conventional metals, there are multiple examples of unconventional metallicity in condensed matter, that one cannot describe with Landau's phenomenology. Does this mean that the hydrodynamic perspective, that we adopted for long-wavelength electron-hole excitations, ceases to be valid? Indeed, very recently it has been questioned whether the notions of hydrodynamics and viscosity apply to non-Fermi liquids, which might be realized in the form of strange metals as in high-Tc superconductors, heavy fermion systems and so forth. It is believed that these are governed by quantum criticality, meaning that the system undergoes phase transitions even at zero temperature [29]. At $T = 0$, the quantum dynamics of such systems would be scale-invariant, while for $T > 0$ these are characterized by extremely short "Planckian" [30] relaxation times $\tau_c \approx \tau_\hbar \sim \hbar/k_B T$ [29,31]. In other words, the intrinsic timescale - the absolutely minimum one - associated with scattering is the one given by the Heisenberg uncertainty principle: collisions are fundamentally governed by quantum mechanics, and this imposes a lower bound on all collision-dependent quantities like viscosity. In fact, we can already see that, inserting $\tau_\hbar \equiv \tau_c$ into the static viscosity formula $\nu(0) \propto \tau_c$ - see section 1.7.2.2 and paper 1 - the resulting viscoelastic coefficient is very small with respect to Fermi liquids, due to the smallness of the equivalent mean free path $\tau_\hbar$ and the lack of intrinsic microscopic scales like $\hbar/E_F$. For these reasons, it has been argued that quantum critical systems may display the highest possible degree of fluidity, i.e. the lowest possible viscosity. This got further impetus by the discovery of the "minimal viscosity-entropy" ratio using the AdS/CFT correspondence [32], which seems confirmed both in the quark gluon plasma created at the heavy ion colliders [33] as well as the cold atom unitary Fermi gas [34] . Resting on these ideas, several proposals have been put forward for applications of quantum critical viscosity to condensed matter, for instance to the

temperature-dependent resistivity of the normal state in high T_c superconductors [35–37], although consensus has not been reached yet. The above arguments suggest that observing viscoelastic modes in quantum critical matter is much more difficult than in Fermi liquids, due to the high degree of fluidity of the former. More comments on these matters are included in paper 1, while in the following we concentrate on charged Fermi liquids as the archetype application of viscoelasticity.

1.7 Charged Fermi liquid

When electric charge is introduced as a degree of freedom of the Fermi liquid, the excitation spectrum of the system is modified: the development of electrical conductivity, dielectric polarization and screening are among the most prominent consequences of long-ranged Coulomb interactions between quasiparticles. Furthermore, the charge degree of freedom allows coupling of the system with electromagnetic radiation, usually treated in dipole approximation [4, 5]; therefore, we can study how the radiation propagates inside the material, by considering the transverse dielectric response. This analysis is necessary to perform optical spectroscopy; the latter allows to excite quasiparticle currents in response to the incident radiation, to observe optical reflection, absorption and transmission, thereby probing quasiparticle properties and their relative correlations. In metals with weak correlations, the dielectric properties are known [5, 7] and the optical conductivity can be calculated from RPA in all relevant regimes of momentum and frequency. However, when correlations come into play, and nonlocal effects start to arise, the picture becomes more involved, and novel approaches are needed to explore the dielectric response. In this respect, Fermi liquids provide an optimal playground for the analysis of correlations, given their much larger sensitivity to nonlocal effects with respect to quantum critical matter [12].

1.7.1 Separation of long-ranged Coulomb interactions

The elementary single-particle electronic excitations in common metals are interacting quasiparticles: therefore, electrons in solid-state metallic systems commonly form a Fermi liquid, with the additional challenge of incorporating the presence of electric charge. In the quantum Boltzmann equation approach of section 1.5, the inclusion of charge means that electron-hole excitations perceive finite electromagnetic potentials $\phi_\sigma(\vec{r}, t)$ and $\vec{A}(\vec{r}, t)$, which enter into the quasiclassical force (A.4) even in the absence of external perturbations [23]. Therefore, the interactions among Landau quasiparticles are modified

by the long-ranged Coulomb interaction $V_{Coul} = \frac{e^2}{\epsilon_0 q^2}$. In principle, this poses a problem since $V_{Coul}(q)$ is divergent for $q \to 0$, while in neutral systems Landau theory assumes short-ranged quasiparticle interactions with a well-defined long-wavelength limit. The solution was first found by Silin [38, 39]: effects due to Coulomb interactions can be separated into a long-ranged part, representing the classical polarization field that provides dielectric screening, and a short-ranged additional quantum component, driven by the virtual creation of electron hole pairs around a charged particle. The polarization field cuts the range of Coulomb interactions to a finite range by dielectric screening, while electron-hole quantum fluctuations modify the short-ranged quasiparticle interactions of neutral systems. Once the quasiparticle interactions are expanded in terms of Landau parameters, the consequence is that the long-ranged spherically symmetric polarization screens quasiparticle interactions in the isotropic $l = 0$ channel, thereby modifying the value of F_0^S only. Hence, Landau parameters are modified by electric charge according to $\tilde{F}_l^S(\vec{q}) = \frac{e^2 N_{el}^*(0)}{\epsilon_0 q^2}\delta_{l0} + F_l^S$ [23]. In particular, for transverse excitations in the $l = 1$ channel, electric charge does not introduce any momentum dependence of F_1^S. In the charged case, the only consequence of Coulomb interaction is that F_1^S differs from the correspondent value in the neutral system, due to the electron-hole short-ranged quantum component. Apart from the values of Landau parameters, one can expect that collective modes are modified by the presence of electric charge. The transverse $l = 1$ channel is particularly intriguing: such transverse excitations can couple to photons, which allows one to probe Fermi liquid collective modes in solids through optical experiments. In the following, we analyze the dielectric response of charged Fermi liquids, and we calculate optical observables which can reveal the characteristic signature of collective modes.

1.7.2 Viscoelastic dielectric response of a Fermi liquid

Now we are familiar with some basic methods to analyze the dielectric response of materials from section 1.3, and we understand that long-wavelength correlations in Fermi liquids as viscoelastic properties of the Fermi surface. Hence, we can ask ourselves what is the dielectric function of a viscoelastic electron liquid. Elasticity theory of continuous media provides the answer. This picture provides analytical results for nonlocal correlations, when the hypothesis for the application to Fermi liquids are satisfied: [6, 19]

$$\begin{aligned} \omega &\gg v_F q, \\ q &\ll k_F, \end{aligned} \tag{1.95}$$

meaning that elasticity is valid for momentum and frequency away from the particle-hole continuum, as electron-hole excitations destroy hydrodynamic equilibrium in the Fermi liquid by Landau damping. These conditions provide the limit in which we derived the viscoelastic dielectric function from many-body theory in section 1.4.4. In this case, the Fermi sphere can be effectively treated as a viscoelastic medium, i.e. a viscous fluid in collisional regime and an elastic solid in collisionless regime; elastic moduli like the bulk modulus K_B or the shear modulus μ_s, as well as dissipation coefficients like bulk viscosity ζ and shear viscosity η, correctly describe the response of the material [6]. As described in section 1.5, in the regime where elastic quantities are well defined, one distinguishes between two conditions, separated in relation with the momentum relaxation time τ_c for quasiparticles: for $\omega\tau_c \ll 1$, quasiparticles can reach thermodynamic local equilibrium before their momentum is relaxed, allowing for a hydrodynamic description of the system; at higher frequencies $\omega\tau_c \gg 1$, the momentum is destroyed before local equilibrium can be achieved among the quasiparticles, and the elastic description leaves its place to a collisionless regime, characterized by vanishing viscosity $\eta(\omega) \to 0$. Such dichotomy based on the collision time τ_c reprises what we discussed for the RPA sound dispersion in section 1.2.

1.7.2.1 Viscoelastic dielectric function

Nonlocal correlations in the regime $\omega \gg v_F q$ and $q \ll k_F$ have been analyzed by C. Conti and G. Vignale applying elasticity theory to an interacting electron liquid [6, 19]; in the following, we derive the longitudinal and transverse dielectric susceptibilities in the viscoelastic approach, and the respective dielectric functions. Consider the macroscopic response of a translationally invariant system composed of n particles per unit volume in d spatial dimensions, with mass m and electric charge e, with respect to an applied electric field $\vec{E}(\vec{r}, t)$: the total electric force acting on the particles will be $\vec{F}_{el}(\vec{r}, t) = -ne\frac{\partial \vec{A}(\vec{r},t)}{\partial t}$ where we have written the electric field in terms of a vector potential $\vec{A}(\vec{r}, t)$, while the linear response will be given by a particle current density $\vec{J}(\vec{r}, t) = n\frac{\partial \vec{u}(\vec{r},t)}{\partial t}$, where $\vec{u}(\vec{r}, t)$ is the particle displacement.

The kinetic equation is given by [6, 19, 40]

$$mn\left[\frac{\partial^2\vec{u}(\vec{r},t)}{\partial t^2}+\frac{1}{\tau_{\vec{k}}}\frac{\partial\vec{u}(\vec{r},t)}{\partial t}\right]= \int dt'\left[\tilde{K}(t-t')+\left(1-\frac{2}{d}\right)\tilde{\mu}(t-t')\right]\nabla\left[\nabla\cdot\vec{u}(\vec{r},t')\right] + \int dt'\tilde{\mu}(t-t')\nabla^2\vec{u}(\vec{r},t')+\vec{F}_{el}(\vec{r},t) \quad (1.96)$$

In equation (1.96), we have defined the generalized elastic constants of the charged fluid [6, 19]

$$\tilde{K}(t-t')=K_B(t-t')+\frac{d}{d(t-t')}\zeta(t-t')$$
$$\tilde{\mu}(t-t')=\mu_S(t-t')+\frac{d}{d(t-t')}\eta(t-t') \quad (1.97)$$

Equation (1.97) contains the bulk modulus $K_B(t-t')$, the shear modulus $\mu_S(t-t')$, the bulk viscosity $\zeta(t-t')$ and the shear viscosity $\eta(t-t')$; these four quantities are causal memory functions depending on the time difference between stimulus and response. Also, notice that there is no generalized shear modulus in one dimension $d=1$, as there can only be longitudinal stresses along one axis, in the absence of another orthogonal space coordinate, logically. By Fourier transformation of equation (1.96) to reciprocal space of wave vectors $\vec{q}$ and frequency ω, we obtain

$$\left(\frac{m}{\tau_{\vec{k}}}-i\omega m\right)\vec{J}(\vec{q},\omega)=\left[\frac{\tilde{K}(\omega)}{n}+\left(1-\frac{2}{d}\right)\frac{\tilde{\mu}(\omega)}{n}\right] \frac{\vec{q}\cdot\left[\vec{q}\cdot\vec{J}(\vec{q},\omega)\right]}{i\omega}+\frac{\tilde{\mu}(\omega)}{n}\frac{q^2}{i\omega}\vec{J}(\vec{q},\omega)+i\omega ne\vec{A}(\vec{q},\omega) \quad (1.98)$$

The elastic constants (1.97), in terms of wave vector $\vec{q}$ and frequency ω, become

$$\tilde{K}(\omega)=K_B(\omega)-i\omega\zeta(\omega)$$
$$\tilde{\mu}(\omega)=\mu_S(\omega)-i\omega\eta(\omega) \quad (1.99)$$

For a given frequency dependence, the causal memory functions in equation (1.99) are subjected to Kramers-Kronig relations. For a fluid, the static shear modulus is null $\mu_S(0)=0$, in accordance with the intuitive notion that a liquid has no resistance to shear. On the other hand, a solid has a finite shear modulus $\mu_S(\omega)$. This suggests that equation (1.98) is capable

of describing both solid and fluid configurations, in the same elasticity formalism [6]. By decomposition of the vector potential $\vec{A} = A_L \vec{u}_n + A_T \vec{u}_\Sigma$ into the longitudinal component $\vec{A}_L = A_L \vec{u}_n$ and the transverse component $\vec{A}_T = A_T \vec{u}_\Sigma$, we can similarly decompose the total current density $\vec{J}(\vec{q},\omega) = \vec{J}_L(\vec{q},\omega)\vec{u}_n + \vec{J}_T(\vec{q},\omega)\vec{u}_\Sigma$. After some algebra, we arrive at the expression for the longitudinal current density $\vec{J}_L = J_L \vec{u}_n$ [6]

$$J_L(\vec{q},\omega) = -\frac{\frac{n}{m} e\vec{A}_L(\vec{q},\omega)}{1 + \frac{i}{\omega\tau_{\vec{k}}} - \left[\frac{\tilde{K}(\omega)}{n^2} + 2\left(1-\frac{1}{d}\right)\frac{\tilde{\mu}(\omega)}{n^2}\right]\frac{nq^2}{m\omega^2}} \tag{1.100}$$

Similarly, the transverse current density $\vec{J}_T = J_T \vec{u}_\Sigma$ reads

$$J_T(\vec{q},\omega) = -\frac{\frac{n}{m} e\vec{A}_T(\vec{q},\omega)}{1 + \frac{i}{\omega\tau_{\vec{k}}} - \frac{\tilde{\mu}(\omega)}{n^2}\frac{nq^2}{m\omega^2}} \tag{1.101}$$

Now, we use the continuity equation $\nabla \cdot \vec{J}_L(\vec{r},t) = -\frac{\partial[\Delta n(\vec{r},t)]}{\partial t}$; after Fourier transformation to momentum and frequency space, this becomes $J_L(\vec{q},\omega) = -\frac{\omega}{q}\Delta n(\vec{q},\omega)$, where $\Delta n(\vec{q},\omega)$ is the perturbation in the particle density due to the electric field $\vec{E}_L(\vec{q},\omega)$. We also need Gauss law $\nabla \cdot \vec{E}_L(\vec{r},t) = -\frac{en(\vec{r},t)}{\epsilon_0[\epsilon_L(\vec{r},t)+1]}$, where we have defined the relative longitudinal dielectric function $\epsilon_L(\vec{r},t)$ [5]. In reciprocal space, the latter dielectric function reads

$$\epsilon_L(\vec{q},\omega) = 1 - \frac{(\omega_p)^2}{\omega^2 + \frac{i\omega}{\tau_{\vec{k}}} - \left[\frac{\tilde{K}(\omega)}{nm} + 2\left(1-\frac{1}{d}\right)\frac{\tilde{\mu}(\omega)}{nm}\right]q^2} \tag{1.102}$$

In equation (1.102), we have defined the plasma frequency $\omega_p = \sqrt{\frac{ne^2}{m\epsilon_0}}$. We notice that the viscoelastic longitudinal dielectric function is nonlocal [6], since it depends quadratically on wave vector $\vec{q}$; the nonlocality coefficient is proportional to the generalized bulk modulus $\tilde{K}(\omega)$ and the generalized shear modulus $\tilde{\mu}(\omega)$, as defined by equations (1.99). Furthermore, for vanishing viscoelastic constants (1.99), that is in the local limit $\tilde{K}(\omega) \to 0$ and $\tilde{\mu}(\omega) \to 0$, equation (1.100) reduces to the Drude dielectric function.

We can derive the transverse dielectric function $\epsilon_T(\vec{r},t)$ [5] analogously, in terms of momentum $\vec{q}$ and frequency ω, from Maxwell's equations: from the wave equation with current density forcing term $\nabla^2\vec{E}(\vec{r},t) - \frac{1}{c^2}\frac{\partial^2\vec{E}(\vec{r},t)}{\partial t^2} = -\nabla\left[\nabla\cdot\vec{E}(\vec{r},t)\right] - \mu_0\frac{\partial\vec{J}_T(\vec{r},t)}{\partial t}$, and equation (1.101), we have

$$\epsilon_T(\vec{q},\omega) = 1 - \frac{(\omega_p)^2}{\omega^2 + \frac{i\omega}{\tau_{\vec{k}}} - \frac{\tilde{\mu}(\omega)}{nm}q^2} \tag{1.103}$$

As for the longitudinal channel (1.102), the transverse dielectric function (1.103) shows a quadratic dependence on momentum $\vec{q}$, due to nonlocality associated with the generalized shear modulus $\tilde{\mu}(\omega)$. Also, for $\tilde{\mu}(\omega) \to 0$ we retrieve the Drude local dielectric function [4,5]. Notice that the transverse channel $\epsilon_T(\vec{q},\omega)$ gives the transverse dielectric function of a viscoelastic charged fluid [6]: defining the frequency-dependent cinematic viscosity coefficient as $\nu(\omega) = i\frac{\mu(\omega)}{nm\omega}$ [41], and inserting this relation into equation (1.103), we obtain equation (3) in reference [12]. We will analyze the transverse collective modes for a viscoelastic charged fluid in detail, in the following section 1.7.4.

The solutions of the longitudinal dielectric function (1.102) for density-density collective modes of the types mentioned in section 1.1, correspond to the poles of the density susceptibility; according to equation (1.43), this also means $\epsilon_L(\vec{q},\omega) = 0$ [5]. Remarkably, in the transverse channel (1.103), we immediately recognize a transverse collective mode whereby $\epsilon_T(\vec{q},\omega) = 0$ [5]: its dispersion is given by

$$\omega^2 + i\frac{\omega}{\tau_{\vec{k}}} - \frac{\tilde{\mu}(\omega)}{nm}q^2 = 0 \tag{1.104}$$

The existence of such a transverse collective mode was pointed out in reference [19], where this dispersion was described as transverse sound. Indeed, in the collisionless regime $\omega\tau_{\vec{k}} \gg 1$, the transverse sound can freely propagate, as described in section 1.5.2. From equation (1.104), we find the viscoelastic dispersion

$$1 - \frac{\mu_S(\omega) - i\omega\eta(\omega)}{nm}\left(\frac{q}{\omega}\right)^2 = 0 \tag{1.105}$$

Equation (1.105) allows us to find the transverse sound velocity in a viscoelastic medium, valid at any dimensionality

$$\tilde{v}_{S,VE} = \frac{\omega}{q} = \sqrt{\frac{\mu_S(\omega)}{nm} - i\omega\frac{\eta(\omega)}{nm}} \tag{1.106}$$

The sound velocity $\tilde{v}_{S,VE}$ is a complex number in general, meaning that viscosity $\nu(\omega)$ damps the sound propagation. Also, knowing that viscosity diminishes [6,12] for $\omega\tau_c \gg 1$, the transverse sound will propagate with less and less damping, and the sound velocity $\tilde{v}_{S,VE}$ will essentially be a measure of the shear modulus $\mu_S(\omega)$,

$$\tilde{v}_{S,VE} \approx v_{S,VE} = \sqrt{\frac{\mu_S(\omega)}{nm}} \tag{1.107}$$

This introduces the shear modulus into play, consistently with equation (1.90) in section

1.5.2 [10].

1.7.2.2 Elastic constants of a Fermi liquid

For a Fermi liquid, the elastic constants in the static limit $\omega = 0$ are known [7, 19]: they directly stem from the microscopic hamiltonian (1.73) for electrically charged quasiparticles. The derivation closely follows the arguments of section 1.5: we write the linearized kinetic equation (A.3) for the quasiparticle distribution function $f_{\vec{p},\sigma,\vec{p}',\sigma'}$ in terms of Legendre polynomials and Landau parameters F_n^α, $\alpha = \{S, A\}$ [7, 8]; this time we retain the vector potential $\vec{A}(\vec{r}, t)$, as we want to calculate the microscopic dielectric response (in section 1.5 we chose $\vec{A}(\vec{r}, t) = 0$ because we calculated collective modes without fields and perturbations). Such steps lead to a microscopic expression for the longitudinal and transversal current densities, $\vec{J}_L(\vec{q}, \omega)$ and $\vec{J}_T(\vec{q}, \omega)$, which are proportional to the vector potential components $\vec{A}_L(\vec{q}, \omega)$ and $\vec{A}_T(\vec{q}, \omega)$, and therefore can be directly compared with the macroscopic expression (1.100) from macroscopic viscoelasticity [6, 19]. This way, we obtain explicit expressions for the static limit of the bulk modulus $K_B(0) = \lim_{\omega\to 0} K_B(\omega)$ and of the shear modulus $\mu_S(0) = \lim_{\omega\to 0} \mu_S(\omega)$ for a Fermi liquid. In $d = 3$ dimensions we have

$$K_B(0) = \frac{2nE_F}{3} \frac{1 + F_0^S}{1 + \frac{1}{3}F_1^S} \tag{1.108}$$

$$\mu_S(0) = \frac{2}{5} nE_F \frac{1 + \frac{F_2^S}{5}}{1 + \frac{1}{3}F_1^S} \tag{1.109}$$

Likewise, in $d = 2$ dimensions we obtain

$$K_B(0) = nE_F \frac{1 + F_0^S}{1 + \frac{1}{2}F_1^S} \tag{1.110}$$

$$\mu_S(0) = \frac{1}{2} nE_F \frac{1 + \frac{F_2^S}{2}}{1 + \frac{1}{2}F_1^S} \tag{1.111}$$

In equations (1.108) - (1.111), we have utilized the symmetric Landau parameters F_n^S $n = \{0, 1, 2\}$. We notice that the bulk moduli (1.108) and (1.110) employ the zero-order and first order Landau parameters, while for the shear moduli (1.109) and (1.109) to be nonzero, one has to include the contribution of F_1^S. This Fermi liquid result is consistent with section 1.5, where we have shown that we need to include F_1^S to reproduce *transverse zero sound*, which depends on a generalized viscoelastic coefficient $\nu(\omega)$ in the limit $q \to 0$. The same holds true for the transverse dielectric response (1.103). In the presence of

quasiparticle damping τ_c, we can repeat the analysis on the microscopic hamiltonian (1.73), now including a damping term in the relaxation time approximation, using the relaxation time τ_c [13, 19]. In the long-wavelength limit $q \to 0^+$, we find that the bulk modulus $K_B(\omega)$ is not affected by collisions, and is essentially independent of frequency, $K_B(\omega) \approx K_B(0)\ \forall \omega$. Then, the generalized bulk modulus in (1.99) becomes

$$\tilde{K}(\omega) = K_B(0) - i\omega\zeta(\omega) \tag{1.112}$$

The complex shear modulus $\tilde{\nu}(\omega)$, on the other hand, is affected by collisions with a first-order pole in the response

$$\tilde{\nu}(\omega) = \frac{[\mu_S(\omega) - i\omega\eta(\omega)]}{1 + \frac{i}{\omega\tau_c}} \tag{1.113}$$

If we consider a liquid with no shear modulus $\mu_S(\omega) \approx 0\ \forall \omega$, then equation (1.113) implies that the shear viscosity $\eta(\omega)$ is damped by a pole due to the collision time τ_c; this is what is assumed in paper 1, on the basis of a memory function for the generalized kinematic viscosity $\nu(\omega)$. We notice that, in the static limit $\omega \to 0$, we have in $d = 3$ dimensions

$$\eta(0) = \mu_S(0)\tau_c = \frac{2}{5} nE_F \frac{1 + \frac{F_2^S}{5}}{1 + \frac{1}{3}F_1^S}\tau_c = \frac{1}{5} nm(v_F)^2 \tau_c \frac{1 + \frac{F_2^S}{5}}{1 + \frac{1}{3}F_1^S}; \tag{1.114}$$

similarly, in $d = 2$ dimensions,

$$\eta(0) = \mu_S(0)\tau_c = \frac{1}{2} nE_F \frac{1 + \frac{F_2^S}{2}}{1 + \frac{1}{2}F_1^S}\tau_c = \frac{1}{4} nm(v_F)^2 \tau_c \frac{1 + \frac{F_2^S}{2}}{1 + \frac{1}{2}F_1^S}. \tag{1.115}$$

This is consistent with the viscosity parameterization of paper 1, for the frequency dependence of the kinematic viscosity $\nu(\omega) = \frac{\eta(\omega)}{nm}$, based on the dispersion relations (1.85) for liquid helium [10, 11]. Furthermore, from section 1.4.3 we understand that this stems from the nonlocal term at the pole of the RPA dielectric function - see sections 1.4.3 and 1.4.4.

1.7.3 Transverse collective modes in the Drude model

In the absence of nonlocal correlations for Landau quasiparticles, the dielectric response reduces to the local limit of independent quasielectrons: this is described by the Drude model for metals in textbooks [4, 5]. For future reference and comparison with the correlated charged Fermi liquid, it is instructive to briefly review the collective modes in the

Drude model. The scattering time $\tau_{\vec{k}} < +\infty$ models the presence of impurities which scatter independent quasiparticles. The self-consistent relations stemming from the Drude dielectric function are

$$\frac{q^2c^2}{\omega^2} = 1 - \frac{(\omega_p)^2}{\omega^2 + i\frac{\omega}{\tau_{\vec{k}}}} \tag{1.116}$$

Solving equation (1.116) for q, we have the Drude dispersion relations

$$q = \pm \frac{i\sqrt{\omega}\sqrt{-i\omega - \omega^2\tau_{\vec{k}} + (\omega_p)^2\tau_{\vec{k}}}}{c\sqrt{i + \omega\tau_{\vec{k}}}} \tag{1.117}$$

At first order in $\omega \to 0$, the dispersion relations (1.117) are quadratic in momentum:

$$q = \frac{\omega_p}{c}\sqrt{i\omega\tau_{\vec{k}}} + O(\omega^{\frac{3}{2}}) \tag{1.118}$$

According to equation (1.118), the Drude model has a long-wavelength imaginary part of the spectrum below the plasma frequency ω_p, which appears due to dissipation induced by a finite scattering time $\tau_{\vec{k}}$. The solutions (1.117) are the electromagnetic collective modes stemming from the coupling of photons to electrons inside the material. Physically, radiation propagates inside the metal, shaking electrons in response; this response is affected by any collective mode, characteristic of the electronic ensemble, that resonates with the exciting radiation: therefore, such photon-electron coupling allows to see the traces of existing electronic collective modes by analyzing the propagation of radiation. These light modes coupled to matter are called polaritons [1, 5, 14].[1] Equation (1.117) becomes the propagating transverse plasmon-polariton for $\omega > \omega_p$, meaning that photons couple to a propagating transverse plasmon. On the other hand, the dispersion is quadratic in momentum for $\omega - \omega_p \to 0^+$. In the limit $\tau_{\vec{k}} \to +\infty$ we have [4, 5]

$$q = \frac{1}{c}\sqrt{\omega^2 - (\omega_p)^2} \tag{1.119}$$

We calculate the full Drude response for any momentum and frequency through the photon propagator (1.18). Employing the relation between $\mathscr{A}_T(\vec{q}, \omega)$ and the dielectric function

[1] In optics literature, it is common practice to refer to polariton modes with the name of the collective excitation to which photons are coupled: for example, polaritons resulting from coupling to phonons can directly be called phonon modes; polaritons stemming from coupling to an electron plasmon are simply named plasmons, and so on.

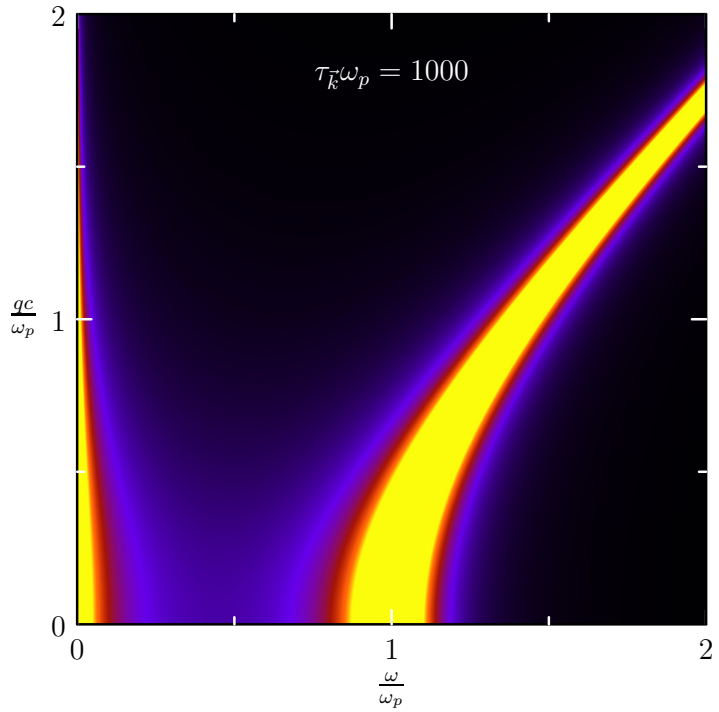

Figure 1.11: Imaginary part of the photon propagator $\epsilon_0(\omega_p)^2 Im\{\mathscr{A}_T(\vec{q},\omega)\}$ for the Drude model (1.120), as a function of adimensional momentum $\frac{qc}{\omega_p}$ and adimensional frequency $\frac{\omega}{\omega_p}$, for scattering time $\tau_{\vec{k}}\omega_p = 1000$.

(1.21), we obtain

$$\mathscr{A}_T(\vec{q},\omega) = \frac{1}{\epsilon_0(\omega_p)^2}\left[\left(\frac{\omega}{\omega_p}\right)^2 - \left(\frac{qc}{\omega_p}\right)^2 - \left(\frac{\omega}{\omega_p}\right)^2 \frac{1}{\left(\frac{\omega}{\omega_p}\right)^2 + i\frac{\omega}{\omega_p}\frac{1}{\tau_{\vec{k}}\omega_p}}\right]^{-1} \tag{1.120}$$

The correspondent transverse many-body polarization is

$$\Pi_{\vec{J}\vec{J}}(\omega) = \epsilon_0\omega^2\left(\epsilon_T(\vec{q},\omega) - 1\right) \equiv \epsilon_0\omega^2\left[\frac{(\omega_p)^2}{\omega^2 + i\frac{\omega}{\tau_{\vec{k}}}}\right] \tag{1.121}$$

We observe that the polarization (1.121) does not depend on wave vector $\vec{q}$ in the Drude model; this makes the dielectric response (1.120) local in real space of positions $\vec{r}$. The imaginary part of the photon propagator (1.120) is due to the presence of scattering. Figure 1.11 shows the imaginary part of the photon propagator $\epsilon_0 Im\{\mathscr{A}_T(\vec{q},\omega)\}$, for a scattering time $\tau_{\vec{k}}\omega_p = 1000$.

1.7.4 Viscoelastic modes in a Fermi liquid

In section 1.7.2 we have derived the longitudinal and transverse dielectric functions for a Fermi liquid in the presence of correlations using elasticity theory, in the regime (1.95). The elastic moduli (1.99) encode residual interactions among Landau quasiparticles and determine the dispersion and the velocity of the collective modes that propagate inside the Fermi liquid; microscopically, these elastic constants depend on Landau parameters and the Fermi velocity. Such collective modes are influenced by electromagnetic radiation due to the electric charge of quasiparticles. Maxwell's equations describe macroscopically the polarization and screening effects due to electromagnetic fields, acting on the interacting system characterized by the elastic moduli (1.99). Comparing these elastic constants (1.99) with the results (1.86) and (1.90) for the transverse sound velocity $\tilde{v}_{S,L}$ in collisional and collisionless regime, we see that $\tilde{v}_{S,L}$ can be simply regarded as the square root of the generalized shear modulus $\tilde{\mu}(\omega)$. It is easy to understand this physically: the d'Alembert equation for an elastic quantity $\alpha(x,t)$ with mass m_o is $\frac{\partial^2\alpha(x,t)}{\partial t^2} - (v_w)^2\frac{\partial^2\alpha(x,t)}{\partial x^2} = 0$ with wave velocity $v_w = \sqrt{\frac{K_L}{m_o}}$, where K_L is the elastic constant of the medium. This is also true for transverse shear modes in a Fermi liquid, to which we can formally assign a generalized shear modulus

$$\tilde{\nu}(\omega) \equiv i\frac{(\tilde{v}_{S,L})^2}{\omega} \tag{1.122}$$

in a viscoelastic description. The frequency evolution of the shear modulus $\mu_S(\omega)$ and shear viscosity $\eta(\omega)$ components in equations (1.99), with $\mu_S(\omega)$ increasing and $\eta(\omega)$ decreasing with ω, mimics macroscopically the frequency evolution of the complex sound velocity $\tilde{v}_{S,L}$ in passing from the collisional $\omega\tau_c \ll 1$ to the collisionless $\omega\tau_c \gg 1$ regimes. Therefore, equation (1.122) provides a microscopic interpretation of the generalized shear modulus in terms of the transverse dispersion relation (1.85), which is valid at RPA level and at first order in Landau parameters F_l^S. Such microscopic interpretation allows us to directly write the microscopic equivalent of the viscoelastic transverse dielectric function (1.103) for a Fermi liquid, as

$$\epsilon_T(\vec{q},\omega) = \frac{(\omega_p)^2}{\omega^2 - \left(\tilde{v}_{S,L}q\right)^2 + i\frac{\omega}{\tau_{\vec{k}}}} \tag{1.123}$$

The form (1.123) allows to directly recognize the dispersion of the transverse collective modes at the denominator of the dielectric function, to which a scattering term $i\frac{\omega}{\tau_{\vec{k}}}$ is added like in the Drude model for metals [4,5]. Equation (1.123) is the main result of this section. Writing the relation between the dielectric function and wave vector $\epsilon_T(\vec{q},\omega) \equiv \frac{q^2c^2}{\omega^2}$ for

electromagnetic waves, we can find the dispersion of polariton modes, coupled to electronic collective modes, from the self-consistent relation

$$\frac{q^2c^2}{\omega^2} = 1 - \frac{(\omega_p)^2}{\omega^2 - \left(\tilde{v}_{S,L}q\right)^2 + i\frac{\omega}{\tau_{\vec{k}}}} \tag{1.124}$$

Equation (1.124) describes the optical modes that propagate inside the material, in the presence of nonlocal correlations that are encoded into the complex sound velocity $\tilde{v}_{S,L}$. As seen in section 1.5.2, $\tilde{v}_{S,L}$ depend solely on the viscosity for $\omega\tau_c \ll 1$, while it depends only on the shear modulus in the limit $\omega\tau_c \to +\infty$. In chapter 2, we will focus on the consequences of these nonlocal self-consistent relations on the surface impedance, on the electric field spatial profiles, and on the plasmon dispersion, while here we concentrate on the details of dispersion relations. Hence, solving expression (1.124) for a real frequency we can obtain the dispersion of the optical modes inside the viscous medium, with a complex wave vector $q \in \mathbb{C}$. We report the details of this analysis in the next sections.

1.7.4.1 The collisionless limit: effective charge solid

In the collisionless limit $\omega\tau_c \to +\infty$, the transverse mode velocity tends to the real result $v_{S,\infty}$ according to equation (1.89) [7]. We assume a nonmagnetic medium, with the vacuum magnetic permeability μ_0, and the scattering time $\tau_{\vec{k}} \propto \tau_c \to +\infty$. The polarization is affected by the collective mode as [17]

$$\Pi_{\vec{j}\vec{j}}(\vec{q},\omega) = \epsilon_0\omega^2\left[\frac{(\omega_p)^2}{\omega^2 - \left(v_{S,\infty}q\right)^2}\right] \tag{1.125}$$

Notice that the self-energy (1.125) is nonlocal due to the momentum dependence of the term $\omega^2 - \left(v_{S,\infty}q\right)^2$ [5,12,16]. This contrasts with the local Fermi liquid model, in which the dependence of the self-energy on momentum is neglected [25]. Inserting equation (1.125) into the dielectric function (1.20) and using the relation $\epsilon_T(\vec{q},\omega) = \frac{q^2c^2}{\omega^2}$ for electromagnetic radiation traveling inside the medium [5], we arrive at the self-consistent relations for the collective modes

$$\frac{q^2c^2}{\omega^2} = 1 - \frac{(\omega_p)^2}{\omega^2 - \left(v_{S,\infty}\right)^2 q^2} \tag{1.126}$$

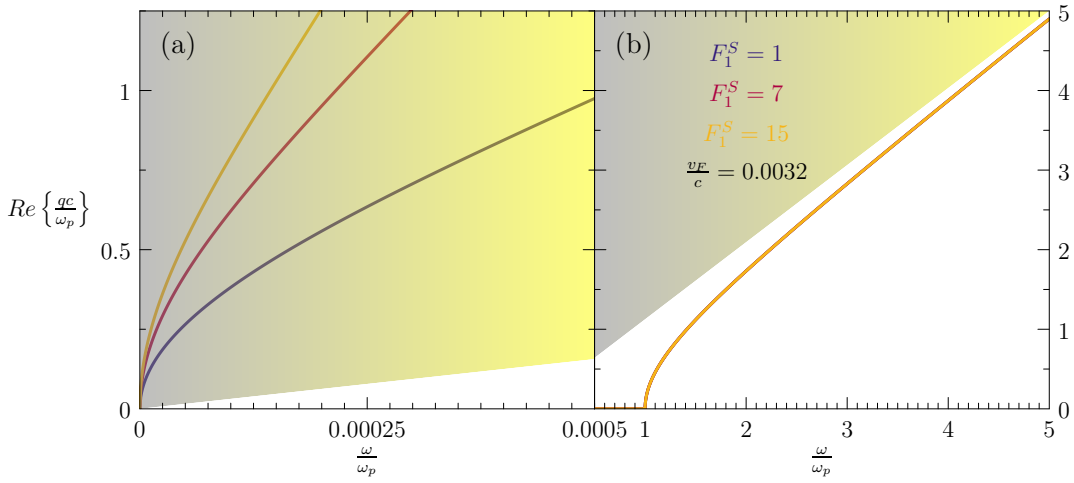

Figure 1.12: Normalized real part of the dispersion relation $\frac{Re\{q\}c}{\omega_p}$, as a function of normalized real frequency $o = \frac{\omega}{\omega_p}$, in collisionless regime $\omega\tau_c \to +\infty$ according to equation (1.127). Panel (a) shows the massless polariton mode, with quadratic dispersion (1.128) for $q \to 0$. Panel (b) shows the plasmon-polariton, which propagates above the plasma frequency ω_p [17]. The shaded area represents the Lindhardt electron-hole continuum $\frac{Re\{q\}c}{\omega_p} \geq \frac{c}{v_F}\frac{\omega}{\omega_p}$. The Fermi velocity is $\frac{v_F}{c} = 0.0032$. Curves of different colors correspond to first Landau parameter $F_1^S = \{1, 7, 15\}$, respectively.

Solving equation (1.126) for $\frac{qc}{\omega}$, we have the two-fold dispersion relation

$$\left(\frac{qc}{\omega_p}\right)^2 = \frac{\left(\frac{\omega}{\omega_p}\right)^2\left[1+(\frac{v_{s,\infty}}{c})^2\right] \pm \sqrt{(4\frac{\omega}{\omega_p}\frac{v_{s,\infty}}{c})^2 + \left(\frac{\omega}{\omega_p}\right)^2\left[-1+(\frac{v_{s,\infty}}{c})^2\right]^2}}{2(\frac{v_{s,\infty}}{c})^2} \tag{1.127}$$

The real parts of the dimensionless wave vector $\frac{qc}{\omega_p}$ for the dispersion relations (1.127) are shown as a function of dimensionless frequency $\frac{\omega}{\omega_p}$ in figure 1.12.

From figure 1.12, we see that the polariton in panel (a) is Landau-damped: the dispersion is real for all frequencies, according to equation (1.128), but it lies inside the electron-hole continuum. On the other hand, the plasma-polariton dispersion is intrinsically damped by a nonzero imaginary part below the plasma frequency ω_p, in accordance with equation (1.129), while it is entirely real above ω_p; in the latter case, the mode propagates undamped outside the Lindhardt continuum. Expanding at first order in ω, we find that the polariton dispersion from equation (1.127) is quadratic in wave vector, according to

$$\frac{qc}{\omega_p} = \sqrt{\frac{1}{v_{S,\infty}}\frac{\omega}{\omega_p}} + O\left[\left(\frac{\omega}{\omega_p}\right)^{\frac{3}{2}}\right] \tag{1.128}$$

The charged system result (1.128) of photons coupled to electrons contrasts with the electrically neutral case (1.89), where we have seen that the density collective excitations have a linear dispersion characteristic of sound-like excitation. This result is consistent with equation (353) in section XI.c of reference [17], where electromagnetism of the "'isotropic Wigner crystal'" is analyzed: in the collisionless limit, the Fermi sea behaves like an electrically charged elastic solid, responding with a shear modulus. Our results of section 1.5.2 allow one to assign a microscopic meaning to the mode velocity $v_{S,\infty}$, (c_T in reference [17]) in the case of Fermi liquids: the collective mode velocity depends on the residual interactions between Landau quasiparticles. In particular, the result (1.89) is valid at RPA level and first interaction order $l = 1$. The Drude model [5, 25] shows quadratic momentum dispersion for $q \to 0$ only with a finite scattering time $\tau_{\vec{k}}$, while the dispersion is linear for $\tau_{\vec{k}} \to +\infty$. On the other hand, the long-wavelength dispersion (1.128) is quadratic because of nonlocal correlations, even in the absence of collisions and scattering. The plasmon propagation can be analyzed by expanding equation (1.126) in Taylor series around $\frac{\omega}{\omega_p} = 1$: at second order in momentum, we have

$$\omega = \omega_p + \frac{c^2 + (v_{S,\infty})^2}{2\omega_p} q^2 + O\left(q^3\right). \tag{1.129}$$

Equation (1.129) confirms that the propagating plasmon has quadratic momentum dispersion at long wavelengths, with a coefficient that depends on the collisionless sound velocity $v_{S,\infty}$. For $F_1^S \gg 1$, the sound velocity tends to the square root of the shear modulus according to equation (1.90): therefore, in the presence of strong quasiparticle residual interactions, the coefficient of the collisionless plasmon dispersion is a measure of the Fermi liquid shear modulus. However, given that $c \gg v_{S,\infty}$ in standard metals, the corrections to the plasmon dispersion (1.129) due to the transverse zero sound velocity are generally very small, making it difficult to see such corrections experimentally. In order to analyze the dielectric response at arbitrary wave vector and frequency, we consider the photon propagator (1.18). For $\omega\tau_c \to +\infty$, the photon propagator is entirely real, as is the self-energy (1.125), since $v_{S,\infty} \in \mathbb{R}$. Therefore, the response is undamped for all momenta and frequency, and the collective modes satisfy simply $\mathscr{A}_T(\vec{q}, \omega) \to \infty$. The absolute value of the photon propagator $\epsilon_0 |\mathscr{A}_T(\vec{q}, \omega)|$ from equation (1.18) is displayed in figure 1.13, for $F_1^S = 7$ and $\frac{v_F}{c} = 10^{-3}$.

In the left panel of figure 1.13, we recognize the massless polariton collective mode which develops at low frequencies consistently with equation (1.127), and which possesses quadratic momentum dispersion at small momenta as described by equation (1.128). The

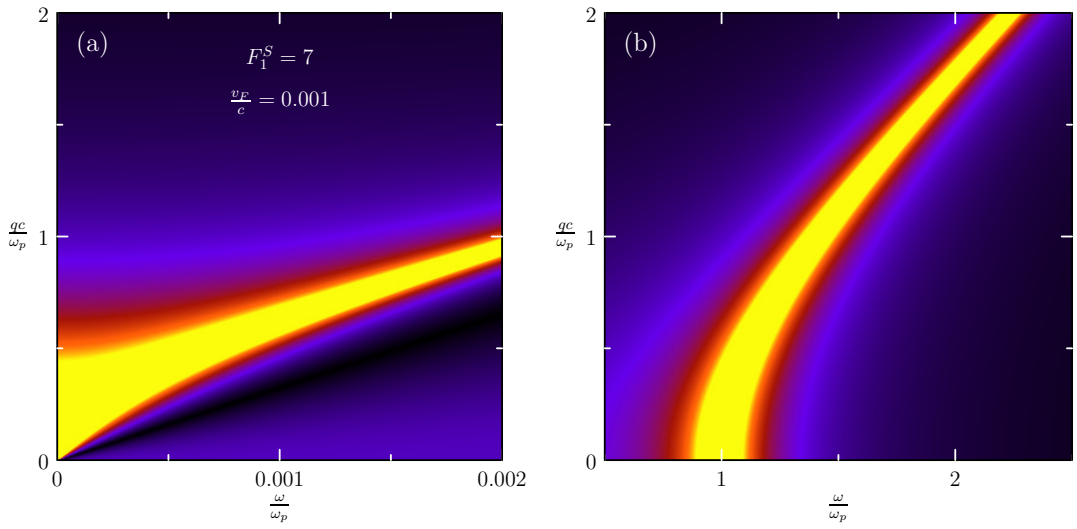

Figure 1.13: Contour plot of the absolute value of the photon propagator $\epsilon_0(\omega_p)^2 |\mathscr{A}_T(\vec{q},\omega)|$ from equation (1.18), as a function of adimensional momentum $\frac{qc}{\omega_p}$ and adimensional frequency $\frac{\omega}{\omega_p}$. Panel (a) shows the massless polariton collective mode from equation (1.128); panel (b) focuses on the high-frequency region with the plasmon-polariton solution (1.129).

right panel of figure 1.13 shows the high-frequency plasmon-polariton solution (1.127). As seen in figure 1.12, the massless polariton is always Landau-damped, while the plasmon-polariton propagates outside the Lindhardt continuum. Such features suggest that observing the quadratic dispersion (1.128) in optical experiments is difficult, even in collisionless regime. The elastic charge solid that we considered in this section is physically different from the Wigner crystal [17]: the former is realized in the collisionless limit of non-scattering Landau quasiparticles, while the latter develops for sufficiently strong interactions in electron liquids [1]. Our results demonstrate that the charged Fermi liquid responds to electromagnetic radiation like an elastic solid, with a real shear modulus, in the absence of scattering.

1.7.4.2 Viscoelastic modes with frequency-independent scattering

When we include scattering and collisions through $\tau_{\vec{k}} \propto \tau_c < +\infty$, the self-consistent relation to solve for polariton modes becomes (1.124). In principle, in a Fermi liquid $\tau_{\vec{k}} \propto \frac{1}{\omega^2}$ - see section 2.5.2.1 - so we should consider frequency-dependent scattering of collective modes. However, a frequency-independent $\tau_{\vec{k}}$ is sufficient to qualitatively illustrate the differences with respect to the collisionless limit; in this section we describe such qualitative differences, deferring the analysis of the frequency-dependent $\tau_{\vec{k}}$ to section 2.5.2.1. Here we also set the collision time $\tau_c = \tau_{\vec{k}}$ for simplicity. The solution for $\frac{qc}{\omega_p}$ is again analytical: when translated in terms of the refractive index $n(\omega) = \frac{qc}{\omega}$ [4, 5], this

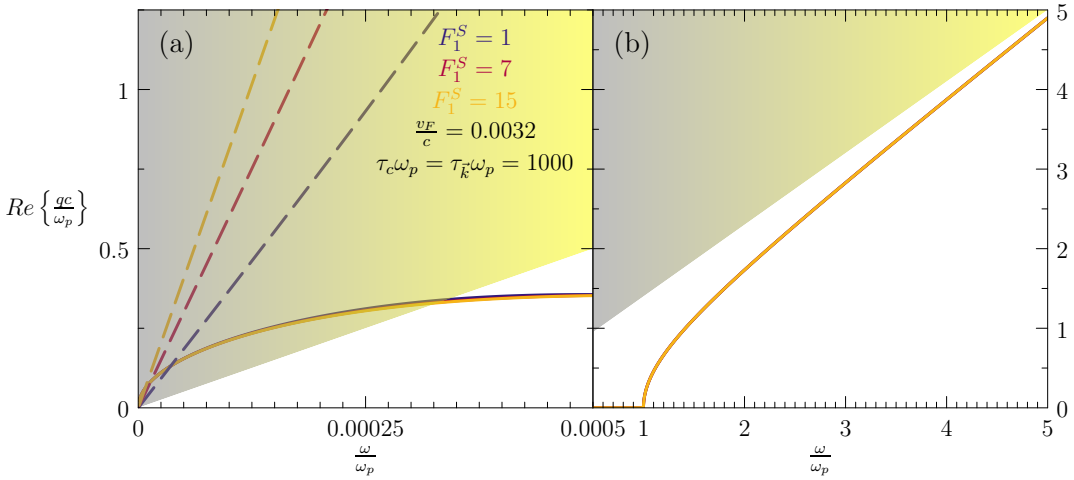

Figure 1.14: Normalized real part of the dispersion relation $\frac{Re\{q\}c}{\omega_p}$, as a function of normalized real frequency $\frac{\omega}{\omega_p}$, in collisional regime $\omega\tau_c < +\infty$. The Fermi velocity is $\frac{v_F}{c} = 0.0032$ and the scattering time is fixed to $\tau_{\vec{k}}\omega_p = \tau_c\omega_p = 1000$. Curves of different colors correspond to first Landau parameter $F_1^S = \{1, 7, 15\}$, respectively. Panel (a) shows the Drude-like mode (1.118) and the viscoelastic mode (1.130) for $q \to 0$. Panel (b) shows the plasmon-polariton, which is the high-frequency continuation of the Drude-like mode (1.118) propagating above the plasma frequency ω_p [17]. The shaded area represents the Lindhardt electron-hole continuum $\frac{Re\{q\}c}{\omega_p} \geq \frac{c}{v_F}\frac{\omega}{\omega_p}$.

solution is equation 4 of paper 1. There, we see that the collective modes dispersion splits in two different branches, which are frequency-degenerate: for each ω, there exist *two electromagnetic modes* inside the viscoelastic Fermi liquid. Expanding the solution for $\frac{qc}{\omega_p}$ for $\omega \to 0$, we find a quadratic branch, which coincides with the Drude result (1.118) and is governed by the scattering time $\tau_{\vec{k}}$. However, we also find an additional branch which is linear in frequency and reads

$$\frac{qc}{\omega_p} = \sqrt{\frac{i + \sqrt{-1 + 4\nu(\omega)(\tau_{\vec{k}}\omega_p)^2}}{2\nu(\omega)\tau_{\vec{k}}\omega_p}\frac{\omega}{\omega_p}} + O\left[\left(\frac{\omega}{\omega_p}\right)^{\frac{3}{2}}\right] \tag{1.130}$$

where $\nu(\omega) = \frac{\nu(0)}{i+\omega\tau_c}$ is the viscoelastic coefficient according to equations (1.87) and (1.114) in collisional regime. The linear dependence $q \propto \omega$ of equation (1.130) becomes apparent when we insert the expression for $\nu(\omega)$. This second mode is governed by the viscoelastic coefficient of the Fermi liquid. We show the long-wavelength twofold solution (1.118) and (1.130) in panel (a) of figure 1.14, with continuous and dashed curves respectively. The parameters are $\frac{v_F}{c} = 0.0032$ and $\tau_{\vec{k}}\omega_p = \tau_c\omega_p = 1000$. Different colors correspond to the calculations for first Landau parameter $F_1^S = \{1, 7, 15\}$.

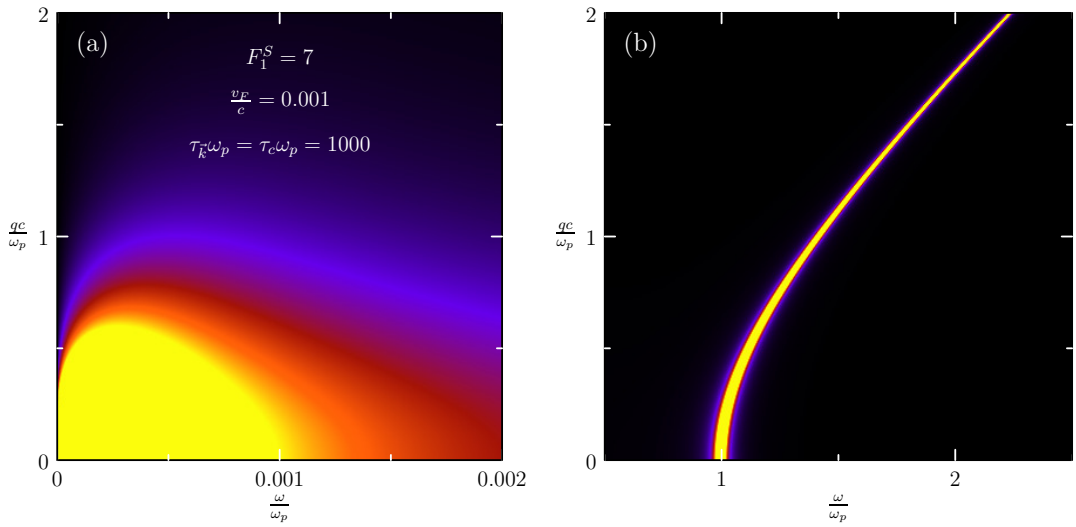

Figure 1.15: Contour plot of the imaginary part of the viscoelastic photon propagator $\epsilon_0(\omega_p)^2 Im\{\mathscr{A}_T(\vec{q},\omega)\}$ from equation (1.18), as a function of adimensional momentum $\frac{qc}{\omega_p}$ and adimensional frequency $\frac{\omega}{\omega_p}$. Panel (a) shows the Drude-like collective mode (1.118), while the viscoelastic mode (1.130) is not visible; panel (b) focuses on the high-frequency region with the propagating plasmon-polariton.

The viscoelastic mode (1.130) is much more sensitive to F_1^S, since it directly depends on the viscoelastic coefficient $\nu(\omega)$. This mode is Landau-damped at all frequencies, as it is inside the electron-hole continuum as indicated by the shaded area. On the other hand, the Drude-like mode (1.118) emerges from the electron-hole continuum at sufficiently high frequency, however it is still intrinsically damped by a finite imaginary part for $\omega < \omega_p$; above ω_p, this mode becomes entirely real: it is the propagating plasmon shown in panel (b), which possesses quadratic frequency dispersion for $\omega \approx \omega_p^+$. In figure 1.15, we plot the imaginary part of the photon propagator (1.18) for the parameters $\frac{v_F}{c} = 0.001$, $F_1^S = 7$ and $\tau_{\vec{k}}\omega_p = \tau_c\omega_p = 1000$, employing the transverse viscoelastic polarization [17]

$$\Pi_{\vec{j}\vec{j}}(\vec{q},\omega) = \epsilon_0\omega^2\left[\frac{(\omega_p)^2}{\omega^2 - \left(\tilde{v}_{S,L}q\right)^2 + i\frac{\omega}{\tau_{\vec{k}}}}\right]. \tag{1.131}$$

Panel (a) of figure 1.15 shows the Drude-like mode (1.118), while the viscoelastic mode (1.130) is not visible due to its smaller pole strength: radiation couples much more with the Drude-like mode than with the viscoelastic one. Panel (b) shows the propagation of the plasmon-polariton, similarly to the Drude model.

1.8 Conclusions and perspectives

Conduction electrons form an electrically charged Fermi liquid in many solid-state systems: the inclusion of electric charge modifies the dispersion relation of collective modes. Long-ranged Coulomb interactions are screened and form weakly-interacting F_l^S charged quasielectrons, which are spatially coherent up to their mean free path. Such correlations allow the Fermi liquid to respond to external perturbation with longitudinal (density) and transverse (current) collective modes. The collective modes influence the many-body polarization in the material, forming resonant charge responses in correspondence with the mode dispersion relation $\omega(\vec{q})$: this can be described by a nonlocal dielectric function $\epsilon_\alpha(\vec{q},\omega)$ in the longitudinal $\alpha = L$ and transverse $\alpha = T$ channels, respectively. The coefficient of the nonlocal momentum dependence is related to the squared phase velocity $\tilde{v}_{S,L}$ of the resonant modes. In the limit $q \to 0$ according to equation (1.95), away from the particle-hole continuum, we can treat the collective modes due to quasiparticle correlations within the viscoelastic model, developed for the electrically neutral case in section 1.5.2: the Fermi surface resonates with viscoelastic waves, the velocity of which can be described by generalized elastic moduli as in section 1.7.2. In the transverse channel, the phase velocity $\tilde{v}_{S,L}$ is equivalent to a generalized viscoelastic coefficient $\nu(\omega)$. In the collisionless limit $\tau_c = \tau_{\vec{k}} \to +\infty$, we find a plasmon-polariton, that becomes propagating above ω_p, and a propagating massless phonon polariton. Both branches depend on the velocity $v_{S,L}$, equivalent to the collisionless shear modulus of the Fermi liquid. The propagating plasmon has also quadratic dispersion, with a slope that is controlled by the shear modulus. These findings are different from the Drude case: for the latter we also have quadratic dispersion at long wavelengths for the plasmon-polariton and phonon-polariton, but this is due to a finite scattering time $\tau_{\vec{k}} < +\infty$, which causes damping of the collective modes for $q \to 0$. When we include scattering and collisions, the long-wavelength dispersion splits in two qualitatively different branches: we have a quadratic tail of the plasmon-polariton governed by scattering as in the Drude model, and an additional *linear* momentum dispersion for a massless phonon-polariton, depending on the viscoelastic coefficient $\nu(\omega)$: this is due to the Fermi liquid responding like a viscous relaxing fluid for $\omega\tau_c \ll 1$. The long-wavelength, low-frequency region $q \to 0^+$, $\omega \to 0^+$ of the excitation spectrum is the most affected by viscoelastic correlations, and is governed by viscosity in the collisional regime, and by the shear modulus in the collisionless limit. Therefore, an experimental determination of the long-wavelength dielectric response for clean samples with $\tau_c \to +\infty$, or for dirty samples with $\omega\tau_c \ll 1$, can provide information on the viscoelastic correlations, through a shear modulus or a shear viscosity respectively. However, most of the spectrum is dominated

by the collisionless regime, characteristic of transverse zero sound in electrically neutral systems. In this case, the dielectric response is qualitatively similar to the Drude results, and differences due to elastic shear properties emerge only quantitatively.

The analysis of correlations in Fermi liquids through generalized elasticity calls for possible experimental techniques that are able to probe such effects in condensed matter systems. One is transport, which could reveal velocity gradients in the longitudinal channel due to viscoelasticity when we accelerate charged carriers with a voltage [42,43]: this could distinguish the coherent and diffusive regimes of electron transport, as sketched in section 1.4.3. Moreover, transverse charged collective modes couple to electromagnetic radiation, which is also transverse and interacts with electric charges: therefore, optical spectroscopy is able to detect transverse charged collective excitations formed by conduction electrons in solids. Furthermore, optics probes the long-wavelength region $q \to 0$ [4,5], which is also the regime where the viscoelastic model for correlations applies [6,19]: hence, optical experiments are suitable to investigate effects due to viscoelasticity in the Fermi sea. Based on the former motivations, we dedicate the next chapter to the calculation of some possible optical observables in the presence of viscoelastic correlations, such as transmission and reflection spectra, surface impedance, and real space profiles of the electric field inside the material.

Chapter 2

Viscoelastic metals: optical properties

2.1 Introduction

The electron liquid in a metal is able to resonate with collective modes of electron density: in chapter 1, we have analyzed how these collective excitations emerge in the Fermi liquid model (1.72), using the diagrammatic as well as the Boltzmann equation approach. In the long-wavelength limit $q \to 0$, such modes can be described with viscoelasticity: the Fermi surface responds to an external excitation by oscillating in space and time, changing its volume and its shape with an elastic and a dissipative component. The dispersion of the collective modes changes qualitatively when the electric charge degree of freedom is considered. This situation applies to metallic solids, where quasielectrons and quasiholes are electrically charged. We noticed that this polar feature allows for direct coupling of the viscoelastic collective excitations to electromagnetic radiation, in the limit $q \to 0$: hence, optical spectroscopy is an ideal way to probe the viscoelasticity of the Fermi liquid. In this chapter, we calculate various optical observables which can exhibit signatures of viscoelastic modes. Among these, the optical transmission and reflection of thin metallic films, the surface impedance, and the plasmon dispersion can directly show the presence of viscoelastic correlations with available experimental techniques. Moreover, the spatial profile of the decaying electric field inside the material shows oscillations as a function of depth from the sample surface, due to nonlocal correlations. The viscoelastic effects are seen in metals at low temperatures, since in this case the mean free path l_{MFP} becomes some orders of magnitude longer than at room temperature: this makes the dielectric response nonlocal, as we have seen in section 1.4.

In the next section, we begin by considering the effects of viscoelastic modes at the conceptual level, before proceeding with some examples of practical implementations using

realistic material parameters. Among all possible applications, Terahertz transmission spectroscopy is a suitable method to probe viscoelasticity in metallic slabs, as we will see by comparing our calculations with experimental data on epitaxial aluminium thin films grown on sapphire substrates.

In order to provide qualitative predictions of optical observables in the entire frequency range available in experiments, we have to specify the different scattering mechanisms that occur in metallic solids, and their respective temperature and frequency dependences. As we have seen in chapter 1, Fermi liquid theory provides a solid foundation to understand scattering in metals. The results obtained for a temperature-dependent but frequency-independent scattering time from Fermi liquid theory are summarized in paper 1, at the end of this chapter. However, when dealing with real systems, additional scattering and collision mechanisms play an important role, with respect to pure Fermi liquid phenomenology,: the phonon contribution at room temperature, and the residual impurity scattering at $T \to 0$ - see section 1.4.1 - can overcome the Fermi liquid component, effectively destroying the signatures of viscoelasticity. We consider qualitatively such effects in the calculations of the finite-temperature results, through the Bloch-Gruneisen formula for phonons and a low-T impurity contribution. These arguments will allow us to consider the transmission spectrum of Fermi-liquid thin films, and the occurrence of negative refraction.

2.2 Optics of viscoelastic charged fluids

2.2.1 Viscoelastic refractive indexes

Nonlocal correlations modify the dielectric function, which is the cornerstone of optical observables calculations. Nonlocality can be treated diagrammatically in self-consistent RPA, as we have seen in section 1.4.3, or equivalently with hydrodynamics [6, 12], considering the transverse linear response of the electrons as a viscoelastic liquid [12] - see section 1.7.2. The refractive index, describing the dispersion and absorption of electromagnetic radiation inside matter [5], is defined as

$$n(\omega) = \sqrt{\epsilon_T(\vec{q},\omega)} = \sqrt{\epsilon_T\left[\frac{\omega}{c}n(\omega),\omega\right]} \tag{2.1}$$

where we have used the dispersion relation $q = \frac{\omega}{c}n(q,\omega)$ for plane electromagnetic waves inside a medium [5]. When we insert the viscoelastic transverse dielectric function (1.103) into the relation (2.1), we realize that the equation for $n(\omega)$ is of second order, therefore there are *two solutions* $\{n_1(\omega),\ n_2(\omega)\}$ for each frequency. We can interpret this physically

as follows: for each incident electromagnetic wave of a given frequency, there exist two frequency-degenerate and mutually coherent polariton modes, that can propagate through the material: this phenomenon depends on the nonlocal dielectric response at finite q, due to the presence of viscoelastic correlations. The fourfold solution for the refractive indexes reads

$$2[n_j(\omega)]^2 = 1 - \frac{1 - i\omega\tau_{\vec{k}}}{\omega^2 \nu_c \tau_{\vec{k}}} \pm \sqrt{\left(1 + \frac{1 - i\omega\tau_{\vec{k}}}{\omega^2 \nu_c \tau_{\vec{k}}}\right)^2 + i\frac{4(\omega_p)^2}{\omega^3 \nu_c}} \tag{2.2}$$

where $j = \{1, 2\}$ for plus or minus sign respectively, and $\nu_c = \frac{\nu}{c^2}$ is the viscoelastic coefficient, with c velocity of light in vacuum. For long-wavelength collective modes in a Fermi liquid, ν is connected to the mode velocity and corresponds to equation (1.122). Out of the four mathematically possible solutions (2.2), two of them are excluded on the basis of the physical argument that electromagnetic waves are damped in space and time throughout their propagation inside the medium, due to absorption [4,5]: this requires $Im\left\{n_j(\omega)\right\} > 0$, so that only the two solutions (2.2) that satisfy this criterion are physical.

An intriguing aspect of this phenomenon is that $n_2(\omega)$ can develop *negative refraction* in a specific low-frequency regime, which depends on the collision time τ_c and on the Fermi velocity v_F. Negative refraction means $Re\{n_2(\omega)\} < 0$ [44], which implies that radiation propagating inside the material disperses in an opposite way with respect to the standard case $Re\{n(\omega)\} > 0$. This generates a variety of new physical properties, which impact the space-time evolution of electric $\vec{E}$ and magnetic $\vec{H}$ fields, and are potentially useful for applications [45]. Some examples are: self-focusing of radiation, which allows to make a perfect lens that goes beyond the diffraction limit; amplification of evanescent electromagnetic waves in the near field; opposite energy flux, given by the Poynting vector $\vec{\mathscr{S}} = c\epsilon_0 \vec{E} \times \vec{H}$, with respect to the phase velocity $v_p = \frac{\omega}{q}$; tuning of the spatial profile of $\vec{E}$ and $\vec{H}$ inside a material. Such physical properties have already been tested using artificial optical nanostructures, i.e. metamaterials, which are specifically designed to show negative refraction [45]. However, there are chances to find negative-refracting systems even in natural materials: the results of chapter 1 tell us that it is possible to probe finite-momentum physics with light in a Fermi liquid, and in such conditions negative refraction can occur according to eq. (2.1). This aspect is further investigated in paper 1.

2.2.2 Reflection and transmission of layers on a substrate

The mode bifurcation, caused by the presence of two refractive indexes (2.1), directly impacts the absorption and dispersion of radiation, which leaves specific signatures in the spectrum of transmission $t(\omega)$ and reflection $r(\omega)$ as a function of frequency, for semi-

infinite interfaces as well as for thin films. The physical reason for this is that the modes $\{n_1(\omega),\ n_2(\omega)\}$ are frequency-degenerate mutually coherent, therefore they can interfere constructively or destructively for different ω, giving rise to standing-wave oscillating patterns in the optical spectra. In general, the expressions for transmission and reflection depend on the constitutive relations at the boundaries of the system, with vacuum or with another material: this tells us how intensity and phase of radiation are modified in traversing an interface between different media; such material-dependent information complements the Maxwell equations of electromagnetism, giving a well-defined problem which often admits solutions in closed form. In the following, we consider radiation at normal incidence with respect to the viscoelastic sample surface, with z as the propagation direction. This way, the problem for the electric field $\vec{E} = \vec{E}(z)$ becomes one-dimensional. The Maxwell equations provide the conditions that $E(z)$ and its space derivative $\frac{\partial E(z)}{\partial z}$ are continuous at the interface. Since we are dealing with a viscoelastic fluid, additional constitutive relations can be retrieved from hydrodynamics, specifically from the properties of Newtonian fluids: while they react to an electric field, the fluid particles also interact with the sample boundaries, which affects the spatial velocity profile in the fluid. In particular, the tangential friction per unit area κ exerted by the moving fluid on the boundary of the solid is, in leading order, proportional to the velocity at the interface $z = 0$,i.e. $\kappa v(0)$. In equilibrium, this has to be balanced by the force exerted by the velocity gradient of the viscous fluid, $\eta \frac{\partial v(z)}{\partial z}$, where $\eta = nmv$ is the dynamic viscosity - see section 1.7.2. This leads to the Navier constitutive relation [46]. To be specific, we consider an electromagnetic wave of frequency ω propagating along z from $-\infty$ to the sample, which has one boundary defined by the plane $z = 0$ and the other by $z = d$. Part of the wave is reflected back, with an amplitude characterized by the reflection coefficient r, the amplitude transmitted to $z > d$ is characterized by the transmission coefficient t. This way, we arrive at the following three constitutive relations at the two interfaces:

$$E(0-\delta) = E(0+\delta) \qquad E(d-\delta) = E(d+\delta) \tag{2.3a}$$

$$\left.\frac{\partial E}{\partial z}\right|_{0-\delta} = \left.\frac{\partial E}{\partial z}\right|_{0+\delta} \qquad \left.\frac{\partial E}{\partial z}\right|_{d-\delta} = \left.\frac{\partial E}{\partial z}\right|_{d+\delta} \tag{2.3b}$$

$$\frac{1}{\lambda_s} = \left.\frac{\partial \ln v}{\partial z}\right|_{0+\delta} \qquad \left.\frac{\partial \ln v}{\partial z}\right|_{d-\delta} = \frac{-1}{\lambda_s} \tag{2.3c}$$

The constant $\lambda_s = \eta/\kappa$ is the slip length, where $\lambda_s = 0$ ($\lambda_s = \infty$) corresponds to the interface being maximally rough (smooth).

Since the refractive index solution (2.1) is twofold, inside the slab the wave-amplitude is a superposition of 4 modes, corresponding to counter-propagating waves for each

mode [5, 12]:

$$E(z)/E(0) = \begin{cases} e^{ikz} + re^{-ikz} & (z < 0) \\ t_1 e^{in_1 kz} + \theta_1 e^{-in_1 kz} + t_2 e^{in_2 kz} + \theta_2 e^{-in_2 kz} & (0 < z < d) \\ te^{ikz} & (z > d) \end{cases} \tag{2.4}$$

Since $Im\{n_j\} > 0$, the two terms $e^{-in_j kz}$ diverge exponentially for $z \to \infty$. Hence, in the limit of a half infinite sample θ_1 and θ_2 converge to zero, and only t_1 and t_2 contribute to the transport of electromagnetic radiation into the material.

The case of a single vacuum-viscoelastic matter interface and of a free-standing viscoelastic slab in vacuum are fully treated in paper 1. However, many slab samples of interest for our studies are epitaxially grown on top of a substrate. For this reason, it is convenient to generalize the problem to the one of a viscoelastic film attached to a non-viscoelastic substrate. This will allow us to directly compare our calculations with Terahertz transmission measurements of Al/sapphire structures. Assume a substrate having refractive index $n_S(\omega)$ and thickness d_S, obeying the standard Fresnel equations of reflection and refraction [4, 5]. Moreover, let us assume radiation impinging first on the substrate. Reflection/transmission at the substrate/sample interface of a half-infinite sample requires to combine Eqs. 2.4 with aforementioned constitutive relations at the substrate-matter interface at $z = 0$. It is worth mentioning that the Navier condition (2.3c) is applied to current density $\vec{J} = nm\vec{v}$, which is proportional to the time-derivative of the electric field:

$$\vec{J}_j(z,\omega) = -i\epsilon_0\omega\left\{\left[n_j(\omega)\right]^2 - 1\right\} t_1 E(z),\ j = \{1,2\} \tag{2.5}$$

Notice the presence of two additive components $J(z,\omega) = J_1(z,\omega) + J_2(z,\omega)$ for the current density, due to the two mutually coherent viscoelastic optical modes. Some algebra leads to the transmission coefficients at the substrate-film interface

$$t_1 = \frac{2n_S}{n_2 + n_S}\left\{\frac{n_1 + n_S}{n_2 + n_S} - \frac{\left(\lambda_s \frac{\omega}{c} n_1 + i\right)\left[(n_1)^2 - 1\right]}{\left(\lambda_s \frac{\omega}{c} n_2 + i\right)\left[(n_2)^2 - 1\right]}\right\}^{-1} \tag{2.6a}$$

$$t_2 = \frac{2n_S}{n_1 + n_S}\left\{\frac{n_2 + n_S}{n_1 + n_S} - \frac{\left(\lambda_s \frac{\omega}{c} n_2 + i\right)\left[(n_2)^2 - 1\right]}{\left(\lambda_s \frac{\omega}{c} n_1 + i\right)\left[(n_1)^2 - 1\right]}\right\}^{-1} \tag{2.6b}$$

where the frequency dependence of the refractive indexes is implicit for compactness. The reflection coefficient stems from

$$r_{fs} = 1 - t_1 - t_2 \tag{2.7}$$

Equation (2.7) is also useful when we have to consider internal reflections in a substrate of thickness d_S: at the substrate-film interface, the viscoelastic properties of the slab influence the reflected waves inside the substrate. On the other hand, at the vacuum-substrate interface we can apply the standard Fresnel equations [5], which give a transmission coefficient

$$t_{vS} = \frac{2}{1+n_S} \tag{2.8}$$

and a reflection coefficient

$$r_{Sv} = \frac{1-n_S}{1+n_S} \tag{2.9}$$

Notice that equations (2.6a) and (2.7) consistently reduce to equation (7) of paper 1 if the substrate is substituted with vacuum, i.e. $n_S \equiv 1$.

In the case of transmission through a viscoelastic slab of thickness d, with substrate on the left side and vacuum on the right one, the field inside the film is a superposition of all 4 solutions of Eq. 2.4 for $0 < z < d$. This approach automatically takes into account Fabry-Perot interference of the electromagnetic modes inside the slab [4]. Taken together with the reflection amplitude r_{film} for $z < 0$ and the transmission amplitude t_{film} for $z > d$, the problem corresponds to a system of 6 linear equations with 6 unknown parameters. We take four of these combinations, and we employ the constitutive relations 2.3a, leading to the matrix expression

$$\begin{bmatrix} 1+\frac{n_1}{n_S} & 1-\frac{n_1}{n_S} & 1+\frac{n_2}{n_S} & 1-\frac{n_2}{n_S} \\ (1-n_1)f_1 & (1+n_1)/f_1 & (1-n_2)f_2 & (1+n_2)/f_2 \\ (1-n_1^2)(1-n_1\xi) & (1-n_1^2)(1+n_1\xi) & (1-n_2^2)(1-n_2\xi) & (1-n_2^2)(1+n_2\xi) \\ (1-n_1^2)(1+n_1\xi)f_1 & (1-n_1^2)(1-n_1\xi)/f_1 & (1-n_2^2)(1+n_2\xi)f_2 & (1-n_2^2)(1-n_2\xi)/f_2 \end{bmatrix} \begin{bmatrix} t_1 \\ \theta_1 \\ t_2 \\ \theta_2 \end{bmatrix} = \begin{bmatrix} 2 \\ 0 \\ 0 \\ 0 \end{bmatrix} \tag{2.10}$$

where we use the compact notations $f_1 = e^{in_1kd}$, $f_2 = e^{in_2kd}$ and $\xi = i\lambda k$. The matrix (2.10) corresponds to equation (9) of paper 1, for $n_S \equiv 1$: only the first row is different for $n_S \neq 1$, due to the condition $\frac{\partial E}{\partial z}\big|_{0-\delta} = \frac{\partial E}{\partial z}\big|_{0+\delta}$ being modified by the presence of a substrate. Matrix inversion provides t_1, θ_1, t_2 and θ_2, from which the reflection and transmission coefficients of the film are obtained using the remaining two constitutive relations

$$\begin{aligned} r_{Sf} &= t_1 + \theta_1 + t_2 + \theta_2 - 1 \\ t_f &= \frac{t_{film}}{t_{vac}} = e^{-ikd}\left\{t_1 e^{in_1kd} + \theta_1 e^{-in_1kd} + t_2 e^{in_2kd} + \theta_2 e^{-in_2kd}\right\} \end{aligned} \tag{2.11}$$

where, as in experimental practice, the transmission is calibrated against the transmission through a slice of vacuum with the same thickness, d, as the film.

Being equipped with the results (2.6a)-(2.11), we are ready to solve the entire problem of transmission through the substrate-sample structure. If we neglect internal reflections inside the substrate, the first-echo transmission is simply

$$t_{(1)} = t_{vS} e^{ikn_S d_S} t_f \tag{2.12}$$

since the radiation enters the substrate, travels for a thickness d_S, then it enters the film and exits in vacuum after internal reflections in the viscoelastic slab. Additional internal reflections in the substrate can be taken into account using the thin-film geometric series [47]

$$t_{FP,S} = t_{vS} e^{ikn_S d_S} \left[1 + r_{Sf} r_{Sv} e^{2ikn_S d_S} + \left(r_{Sf} r_{Sv} e^{2ikn_S d_S} \right)^2 + \cdots \right] \tag{2.13}$$

For infinite reflections, the total contribution is then

$$t_{FP,S} = \frac{t_{vS} e^{ikn_S d_S}}{1 - r_{Sf} r_{Sv} e^{2ikn_S d_S}} \tag{2.14}$$

and the total transmission through substrate and layer becomes

$$t_{(\infty)} = t_{FP,S} t_f \tag{2.15}$$

The expressions (2.12) and (2.15) find an immediate application in the analysis of Terahertz time-domain transmission spectroscopy [48, 49]: indeed, subsequent pulses in the time-domain interferogram correspond to an increasing number of internal reflections (2.13) inside the substrate, provided that $d_S \gg d$; the first pulse only contains internal reflections inside the slab, which is described by equation (2.12). In section 2.3, we will apply the formalism developed so far to a structure composed of an aluminium thin film on a sapphire substrate, in order to demonstrate the presence of nonlocal correlations at low temperatures.

2.2.3 Surface impedance

Another optical observables which is affected by a nonlocal dielectric response, and that one can measure with state of the art equipment, is the surface impedance $Z = Z(\omega, T)$ of a metal. Here below, we calculate those effects for a viscous charged fluid, and later we specialize to the Fermi liquid case, which gives a higher chance of observing viscous phenomena with respect to the quantum critical case 1.6, the latter possessing a very high

degree of fluidity [35]. Our result will allow us to compare the viscoelastic model for a Fermi liquid to the full nonlocal theory of anomalous skin effect by G. E. H. Reuter and E. H. Sondheimer [50, 51].

In general, the complex surface impedance $Z = Z(\omega, T)$ is defined as the ratio of the electric field $\vec{E}$ normal to the surface of a metal to the total current density $\vec{J}$ induced in the material [4, 5]

$$Z(\omega) = \frac{E(z,\omega)_{z=0^+}}{\int_0^{+\infty} J(z,\omega)dz} \tag{2.16}$$

Here, we defined the orthogonal coordinate z with respect to the metallic surface $z = 0$. $J(z,\omega)$ is the spatially dependent current density per unit area, which decays with increasing distance z from the surface. We begin by recalling the standard Fresnel expression for the reflection coefficient

$$r_D(\omega) = \frac{1 - n(\omega)}{1 + n(\omega)} \tag{2.17}$$

From there, the surface impedance is easily obtained through the general relation valid for specular reflection at normal incidence, at the boundary between vacuum and a dielectric medium [5]

$$r(\omega) = \frac{Z_D(\omega) - Z_0}{Z_D(\omega) + Z_0} \tag{2.18}$$

with Z_0 vacuum surface impedance, which we set to 1. The Drude surface impedance becomes $Z_D(\omega) = \frac{1+r(\omega)}{1-r(\omega)}$; considering equation (2.17), this gives simply

$$Z_D(\omega) = \frac{1}{n(\omega)} \tag{2.19}$$

The graphs of the real and imaginary parts of the Drude surface impedance are well analyzed in multiple references; see for example [4] and [5].
Now, we derive an explicit expression for the surface impedance in the viscoelastic model [12], for a vacuum-viscoelastic layer interface. In this case, the refractive indexes of the two degenerate electromagnetic modes are given by equation (2.2), and the transmission and reflection coefficients at such an interface are given by equation (7) of paper 1, or equivalently by equations (2.6a) and (2.7) with $n_S \equiv 1$.

We can again employ the general relation (2.18) for the surface impedance, which gives $Z(\omega) = \frac{1+r(\omega)}{1-r(\omega)}$; inserting the expression for the viscoelastic reflection coefficient r, we obtain

$$Z(\omega) = \frac{n_1 + n_2 + i\frac{\lambda_s}{c}\omega\left[1 - (n_1)^2 - (n_2)^2 - n_1 n_2\right]}{1 + n_1 n_2\left[1 - i\frac{\lambda_s}{c}\omega(n_1 + n_2)\right]} \tag{2.20}$$

One can verify that the surface impedance (2.20) reduces to the Drude expression (2.19) consistently, whenever only one optical mode is propagating in the metal, that is $n_1 \to +\infty$ or $n_2 \to +\infty$: this is the standard, non-viscous limit. Notice that, given that the dielectric function $\epsilon = \epsilon(\vec{q}, \omega)$ which generates the refractive indexes (2.2) is nonlocal, the expression (2.20) describes nonlocal electrodynamics: the material reacts to the incident electric field not only locally at $z = 0$, but quasiparticles respond collectively also at other coordinates $z > 0$ inside the medium, up to a distance of the order of the mean free path l_{MFP}; this is reminiscent of the phenomenon of electron diffusion, which we studied diagrammatically in section 1.4. In the context of optics, the nonlocal response modifies the usual exponential damping of electromagnetic waves inside a metal due to screening, i.e. skin effect, so that radiation can penetrate more inside the material than in standard conditions: this is called *anomalous skin effect*. Indeed, we will see that the surface impedance derived in the context of viscosity reproduces the anomalous skin effect of metals, whereby a nonlocal dielectric response arises at low temperatures [12] - see also paper 1. On the other hand general theory of nonlocal response for anomalous skin effect [50, 51] requires numerical integration of the nonlocal kernel, in order to calculate the surface impedance $Z(\omega)$ from the spatial distribution of the current response. The viscoelastic approach, while showing slight quantitative differences with respect to the full numerical output, has the advantage of giving a simpler solution in closed form, which still reproduces the same physics - see figure 2 of paper 1, and figure 2.1.

After the work by Pippard [52–54], who developed an effective model to interpret experimental results on the dielectric response at cryogenic temperatures, it is customary to plot the surface impedance as $\frac{1}{Re\{Z(\omega)\}}$ as a function of the square root of the Drude conductivity $\sqrt{\sigma_D}$; the latter is defined as [3]

$$\sigma_D = \frac{ne^2\tau_{\vec{k}}}{m} \tag{2.21}$$

In passing, we notice that equation (2.21) corresponds to the local regime of the DC conductivity (1.48).

Given the proportionality between the Drude conductivity σ_D and the scattering time $\tau_{\vec{k}}$ in equation (2.21), it is sufficient for us to make the graph of $\frac{1}{Re\{Z(\omega)\}}$ as a function of $\sqrt{\tau_{\vec{k}}}$. The result is shown in figure 2.1: the cases of slip lengths $\frac{\lambda_s \omega_p}{c} = \{0, +\infty\}$ are shown as the red and gold line, respectively; the dashed gray line shows Drude result (2.19)for comparison. The frequency is $\omega = 0.001\omega_p$, and we have utilized the viscosity parameterization (1.94) of paper 1 with $\frac{v_F}{c} = 0.001$, $\tau_c = \tau_{\vec{k}}$ meaning umklapp

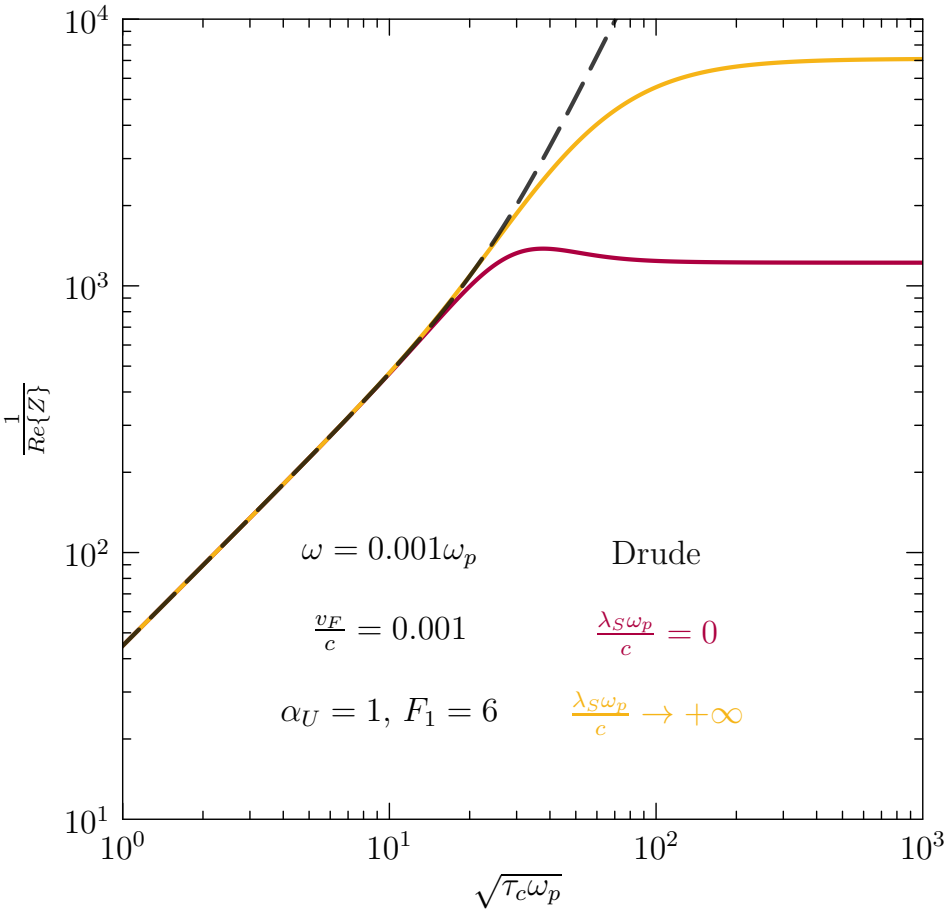

Figure 2.1: Inverse real part of the surface impedance $\frac{1}{Re\{Z(\omega)\}}$, given by equation (2.20), as a function of the square root of the scattering time $\sqrt{\tau_{\vec{k}}}$, for $\tau_{\vec{k}} = \tau_c$ and $\frac{\lambda_s \omega_p}{c} = \{0, +\infty\}$ (red and gold curves, respectively); the Drude result (gray dashed curve) from (2.19) is also shown for comparison. The frequency is fixed to $\omega = 0.001\omega_p$, and the viscosity is calculated from the parameterization (1.94) with $\frac{v_F}{c} = 0.001$, $\tau_c = \tau_{\vec{k}}$ meaning umklapp efficiency $\alpha_U = 1$, and $F_1 = 6$.

efficiency $\alpha_U = 1$, and $F_1 = 6$. From figure 2.1, we see that the viscous response shows the same saturation of $\frac{1}{Re\{Z(\omega)\}}$ with scattering time $\tau_{\vec{k}}$, which is typical of anomalous skin effect, consistently with the phenomenological model by Pippard [52–54] and with the nonlocal theory by Reuter and Sondheimer [50]; this kind of saturation has been observed experimentally for metals at low temperatures [52, 55]. On the other hand, the classical Drude response (2.19) keeps increasing with scattering time, without saturating. Hence, the viscoelastic approach reproduces anomalous skin effect - see also figure 2 of paper 1: this makes sense, as anomalous skin effect is another manifestation of nonlocal electromagnetic response of the material, which can be interpreted as the transverse response of a viscoelastic fluid - see section 1.4.4.

2.2.4 Electric field profiles

The effect of viscoelastic modes can be seen in the spatial damping of an electromagnetic wave, with electric field $E(z,\omega)$, penetrating inside the medium: the dielectric screening, which causes the damping of the field intensity as the wave propagates through, is influenced by nonlocal correlations, so that the standard exponential attenuation predicted by the classical skin effect [4, 5] is modified [12]. Hence, as for the thin film transmission, we expect the interference of the optical modes (2.2) to cause a standing wave pattern in the electric field profile $\frac{|E(z,\omega)|}{|E(0,\omega)|}$ as a function of spatial coordinate z, superimposed to the exponential damping of each mode. When the transmission coefficient $\{t_1, t_2\}$ at the vacuum-medium interface $z = 0$ has comparable modulus for the two modes, the aforementioned standing wave oscillations can be observed. In principle, one could also think to find a region of parameter space where only $n_2(\omega)$ is transmitted through a vacuum-viscous medium interface, while $n_1(\omega)$ is totally reflected, in order to isolate the negative-refracting mode. However, as demonstrated in appendix C, it is impossible to transmit only one degenerate mode through an interface, so both modes always contribute to the transmission inside a viscous medium.

If the two modes $\{n_1(\omega), n_2(\omega)\}$ always appear in pair through an interface, we can still see if it is possible to modulate their intensity as they propagate inside the material, along the normal coordinate z to the surface. From equations (2.2) and (C.1), we are able to calculate the electric field intensity at a distance $z > 0$ through

$$\frac{|E_1(z) + E_2(z)|^2}{|E(0)|^2} = \left| t_1 e^{i\frac{\omega}{c} n_1(\omega) z} + t_2 e^{i\frac{\omega}{c} n_2(\omega) z} \right|^2 \tag{2.22}$$

with $\{E_1(z), E_2(z)\}$ electric field at distance $z > 0$ for modes 1 and 2, respectively. This equation can be separated into an incoherent part, giving the two exponential dampings of the modes inside the material, and a coherent part, stemming from the interference of the two modes [56]; the expression, valid for any pair of complex-valued fields, is

$$\begin{aligned}\left| t_1 e^{i\frac{\omega}{c} n_1(\omega) z} + t_2 e^{i\frac{\omega}{c} n_2(\omega) z} \right|^2 = \left| t_1 e^{i\frac{\omega}{c} n_1(\omega) z} \right|^2 + \left| t_2 e^{i\frac{\omega}{c} n_2(\omega) z} \right|^2 \\ + 2Re\left\{ t_1 e^{i\frac{\omega}{c} n_1(\omega) z} \left[t_2 e^{i\frac{\omega}{c} n_2(\omega) z} \right]^* \right\}\end{aligned} \tag{2.23}$$

Separating real and imaginary parts for the refractive indexes $n_1(\omega)$ and $n_2(\omega)$, we can recognize the two attenuations of the fields $\left\{\vec{E}_1(z), \vec{E}_2(z)\right\}$, which follow the standard

exponential evolution individually

$$\frac{\left|\vec{E}_1(z)+\vec{E}_2(z)\right|^2}{\left|\vec{E}(0)\right|^2} = \left|t_1 e^{i\frac{\omega}{c}Re\{n_1(\omega)\}z}\right|^2 e^{-2\frac{\omega}{c}Im\{n_1(\omega)\}z} + \left|t_2 e^{i\frac{\omega}{c}Re\{n_2(\omega)\}z}\right|^2 e^{-2\frac{\omega}{c}Im\{n_2(\omega)\}z} + 2Re\left\{t_1 e^{i\frac{\omega}{c}n_1(\omega)z}\left[t_2 e^{i\frac{\omega}{c}n_2(\omega)z}\right]^*\right\} \quad (2.24)$$

The third term in equation (2.24) tells us that a possibility to observe the effects of viscosity is to analyze the coherent interference between the two degenerate modes. We cannot go much further than equation (2.24) analytically, without making assumptions. However, we know that the condition for the standing wave patterns, between the two electric fields $\left\{\vec{E}_1(z), \vec{E}_2(z)\right\}$, to be visible is that the intensity of the two modes is comparable [12], in other words $|t_1| \approx |t_2|$. Therefore, in this condition equation (2.24) is simplified, and the interference term $I_{int} = 2Re\left\{t_1 e^{i\frac{\omega}{c}n_1(\omega)z}\left[t_2 e^{i\frac{\omega}{c}n_2(\omega)z}\right]^*\right\}$ becomes simply

$$\begin{aligned} I_{int} &= 2|t_1||t_2| e^{-\frac{\omega}{c}(Im\{n_1(\omega)\}+Im\{n_2(\omega)\})z} \cos\left[\phi_1 - \phi_2 + \frac{\omega}{c}(Re\{n_1(\omega)\} - Re\{n_2(\omega)\})z\right] \\ &\approx 2|t_1|^2 e^{-\frac{\omega}{c}(Im\{n_1(\omega)\}+Im\{n_2(\omega)\})z} \cos\left[\phi_1 - \phi_2 + \frac{\omega}{c}(Re\{n_1(\omega)\} - Re\{n_2(\omega)\})z\right] \end{aligned} \quad (2.25)$$

where $\phi_j = Arg\left\{t_j\right\}$, $j = \{1, 2\}$. Equation (2.25) tells us that the coherent interference part I_{int} is exponentially attenuated, depending on the sum of the imaginary parts of the refractive indexes of the two modes, and has an oscillatory pattern, depending on the difference between the phases of the transmission coefficients t_1 and t_2, and on the difference between the real parts of the two refractive indexes $n_1(\omega)$ and $n_2(\omega)$. For compactness, we rewrite the total field profile as

$$I_{tot} = \frac{\left|\vec{E}_1(z)+\vec{E}_2(z)\right|^2}{\left|\vec{E}(0)\right|^2} = I_1 + I_2 + I_{int} \quad (2.26)$$

where we have defined the individual exponential attenuations of the mode fields $\left\{\vec{E}_1(z), \vec{E}_2(z)\right\}$

$$I_\alpha = |t_\alpha|^2 e^{-2\frac{\omega}{c}Im\{n_\alpha(\omega)\}z},\ \alpha = \{1, 2\} \quad (2.27)$$

We show the full electric field profile given by equation (2.22), together with the coherent interference pattern of equation (2.25), and the exponential attenuations in (2.27), in figure 2.2.

These calculations are made for $\tau_{\vec{k}}\omega_p = 1000$, with $\tau_{\vec{k}} = \tau_c = \bar{\tau}$, τ_c collisional

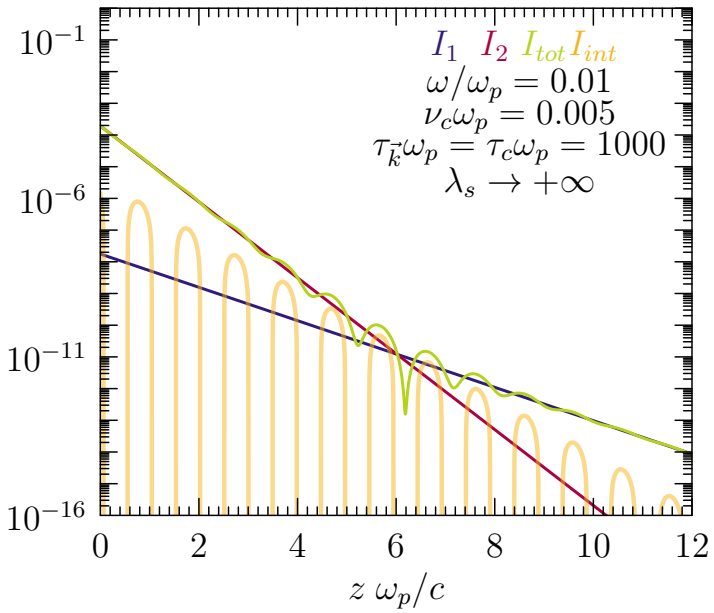

Figure 2.2: Electric field profile as a function of propagation distance $\frac{z\omega_p}{c}$, given by equation (2.22), together with the coherent interference pattern of equation (2.25), and the exponential attenuations in (2.27). The parameters are: $\tau_{\vec{k}}\omega_p = 1000$, with $\tau_{\vec{k}} = \tau_c = \bar{\tau}$, τ_c collisional lifetime, and $\nu(\omega) = \frac{\nu_c}{1-i\omega\bar{\tau}}$ [12]; $\nu_c\omega_p = 0.005$; $\omega = 0.01\omega_p$. We assume a perfectly clean surface of infinite slip length, $\lambda_s \to +\infty$.

lifetime, and $\nu(\omega) = \frac{\nu_c}{1-i\omega\bar{\tau}}$ [12]. The viscoelastic coefficient is set to $\nu_c\omega_p = 0.005$, and the frequency is $\omega = 0.01\omega_p$. In principle, both the scattering time and ν_c depend on frequency, as we will know for Fermi liquids; however, having fixed $\omega = 0.01\omega_p$, we can think of figure 2.2 as an example of results at fixed radiation frequency. We assume a perfectly clean surface of infinite slip length, $\lambda_s \to +\infty$. Being $\nu_c\tau_{\vec{k}}(\omega_p)^2 > 1$, and $\tau_{\vec{k}}\omega > 1$, the character of the modes $n_1(\omega)$ and $n_2(\omega)$ is swapped, that is $n_2(\omega)$ goes to the standard Drude result for zero viscosity, while $n_1(\omega)$ is the additional mode due to viscosity, which disappears for $\nu_c = 0$ [12]. Here, we see that the total field profile I_{tot} follows the damping constant of mode $n_2(\omega)$ close to the interface $z = 0$: this happens because $n_2(\omega)$ has a higher intensity I_2 close to the interface, with respect to I_1, for low enough frequency. Being the mode $n_2(\omega)$ associated to the standard Drude result in this case, we conclude that the transmission close to $z = 0$ still follows a conventional exponential attenuation according to the classical skin effect [5]. On the other hand, after $z\omega_p/c \approx 6$, the profile I_{tot} undergoes a slope change, and follows the damping constant of the other mode $n_1(\omega)$, which is the additional mode associated to viscosity effects. The argument shows that, even when we do not see the coherent oscillating pattern I_{int} between the two viscous modes, we can in principle detect the presence of viscosity by looking at the exponential attenuation constant of the field profile, far from the interface $z \gg 0$: for a viscous system

in the regime $\tau_{\vec{k}}\omega > 1$, the damping will be governed by the viscous mode $n_1(\omega)$, and not by the standard mode $n_2(\omega)$ that is present also in the Drude case; in other words, this is another demonstration that viscoelasticity alters the damping constant of the exponential attenuation of the electric field, with respect to the standard classical skin depth [4, 5]. Figure 2.2 also shows that the oscillation patterns of the profile (2.22) are seen when the intensities I_1 and I_2 of the two modes have comparable magnitude, consistently with the discussion preceding equation (2.25); indeed, the periodicity of the coherent oscillations I_{int} follows the approximation $I_{int} \propto \cos\left[\frac{\omega}{c}(Re\{n_1(\omega)\} - Re\{n_2(\omega)\})z\right]$, consistently with (2.25).

A finite slip length $\lambda_s < +\infty$ can modify the results of figure 2.2: in general, lower slip lengths enhance viscoelastic effects due to additional friction of the fluid at the boundary of the sample, however the interference pattern in figure 2.2 results from bulk propagation of the modes and should not be influenced significantly. On the other hand, the ratio between $I_1(z)$ and $I_2(z)$ may be more influenced by $\lambda_s < +\infty$ near the boundary $z = 0$. The results in figure 2.2 cannot easily be tested experimentally, as ideally one should insert local probes of the electromagnetic field along its propagation inside the material; also, realistic samples have a finite thickness d and hence have two boundaries: the two modes mix together once again when transmitted on the other side of the sample. However, viscoelastic effects can leave visible traces in metallic slabs at low temperature: the next section is dedicated to the problem of THz transmission of such thin films.

2.3 Low-frequency application: Terahertz transmission

Having highlighted some of the most prominent consequences of viscoelastic correlations for optics, the natural follow-up question is whether such signatures can be identified in experiments using current technology. In section 2.2, we have seen that possible probes of viscoelasticity involve the interference between the modes (2.2) inside the medium, which recombine coherently at the sample boundaries and affect the laws of transmission. However, metallic samples are highly reflecting below the plasma frequency ω_p, and they effectively screen any electric field within a distance of the order of the skin depth [5]: bulky samples can be excluded for such reason, and this suggests the utilization of thin metallic films, to obtain a sufficiently high intensity in transmission mode. Furthermore, since the results of section 2.2.2 affect *both the modulus and the phase* of the transmission coefficient $t(\omega)$, it is convenient to employ an experimental technique that is able to record both the intensity and the phase information, like time-domain Terahertz spectroscopy. In this case, one propagates a pulse in the THz frequency range through a sample, and

measures the transmitted electric field $\vec{E}(z,t)$ as function of time t. This is made possible by the simultaneous presence of two optical lines for pulses, one passing through the sample and the other through vacuum; the detector measures the time delay between the two recombined lines, giving a time-domain interferogram that encodes the interaction of radiation with the sample. The transmission spectrum is obtained by Fourier transform of the collected interferogram and calibration against the transmission in vacuum (without sample but with the sample holder, in practice). Further details on Terahertz spectroscopy can be retrieved in multiple reviews [5, 48, 49].

We now employ the formalism developed in section 2.2.2 to a structure composed of an aluminium layer on a sapphire substrate (Al/sapphire). In this case, we can benefit from a simplification of the formalism, as the scattering time $\tau_{\vec{k}}$ and the collision time τ_c have negligible frequency dependence in the THz regime, and they roughly correspond to their DC ($\omega = 0$) value. Then, the only relevant parameter for scattering is temperature. In this section, we take the empirical approach of extracting the scattering time from the T-dependent electrical resistivity, given by the Drude expression (2.21) [3]. In the following, we set the collision time to $\tau_c = \tau_k$ for maximum umklapp efficiency [12]. Knowing the experimental resistivity $\rho_{el} := \frac{1}{\sigma_D}$, for the given material such as aluminium Al, we can therefore calculate the scattering time τ_k from (2.21).
From the experimental resistivity $\rho_{el}(T)$ values, we checked the consistency of the calculated scattering times τ_k for each temperature T; for example, for aluminium Al at room temperature $T = 300\,K$, the resistivity is $\rho_{el} = 4\ 10^{-8}\ \Omega m$, and knowing the plasma frequency $\omega_p = 15.7924\,eV$, the resulting scattering time is $\tau_k = 0.492\ 10^{-14}\,s$, which is about half the value $\tau_k = 0.8\ 10^{-14}\,s$ quoted by Ashcroft and Mermin [3] at page 10, for a slightly lower resistivity of $\rho_{el} = 2.45\ 10^{-8}\ \Omega m$.

The calculation of the transmission $t(\omega, T)$, for different temperatures T, follows from section 2.2.2. For aluminium, we employ the plasma frequency $\omega_p = 15.7924\ eV$ [3], obtained from a free electron density of $n = 18.1\ 10^{22} cm^{-3}$ [3]. The slab thickness is chosen to be $d = 100\ nm$. Table 2.1 reports the given value of resistivity $\rho_{el}(T)$ at temperatures $T = 300\,K$ and $T = 5\,K$; the latter has been calculated from the RRR ratio of 100, as $RRR = \frac{\rho_{el}(300)}{\rho_{el}(0)}$, assuming a linear temperature dependence of $\rho_{el}(T)$ in the entire temperature range.

Employing equation (2.21) on the $T = 5\,K$ case of table 2.1, we find a mean free path $\lambda_{MFP} = 864.3\ nm$, which is longer than the film thickness $d = 100\ nm$. We assume the first Landau parameter $F_1 = 6$; the viscosity at zero frequency is set by $\left(\frac{v_F}{c}\right)^2 = 4.556\ 10^{-5}$.

$T\ [K]$	$\rho_{el}(T)\ [\mu\Omega\ cm]$	$\tau_k\ [10^{-14}\ s]$	$\nu(0)\left[\frac{m^2}{s}\right]$
300	4	0.492	$1.343\,10^{-3}$
5	0.046	42.783	0.117

Table 2.1: First column: temperature; second column: experimental values of the electrical resistivity $\rho_{el}(T)$ for aluminium, with a RRR ratio of 10; third column: scattering time for the aluminium plasma frequency $\omega_p = 15.7924\ eV$; fourth column: zero-frequency cinematic viscosity coefficient $\nu(0) = \frac{\eta(0)}{nm}$ according to equation (1.114).

The clean limit of a smooth surface, with infinite slip length $\lambda_s \to +\infty$, and the dirty limit of a maximally rough boundary $\lambda_s = 0$, are both considered for each temperature. For the substrate, we assume an oxide with frequency-independent dielectric function $\epsilon_s = 10 + i0.01 \forall \omega$, giving a refractive index $n_s = \sqrt{\epsilon_s}$. The substrate thickness is set to $d_s = 0.5\ mm$.

With aforementioned parameters, we can compare the viscoelastic results from equation 2.13 with the standard Drude case. For the latter, the transmission coefficient from film to substrate t_{fs}, and the reflection coefficients from film to substrate r_{fs} and from substrate to film r_{sf}, comprising Fabry-Perot reflections, [4, 5, 47] give equivalent results with respect to the limit $\nu \to 0$.

We focus on the first transmission echo: this corresponds to radiation first traversing the substrate with no Fabry-Perot internal reflections, then traversing the viscoelastic film with internal reflections, and finally being transmitted to vacuum. Subsequent echoes correspond to an increasing number of Fabry-Perot round trips into the substrate, as mentioned in section 2.2.2, and therefore they carry no additional information on the metallic layer. Notice that we must take into account reflections inside the layer because $d \ll d_S$: radiation can bounce back and forth inside the thin slab many times during a single substrate transmission, while it would take much more time to produce internal substrate reflections.

Figure 2.3 shows the viscoelastic transmission modulus $\left|t_{(1)}(\omega)\right|$ for the first echo as a function of frequency ω in the THz regime. Panel (a) shows the results at $T = 300\ K$, while panel (b) shows the computations for $T = 5\ K$, according to the scattering time in table 2.1. Solid curves stem from the viscoelastic expression (2.12), for slip length $\lambda_s = \{0, 1, +\infty\}$. The Drude case is reported as a dashed gray line for comparison.

Panel (a) of figure 2.3 demonstrates that the effects of viscoelastic correlations at room temperature are negligible with respect to the low-temperature case, as all solid curves are in the range $\left|t_{(1)}(\omega)\right| = \{1 \div 3\}\ 10^{-3}$ in the shown frequency interval. Nevertheless, the

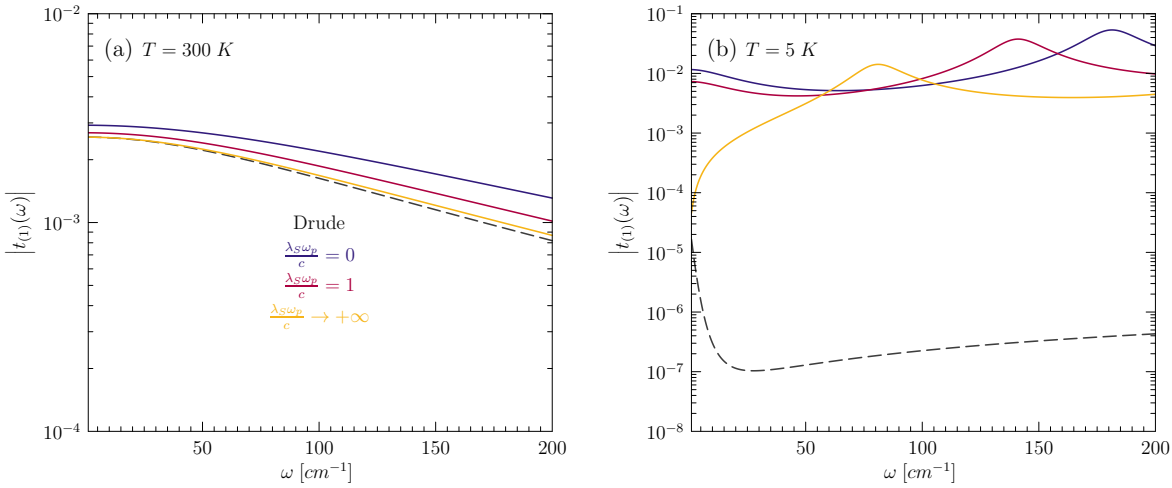

Figure 2.3: Absolute value of the transmission coefficient $\left|t_{(1)}(\omega)\right|$ for the first THz transmission echo of an Al slab of thickness $d = 100\ nm$ on a sapphire substrate of thickness $d_S = 0.5\ mm$. The blue, red and gold curves correspond to the results for a slip length $\frac{\lambda_S \omega_p}{c} = \{0, 1, \infty\}$ respectively. The Fermi velocity is $\left(\frac{v_F}{c}\right)^2 = 4.556\ 10^{-5}$, and the first Landau parameter is $F_1^S = 6$. The dashed gray curve is the Drude result, for the same parameters.

$T = 5\ K$ situation of panel (b) shows a qualitatively different evolution with frequency for the viscoelastic model: $\left|t_{(1)}(\omega)\right|$ *increases* with frequency in the THz regime, while in the Drude case the transmission decreases up to $\omega \approx 25\ cm^{-1}$ and then it stays in the range $\left|t_{(1)}(\omega)\right| = \{1 \div 4\}\ 10^{-7}$ in the shown frequency interval.

Figure 2.4 shows the phase of the viscoelastic transmission coefficient $Arg\left\{t_{(1)}(\omega)\right\}$ in radians for the first echo, divided by frequency ω in cm^{-1}, as a function of ω. Panel (a) reports the results at $T = 300\ K$, while panel (b) shows the output for $T = 5\ K$. The color code of all curves is the same as for figure 2.3.

The room-temperature normalized phase in panel (a) of figure 2.3 shows the same behaviour as the correspondent modulus in figure 2.3, in that differences with respect to the Drude model only appear at the third decimal digit. However, the $T = 5\ K$ situation of panel (b) highlights non-neglibile effects due to correlations: the decrease with frequency is less pronounced for the viscoelastic case with respect to the Drude result, particularly for a small slip length $\lambda_s \to 0$.

2.4 Fermi liquid quasiparticle scattering time

Increasing frequency from the THz regime, scattering starts to exhibit a non-negligible frequency dependence, which must be considered in calculations. In order to model this effect

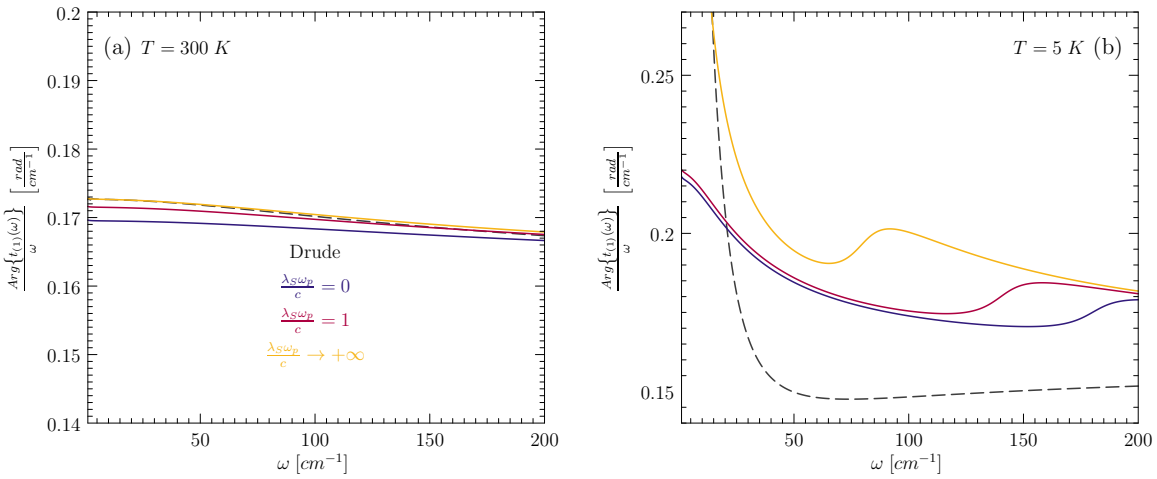

Figure 2.4: Phase of the transmission coefficient $Arg\left\{t_{(1)}(\omega)\right\}$, normalized to frequency $\omega\ [cm^{-1}]$, for the first THz transmission echo of an Al slab of thickness $d = 100\ nm$ on a sapphire substrate of thickness $d_S = 0.5\ mm$. The blue, red and gold curves correspond to the results for a slip length $\frac{\lambda_S \omega_p}{c} = \{0, 1, \infty\}$ respectively. The Fermi velocity is $\left(\frac{v_F}{c}\right)^2 = 4.556\ 10^{-5}$, and the first Landau parameter is $F_1^S = 6$. The dashed gray curve is the Drude result, for the same parameters.

for metallic solids, we can refer to the Landau phenomenology of Fermi liquids, which we considered in section 1.5. In solids at nonzero temperature, Landau quasiparticles acquire a finite lifetime due to multiple scattering channels. The inelastic quasiparticle scattering rate in a Fermi liquid is $\frac{1}{\tau_{qp}} \propto \left[(\hbar\omega)^2 + (\pi k_B T)^2\right]$, due to the phase space limitation for scattering events imposed by the Pauli exclusion principle [7, 23]. The ω^2 dependence is intimately related to the linear frequency dependence of the imaginary part of the susceptibility $Im\{\chi(\omega)\} \propto \omega$, which itself is a consequence of Fermi-liquid behaviour [25]. Additional scattering mechanisms to consider for realistic solids are momentum relaxation due to phonons, and also to impurities, which can become the dominating channel at room temperature and at low temperature for dirty samples, respectively. Hence, one may pose into question whether a pure Fermi liquid scattering time τ_{qp} can be observed in practice. However, in many instances Fermi liquid behaviour has been identified at low temperatures: Sr_2RuO_4 [57, 58] shows a $(\hbar\omega)^2 + (2\pi k_B T)^2$ dependence of the optical conductivity, including the factor of 2π [59]. Low-temperature transport experiments confirmed the relation $\tau_{qp} \propto T^2$ in doped $SrTiO_3$ [60], TiS_2 [61], and heavy fermions [62]. In underdoped cuprates, optical measurements report an energy- and temperature-dependent scattering time $\tau \propto (\hbar\omega)^2 + (p\pi k_B T)^2$, with $p \approx 1.5$ [63]. Experimental resistivities $\rho_{el} \propto T^2$ are unexpected on the basis of standard Fermi liquid theory [7, 64], as resistivity requires momentum relaxation, while in a translationally invariant system of interacting electrons

the current operator commutes with the Hamiltonian and hence the Coulomb interaction conserves the current [13]. However, the presence of a crystalline lattice in solids breaks galileian invariance, and can relax momentum through umklapp processes [65], Baber scattering [66], or other processes involving phonons [60]. Breaking of translational invariance also allows to relax momentum through electron-impurity scattering [67]. The precise contribution of the different proposed relaxation mechanisms in experimental Fermi liquids has yet to be assessed, although the quadratic energy and temperature dependence of the scattering time is regarded as a confirmation of Fermi liquid physics.
As for the electrically neutral case of section 1.5.2, the quasiparticle relaxation rate determines the quality of dielectric response for charged electrons in solids: we expect viscous hydrodynamic behaviour for $\omega\tau_c \ll 1$, and solid-like shear stress for $\omega\tau_c \gg 1$. Andreev, Kivelson and Spivak recently pointed out that hydrodynamics is at work when the electron liquid attains local equilibrium on the scale of the electron-electron mean-free path l_{mfp} [42]. For this to happen, l_{mfp} must become shorter than the electron-phonon mean free path, a condition only met at temperatures of a few Kelvin in most metals. However, strongly correlated materials typically show Fermi-liquid-like characteristics at much higher temperatures, thereby extending the regime of fluid-like response. Hydrodynamic vorticity has been theoretically predicted in high-mobility graphene as a diagnostics for viscous transport [43]. Hydrodynamic electron flow was experimentally observed in the differential resistance of electrostatically defined wires, in the two-dimensional electron gas at (Al,Ga)As heterostructures [68]. On the other hand, elastic shear stresses are predicted in collisionless regime [17] - see section 1.7.4.1. A suitable experimental test is offered by optics, that can probe long-wavelength transverse excitations of correlated Fermi liquids [12]. For this reason, the following sections collect optical transmission calculations for thin films of Fermi liquids, which can show signatures of viscoelastic correlations.

2.5 Optical transmission of Fermi liquid thin films

We calculate the optical transmission spectra of Fermi liquid thin films, in the presence of the viscoelastic transverse collective modes analyzed in sections 1.7.4.1 - 2.4. Using the dispersion relations (1.85) of the neutral case, we extend the formalism developed for viscous charged fluids in reference [12] (paper 1) to the whole crossover from viscous/collisional to shear/collisionless regime. We begin by the latter regime, modeling the metallic zero-temperature case, where the free propagation of transverse shear modes allows for qualitative changes in the Fermi liquid transmission spectrum.

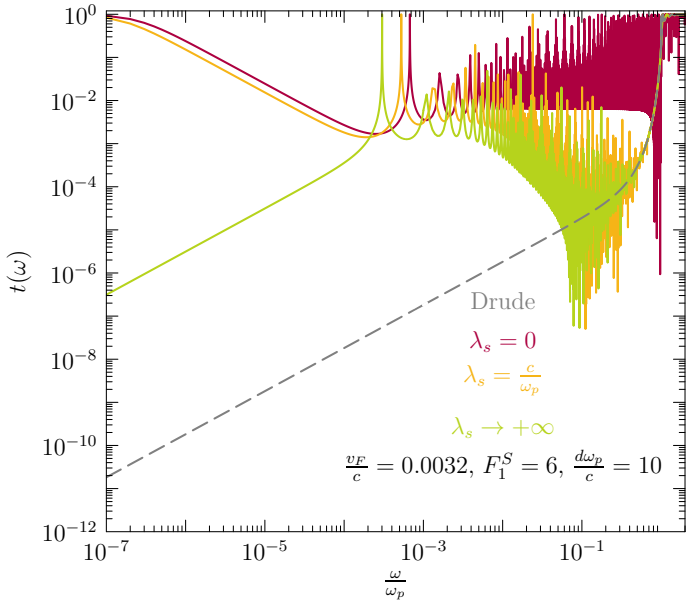

Figure 2.5: Absolute value of the transmission coefficient $|t(\omega)|$ for a Fermi liquid thin film of thickness $\frac{d\omega_p}{c} = 10$, in the collisionless regime $\tau_c = \tau_{\vec{k}} \to +\infty$. The orange, green and red curves correspond to the results for a slip length $\frac{\lambda_S \omega_p}{c} = \{0, 1, \infty\}$ respectively. The Fermi velocity is $\frac{v_F}{c} = 0.0032$, and the first Landau parameter is $F_1^S = 6$. The dashed gray curve is the Drude result, for the same parameters.

2.5.1 Collisionless limit and shear mode

Using the dielectric function (1.20) and the real sound velocity (1.89) for propagating shear modes, we derive the refractive indexes for electromagnetic modes inside the medium through the definition $n_i(\omega) = \sqrt{\epsilon_T(\vec{q}, \omega)}$, where one substitutes $q = \frac{\omega}{c} n_i(\omega)$ for propagating electromagnetic waves [5]. One finds two refractive indexes $i = \{1, 2\}$ for degenerate optical modes, consistently with the two-fold dispersion (1.127) and with the viscous charged fluid calculation [12]. However, the collisionless limit lacking dissipation [24], there is no negative refraction: the two refractive indexes have positive real part at all frequencies. The calculation of the thin film transmission proceeds as in section IV.E of reference [12], utilizing the refractive indexes $n_i(\omega)$. Figure 2.5 shows the collisionless transmission coefficient modulus $|t(\omega)|$ as a function of $\frac{\omega}{\omega_p}$, for a Fermi liquid thin film of thickness $\frac{d\omega_p}{c} = 10$. Different solid curves are obtained for slip lengths $\frac{\lambda_S \omega_p}{c} = \{0, 1, \infty\}$, which are determined by the ratio between the boundary tangential friction and the Fermi liquid velocity gradient [46]. The Fermi velocity is $\frac{v_F}{c} = 0.0032$, and the first Landau parameter is $F_1^S = 6$. The dashed curve shows the Drude result, for the same parameters [5].

The oscillation patterns in the elastic shear cases of figure 2.5 are due to the quantum

interference between the two propagating optical modes $n_i(\omega)$ inside the Fermi liquid: therefore, this is a signature of shear mode propagation. At lower frequencies, the clean boundary limit $\frac{\lambda_S \omega_p}{c} \to +\infty$ has the same slope as the Drude result, but higher transmission due to the presence of the shear mode, which helps radiation propagation inside the medium. Higher roughness towards the limit $\frac{\lambda_S \omega_p}{c} = 0$ further amplifies $|t(\omega)|$, by slowing down and eventually pinning quasiparticles at the boundaries and increasing velocity gradients over the slab thickness. At the lowest frequencies, the transmission becomes unitary as all shear stresses are transmitted without dissipation: this is the response of an *elastic solid*, as emphasized in section 1.7.4.1. This represents the zero-temperature limit for a Fermi liquid, where the system responds according to the electrodynamics of the isotropic Wigner crystal [17].

2.5.2 Scattering in the viscoelastic Fermi liquid

In practice, multiple scattering sources can diminish correlation effects in Fermi liquids at finite temperature, as mentioned in section 2.4. In order to evaluate qualitatively the effect of scattering on the optical transmission of section 2.5.1, we include the contributions due to Landau quasiparticle relaxation, phonons and impurities. We sum these contributions using Matthiessen's rule

$$\frac{1}{\tau_{tot}} = \sum_{i=1}^{N_p} \frac{1}{\tau_i} \tag{2.28}$$

which simply adds the rates $\frac{1}{\tau_i}$ for the different processes $i = \{1, \cdots N_p\}$, to obtain the total rate $\frac{1}{\tau_{tot}}$.

One must be careful in checking that the dielectric function calculated with the total scattering time (2.28) still obeys Kramers-Kronig relations [1, 5]. For the Fermi liquid scattering time (2.29) Kramers-Kronig relations are preserved, but other frequency-dependent contributions to τ_{tot}, e.g. phonons, do not automatically satisfy such relations. In the following, we take a frequency-independent but temperature-dependent acoustic phonon contribution according to the Bloch-Gruneisen formula, to show the qualitative effect of phonons. More realistic frequency-dependent phonon contributions are expected to produce quantitative changes on the transmission spectra.

2.5.2.1 Quasiparticle scattering time from phase space limitation

In Fermi liquids, Landau quasiparticles acquire a finite lifetime τ_{qp} due to the Pauli exclusion principle, which limits the available phase space for scattering [1, 13, 23]. As previously

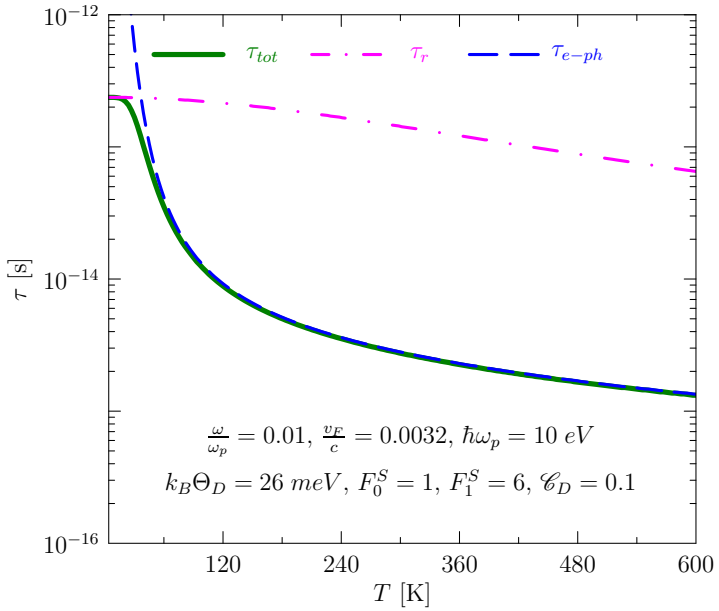

Figure 2.6: Contributions to the total scattering time τ_{tot} in a Fermi liquid coupled to phonons, as a function of temperature T: the dash-dotted curve is the Fermi liquid component τ_{ee}, according to equation (2.31); the dashed curve is the phonon contribution τ_{e-ph}, stemming from equation (2.34); the full curve is the total lifetime τ_{tot} stemming from Mathiessen's rule (2.28). The parameters of the calculations are: frequency $\omega = 0.01$; plasma frequency $\omega_p = 10\ eV$; Fermi velocity $\frac{v_F}{c} = 3.2 \cdot 10^{-3}$; umklapp efficiency $\Delta_u = 1$; Landau parameters $F_0^A = F_1^A = 0$, $F_0^S = 1$, $F_1^S = 6$; Debye temperature $\frac{k_B\Theta_D}{\hbar\omega_p} = 2.6\ 10^{-3}$; Debye constant $\mathscr{C}_D = 0.1\omega_p\ s^{-1}$. For the explanation of the parameter values, see the main text.

mentioned, this mechanism alone redistributes energy among quasiparticles, but cannot relax momentum unless translational invariance is broken, for instance by the underlying crystalline lattice in solids. In the latter case, at each collision a portion of the quasielectrons momentum can be damped into the lattice through phonons, thus allowing for quasiparticle relaxation [60, 65, 66] in a time τ_{ee}. We model this by an umklapp efficiency $\Delta_u = \frac{\tau_{ee}}{\tau_{qp}} < 1$, which represents the efficiency of the system in converting electronic scattering into lattice relaxation through umklapp processes [12]. From Fermi liquid theory, the collision time has the quadratic energy-temperature dependence [13, 25]

$$\frac{\hbar}{\tau_r} = \frac{\pi}{E_F^*}(\lambda_t)^2 \Delta_u \left[(\hbar\omega)^2 + (\pi k_B T)^2\right] \tag{2.29}$$

where $\hbar\omega$ is the excitation frequency, $k_B T$ is the thermal energy at temperature T, $E_F* = \frac{\hbar^2 k_F^2}{2m^*}$ is the renormalized Fermi level, and $(\lambda_t)^2$ stems from the angular integration of the scattering probability and depends on the Landau parameters $\left\{F_l^S, F_l^A\right\}$. The exact expression for $(\lambda_t)^2$ and its derivation in the case of s-p scattering [1, 13] is reported in appendix D. Equation (2.29) implies $\tau_r \propto \frac{1}{\omega^2 + (\pi k_B T)^2}$, which is a signature of Fermi liquid behaviour. However, the growth of τ_r in the limit $T \to 0$ is limited by a fundamental physical constraint: electrons cannot interact on lengths that are shorter than the average interparticle distance [23]. This gives the upper limit for the relaxation time

$$\tau_r \geq \tau_F = \frac{\hbar}{E_F} \tag{2.30}$$

We implement the condition (2.30) into the relaxation time through

$$\tau_r = \tau_{ee} + \tau_F \tag{2.31}$$

Using the plasma frequency $\omega_p = \sqrt{\frac{ne^2}{m\epsilon_0}}$ and the renormalized Fermi energy $E_F^* = \frac{1}{2} m^* (v_F^*)^2$, with $m^* = m\left(1 + \frac{F_1^S}{3}\right)$, we obtain in dimensionless form

$$\frac{1}{\omega_p \tau_r} = \frac{2\pi\left(1 + \frac{F_1^S}{3}\right)}{\left(\frac{v_F}{c}\right)^2 \frac{mc^2}{\hbar\omega_p}} (\lambda_t)^2 \Delta_u \left[\left(\frac{\omega}{\omega_p}\right)^2 + \pi^2 \left(\frac{k_B T}{\hbar\omega_p}\right)^2\right] \tag{2.32}$$

and

$$\frac{1}{\omega_p \tau_F} = \frac{\hbar\omega_p mc^2}{\left(\frac{v_F}{c}\right)^2} \tag{2.33}$$

The scattering time (2.31) is depicted in figure 2.6 as a function of temperature, for frequency $\omega = 0.01\omega_p$ and using the following typical parameters of simple metals: $\omega_p = 10\ eV$; $\frac{v_F}{c} = 3.2 \cdot 10^{-3}$. To fix ideas, we set maximum umklapp efficiency $\Delta_u = 1$, Landau parameters $F_0^A = F_1^A = 0$, $F_0^S = 1$, $F_1^S = 6$, and room temperature for which $k_B T \approx 26\ meV$. Comparing τ_{ee} in figure 2.6 with the Drude scattering time of simple metals at room temperature [3], we see that τ_{ee} is about one order of magnitude larger than in experiments. Indeed, for $T \gg 0$ the scattering time is mainly limited by phonons [3], while electronic correlations given by Fermi liquid theory become dominant for clean metals at low temperatures.

2.5.2.2 Phonon scattering time

The phonon contribution to the total scattering rate (2.28) becomes dominant at room temperature with respect to Fermi liquid correlations. To evaluate this effect qualitatively, we consider normal processes for acoustic phonons [69]: in this case, the electron-phonon scattering time can be described by the Bloch-Grüneisen model

$$\frac{1}{\tau_{e-ph}} = \mathscr{C}_D \left(\frac{\Theta_D}{T}\right)^5 \int_0^{\frac{T}{\Theta_D}} dx \frac{x^5}{(e^x - 1)(1 - e^{-x})} \tag{2.34}$$

where $\mathscr{C}_D$ is a material-dependent constant [69], and Θ_D is the Debye temperature. For $T \gg \Theta_D$, equation (2.34) gives a linear term $\frac{1}{\tau_{e-ph}} \propto T$, while for $T \ll \Theta_D$ we have $\frac{1}{\tau_{e-ph}} \propto T^5$: comparing these behaviours with $\frac{1}{\tau_{ee}} \propto T^2$ from equation (2.31), we immediately see that the phonon term is bigger at room temperature, while Fermi liquid processes prevail in the limit $T \to 0$. This suggests that phonons will mainly impact room-temperature calculations of the transmission spectra, while lattice terms will freeze out at low temperatures unveiling the Fermi liquid evolution (2.31). The electron-phonon rate (2.34) is shown in figure 2.6 as a function of temperature, for $\frac{k_B \Theta_D}{\hbar \omega_p} = 2.6\ 10^{-3}$, that corresponds to $\Theta_D \approx 300\ K$ for $\omega_p = 10\ eV$. The constant $\mathscr{C}_D$ is fixed by the requirement that the expression (2.34) gives the same order of magnitude of the experimental Drude scattering time $\tau_D \approx 10^{-15}\ s$ of simple metals [3]: consistently with this, we set $\mathscr{C}_D = 0.1\omega_p\ s^{-1}$.

2.5.2.3 Impurity scattering time

At first approximation, we can model the presence of impurities in the system with a constant scattering time $\tau_{imp} \in \mathbb{R}^+$, independent of frequency and temperature. Microscopically, this lifetime is inversely proportional to the density of impurities. Macroscopically, this contribution is responsible for the nonzero residual resistivity of metals down to zero

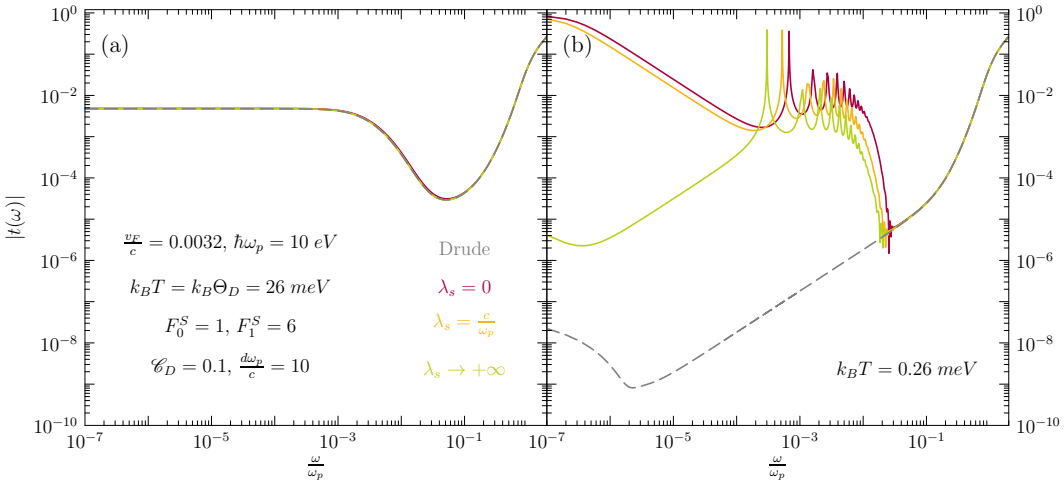

Figure 2.7: Absolute value of the transmission coefficient $|t(\omega)|$ for a Fermi liquid thin film of thickness $\frac{d\omega_p}{c} = 10$, coupled to acoustic phonons. The orange, green and red curves correspond to the results for a slip length $\frac{\lambda_S\omega_p}{c} = \{0, 1, \infty\}$ respectively. Panel (a) shows the calculation at room temperature, $k_BT = 26\,meV$, while panel (b) illustrates the low-temperature results $k_BT = 0.26\,meV$, for the same parameters. The parameters common to all calculations are: plasma frequency $\omega_p = 10\ eV$; Fermi velocity $\frac{v_F}{c} = 3.2 \cdot 10^{-3}$; umklapp efficiency $\Delta_u = 1$; Landau parameters $F_0^A = F_1^A = 0$, $F_0^S = 1$, $F_1^S = 6$; Debye temperature $\frac{k_B\Theta_D}{\hbar\omega_p} = 2.6\,10^{-3}$; Debye constant $\mathscr{C}_D = 0.1\omega_p\ s^{-1}$. The dashed gray curve is the Drude result, for the same parameters.

temperature [3], if the material is not a superconductor. Since τ_{imp} imposes an upper limit on the zero-temperature total scattering time (2.28), we can already see that impurities will limit the low-T growth of the Fermi liquid lifetime $\tau_{ee} \propto \frac{1}{(\hbar\omega)^2+(\pi k_BT)^2}$: this means that increasing the impurity concentration diminishes nonlocal effects due to a smaller scattering time, and therefore it decreases the difference of the optical spectra with respect to the Drude model at low temperatures.

2.5.3 Clean Fermi liquid with acoustic phonons

Modeling the quasiparticle and phonon contributions to the scattering time as in sections 2.5.2.1 and 2.5.2.2, we have now obtained a qualitative picture of the total scattering time (2.28) for a Fermi liquid coupled to acoustic phonons. This allows us to analyze the differences of the optical transmission with respect to the collisionless regime 2.5.1, once we include scattering and relaxation effects. We calculate the thin film transmission in accordance with IV.E of reference [12], as for section 2.5.1, but now we include the frequency- and temperature-dependent scattering time (2.28), summing the contributions (2.31) and (2.34). In all subsequent calculations, we set $\Delta_u = 1$, meaning $\tau_c = \tau_{\vec{k}}$: this

is an upper limit for the umklapp efficiency. First, we calculate the dielectric function (1.20) using the full solution (1.85) for the complex sound velocity $\tilde{v}_{S,L}$ and the lifetime $\tau_c = \tau_{\vec{k}} = \tau_{tot}(\omega, T)$. This way, we derive the refractive indexes for electromagnetic modes $n_i(\omega) = \sqrt{\epsilon_T(\vec{q}, \omega)}$ as in section 2.5.1. Due to scattering and relaxation, one of the two complex refractive indexes $i = \{1, 2\}$ exhibits negative refraction, meaning $Re\{n_2(\omega)\} < 0$; this happens in a low-frequency range, the extension of which depends on the scattering time $\tau_{\vec{k}}$ [12]. In section 2.6, we will analyze negative refraction in the context of our model, while here we highlight the different physics in comparison with the collisionless regime 2.5.1: quasiparticle collisions cause dissipation of collective modes, which is reflected in $Im\left\{\tilde{v}_{S,L}\right\} \neq 0$. This qualitatively changes the nonlocal dielectric response, similarly to the neutral case 1.5.2: for $\omega\tau_c \ll 1$, the system responds like a *viscous charged fluid*, and the sound velocity (1.87) is determined by a single viscosity coefficient. Therefore, while in the collisionless limit the Fermi sea reacts like a solid object with a shear modulus, in the collisional regime the Fermi liquid really responds like a viscous fluid [12]. Such viscous behaviour deeply affects optical observables like refractive indexes and thin film transmission. In particular, the concomitant presence of spatial nonlocality and dissipation allows for negative refraction, in accordance with general principles based on the dielectric function approach [24].

Figure 2.7 shows the transmission coefficient modulus $|t(\omega)|$ as a function of $\frac{\omega}{\omega_p}$, for a Fermi liquid thin film of thickness $\frac{d\omega_p}{c} = 10$, coupled to acoustic phonons. Different solid curves are obtained for slip lengths $\frac{\lambda_S \omega_p}{c} = \{0, 1, \infty\}$. The material parameters are chosen to agree with typical values for simple metals [3]: plasma frequency $\omega_p = 10\, eV$, and Fermi velocity $\frac{v_F}{c} = 3.2 \cdot 10^{-3}$. The Landau parameters are $F_0^A = F_1^A = 0$, $F_0^S = 1$, and $F_1^S = 6$. The acoustic phonon contribution is taken to follow a Debye spectrum with Debye temperature $\frac{k_B \Theta_D}{\hbar \omega_p} = 2.6\ 10^{-3}$; the Debye constant $\mathscr{C}_D = 0.1\omega_p\ s^{-1}$ in equation (2.34) is set to match the order of magnitude of the experimental Drude scattering time in simple metals [3], as described in section 2.5.2.2. The film thickness is set by $\frac{d\omega_p}{c} = 10$. Dashed gray curves in figure 2.7 show the Drude result, for the same material parameters [5]. Panel (a) of figure 2.7 illustrates the room-temperature case, i.e. $k_B T = 26\, meV$. In this situation, the scattering time (2.28) is dominated by the phonon contribution, as seen in figure 2.6. Fermi liquid features are overwhelmed by thermal effects [25, 60], and the mean free path $l_{MFP} = v_F \tau_{tot}$ is much smaller than at low temperatures, so nonlocality plays a relatively marginal role in the dielectric response. For this reason, the nonlocal dielectric function with the sound velocity (1.85) falls on top of the standard Drude result for all slip lengths. This suggests that signatures of Fermi liquid collective modes can hardly

be found at room temperature, due to phonons suppressing nonlocal effects.

The situation is different at low temperatures: panel (b) of figure 2.7 shows the calculations for $k_B T = 0.26\ meV$. As seen in figure 2.6, the scattering time (2.28) is governed by Fermi liquid correlations in this case. The mean free path $l_{MFP} = v_F \tau_{tot}$ is two orders of magnitude longer than at room temperature, which enhances nonlocal effects [12,24]. Consequently, we retrieve the oscillatory patterns of $|t(\omega)|$ characteristic of the two degenerate refractive indexes, governed by the collective mode dispersion (1.85); this is qualitatively similar to the collisionless case of figure 2.5. However, the nonlocal theory merges with the Drude result above $\omega \approx 10^{-2}\omega_p$: this is an effect of the Fermi cutoff (2.30) acting on the quasiparticle scattering time (2.31) and making the latter saturate to a frequency- and temperature- independent value. Physically, the constraint that quasiparticles cannot interact on lengths shorter than the average interparticle distance suppresses quasiparticle correlations and associated nonlocal effects, at high frequency. The low-frequency behaviour of the collisional regime is mainly determined by the slip length λ_S, similarly to figure 2.5 in the collisionless limit: the limiting velocity at the slab boundaries λ_S governs the low-frequency limit of the optical transmission [12], regardless of the presence or absence of collisions. In summary, the calculations of figure 2.7 suggest that signatures of Fermi liquid collective modes could be observed in the optical transmission of simple metals at low temperatures, for sufficiently low frequency $\omega \ll \omega_p$. However, care must be taken in evaluating the generality of these results: here we consider a clean Fermi liquid coupled to an acoustic phonon branch. Additional contributions of optical phonons and other scattering mechanisms can suppress nonlocal effects even at cryogenic temperatures, as we illustrate in the following section 2.5.4. Furthermore, the exact values of material-dependent parameters can quantitatively change the results here presented. In particular, as we discussed at the beginning of section 1.7, short-ranged quasiparticle residual interactions, and the associated Landau parameters, are modified by Coulomb repulsion with respect to their electrically neutral counterpart. Therefore, different values of F_0^S, F_1^S and the presence of nonzero asymmetric contributions F_0^A, F_1^A would affect the results of this section. Similarly, a non-unitary umklapp efficiency $\Delta_u < 1$ modifies the frequency evolution of the sound velocity $\tilde{v}_{S,L}$ and the associated thin film transmission. Nevertheless, the qualitative picture of Fermi liquid collective modes being potentially observable at low temperatures is independent from the exact values of material parameters: we believe that this conclusion applies in general to simple metallic solids.

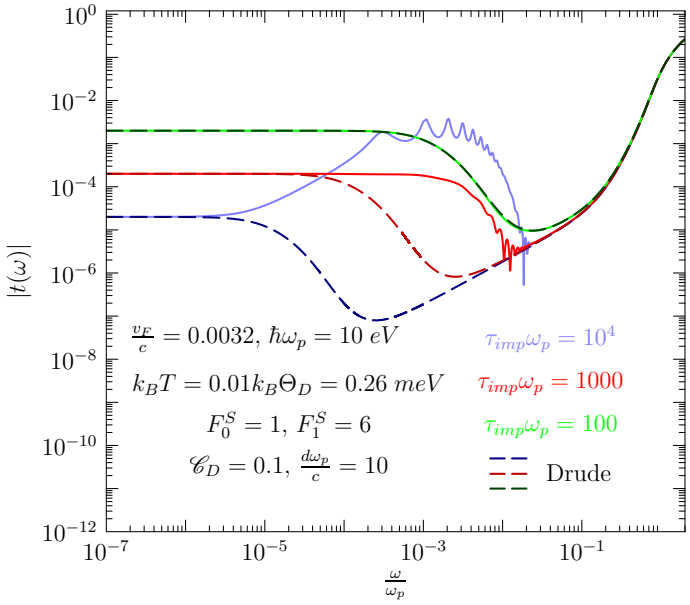

Figure 2.8: Absolute value of the transmission coefficient $|t(\omega)|$ for a Fermi liquid thin film of thickness $\frac{d\omega_p}{c} = 10$ coupled to acoustic phonons, in the presence of impurity scattering. The green, red and blue curves are the results for an impurity scattering time $\tau_{imp}\omega_p = \{10^4, 1000, 100\}$ respectively. The slip length is $\lambda_S \to +\infty$ for all calculations. All other parameters are the same as in panel (b) of figure 2.7: plasma frequency $\omega_p = 10\ eV$; Fermi velocity $\frac{v_F}{c} = 3.2 \cdot 10^{-3}$; umklapp efficiency $\Delta_u = 1$; temperature $k_BT = 0.26\ meV$; Landau parameters $F_0^A = F_1^A = 0$, $F_0^S = 1$, $F_1^S = 6$; Debye temperature $\frac{k_B\Theta_D}{\hbar\omega_p} = 2.6\ 10^{-3}$; Debye constant $\mathscr{C}_D = 0.1\omega_p\ s^{-1}$. The three dashed curves are the Drude result, using the same parameters as the full curves of the nonlocal theory.

2.5.4 Effect of impurity scattering at low temperatures

Impurity scattering in metals is a fundamental issue at low temperatures [3], and it is a crucial parameter for epitaxial growth of thin films. For these reasons, it is important to consider the extent to which the results of section 2.5.3 are modified by the presence of impurities. In order to model these effects, we employ the simple frequency- and temperature-independent model of section 2.5.2.3, and we add this contribution to the total lifetime τ_{tot} of section 2.5.3 according to Mathiessen's rule (2.28). Then, we recalculate the thin film transmission modulus as in section 2.5.3, keeping the same values of all other parameters. Since the high-temperature case in panel (a) of figure 2.7 already reduces to the standard Drude result, no qualitative changes due to additional scattering contributions occur. Hence, in figure 2.8 we only show the low-temperature case $k_BT = 0.26\ meV$. Also, since impurities act similarly on the calculations for all slip lengths λ_S, we only focus on the clean-boundary limit $\lambda_S \to +\infty$.

Figure 2.8 shows the calculations of the frequency-dependent transmission modulus $|t(\omega)|$ for different impurity scattering times $\tau_{imp}\omega_p = \{10^4, 1000, 100\}$. Increasing the impurity contribution of section 2.5.2.3, the lifetime τ_{imp} diminishes until it is smaller than the Fermi liquid value (2.31), eventually limiting the low-temperature value of the total lifetime τ_{tot}. Therefore, the higher the impurity scattering rate is, the lower the mean free path $l_{MFP} = v_F\tau_{tot}$ is, and the smaller nonlocal collective mode effects are. In figure 2.8, the local Drude result is essentially recovered for $\tau_{imp}\omega_p = 100$. Hence, in order to experimentally observe Fermi liquid collective modes in metallic thin films, a sufficiently high epitaxial quality and low impurity concentration is required. However, experimental values of the mean free path of thin films at low temperatures can give $\tau_{tot}\omega_p \geq 1000$ [3, 13, 70]. This suggests that the conditions to optically observe Fermi liquid collective modes may be reached with the current thin film growth technology.

2.6 Negative refraction in Fermi liquids

The low-temperature oscillations of the optical transmission spectra in sections 2.5.2.1 - 2.5.4 are direct consequences of spatial nonlocality: the mean free path $l_{MFP} \propto \tau_{tot}$ increases for decreasing temperature, until electronic correlations become the dominant source of scattering in the system. This phenomenon is even enhanced in a Fermi liquid near a resonance with a collective mode (1.85): in this case, correlated quasiparticles move in a coordinated way in accordance with the collective excitation, thus affecting the $\vec{q}$-dependent dielectric function (1.20). The oscillations of $|t(\omega)|$ are only one possible manifestation of nonlocal effects, that reveals the underlying physics of nonlocality: as mentioned in sections 2.5.1 and 2.5.3, the solution for the refractive indexes $n_i(\omega) = \sqrt{\epsilon_T(\vec{q},\omega)}$ is twofold, meaning that there are two frequency-degenerate optical modes that propagate in the system [12]. These coherent modes interfere with each other, originating the oscillating pattern in the thin film transmission of figures 2.5, 2.7, 2.8.

In the absence of scattering, i.e. in the collisionless limit of section 2.5.1, there is no dissipation and zero sound propagates like in a charged solid with a shear modulus. In this case, both refractive indexes $n_1(\omega)$ and $n_2(\omega)$ have positive real part for all frequencies, analogously to the standard Drude result. However, when we allow for a finite collision time $\tau_c = \tau_{tot}$ as in section 2.5.3, such momentum relaxation causes dissipation, in analogy with a viscous charged fluid. Specifically, in the low-T regime where the total lifetime τ_{tot} is dominated by the Fermi liquid component τ_{ee}, the dielectric response is characterized by the simultaneous presence of *both* dissipation and spatial nonlocality. These are necessary conditions for the occurrence of negative refraction for the nonlocal dielectric function

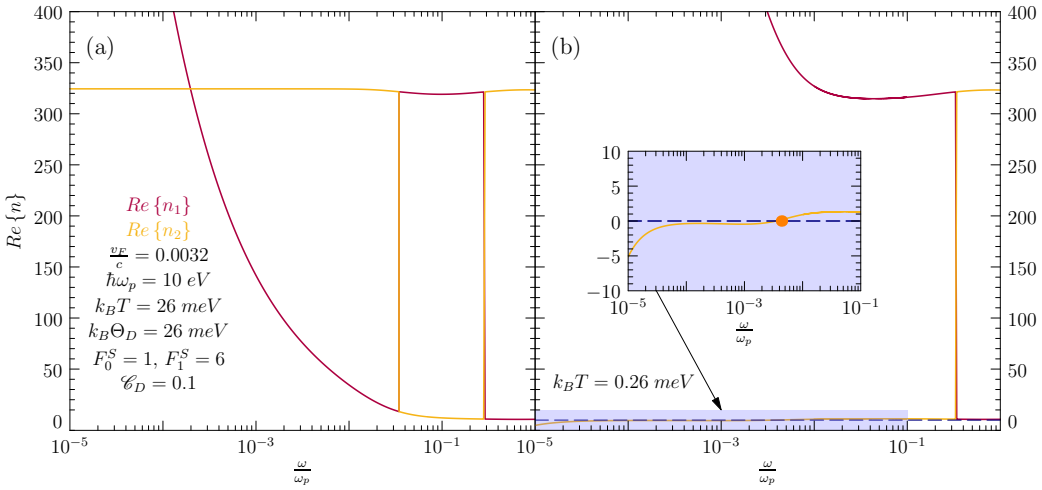

Figure 2.9: Real part of the refractive indexes $Re\{n_i\}$ $i = \{1,2\}$ for the degenerate optical modes as a function of normalized frequency $\frac{\omega}{\omega_p}$, for a Fermi liquid coupled to acoustic phonons. All parameters are the same as in figure 2.7: plasma frequency $\omega_p = 10\ eV$; Fermi velocity $\frac{v_F}{c} = 3.2 \cdot 10^{-3}$; umklapp efficiency $\Delta_u = 1$; Landau parameters $F_0^A = F_1^A = 0$, $F_0^S = 1$, $F_1^S = 6$; Debye temperature $\frac{k_B\Theta_D}{\hbar\omega_p} = 2.6\ 10^{-3}$; Debye constant $\mathscr{C}_D = 0.1\omega_p\ s^{-1}$. Panel (a) shows the high-temperature case $k_BT = 26\ meV$, while panel (b) shows the calculations at low-temperature $k_BT = 0.26\ meV$. The orange curve for $Re\{n_2\} = 0$ becomes negative for $\tau_{tot}\frac{iRe\{\tilde{v}_{S,L}\}}{\omega}(\omega_p)^2 > 1$ [12]; the condition $Re\{n\} = 0$ is highlighted by an orange circle in the inset of panel (b).

(1.20) [24], which implies that the real part of the refractive index becomes negative [44,45]. Hence, when the Fermi liquid responds like a viscous fluid, one of the two degenerate optical modes $n_i(\omega)$ can experience negative refraction [12, 16], that is $Re\{n_2(\omega)\} < 0$. The region of parameter space when this occurs is $\tau_{tot}\frac{iRe\{\tilde{v}_{S,L}\}}{\omega}(\omega_p)^2 > 1$, in accordance with reference [12]. We can see this phenomenon by plotting the real parts of the refractive indexes $n_1(\omega)$ and $n_2(\omega)$ for the same parameters of figure 2.7, as shown in figure 2.9. Panel (a) shows the high-temperature case $k_BT = 26\ meV$: the phonon-dominated collisions suppress nonlocal effects, as described in section 2.5.3, therefore no negative refraction is observed. It is only in the low-temperature situation $k_BT = 0.26\ meV$ of panel (b) that nonlocal correlations dominate momentum relaxation, and the concomitant presence of nonlocality and dissipation allows for negative refraction in the Fermi liquid. The threshold $\tau_{tot}\frac{iRe\{\tilde{v}_{S,L}\}}{\omega}(\omega_p)^2 = 1$ marks the point where $Re\{n_2(\omega)\} = 0$: this is indicated by an orange circle in the inset of of fig. 2.9 (b). However, the negative-refracting mode is always significantly damped, i.e. it is an evanescent wave, which makes a direct experimental detection of negative refraction unlikely. Another feature of the degenerate optical modes is that at any occurrence of $\omega\tau_{tot} = 1$ we have a bifurcation point, where the values of $Re\{n_1(\omega)\}$ and $Re\{n_2(\omega)\}$ swap [12]: this happens three times for the case $k_BT = 26\ meV$ of panel (a) (one instance being at $\frac{\omega}{\omega_p} \approx 1.5$ outside the plotting range), and once for the case $k_BT = 0.26\ meV$ of panel (b).

2.7 Conclusions and perspectives

The nonlocal response of Fermi liquids at low temperatures leaves observable traces in the optical spectra, which can be analyzed in the context of viscoelasticity. The coherent interference of the two frequency-degenerate optical modes that develop in charged Fermi liquids generates oscillatory patterns that can be retrieved in the bulk optical transmission as a function of depth inside the material, as well as in the transmission of thin films. The effects of viscoelastic correlations are particularly prominent at low temperatures and low frequencies, in clean samples. The model also reproduces anomalous skin effect in the surface impedance, which is another manifestation of nonlocal electromagnetic response. The contributions of phonons and impurities to scattering in a Fermi liquid diminish the effect of viscoelastic correlations. Possible further generalizations of the model include the analysis of light-matter interaction with radiation incident at an arbitrary angle, including both longitudinal and transverse components of the electric field, which would allow to describe ellipsometry experiments. The zero-frequency limit of the response functions can also be compared with transport experiments, that can also detect nonlocal behaviour of

the electron liquid as spatial gradients of the current density.

PHYSICAL REVIEW B **90**, 035143 (2014)

Electromagnetic properties of viscous charged fluids

Davide Forcella,[1] Jan Zaanen,[2] Davide Valentinis,[3] and Dirk van der Marel[3]
[1]*Physique Théorique et Mathématique and International Solvay Institutes, Université Libre de Bruxelles, C.P. 231, 1050 Bruxelles, Belgium*
[2]*The Instituut-Lorentz for Theoretical Physics, Leiden University, Leiden, The Netherlands*
[3]*Département de Physique de la Matière Condensèe, Université de Genève, 24 quai Ernest-Ansermet, 1211 Genève 4, Switzerland*
(Received 3 June 2014; published 30 July 2014)

We provide a general theoretical framework to describe the electromagnetic properties of viscous charged fluids, consisting, for example, of electrons in certain solids or plasmas. We confirm that finite viscosity leads to multiple modes of evanescent electromagnetic waves at a given frequency, one of which is characterized by a negative index of refraction, as previously discussed in a simplified model by one of the authors. In particular, we explain how optical spectroscopy can be used to probe the viscosity. We concentrate on the impact of this on the coefficients of refraction and reflection at the sample-vacuum interface. Analytical expressions are obtained relating the viscosity parameter to the reflection and transmission coefficients of light. We demonstrate that finite viscosity has the effect to decrease the reflectivity of a metallic surface, while the electromagnetic field penetrates more deeply. While on a phenomenological level there are similarities to the anomalous skin effect, the model presented here requires no particular assumptions regarding the corpuscular nature of the charge liquid. A striking consequence of the branching phenomenon into two degenerate modes is the occurrence in a half-infinite sample of oscillations of the electromagnetic field intensity as a function of distance from the interface.

DOI: 10.1103/PhysRevB.90.035143 PACS number(s): 42.25.Gy, 41.20.Jb, 78.20.Ci, 51.20.+d

I. INTRODUCTION

The flow properties of everyday fluids like water are governed by the Navier-Stokes theory of hydrodynamics. The key parameter governing the dissipative aspects of such fluids are the bulk and shear viscosities. The most abundant electrically charged fluids are formed by electrons in metals. The theory of transport in *normal* metals is well understood. These form Fermi liquids; although at precisely zero temperature this supports a "collisionless" quantum hydrodynamics which is noticeably different from the classical Navier-Stokes hydrodynamics at any finite temperature and at sufficiently long times the gas of thermally excited quasiparticles takes over forming yet again a "collision-full" effective classical fluid [1]. These notions were successfully verified in the 1960's and 1970's in the neutral Fermi liquid realized in ^{3}He, in the form of the famous maximum in the attenuation of zero sound [2]. The zero sound of the collisionless regime corresponds to a coherent vibration of the Fermi surface with a damping proportional to the microscopic collision rate of the quasiparticles $1/\tau_{\rm coll} \sim T^2$, while in the classical regime the damping is just viscous. The damping is in turn determined by $\Gamma \simeq (E_F/m_e)\tau_{\rm coll}$, where E_F is the Fermi energy [3].

The shear viscosity of the Fermi liquid is given by $\eta \simeq nE_F\tau_{\rm coll}$ and it is noticed that the viscosity (and attenuation) is now proportional to the quasiparticle collision time, diverging like $1/T^2$ at low temperatures. Why is it so that this quantity does not play any role in the transport theory of electrons in metals? The reason is well understood. For a hydrodynamical description to make sense, the conservation of total momentum of the fluid flow in a finite density system is required at least on the time and length scales associated with the establishment with local equilibrium. This in turn requires the Galilean invariance at least on the microscopic scale, and in normal metals, this is explicitly broken by the atomic lattice. Even when this is perfectly periodic, it is detrimental for the momentum conservation in a Fermi liquid. The reason is that the quasiparticles are characterized by a large Fermi momentum k_F, which is of order of the umklapp wave vector $\vec{Q}$ with the effect that the states at k_F have always a finite admixture of umklapp copies. This in turn has the effect that at every microscopic collision a certain amount of momentum is dumped in the lattice expressed in terms of the "umklapp efficiency" Δ, such that the (microscopic) momentum relaxation rate $1/\tau_K = \Delta/\tau_{\rm coll}$ while $\Delta \sim 0.5$ in the transition metals [4].

Momentum conservation is therefore already destroyed at the microscopic cutoff in normal metals. More concretely this implies that in an expansion of the time and coordinate derivatives of the current density with τ_K as the expansion parameter, the leading term gives the dissipation of the local current density proportional to $1/\tau_K$, followed by terms proportional to dissipation caused by gradients of the current density. The latter terms thus represent a correction on the leading momentum dissipation, where the constant of proportionality defines η. One of the challenges yet to be met is to determine the value of η in a non-Gallilean invariant setting, and its dependence on temperature and frequency. In the context of this paper, we will simply assume that this higher-order correction exists, and work out a number of physical consequences. For this, we will adopt values for η, which seem plausible at this moment, but which need to be determined ultimately on the basis of first principles and/or experimental data. As discussed recently by Andreev, Kivelson, and Spivak, it might well be that an exception is presented in electron systems with a very low density, where k_F becomes very small, and density of scattering centers is small compared to $1/Q$. In this case, other interesting transport properties could emerge due to interaction of the scattering centers with the viscous charged fluid [5].

Very recently it has been questioned to what extend these notions apply to *non-Fermi liquids*, which might be realized in the form of strange metals as in high-T_c superconductors, heavy fermion systems and so forth. It is believed that these are governed by quantum criticality. At zero temperature,

their quantum dynamics would be scale invariant while the expectation is that at finite temperatures these are characterized by extremely short "Planckian" [6] relaxation times $\tau_\hbar \sim \hbar/k_B T$ [7,8]. This got further impetus by the discovery of the "minimal viscosity-entropy" ratio using the AdS/CFT correspondence [9], which seems confirmed both in the quark-gluon plasma created at the heavy ion colliders [10] as well as the cold-atom unitary Fermi gas [11]. It is possible that such quantum critical systems are much less sensitive to umklapp scattering since these lack intrinsic microscopic scales like $1/k_F$. It was argued that it could therefore well be that *first* hydrodynamics is realized in such systems, while only at longer-time scales, the lack of the Galilean invariance becomes noticeable [12]. Resting on these ideas, several proposals appeared recently for the explanation of the mysterious linear resistivity of, for instance, the normal state of the high-T_c superconductors [13–15].

Electron systems in metals can be probed most conveniently by electromagnetic fields. The question arises, what would be the fingerprint of (non)hydrodynamical behavior of the electrons in the electromagnetic responses that can be measured in the laboratory? Perhaps surprisingly, to the best of our knowledge, a general theoretical framework to describe the electromagnetic effects of finite viscosity for charged fluids is not available. The goal of this paper is to construct such a general phenomenological description. In the context of heavy fermion superconductivity, sound attenuation experiments have also been discussed as a probe of the viscosity tensor [16,17]. The existence of at least two different methods for probing the viscosity would allow to calibrate the various different methods against each other. In Refs. [18] and [19], the effect of viscosity on the refractive index was discussed for different systems, using a string theory setup in the former and linear response theory for pure hydrodynamics plus electromagnetism in the latter. In particular, a prediction was given for the generic presence of negative refraction that should be manifest in actual systems such as a quark-gluon plasma. In Ref. [20], the existence of multiple electromagnetic waves with the same frequency was addressed. In Ref. [21], these works were extended for intrinsically strongly coupled materials beyond the hydrodynamic limit, using the AdS/CFT correspondence. In principle, these phenomena could also be present in the electron liquid for certain parameter ranges. For the interpretation of practical experiments, two more steps are needed: generalize the theoretical framework to include the retarded effect for the viscosity and the presence of a lattice or impurities; relate transmission or reflection coefficients to the parameters describing the electron liquid. The purpose of the present paper is to fill this gap and describe the phenomenology of charged fluids.

The basic strategy of the approach in this paper is to provide a general equation describing the viscous dynamics of the transverse velocity of the fluid and couple it to Maxwell equations to arrive to a theory of the electromagnetic response. Such a closed system leads *inter alia* to negative refraction and a bifurcation into two modes inside the viscous charge liquid instead of one at any given frequency. In the paper, we apply this formalism to the response of a Fermi liquid with finite momentum relaxation to a transverse force [2], where it is easy to incorporate the viscous response on a phenomenological level, however, it should be understood that our theoretical framework and its main consequences apply more broadly, without the need to stack on a specific model. The description of transmission and reflection at the interface involves three constituent relations at the interface instead of the usual two relations. The corresponding modification of the Fresnel equations is derived in analytical closed form. The resulting reflection coefficient exhibits a peak for $\omega \approx 1/\tau_K$, which disappears in the limit of zero viscosity. The transmission through a thin metallic film exhibits an increased transparency if the electronic viscosity is finite, which is accompanied by a strong frequency dependence of the phase, which is a sensitive parameter of the viscosity. Finally, in the limit of a weakly interacting Fermi liquid, the surface impedance corresponds closely to the results for the anomalous skin effect obtained in the Reuter-Sondheimer approach [22,23], obtained with the same parameters. The model presented here can be regarded as a generalization of the Reuter-Sondheimer model to viscous charge liquids at large.

II. EQUATIONS OF TRANSVERSE MOTION OF A VISCOUS CHARGED FLUID

A. Electromagnetic field coupled to a viscous charged fluid

The velocity field, $\vec{v}(t,\vec{r})$, of a liquid of particles of charge e, mass m and density n gives rise to an electrical current density $\vec{J}(t,\vec{r}) = ne\vec{v}(t,\vec{r})$. Here, we will concentrate on fields polarized transverse to the direction of propagation corresponding to the wave vector $\vec{q}$. The wave propagation of the transverse electric (E^T) fields is described by the Maxwell equations. For the velocity distribution of the currents (v^T) [24], we need to take into account the inertial response to a force, the force exerted by the electric field, the momentum relaxation rate to the crystal lattice, and the nonlocal coupling within the fluid. The nonlocal corrections can be written as an expansion in the coordinate derivatives of the velocity field. The leading nonlocal correction for the transverse velocity field is then given by the Laplacian $\Delta v(t,\vec{r})$. If a given flow pattern is suddenly switched off at $t = 0$, a nonequilibrium situation will persist on the time scale of the interparticle collision time $\tau_{\rm coll}$. Consequently, the individual particles respond to the flow pattern that has existed in the past, i.e., the force, is $\int_{-\infty}^{0} M_v(t)\Delta v(t,\vec{r})dt$, where $M_v(t)$ is the memory function related to the viscosity. In the frequency domain, this can be represented as $\nu(\omega)\Delta v(\vec{r})$, where, according to the preceding argument, the generalized viscosity $\nu(\omega)$ is a causal response function corresponding to the Fourier transform of $M_v(t)$. For fields and currents with a time dependence described by $\exp(-i\omega t)$, the corresponding set of differential equations forms a simple closed system:

$$(c^2\Delta + \omega^2)E(\vec{r}) = -4\pi i\omega J(\vec{r}), \tag{1}$$

$$\left[\tau_K^{-1} - i\omega - \nu(\omega)\Delta\right]v = eE(\vec{r})/m. \tag{2}$$

For $\tau_K^{-1} = 0$, the second equation is the Navier-Stokes equation for transverse currents, generalized to a frequency dependent $\nu(\omega)$. The eigenstates of Eqs. (1) and (2) are linear superpositions of terms of the form $\exp(iq_j z - i\omega t)$ having the same frequency ω, and q_j satisfies the self-consistent

relation

$$\frac{q^2c^2}{\omega^2} = 1 - \frac{\omega_p^2}{\omega\left(\omega + i\tau_K^{-1} + i\nu(\omega)q^2\right)}, \tag{3}$$

where we defined $\omega_p^2 \equiv 4\pi ne^2/m$. The q^2 dependence of the pole results from the nonzero viscosity of the medium and gives rise to all the exotic effects that we describe in this paper. For $\nu(\omega) = 0$, Eq. (3) reduces to the dielectric function described by the Drude model. Previously, Benthem and Kronig have derived a similar relation, where they neglected the displacement current as being small compared with the conduction current (Eq. (6) of Ref. [25]). From this expression, they calculated the surface impedance, assuming for ν the universal value $\sim\hbar/m$. Combining Maxwell's equations with the general expression for the convective derivative for the velocity of an electron, Gilberd arrived at a different result [26], where in the denominator of the expression for q^2c^2/ω^2 a real term proportional to q/ω appeared instead of the imaginary dispersive term $i\nu q^2$ of Eq. (3) [27]. A similar situation exists when light is absorbed by excitations exhibiting a non-negligible dispersion as a function of q. This is known to occur for excitons in semiconductors [28] and has been predicted for strongly dispersing optical phonons [29]. Unlike Eq. (3), in these cases, the q dispersion enters through a nondissipative term in the denominator of the dielectric function. Using the relation $q_j = n_j k$ between wave vector and refractive index where $k \equiv \omega/c$ is the wave number in vacuum, and solving Eq. (3) for q_j, we obtain

$$2n_j^2 = 1 - \frac{1 - i\omega\tau_K}{\omega^2\nu_c\tau_K} \pm \sqrt{\left(1 + \frac{1 - i\omega\tau_K}{\omega^2\nu_c\tau_K}\right)^2 + \frac{i4\omega_p^2}{\omega^3\nu_c}}, \tag{4}$$

where we adopted the compact notation $\nu_c = \nu(\omega)/c^2$ and n_j and ν_c have implicit frequency dependence. The electro-hydrodynamical properties are thus characterized by the two time scales ν_c and τ_K and by the plasma frequency ω_p. The first interesting observation is that for any given frequency ω, *two* modes of electromagnetic field coupled to matter (labeled $j = 1,2$) exist in a viscous charged liquid, which are distinguished by the two possible values of $n_j^2(\omega)$, a phenomenon described as additional light waves in Ref. [30].

B. Behavior at the vacuum/matter interface

Here, we concentrate on experiments that can be performed with state of the art methods, namely, reflection at the surface of a sample and transmission through a film. The Maxwell equations provide the conditions that at each interface $E(z)$ and $\partial E/\partial z$ are continuous. An additional condition follows from the properties of Newtonian fluids. The tangential friction per unit area exerted by the moving fluid on the boundary of the solid is, in leading order, proportional to the velocity at the interface, $\kappa\upsilon$. In equilibrium, this has to be balanced by the force exerted by the velocity gradient of the viscous fluid, $\eta\partial\upsilon/\partial z$, leading to the Navier constitutive relation [31]. Taken together, we arrive at the following three constitutive relations at the two interfaces:

$$\begin{gathered} E(0-\delta) = E(0+\delta), \quad E(d-\delta) = E(d+\delta), \\ \left.\frac{\partial E}{\partial z}\right|_{0-\delta} = \left.\frac{\partial E}{\partial z}\right|_{0+\delta}, \quad \left.\frac{\partial E}{\partial z}\right|_{d-\delta} = \left.\frac{\partial E}{\partial z}\right|_{d+\delta}, \\ \frac{1}{\lambda} = \left.\frac{\partial \ln\upsilon}{\partial z}\right|_{0+\delta}, \quad \left.\frac{\partial \ln\upsilon}{\partial z}\right|_{d-\delta} = \frac{-1}{\lambda}. \end{gathered} \tag{5}$$

The constant $\lambda = \eta/\kappa$ is the slip length, where $\lambda = 0$ ($\lambda = \infty$) corresponds to the interface being maximally rough (smooth). To be specific, we consider an electromagnetic wave of frequency ω propagating along z from $-\infty$ to the sample, which has one boundary defined by the plane $z = 0$ and the other by $z = d$. Part of the wave is reflected back, with an amplitude characterized by the reflection coefficient r, the amplitude transmitted to $z > d$ is characterized by the transmission coefficient t, and inside the slab the wave amplitude is a superposition of the four modes:

$$\begin{aligned} E(z)/E(0) &= e^{ikz} + re^{-ikz} && (z < 0), \\ &= t_1 e^{in_1 kz} + \theta_1 e^{-in_1 kz} + t_2 e^{in_2 kz} + \theta_2 e^{-in_2 kz} && (0 < z < d), \\ &= te^{ikz} && (z > d). \end{aligned} \tag{6}$$

Since $\mathrm{Im}n_j > 0$, the two terms $e^{-in_j kz}$ are exponentially diverging for $z \to \infty$. In the limit of a half-infinite sample, θ_1 and θ_2 therefore converge to zero, and only t_1 and t_2 contribute to the transport of electromagnetic radiation into the material.

In the case of reflection/transmission at the vacuum/sample interface of a half-infinite sample, we combine Eq. (6) with aforementioned constitutive relations at the vacuum-matter interface at $z = 0$, which leads in a straightforward fashion to the transmission and reflection coefficients at such an interface:

$$\begin{aligned} t_j &= \frac{2(n_{\underline{j}} - 1)}{(n_j + 1)(n_{\underline{j}} - n_j)} \frac{1 - n_{\underline{j}} i\lambda k}{1 + (1 - n_{\underline{j}} - n_j) i\lambda k}. \\ r &= t_1 + t_2 - 1. \end{aligned} \tag{7}$$

The surface impedance Z is obtained from the second member of Eq. (7), using the general expression relating surface impedance and reflection coefficient:

$$\frac{Z}{Z_0} = \frac{1 + r}{1 - r}, \tag{8}$$

where Z_0 is the vacuum impedance.

Another relevant case is that of a film of thickness d with vacuum on either side. The field inside the film is a superposition of all four solutions of Eq. (4), i.e., the exponentially decaying as well as the exponentially increasing ones. Taken together with the reflection amplitude r_{film} for $z < 0$ and the transmission amplitude t_{film} for $z > d$ the problem of the constitutive relations at both interfaces corresponds to a

system of six linear equations with six unknown parameters. By combining the constitutive relations defined in Eq. (5), four of these combinations provide the matrix expression

$$\begin{bmatrix} 1+n_1 & 1-n_1 & 1+n_2 & 1-n_2 \\ (1-n_1)f_1 & (1+n_1)/f_1 & (1-n_2)f_2 & (1+n_2)/f_2 \\ (1-n_1^2)(1-n_1\xi) & (1-n_1^2)(1+n_1\xi) & (1-n_2^2)(1-n_2\xi) & (1-n_2^2)(1+n_2\xi) \\ (1-n_1^2)(1+n_1\xi)f_1 & (1-n_1^2)(1-n_1\xi)/f_1 & (1-n_2^2)(1+n_2\xi)f_2 & (1-n_2^2)(1-n_2\xi)/f_2 \end{bmatrix} \begin{bmatrix} t_1 \\ \theta_1 \\ t_2 \\ \theta_2 \end{bmatrix} = \begin{bmatrix} 2 \\ 0 \\ 0 \\ 0 \end{bmatrix}, \tag{9}$$

where we use the compact notations $f_1 = e^{in_1kd}$, $f_2 = e^{in_2kd}$, and $\xi = i\lambda k$. Numerical inversion provides t_1, θ_1, t_2, and θ_2, from which the reflection and transmission coefficients of the film are obtained using the remaining two constitutive relations:

$$\begin{aligned} r_{\text{film}} &= t_1 + \theta_1 + t_2 + \theta_2 - 1, \\ \frac{t_{\text{film}}}{t_{\text{vac}}} &= e^{-ikd}(t_1 e^{in_1kd} + \theta_1 e^{-in_1kd} + t_2 e^{in_2kd} + \theta_2 e^{-in_2kd}), \end{aligned} \tag{10}$$

where, similar as in experimental practice, the transmission is calibrated against the transmission through a slice of vacuum with the same thickness d as the film.

III. RELEVANT PARAMETER RANGE OF MOMENTUM RELAXATION AND VISCOSITY COEFFICIENT

Before we turn to the examples based on a numerical solution of the expressions in the previous section, it will be useful to explore the relevant parameter range for the viscosity and the relaxation rate. Two limiting cases have been explored theoretically in some detail in the literature: Fermi liquids and quantum critical states.

Since in a Fermi-liquid context viscosity and diffusivity correspond to the same quantity [3], it therefore follows that $\nu(0) = v_F^2 \tau_{\text{coll}}$. For our numerical examples, we make the reasonable approximation that the memory function follows an exponential decay, i.e., $M_\nu(t)\tilde{\tau} = \nu(0)\exp(-t/\tilde{\tau})$, so that $\nu(\omega) = \nu(0)/(1 - i\omega\tilde{\tau})$. Definitions of $\tilde{\tau}$, $\tilde{v}_F$, and further details are provided in Appendix. When we solve Eq. (2) with this function, we obtain the relations for transverse sound in a Fermi liquid describing the dispersion [Re $q(\omega)$] and the attenuation [Im $q(\omega)$] of the first ($\omega\tau \ll 1$) and zero ($\omega\tau \gg 1$) transverse sound of liquid ^{3}He in the normal state. We thus obtain the following expression for the generalized viscosity:

$$\frac{\nu_c(\omega)}{\tilde{\tau}} \sim \frac{(\tilde{v}_F/c)^2}{1 - i\omega\tilde{\tau}}. \tag{11}$$

The result for $\nu(\omega)$ in the hydrodynamic limit ($\omega \to 0$) is a real number, hence the viscous response is purely dissipative. In the "collisionless" limit, i.e., for frequencies high compared to the collision rate, this crosses over to purely reactive response. Moreover, $\nu(\omega)$ is proportional to v_F^2, implying that materials with a high Fermi velocity such as aluminum (having $v_F/c \sim 0.003$) are expected to be record holders for viscosity related phenomena.

Despite its equally high Fermi velocity, a drastically different situation has been anticipated for graphene as a result of the quantum criticality of this system [7], therefore bringing it close to the lower bound conjectured in the context of the quark-gluon plasma. In this case, the dynamic viscosity (related to the kinematic viscosity as $\eta = mn\nu$) is given by the relation [32] $\eta/s \geqslant A\hbar/k_B$, where s is the entropy density. We associate an elastic mean free path l_0 with the breaking of the Galilean invariance, and the kinematic viscosity ν with the diffusivity. Besides the assumption that intrinsic rapid relaxation processes are governing the electron system, an additional condition is that the length scales associated with the momentum relaxation processes are still large. Operationally, this means that l_0 has to be large compared to the lattice constant: this is a "clean-limit" notion. The transport of quantum critical systems can also be addressed—to a degree—in the dirty limit [33] where very different principles are at work. The momentum relaxation rate is in such simple liquids (and also the local quantum critical liquid computed holographically in Ref. [13]) $1/\tau_K = \nu/l_0^2$. Taken together, these arguments then lead to the simple result

$$\frac{v_c}{\tau_K} \sim \left(\frac{\lambda_e}{2l_0}\right)^2 \left(\frac{s}{nk_B}\right)^2, \tag{12}$$

where $\lambda_e = 2.4 \times 10^{-14}$ cm is the Compton wavelength for electrons. Since l_0 must be larger than the interatomic distance, $l_0 > 10^{-8}$ cm and s can not exceed the equipartition value, $s < k_B n$, we conclude that $v_c/\tau_K < 10^{-12}$, i.e., some seven orders of magnitude below the Fermi liquid estimate. It may therefore be difficult in practice to experimentally access the regime relevant to the quantum critical state. For a Fermi liquid on the other hand, the parameters are much more favorable for experimental observation.

IV. NUMERICAL EXAMPLES

A. Refractive indices

In Fig. 1, the real and imaginary parts of the two refractive indices are displayed for selected values of the parameters describing the fluid, utilizing Eq. (A5) for the frequency dependence of the viscosity parameter. For the range $\omega\tau_K < 1$, the two solutions of Eq. (3) are described by the leading-order terms of the expansion in $v_c\omega$ and $\omega\tau_K$:

$$\begin{aligned} n_1 &\approx \omega_p \sqrt{\frac{i\tau_K}{\omega}} \left(1 - \frac{i}{2} v_c \omega \tau_K^2 \omega_p^2\right), \\ n_2 &\approx \sqrt{\frac{\tau_K}{4v_c}} (1 - v_c \tau_K \omega_p^2) + \frac{i}{\omega\sqrt{v_c\tau_K}}. \end{aligned} \tag{13}$$

In the nonviscous limit, n_1 converges to the conventional expression of an evanescent electromagnetic wave; in this limit, the second mode has $\text{Im}n_2 \to \infty$, so that the wave

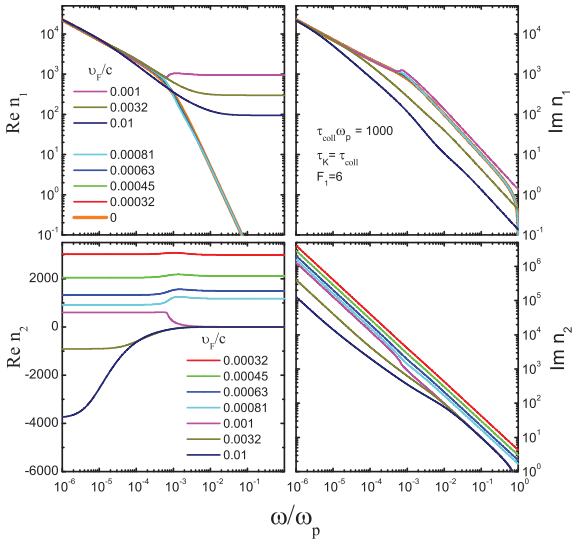

FIG. 1. (Color online) The real and imaginary parts of the refractive indices n_1 and n_2, as a function of the normalized frequency for selected values of the Fermi velocity in units of light velocity, v_F/c. In all panels, the relaxation time $\tau_K = 1000/\omega_p$. In the two top panels showing Ren_1 and Imn_1, the curves for $v_F/c = 0.00032$ coincide within plotting accuracy with the Drude result, $v_F = 0$.

amplitude, $\exp(-\mathrm{Im}n_2 kz)$, vanishes for all z. Consequently, the n_1 mode is the sole nontrivial solution for $\nu = 0$. For the viscous case, there exist two solutions for the same ω, corresponding to collective modes of different admixtures of the coupled charge-liquid and the electromagnetic field. At low frequencies, the n_1 branch approaches the usual evanescent electromagnetic wave. The second branch n_2 has, by virtue of the constant real part, the characteristics of transverse sound, with an attenuation constant diverging as $1/\omega$. This mode is similar in character to aforementioned attenuated transverse sound of ^{3}He [2]. Another intriguing aspect of this mode is the fact that for $\nu_c\tau_K\omega_p^2 > 1$, the real part of n_2 is negative at low frequencies. This is the footprint of a very interesting phenomenon called negative refraction [34–36], in which the phase velocities and the energy flux are in opposite direction. It was discussed in the context of charged fluids in Refs. [18] and [19], where a particular form of Eqs. (1) and (2) was considered, for which the viscosity is real and frequency independent, and the momentum is not dissipated: $1/\tau_K = 0$. The frequency $\omega\tau_K = 1$ constitutes a peculiar bifurcation point: for $\omega\tau_K > 1$, the character of n_1 and n_2 is swapped when the viscosity drops below the critical value $\nu_c\tau_K\omega_p^2 = 1$; i.e., for $\nu_c\tau_K\omega_p^2 < 1$ the n_1 branch has Re$n_1 \sim 1$ and Re$n_2 \gg 1$, whereas for $\nu_c\tau_K\omega_p^2 > 1$, this is the other way around.

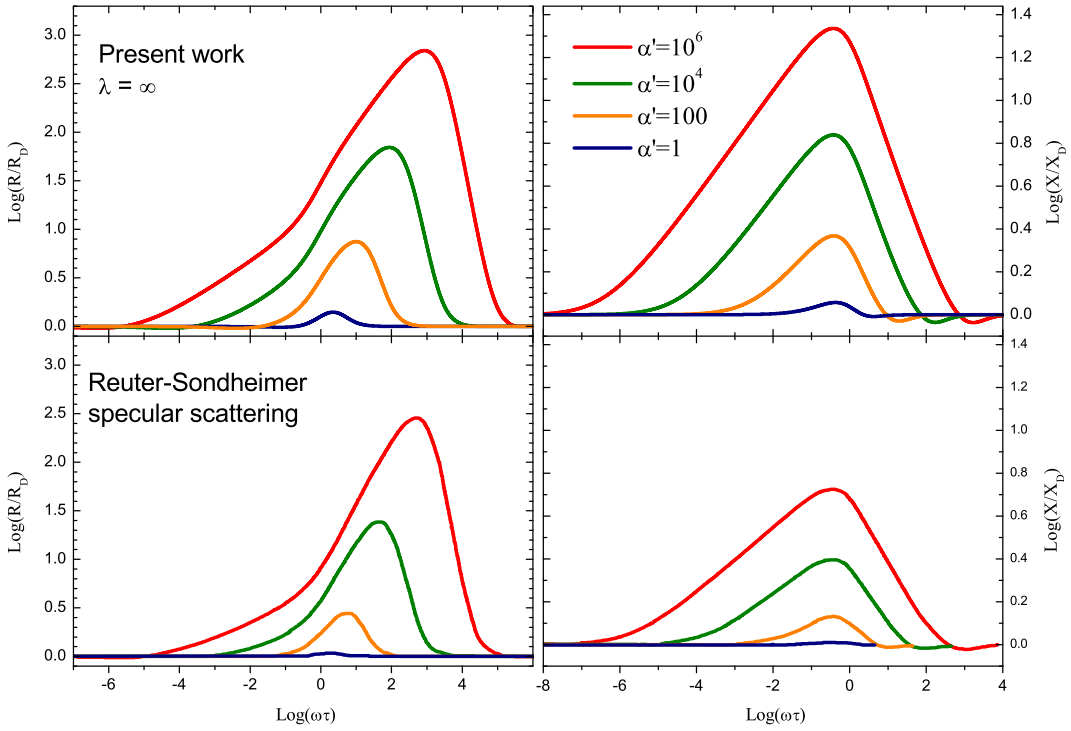

FIG. 2. (Color online) Frequency dependence of the surface resistance (left) and reactance (right) relative to the Drude limit ($v_F = 0$) for different values of the parameter $\alpha' = (3/4)(\tau_{\mathrm{coll}}\omega_p v_F/c)^2$. The calculations were done for $\tilde{\tau} = \tau_K = \tau_{\mathrm{coll}}$ and a frictionless surface ($\lambda = \infty$). For comparison, the results for the limit of specular scattering of Reuter and Sondheimer (Figs. 2 and 3 of Ref. [22]) are reproduced in the lower panel on the same scale and for the same values of α'.

B. Surface impedance

In Fig. 2, the resulting spectra of R/R_D and X/X_D represent the real and imaginary parts of the surface impedance relative to the corresponding Drude limit ($\upsilon_F = 0$). Ordinates and abscissas are shown on a $\log_{10}$ scale. The results in Fig. 2 are in fact almost identical to the calculations of Reuter and Sondheimer, displayed in Fig. 3 of Ref. [22] for the same parameter choices of $\alpha' = (3/4)(\tau\omega_p\upsilon_F/c)^2$. As is the case in Ref. [22], the resulting curves for any given value of α' are universal, i.e., they do not depend on the particular choice of υ_F/c and $\tau\omega_p$. The Reuter-Sondheimer model parts from a weakly interacting electron model, for which the Boltzmann equations are solved in the case where the mean free path is longer than penetration of the electromagnetic rays. The situation at the surface is treated in terms of a fraction p of particles, which are scattered specularly, and $1 - p$, which is scattered diffusively. The results in Fig. 3 Ref. [22] are for the limit of pure specular scattering, corresponding to a perfectly smooth interface for which $\lambda = \infty$. The close correspondence between the Reuter-Sondheimer prediction and the present result implies that, for the case of weakly interacting electrons, we have obtained an alternative formulation of the anomalous skin effect, with a set of simple expressions in analytically closed form. At the same time, the present approach has a potentially broader applicability since it does not rely on any particular assumptions regarding the corpuscular nature of the charge liquid and is of particular interest for the optical properties of quantum critical matter.

C. Reflection at vacuum/matter interface of a half-infinite sample

The result for the reflection coefficient is displayed in Fig. 3 for selected values of the parameters. For a clean material with a perfectly smooth surface, the expected behavior corresponds to the result shown in the rightmost panel with $\lambda\omega_p = \infty$. Based on the estimates made above for the viscosity and relaxation time, the curve with $\upsilon_F/c = 0.0032$ comes closest to the expected parameter range of a Fermi liquid. We should contrast this curve to the Drude curve (orange). Clearly, the viscosity has the effect of suppressing the reflection coefficient, or increasing the absorption on the solid: the absorption forms a peak at $\omega\tau_K \approx 1$, where the maximum increases from about 0.002 in the Drude limit to 0.004 for $\upsilon_F/c = 0.0032$. Increasing the surface roughness (left panel of Fig. 3) demonstrates the increased effects of finite viscosity on the absorption of the material. Intuitively, this confirms what one expects: extreme surface roughness forces the current to be zero at the sample surface. Due to the viscosity this slows also the current deeper in the fluid, which therefore is less effective in screening the external electromagnetic field, and so becomes a less effective mirror. The phase shown in the lower panels is a much less sensitive probe of the viscosity parameter. Since the phase of a reflectivity signal is already notoriously difficult to measure, for all practical purposes, the best strategy for experiments is probably to concentrate on the absorption coefficient $1 - |r(\omega)|^2$.

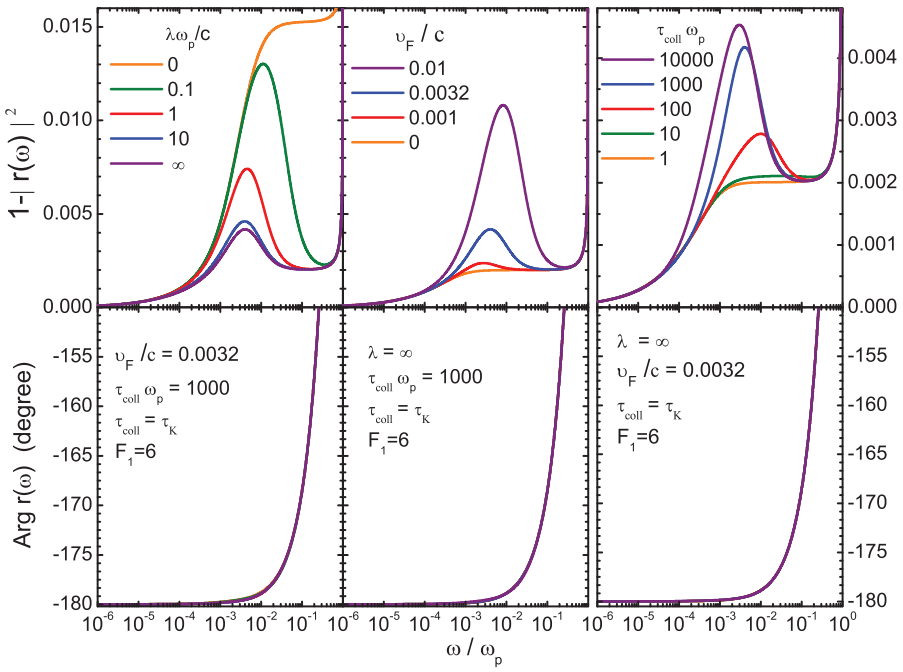

FIG. 3. (Color online) Spectra of the absorption coefficient ($A = 1 - |r|^2$) and the phase (in degrees) of the reflection coefficient as a function of frequency for selected values of the slip length λ (left), relative Fermi velocity υ_F/c (middle), and relaxation time, $\tau_{\rm coll} = \tau_K$ (right).

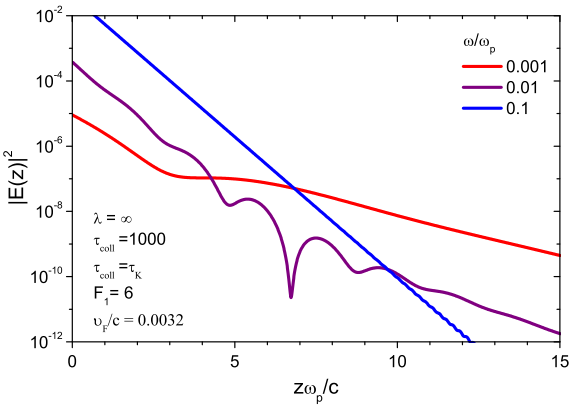

FIG. 4. (Color online) Oscillations of the electric field intensity resulting from interference by the two degenerate modes of the same frequency, as a function of penetration away from the vacuum/sample interface.

D. Nonexponential decay and amplitude oscillations inside the viscous charge liquid

An electromagnetic wave of frequency ω incident at the surface will excite two modes of the same frequency inside the material, with amplitudes given by the transmission coefficients t_j at the vacuum-matter interface. Both solutions are exponentially decaying as a function of distance, each with a different decay length. An additional consequence is that, since n_1 and n_2 have different real parts, the intensity $|t_1 \exp(in_1 kz) + t_2 \exp(in_2 kz)|^2$ exhibits standing wave patterns as a function of distance from the interface in the range where both modes are of comparable amplitude. An example of this behavior is shown in Fig. 4. In principle, experimental methods can be devised to measure these oscillations of the field by local probe techniques.

E. Thin-film transmission

As pointed out at the end of Sec. II B, the thin-film transmission can be calculated numerically from the reflection and transmission amplitudes at both interfaces using Eq. (10), and a numerical inversion of the 4×4 matrix of Eq. (9) describing the four rays inside the film. Examples for representative parameters are shown in Fig. 5. Just as for the reflectivity of a thick sample, the viscosity has the effect of changing the spectral appearance: for the Drude model without viscosity the transmission spectrum has a plateau for $\omega\tau_K < 1$, followed by a minimum at $\omega\tau_K \approx 1$ and a rise to about $|t| = 1$ for $\omega \to \omega_p$. Increasing the viscosity has several effects: the transmission develops a maximum at $\omega\tau_K \approx 1$, the minimum is pushed

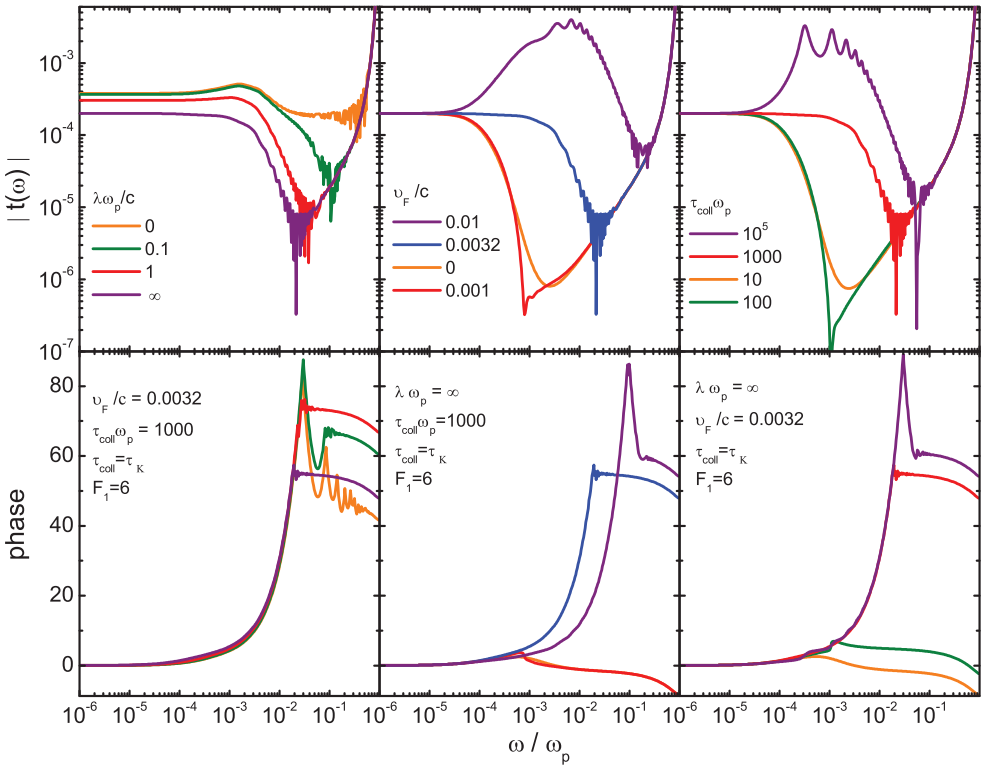

FIG. 5. (Color online) Spectra of amplitude and phase (in radians) of the transmission of a film of viscous charged fluid of thickness $d = 10c/\omega_p$ for selected values of the slip length λ (left), relative Fermi velocity v_F/c (middle), and collision time, τ_{coll} (right). The phase values are calibrated against vacuum, i.e., if the sample is replaced with vacuum, the phase is zero at all frequencies.

to somewhat higher frequencies, and also in this case the transmission rises to $|t| = 1$ for $\omega \to \omega_p$. Interestingly, in the frequency range between the maximum and the minimum, there are the Fabry-Perot resonances, associated with the n_1 branch, which has a relatively weak attenuation in this frequency range. Note that the propagation of the n_1 mode becomes similar to a standard polariton mode in an insulating material despite that we are dealing with a metal. We also see that the phase of the transmission spectrum is an extremely sensitive probe of the viscosity for $\omega\tau_K \gg 1$. In particular, while for small values of $\nu_c(0)$ it is a weakly decreasing function of frequency, it has a rapid rise for $v_F/c > 0.003$.

V. CONCLUSIONS

We have derived a general framework to deal with electromagnetic properties of charged fluids and we have derived some of their main properties. We have shown the existence of two coupled electromagnetic-matter modes for a given frequency inside a viscous charged fluid, one of these two has a negative value for the real part of the index of refraction for low frequency. Moreover, we have computed some observables: reflection and transmission coefficients, that could be measured in actual experiments. Our results provide perspectives for a generation of experiments and devices for the detection of viscosity in charged or electron liquids and the possible exploitation of multiple waves and negative refraction in such systems.

ACKNOWLEDGMENTS

DvdM acknowledges illuminating discussions with Jean-Louis Barrat, Teun Klapwijk, and Pierce Coleman. This work was supported by the Swiss National Science Foundation (SNSF) through Grant 200021-153405. J.Z. acknowledges support of a grant from the John Templeton foundation. The opinions expressed in this publication are those of the authors and do not necessarily reflect the views of the John Templeton Foundation. D.F. is F.R.S-FNRS Chargé de Recherches. He acknowledges support by the F.R.S.-FNRS, by IISN - Belgium through conventions 4.4511.06 and 4.4514.08, by the Communauté Francaise de Belgique through the ARC program and by the ERC through the SyDuGraM Advanced Grant. D.F. acknowledges the kind hospitality of the LPTHE, where part of this research has been implemented.

APPENDIX: NEUTRAL FERMI LIQUID

For our numerical examples, we adopt the dispersion $q(\omega)$ of transverse sound of the neutral Fermi liquid, which is obtained in two steps [2,37]. First, x is solved for a given (real) frequency ω from the transcendental relation

$$(1-x^2)\left[1-\frac{x}{2}\ln\left(\frac{x-1}{x+1}\right)\right] = \frac{1+(1-i\omega\tau_{\rm coll})(F_1-6)/9}{1+(1-i\omega\tau_{\rm coll})F_1/3}, \tag{A1}$$

where, in general, the solutions for x have a complex value. Here, F_1 is the Landau parameter characterizing the interaction in the $l = 1$ angular momentum channel, and Landau parameters of the higher angular momentum channels are assumed to be negligible. In the second step, $q(\omega)$ is calculated from

$$q(\omega) = \frac{i+\omega\tau_{\rm coll}}{x v_F \tau_{\rm coll}}. \tag{A2}$$

We see, that the function $q(\omega)$ depends uniquely on the collision rate $\tau_{\rm coll}^{-1}$, the Fermi- v_F, and F_1. We obtained the following parametrization by fitting to the numerical solution of Eq. (A1):

$$q^2 v_F^2 \tau_{\rm coll}^2 = 5i\omega\tau_{\rm coll}(1 - i\omega\tau_{\rm coll}\sqrt{F_1}7/32)/(1 + F_1/3). \tag{A3}$$

This expression merges with the exact solution for $\omega \to 0$, and it is rather accurate for all other frequencies and parameters.

To obtain the viscosity from this, we observe that the hydrodynamic free propagation of transverse polarized modes in a neutral liquid is described by $\partial v/\partial t = \nu\Delta v$, from which $i\omega = \nu q^2$. In order to extend the description to finite frequencies beyond the hydrodynamic limit, we introduce the frequency dependent memory function

$$\nu(\omega) = \frac{i\omega}{q^2} \tag{A4}$$

with $q(\omega)$ given by either the solution of Eq. (A1) or the parametrization, Eq. (A3). In the latter case, we obtain the expression

$$\nu(\omega) = \frac{v_F^2\tau_{\rm coll}(1+F_1/3)/5}{1 - i\omega\tau_{\rm coll}\sqrt{F_1}7/32}. \tag{A5}$$

We recognize here Eq. (11), where the various parameters are related as

$$\tilde{\tau} = \frac{7\sqrt{F_1}}{32}\tau_{\rm coll}, \quad \tilde{v}_F^2 = v_F^2\frac{1+F_1/3}{\sqrt{F_1}}\frac{32}{35}, \quad \frac{1}{\tau_K} = \frac{7\sqrt{F_1}}{32}\frac{\Delta}{\tilde{\tau}}. \tag{A6}$$

[1] L. Landau, Zh. Eksp. Teor. Fiz. **30**, 1058 (1956)[Sov. Phys. JETP **3**, 920 (1957)].
[2] P. T. Roach and J. B. Ketterson, Phys. Rev. Lett. **36**, 736 (1976).
[3] D. Forster, *Hydrodynamical Fluctuations, Broken Symmetry, and Correlation Functions* (Westview Press, Boulder, CO, 1995).
[4] W. E. Lawrence and J. W. Wilkins, Phys. Rev. B **7**, 2317 (1973).
[5] A. V. Andreev, S. A. Kivelson, and B. Spivak, Phys. Rev. Lett. **106**, 256804 (2011).
[6] J. Zaanen, Nature (London) **430**, 512 (2004).
[7] M. Muller, J. Schmalian, and L. Fritz, Phys. Rev. Lett. **103**, 025301 (2009).
[8] S. Sachdev, *Quantum Phase Transitions* (Cambridge University Press, Cambridge, 1999).
[9] G. Policastro, D. T. Son, and A. O. Starinets, Phys. Rev. Lett. **87**, 081601 (2001).
[10] A. Rebhan and D. Steineder, Phys. Rev. Lett. **108**, 021601 (2012).

[11] L. Luo and J. E. Thomas, J. Low Temp. Phys. **154**, 1 (2009).
[12] S. A. Hartnoll and D. M. Hofman, Phys. Rev. Lett. **108**, 241601 (2012).
[13] R. A. Davison, K. Schalm, and J. Zaanen, Phys. Rev. B **89**, 245116 (2014).
[14] S. A. Hartnoll, R. Mahajan, M. Punk, and S. Sachdev, Phys. Rev. B **89**, 155130 (2014).
[15] A. Lucas, S. Sachdev, and K. Schalm, Phys. Rev. D **89**, 066018 (2014).
[16] C. J. Pethick and D. Pines, Phys. Rev. Lett. **57**, 118 (1986).
[17] J. Moreno and P. Coleman, Phys. Rev. B **53**, R2995 (1996).
[18] A. Amariti, D. Forcella, A. Mariotti, and G. Policastro, J. High Energy Phys. 04 (2011) 036.
[19] A. Amariti, D. Forcella, and A. Mariotti, J. High Energy Phys. 01 (2013) 105.
[20] A. Amariti, D. Forcella, and A. Mariotti, arXiv:1010.1297.
[21] D. Forcella, A. Mezzalira, and D. Musso, arXiv:1404.4048.
[22] G. E. H. Reuter and E. H. Sondheimer, Proc. R. Soc. A **195**, 336 (1948).
[23] E. H. Sondheimer, Adv. Phys. **50**, 499 (2001).
[24] The remainder of the discussion is entirely devoted to transverse polarized fields. For the sake of compactness of notation, we will drop the suffix T from here on.
[25] C. W. Benthem and R. Kronig, Physica **20**, 293 (1954).
[26] P. W. Gilberd, J. Phys. F: Met. Phys. **12**, 1845 (1982).
[27] The difference can be traced back to the fact that in the present manuscript we discuss electromagnetic waves in matter having purely transverse polarization. Terms like, e.g., $(\vec{\hat{z}} \cdot \nabla)\vec{j}$ and $(\vec{\hat{z}} \cdot \nabla)\vec{B}$(occurring in Eqs. (22) and (23) of Ref. [26], respectively) are only finite if there is a field component perpendicular to the interface, which is in the present case parallel to the propagation direction of the electromagnetic waves.
[28] G. H. Cocoletzi and W. L. Mochan, Surf. Sci. Rep. **57**, 1 (2005).
[29] I. Kaelin, Ch. Helm, and G. Blatter, Phys. Rev. B **68**, 012302 (2003).
[30] S. I. Pekar, Zh. Eksp. Teor. Fiz. **74**, 1485 (1978)[Sov. Phys. JETP **47**, 762 (1978)].
[31] L. Bocquet and J.-L. Barrat, Soft Matter **3**, 685 (2007).
[32] P. K. Kovtun, D. T. Son, and A. O. Starinets, Phys. Rev. Lett. **94**, 111601 (2005).
[33] S. A. Hartnoll, arXiv:1405.3651.
[34] V. G. Veselago, Sov. Phys. Usp. **10**, 509 (1968).
[35] V. M. Agranovich and Y. N. Gartstein, Phys.-Usp. **49**, 1029 (2006).
[36] J. B. Pendry, Phys. Rev. Lett. **85**, 3966 (2000).
[37] A. Abrikosov and I. Khalatnikov, Rep. Prog. Phys. **22**, 330 (1959).

Chapter 3

Superconductivity at the band edge

3.1 Introduction to pairing correlations

One of the most spectacular effects of electronic correlations in metals is electronic pairing, whereby the effective interaction between two given conduction electrons becomes attractive, and bound states of electronic pairs appear in the Fermi sea: these many-body effects generate a phase transition to a new ground state, with the consequence that electron pairs are able to propagate in the system *without any dissipation*, and to respond to external magnetic fields as a *perfect diamagnet*. This phenomenon is known as superconductivity.

In this chapter, we will first review the phenomenon of Cooper pairing, by which two given electrons in the Fermi sea perceive a net mutually attractive interaction, thus forming bound states of pairs. The treatment of electron-phonon coupling in second quantization will lead us to BCS theory: utilizing this microscopic model, we are able to study the elementary excitations and the critical properties of a superconductor, like the energy gap $\Delta_{\vec{k}}$ or the critical temperature T_c, whenever the effective electron-electron interaction, stemming from electron-phonon interaction, can be assumed to be attractive and constant in the relevant energy range for pairing.

Since we are ultimately interested to study systems where the Fermi energy E_F can be comparable with typical phonon energies $\hbar\omega_D$, we will focus on what happens to a BCS superconductor at low density. In this situation, one realizes that the standard high-density and weak coupling approximations, like $E_F \gg \hbar\omega_D$ and $k_B T_c \ll \hbar\omega_D$, cannot be employed: the chemical potential μ lies close to the inferior edge of a band, and this has profound consequences on the dynamics of pairing and on T_c. Furthermore, this analysis will pave the way for the next chapter, where we will analyze the influence of quantum confinement on a BCS superconductor: in reduced dimensionality, μ crosses confinement-induced

subbands by varying density and coupling; whenever this happens, band-edge effects must be considered in order to provide a physical description of superconductivity.

3.2 Pairing interactions and mean-field theory

Correlations leading to the Fermi liquid ground state do not exhaust the variety of phenomena exhibited by correlated electron systems. In chapter 1, we have analyzed how Coulomb and exchange processes affect the physical properties of conduction electrons in metals: when the energy scale of these properties is small with respect to the electronic kinetic energy, the net effect of screening (by the surrounding lattice, free charge carriers, etcetera) and Pauli exchange is the formation of Landau quasiparticles [64], in direct correspondence with the noninteracting electron gas [8]. In other words, the electron-hole elementary excitations of the Fermi sea are nearly independent and only interact via short-ranged residual forces, that we can treat perturbatively. This framework greatly simplifies the mathematical analysis, while simultaneously providing ways to test the limits of the theory, by estimating the magnitude of the residual quasiparticle correlations. In chapter 1, we described such correlations with electron-hole polarization bubbles, and we unveiled the intrinsically nonlocal nature of these processes in the limit when the electronic mean free path is large compared to the average quasiparticle spacing. This is sufficient to explore a wide variety of novel phenomena occurring in the Fermi sea: for example, in chapter 1 we have seen that nonlocal correlations, treated in the viscoelastic model, qualitatively affect experimental observables that can be measured by optical spectroscopy and transport.

However, the picture of nearly-independent Landau quasiparticles does not contemplate additional two-body correlations, which can become relevant at sufficiently low temperatures and trigger the phase transition to a new ground state. In fact, these two-body processes lead to electronic pairing and superconductivity. In order to describe the superconducting state, we have to add such processes to the theory.

In many superconducting materials, pairing correlations are provided by the coupling of the Fermi sea with an underlying bosonic field: if the Fermi sea coexists and is coupled with an external *ensemble* having bosonic collective excitations, quasielectrons can exchange such collective excitations. In the appropriate momentum and frequency range, the negative (attractive) energy due to boson exchange between two quasielectrons can overcome the residual repulsive interactions: bosons can make the total interaction between electrons *attractive*, thereby mediating electronic pairing. In crystalline solids, the bosonic field can be formed by phonons, i.e. quanta of the ionic lattice vibrational collective modes; other bosons that can mediate pairing in magnetic systems are magnons [71–73], that are quanta

of spin waves. Purely electronic mechanisms for pairing are also possible, with attractive two-body forces provided for instance by overscreening of the Coulomb repulsion through Friedel oscillations [74, 75].

Electronic pairing emerges from the complexity of the many-body problem constituted by electrons coupled to bosons. In general, the total hamiltonian for such problem is

$$\hat{H} = \hat{H}_{K,el} + \hat{H}_{Coul} + \hat{H}_{K,b} + \hat{H}_{b-b} + \hat{H}_{el-b} \tag{3.1}$$

where $\hat{H}_{K,el} = \sum_{\vec{k},\sigma} \xi_{\vec{k},\sigma} \hat{c}^{\dagger}_{\vec{k},\sigma} \hat{c}_{\vec{k},\sigma}$ is the kinetic hamiltonian of electrons, $\hat{H}_{Coul} = \sum_{\vec{k},\vec{k}',\vec{q},\sigma,\sigma'} V_{Coul}(\vec{q}) \hat{c}^{\dagger}_{\vec{k}+\vec{q},\sigma} \hat{c}^{\dagger}_{\vec{k}'-\vec{q},\sigma'} \hat{c}_{\vec{k}',\sigma'} \hat{c}_{\vec{k},\sigma}$ is the Coulomb hamiltonian for electrons, $\hat{H}_{K,b} = \sum_{\alpha} \varepsilon_{\alpha} \hat{b}^{\dagger}_{\alpha} \hat{b}_{\alpha}$ is the boson kinetic hamiltonian, $\hat{H}_{b-b} = \frac{1}{2} \sum_{\alpha\beta\nu_1\nu_2} V^{b-b}_{\alpha\beta\nu_1\nu_2} \hat{b}^{\dagger}_{\alpha} \hat{b}^{\dagger}_{\beta} \hat{b}_{\nu_2} \hat{b}_{\nu_1}$ is the boson-boson interaction hamiltonian and $\hat{H}_{el-b}$ is the electron-boson coupling hamiltonian,

$$\hat{H}_{el-b} = \sum_{\vec{k},\vec{k}',\alpha,\sigma} V^{el-b}_{\vec{k}\vec{k}'\sigma\alpha} \hat{c}^{\dagger}_{\vec{k},\sigma} \hat{c}_{\vec{k},\sigma} \left(\hat{b}^{\dagger}_{\alpha} + \hat{b}_{\alpha} \right). \tag{3.2}$$

Here we have utilized the annihilation and creation operators for electrons $\left\{ \hat{c}_{\vec{k},\sigma}, \hat{c}^{\dagger}_{\vec{k},\sigma} \right\}$ in the representation of wave vector $\vec{k}$ and spin σ, and the correspondent quantities for bosons $\left\{ \hat{b}_{\alpha}, \hat{b}^{\dagger}_{\alpha} \right\}$ in states generically labeled by the index α. The many-body hamiltonian (3.1) has formidable complexity, which prevents one from finding a general solution of this problem. Even a system composed by free electrons ($\hat{H}_{K,el}$) and free bosons ($\hat{H}_{K,b}$) coupled through an interaction $\hat{H}_{el-b}$ has many-body character, whereby electrons and bosons interact and influence each other leading to new physical phenomena: for instance, electron-phonon coupling can lead to the formation of polarons [76, 77]. Therefore, instead of solving the hamiltonian (3.1) directly, another strategy is to rewrite an *effective* hamiltonian for the electrons, which is assumed to be the net result of all many-body interactions of electrons and bosons, and which displays the essential physics of pairing. The philosophy of such approach is analogous to the one for the Fermi liquid phenomenology, which applies to electrons in simple metals - see section 1.5 of chapter 1: in that case, we have seen that the net result of interactions is to leave *weakly-interacting quasiparticles*, i.e. quasielectrons and quasiholes living in the Fermi sea (1.72). This provides the groundings for the description of the normally-conducting state [8, 78], from which the transition to the paired state begins in conventional superconductors. However, as previously mentioned, pairing interactions lead to a different ground state with respect to the Fermi liquid. In fact, when we add bosons to the electronic system, new interaction processes for electrons are possible due to electron-boson coupling. In the following, we focus on electron-phonon coupling, which is

amongst the most common sources of pairing in known superconductors. In the presence of electron-phonon coupling, we can follow aforementioned strategy and rewrite the problem of electrons coupled to phonons in terms of an effective hamiltonian for quasielectrons, interacting through a two-body potential; the latter is the net result of all initial interactions comprising Coulomb, electron-phonon, and so on. Perturbation theory demonstrates the validity of this approach: the perturbative expansion of the Green's function for electrons coupled to phonons can be rewritten as an expansion in terms of effective electron-electron interactions through an effective potential $V^{ph}_{el-el}(\tau)$; the latter is retarded in time τ -i.e. energy-dependent $V^{ph}_{el-el}(\omega)$ in Fourier space - because phonons travel at a finite velocity and it takes a finite time for them to mediate the interaction with electrons. Physically, this means that a phonon is emitted (absorbed) at some time τ by the electronic system, and absorbed (emitted) at some later time $\tau^{'}$, leading to a retarded interaction [2]. This is visually represented by the diagram 3.2 for the the electron-phonon interaction vertex.

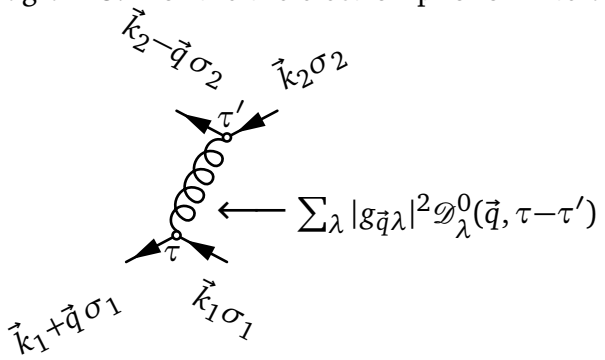

As we see in the diagram 3.2, the total momentum of the system is conserved, since the involved electrons exchange a phonon momentum $\vec{q}$. However, they also exchange an energy $\Omega = \omega_\lambda(\vec{q})$, with $\omega_\lambda(\vec{q})$ phonon dispersion relation for branch λ, which reflects the energy dependence of the electron-phonon potential $V^{ph}_{el-el}(\omega)$ due to retardation effects. Phonon emission and absorption always come in pairs in these processes, so we can define creation-annihilation operators of phonon pairs as $\hat{B}_{\vec{q},\lambda} = \hat{b}^\dagger(\vec{q},\lambda) + \hat{b}(-\vec{q},\lambda)$ and its hermitian conjugate. Phonons have to physically propagate in order to reach the second electron after being emitted by the first electron: therefore, the process depends on the *phonon propagator*. The free phonon propagator for the branch λ reads

$$\mathscr{D}^\lambda_0(\vec{q},\tau) = -\left\langle \mathscr{T}_\tau \hat{B}_{\vec{q},\lambda}(\tau)\hat{B}^\dagger_{\vec{q},\lambda}(0)\right\rangle \tag{3.3}$$

where $\mathscr{T}_\tau$ is the time-ordering operator [1]. In frequency space, equation (3.3) corresponds to [1, 2, 9, 78]

$$\mathscr{D}^\lambda_0(\vec{q},\Omega) = \frac{1}{\Omega-\omega_\lambda(\vec{q})} - \frac{1}{\Omega+\omega_\lambda(\vec{q})} = \frac{2\omega_\lambda(\vec{q})}{\Omega^2-[\omega_\lambda(\vec{q})]^2} \tag{3.4}$$

The explicit form of the electron-phonon interaction vertex is then

$$V_{el-el}^{ph}(\tau) = \frac{1}{2}\sum_{\vec{k}_1\sigma_1}\sum_{\vec{k}_2\sigma_2}\sum_{\vec{q}}\int_0^{\frac{1}{k_BT}} d\tau' V_{el-el}^{eff}(\vec{q},\tau-\tau')\hat{c}^{\dagger}_{\vec{k}_1+\vec{q},\sigma_1}(\tau)\hat{c}^{\dagger}_{\vec{k}_2-\vec{q},\sigma_2}(\tau')\hat{c}_{\vec{k}_2,\sigma_2}(\tau')\hat{c}_{\vec{k}_1,\sigma_1}(\tau) \tag{3.5}$$

where we have the $\vec{q}$ and $\tau-\tau'$ component of the interaction potential

$$V_{el-el}^{eff}(\vec{q},\tau)) = \sum_{\lambda}\left|g_{\vec{q},\lambda}\right|^2 \mathscr{D}_0^{\lambda}(\vec{q},\tau), \tag{3.6}$$

where $g_{\vec{q},\lambda}$ is the electron-phonon coupling matrix element. In the frequency domain, equation (3.7) reads

$$V_{el-el}^{eff}(\vec{q},\Omega) = \sum_{\lambda}\left|g_{\vec{q},\lambda}\right|^2 \mathscr{D}_0^{\lambda}(\vec{q},\Omega). \tag{3.7}$$

As previously mentioned, the potential (3.5) represents an effective interaction between quasielectrons, which exchange the excitation momentum $\vec{q}$ and the energy $\omega_\lambda(\vec{q})$. This directly affect electronic correlations. Indeed, the structure of $V_{el-el}^{ph}(\tau)$ is similar to the two-body Coulomb repulsion between electrons, with the exceptions that $V_{el-el}^{ph}(\tau)$ is second order in the matrix element $g_{\vec{q},\lambda}$ and it is retarded in time - i.e. energy-dependent. It is this energy dependence, given by phonon dynamics, that can make $V_{el-el}^{ph}(\Omega) < 0$: the effective phonon-mediated electron-electron interaction can become *negative*, i.e. attractive. This is encoded into the phonon Green's function (3.4), which is indeed negative for physical frequencies $\Omega < \omega_\lambda(\vec{q})$. Such negative contribution is able to trigger the transition to the superconducting state, with an effective attraction between electrons that couples them into Cooper pairs [2, 78]. By comparison, the Coulomb interaction is always positive, being energy-independent: in fact, the Coulomb interaction reads

$$\hat{V}_{Coul} = \frac{1}{2}\sum_{\vec{k}_1,\sigma_1,\vec{k}_2,\sigma_2}\sum_{\vec{q}} V_{Coul}(q)\hat{c}^{\dagger}_{\vec{k}_1+\vec{q},\sigma_1}\hat{c}^{\dagger}_{\vec{k}_2-\vec{q},\sigma_2}\hat{c}_{\vec{k}_2,\sigma_2}\hat{c}_{\vec{k}_1,\sigma_1} \tag{3.8}$$

where $V_{Coul}(q) = \frac{e^2}{\epsilon_0 q^2}$. Comparing equations (3.5) and (3.8), we immediately realize that we can treat the phonon-mediated electron correlations on the same ground as Coulomb processes, i.e. as effective electronic interactions. Hence, we can proceed along the same lines as for the Fermi sea (1.72), and write the effective electronic hamiltonian comprising the electron-phonon contribution in a similar way as for Fermi liquid phenomenology. Consistently with section (1.5), some interaction effects are already considered in the renormalized properties of Landau quasiparticles, e.g. their effective mass m^*; these quasiparticles act as nearly-independent elementary excitations. For this reason, we build

a first contribution to our effective hamiltonian by considering the kinetic term

$$\hat{H}^0_{FL} = \sum_{\vec{k},\sigma} \xi_{\vec{k},\sigma} \hat{c}^\dagger_{\vec{k},\sigma} \hat{c}_{\vec{k},\sigma} \tag{3.9}$$

where $\xi_{\vec{k},\sigma}$ are the energy eigenvalues of Landau quasiparticles, already including mass renormalization effects due to Coulomb and electron-phonon interactions. In the same spirit as in Landau theory, the quasiparticles are still interacting via a two-body hamiltonian, which can act in the singlet channel between electrons of opposite spins

$$\hat{H}^S_{el-el} = \sum_{\vec{k},\vec{k}',\vec{q}} V_S(\vec{k},\vec{k}',\vec{q}) \hat{c}^\dagger_{\vec{k}+\frac{1}{2}\vec{q},\uparrow} \hat{c}^\dagger_{-\vec{k}+\frac{1}{2}\vec{q},\downarrow} \hat{c}_{-\vec{k}'+\frac{1}{2}\vec{q},\downarrow} \hat{c}_{\vec{k}'+\frac{1}{2}\vec{q},\uparrow}, \tag{3.10}$$

with $V_S(\vec{k},\vec{k}',\vec{q})$ effective singlet interaction, or in the triplet channel between electrons having the same spin. [9, 79]. In a translationally-invariant system carrying no current, the $q = 0$ paired state has the largest instability to precipitate into the superconducting state [78]. Hence, we restrict our attention to the case $q = 0$, so that the pairing potential becomes $V_S(\vec{k},\vec{k}',0) \equiv V_S(\vec{k},\vec{k}')$. Also, we assume singlet pairing interaction, which is energetically favored with respect to triplet for what concerns exchange correlations [3]. In fact, the Pauli exchange energy is lower for antiparallel than for parallel spins. Although singlet pairing is realized in many conventional superconductors, there are exceptions, with Sr_2RuO_4 as a possible candidate for triplet superconductivity [80, 81]. The total singlet hamiltonian becomes

$$\hat{H}^0_S = \hat{H}^0_{FL} + \hat{H}^S_{el-el} \tag{3.11}$$

The hamiltonian (3.11) is at the foundations of many microscopic theories of superconductivity. The origin of pairing stems from the energy dependence of the electron-phonon interaction potential (3.5): for a given superconductor and in appropriate momentum and frequency ranges, the electron-boson potential $V^{ph}_{el-el}(\Omega)$ is negative, leading to an effective attractive electron-electron interaction (3.10) between quasielectrons. Also, when the boson-mediated electron-electron interaction $V^{ph}_{el-el}(\Omega) < 0$ overcomes the Coulomb repulsion (3.8), quasielectrons experience a *net mutual attraction*, which generates bound states of Cooper pairs in the Fermi sea and determines a many-body phase transition to the superconducting ground state. This means $V_S(\vec{k},\vec{k}',\vec{q}) < 0$ in the effective hamiltonian formulation (3.10). The remarkably small energy difference between the normally-conducting and the superconducting state of a metal (of the order of $10^{-8}\ eV$ per electron [78]) suggests that only a subtle shift in electron correlations occurs in going to the superconducting state. This subtle energy balance does not always work: indeed, some materials become

superconductors while others do not. Now we have replaced the complicated problem (3.1) of electrons coupled to phonons by the effective electronic hamiltonian (3.11), where a pairing (negative) interaction $V_S(\vec{k},\vec{k}')$ reproduces the essential low-energy physics of the effective electron-electron attraction mediated by phonons $V^{ph}_{el-el}(\tau)$. We still have to specify an explicit form of the pairing potential $V_S(\vec{k},\vec{k}')$ which mimics $V^{ph}_{el-el}(\tau)$. For that reason, in the following section we look at the electrodynamics of electron-phonon coupling more in detail, and we define the BCS caricature of the pairing potential, which is able to grasp the essential features of superconductivity at weak coupling.

3.2.1 Electron-phonon coupling and BCS theory

In many superconductors, the mechanism generating the net electron-electron attraction is the exchange of phonons; this physical picture is at the basis of the BCS model by J. Bardeen, L. N. Cooper and J. R. Schrieffer [82], and of its strong-coupling extension by A. B. Migdal and G. M. Eliashberg [78, 83, 84]. By virtue of electron-phonon coupling, quasielectrons exchange quanta of lattice vibrations as depicted in the diagram 3.2. Since lattice ions carry positive electric charge, the electron-phonon interaction has electrodynamic nature, in the same way as Coulomb repulsion between electrons; this reinforces the similarities between the two aforementioned interactions. Hence, the phonon mechanism can be regarded as a phenomenon of anomalous dielectric screening: the overscreening of the Coulomb repulsion by phonons reverses the sign of the net electron-electron interaction.

In order to get a glimpse at the dynamics of overscreening, we have to analyze phonon exchange; this is best done using the many-body formalism, which allows us to gain immediate physical insight into the pairing mechanism. The propagation of free phonons is described by the Green's function (3.4). However, phonons coupled to electrons are not free since the former interact with the latter: the free phonon propagator (3.3) becomes the non-free propagator $\mathscr{D}_\lambda(\vec{q},\Omega)$: phonons acquire a self-energy, i.e. a modified spectral function and a finite lifetime (like electrons, see section 1.4.1), through electron-phonon interaction. Likewise, the free electron Green's function $\mathscr{G}^0(\vec{k},\omega)=\frac{1}{\omega-\xi_{\vec{k}}}$ acquires a self-energy from interactions with phonons and becomes the non-free propagator $\mathscr{G}(\vec{k},\omega)$. Finally, the electron-phonon matrix element $g_{\vec{q},\lambda}$ is also screened, because interactions occur between *dressed* - i.e. non-free - quasiparticles, quasielectrons and dressed phonons. The final form of the electron-phonon interaction depends on the phonon dispersion relations $\omega_\lambda(\vec{q})$, on the electronic properties like density and mass, and on which classes of electron-phonon processes we consider in the many-body theory. However, we can generally interpret the results in terms of dielectric screening in the system of electrons and phonons, since the

latter interact through electrodynamic forces. As we are dealing with screening, one useful way to consider the many-body problem of electrons coupled to longitudinal phonons is RPA, as we did for electrons alone in section 1.2. In this case, one retrieves the results for electrons interacting with longitudinal phonons in the jellium model: the screened phonons acquire acoustic dispersion relations, the Coulomb interaction is screened as well as the electron-phonon coupling. Here, we first quote the essential results for the effective electron-electron interaction in the case of acoustic phonons, characterized by a Debye spectrum [3]. Given a phonon spectrum $\omega_\lambda(q)$, the electron-electron effective interaction stems from equations (3.7) and (3.4)[1]:

$$V^{eff}_{el-el}(\vec{q},\Omega) = \sum_\lambda \left|g_{\vec{q},\lambda}\right|^2 \frac{2\omega_\lambda(\vec{q})}{\Omega^2 - [\omega_\lambda(\vec{q})]^2}. \tag{3.12}$$

Let us analyze the frequency dependence of the effective electron-electron interaction (3.12), with the aim of extracting a characteristic value for a given phonon spectrum. This effective interaction can be parameterized as a function of frequency by introducing the Eliashberg function $\alpha^2F(\omega)$ [84], which is an average over the Fermi surface of the electron-phonon interaction matrix element squared, multiplied by the phonon density of states $F(\omega) = \sum_{\lambda,\vec{q}} \delta\left[\omega - \omega_\lambda(\vec{q})\right]$. Physically, $\alpha^2F(\omega)$ tells us how the phonon spectrum of the material is modified by electron-phonon coupling. Therefore, from equation (3.12) we can write

$$V^{eff}_{el-el}(\vec{q},\Omega) \approx V^{eff}_{el-el}(\Omega) = 2\int_0^{+\infty} d\omega \alpha^2F(\omega)\frac{\omega}{\Omega^2-\omega^2}. \tag{3.13}$$

Let us take the example of a Debye phonon spectrum [3] $\alpha^2F(\omega) = V_D\left(\frac{\omega}{\omega_D}\right)^2\theta(\omega_D-\omega)$, where ω_D is the Debye frequency. This corresponds to the acoustic dispersion relation $\omega(\vec{q}) = v_S q\theta(q_D - q)$, where v_S is the sound velocity and $q_D = \frac{\omega_D}{v_S}$ is the Debye wave vector. In this case, the effective electron-electron interaction (3.13) becomes

$$V^{eff}_{el-el}(\Omega) = 2V_D\int_0^{\omega_D} d\omega\left(\frac{\omega}{\omega_D}\right)^2\frac{\omega}{\Omega^2-\omega^2} = V_D\left\{-1+\left(\frac{\Omega}{\omega_D}\right)^2\ln\left[\frac{\left(\frac{\Omega}{\omega_D}\right)^2}{1-\left(\frac{\Omega}{\omega_D}\right)^2}\right]\right\} \tag{3.14}$$

The frequency evolution of the effective electron-electron interaction (3.14) is shown by

[1] For acoustic phonons, we should substitute $\mathscr{D}^\lambda_0(\vec{q},\Omega)$ in equation (3.4) with the non-free phonon propagator $\mathscr{D}^\lambda(\vec{q},\Omega) = \frac{2\omega_\lambda(\vec{q})}{\Omega^2-[\omega_\lambda(\vec{q})]^2}$, where $\omega_\lambda(\vec{q}) = v_S q$, since acoustic phonons emerge from the renormalization of phonon dispersion relations, due to electron-phonon coupling [1, 9]

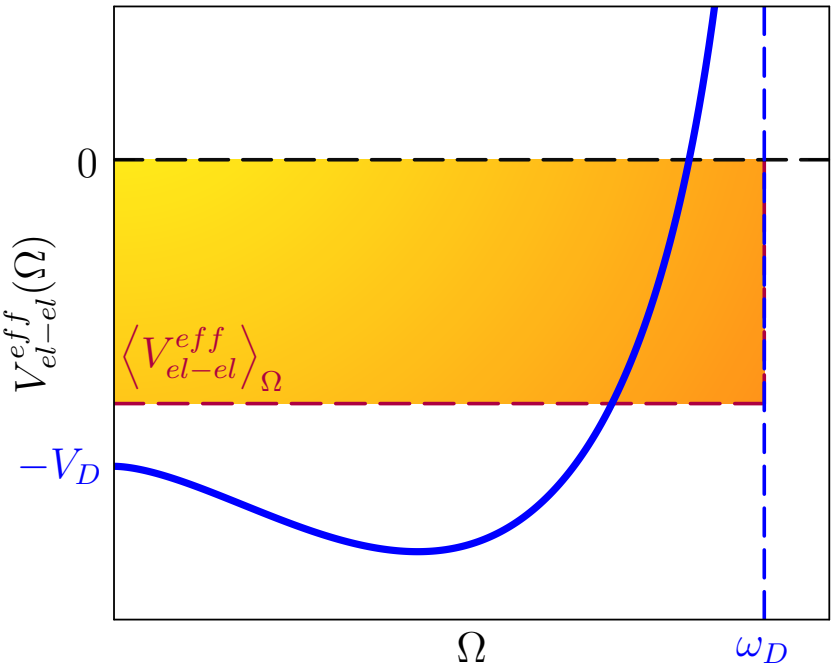

Figure 3.1: Frequency evolution of the electron-electron effective interaction mediated by coupling to a Debye phonon spectrum (3.14), characterized by the Debye frequency ω_D and the interaction strength V_D. The blue curve shows effective interaction according to equation (3.14). The shaded area shows the average value of the electron-electron attraction $\left\langle V^{eff}_{el-el} \right\rangle_{\Omega}$ up to the Debye frequency, in accordance with equation (3.15).

the blue curve in figure 3.1: the effective interaction is negative, i.e. *attractive*, due to electron-phonon coupling, up to a frequency $\left[1 + W\left(\frac{1}{e}\right)\right]^{-\frac{1}{2}} \omega_D = 0.884\omega_D$, where $W(x)$ is the Lambert function, solution to $x = We^W$; above this frequency, the effective interaction becomes positive, i.e. repulsive. Therefore, in the case of a Debye spectrum, ω_D sets the characteristic frequency scale within which the interaction is attractive.

Performing an average over frequency of equation (3.14), we can deduce the average value of the effective electron-electron attraction:

$$\left\langle V^{eff}_{el-el} \right\rangle_{\Omega} = \frac{1}{\omega_D} \int_0^{\omega_D} d\Omega V^{eff}_{el-el}(\Omega) = \frac{1}{3}(-1 - \ln 4)\, V_D = -0.795 V_D. \tag{3.15}$$

Hence, we can utilize the average value from equation (3.15) as a characteristic magnitude of the electron-electron attraction which occurs in the frequency interval $\{0, \omega_D\}$. This provides a simplified sketch of the electron-electron effective attraction, shown by the shaded area in figure 3.1, which is able to reproduce the mechanism of pairing while neglecting the frequency dependence of $V^{eff}_{el-el}(\Omega)$. This procedure, here outlined for a simple Debye phonon spectrum, can be repeated for a more complicated function $\alpha^2 F(\omega)$.

As previously mentioned, apart from generating acoustic phonon dispersion relations, electronic screening affects both the Coulomb repulsion $V_{coul}(q)$, as well as the electron-phonon coupling vertex $g_{\vec{q},\lambda}$: taking a static approximation of dielectric screening, the former becomes the screened Coulomb repulsion $W_{Coul}(q) = \frac{V_{Coul(q)}}{\epsilon(\vec{q},0)}$, while the latter is renormalized according to $\frac{g_{\vec{q},\lambda}}{\epsilon(\vec{q},0)}$, where $\epsilon(\vec{q},\omega)$ is the dielectric function [9]. For a Fermi liquid, the dielectric function can be calculated in RPA, as we did in section 1.2. Hence, in the presence of screening, the effective phonon-mediated electron-electron interaction becomes

$$V^{eff}_{el-el}(\vec{q},\Omega) = \sum_{\lambda} \frac{\left|g_{\vec{q},\lambda}\right|^2}{\left[\epsilon(\vec{q},0)\right]^2} \mathscr{D}^{\lambda}(\vec{q},\Omega). \tag{3.16}$$

From equation (3.16), we see that whenever the sum of the effective phonon-mediated electron-electron interaction $V^{eff}_{el-el}(\vec{q},\Omega)$ and of the screened Coulomb repulsion $W_{Coul}(q)$ is negative, the effective electron-electron interaction becomes *attractive*. This qualitatively illustrates the origin of Cooper pairing from electron-phonon coupling, even in the presence of Coulomb repulsion. The qualitative frequency evolution of the effective potential (3.16) for a given momentum $\vec{q}$ is sketched in the left panel of figure 3.2.

While we have reviewed the interaction of electrons with longitudinal phonons in the jellium model, one can consider also optical phonons, and use more sophisticated many-body resummation techniques instead of RPA. We cannot use the momentum- and frequency-dependent potential $V^{eff}_{el-el}(\vec{q},\Omega)$ directly into the effective hamiltonian (3.10), precisely because $V^{eff}_{el-el}(\vec{q},\Omega)$ depends on frequency, while a two-body potential must be local in time in a hamiltonian scheme [78]. Hence, retardation effects are best treated with a many-body formalism [78, 83, 84], while if we insist on using the effective hamiltonian (3.11) we must find an appropriate caricature $V_S(\vec{k},\vec{k}')$ that catches the qualitative signature of pairing. The strategy to achieve such caricature follows the example that we sketched for a Debye spectrum in equations (3.13) - (3.15). In the low-energy pairing range, we can neglect the frequency dependence of $V^{ph}_{el-el}(\Omega)$ if such dependence is sufficiently weak in the Ω interval where the interaction is attractive, i.e. $V^{ph}_{el-el}(\Omega) \approx \left\langle V^{eff}_{el-el} \right\rangle_{\Omega} \ \forall \Omega < \omega_{\lambda}(\vec{q})$, where we consider only one phonon branch λ with the typical phonon energy $\omega_{\lambda}(\vec{q}) \approx \omega_D$. Thus, the only energy dependence of coupling comes from the typical cutoff energy $\hbar\omega_D$ in figure 1.5 (b), which qualitatively sketches the sign change of the interaction at $\omega_{\lambda}(\vec{q})$ in figure 3.2 (a). Outside the pairing window $(-\hbar\omega_D, \hbar\omega_D)$, we neglect the repulsive portion of the potential in figure 3.2 (a), simply assuming zero interaction. Therefore, in this approximation we can take $\epsilon(\vec{q},\Omega) = 1$ and $\mathscr{D}^0_{\lambda}(\vec{q},\Omega) = \Theta(\omega_D - \Omega) - \Theta(\Omega + \omega_D)$. This considerably simplifies the problem, since retardation effects only appear in the theory

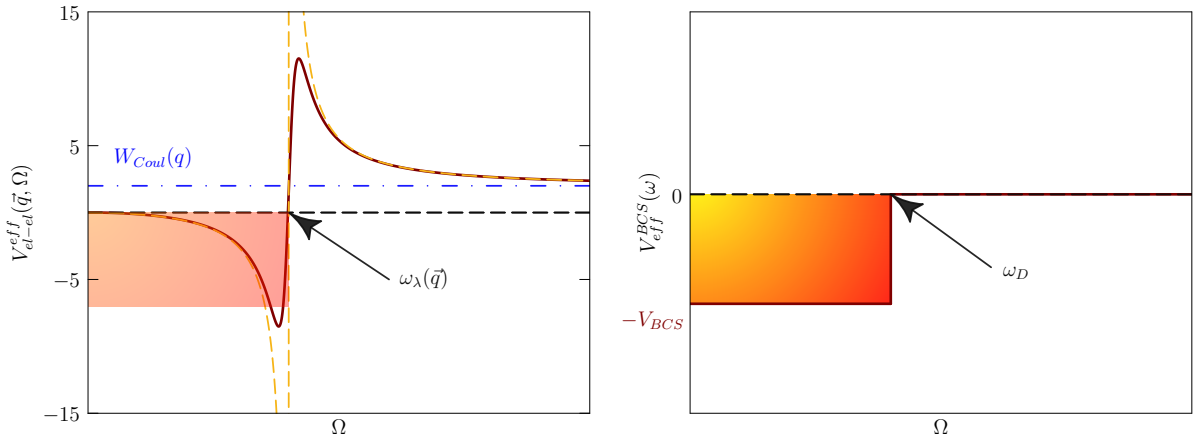

Figure 3.2: Left panel: schematic diagram of the effective electron-electron interaction $V^{eff}_{el-el}(\vec{q},\Omega)$, for a given momentum $\vec{q}$, as a function of frequency Ω, which is controlled by the energy dependence of the phonon Green's function - equation (3.4) for free phonons - and which becomes equation (3.16) in the presence of static electronic screening. $V^{eff}_{el-el}(\vec{q},\Omega)$ is attractive below the phonon frequency $\omega_\lambda(\vec{q})$ due to overscreening of the Coulomb interaction $W_{Coul}(q)$, while the latter dominates for $\Omega \gg \omega_\lambda(\vec{q})$ so that $V^{eff}_{el-el}(\vec{q},\Omega)$ asymptotically reaches the positive value $W_{Coul}(q)$ [1, 9, 78]. The dashed gold curve is obtained for free phonons - see equation (3.4)- while real - i.e. non-free - phonons have an imaginary part in their dispersion relation, which suppresses the singularity at $\omega_\lambda(\vec{q})$ and gives the red continuous curve. Right panel: simplified Bardeen-Cooper-Schrieffer interaction $V^{BCS}_{eff}(\Omega)$ for the electron-phonon mechanism of the left panel. The interaction is attractive and constant up to a typical phonon frequency, taken as the Debye frequency ω_D [82]. The colored area represents the energy window in which Cooper pairing occurs according to the BCS model: this mimics qualitatively the region where $V^{eff}_{el-el}(\vec{q},\Omega) < 0$, as highlighted in the left panel by a colored area as well.

through the energy cutoff $\hbar\omega_D$. The effective singlet potential $V_S(\vec{k},\vec{k}')$ is then

$$V_S(\vec{k},\vec{k}') \equiv V_{eff}^{BCS}(\xi_{\vec{k}}) = -V_{BCS}\eta(\xi_{\vec{k}})\eta(\xi_{\vec{k}'}) \tag{3.17}$$

where the function $\eta(\xi) = \Theta(\xi+\hbar\omega_D) - \Theta(\xi-\hbar\omega_D)$ implements the cutoff at energy $\hbar\omega_D$ for the quasielectron energy levels $\xi_{\vec{k}}$ measured with respect to the chemical potential μ.

This way, we arrive at the effective BCS hamiltonian

$$\hat{H}_{BCS} = \hat{H}^0_{FL} + \hat{H}^S_{el-el} = \sum_{\vec{k},\sigma} \xi_{\vec{k},\sigma}\hat{c}^\dagger_{\vec{k},\sigma}\hat{c}_{\vec{k},\sigma} - V_{BCS}\sum_{\vec{k},\vec{k}'}\eta(\xi_{\vec{k}})\eta(\xi_{\vec{k}'})\hat{c}^\dagger_{\vec{k},\uparrow}\hat{c}^\dagger_{-\vec{k},\downarrow}\hat{c}_{-\vec{k}',\downarrow}\hat{c}_{\vec{k}',\uparrow} \tag{3.18}$$

Now we have the simplified pairing model (3.18), based on a caricature of electron-phonon coupling in Fermi liquids, which is able to describe the essential features of singlet superconductivity at weak coupling. We still have to solve the hamiltonian $\hat{H}_{BCS}$, to find the new superconducting ground state and its elementary excitations. Of course, the two-body interaction term in equation (3.18) complicates the analysis, and analytical solutions are prevented without making further simplifications. In order to proceed, BCS opted for a mean-field solution: this stems from either variational analysis with respect to a guessed ground state Ψ_{BCS}, or through mean-field decoupling of the two-body interaction. In the next section, we briefly review the method of mean-field decoupling in second quantization to highlight its physical meaning; in the next chapter, we will apply this method to obtain the Gor'kov equations, in order to derive the gap equation for a BCS superconductor expressed in a generic single-particle basis.

3.2.2 Mean-field decoupling

The BCS pairing instability, characterizing the hamiltonian (3.18), generates the phase transition to the BCS ground state Ψ_{BCS}, in which a macroscopically large number of electrons condenses in pairs of opposite momenta and spin. Therefore, the BCS state represents an electronic condensate, with a large number of Cooper pairs mutually overlapping in real space [85, 86]. Since the condensed phase is macroscopically occupied, we can look at the average condensate occupation and its deviations with respect to equilibrium, which we assume perturbatively small. In this case, the average properties will be reliably representative of the entire *ensemble*. This procedure is known as mean-field decoupling, since it allows to decompose two-body correlations, like the Coulomb term (3.8) or the BCS two-body term in (3.18), into an independent-particle problem; for conventional superconductors like Al, this is a good approximation. For the Fermi liquid (1.72), mean-field decoupling

is equivalent to the Hartree-Fock approximation [2], while in the presence of pairing it becomes the BCS theory [2, 78]. In second quantization, we define the thermodynamic average in the condensed state $\left\langle \hat{c}^{\dagger}_{\vec{k},\uparrow}\hat{c}^{\dagger}_{-\vec{k},\downarrow}\right\rangle$ and its hermitian conjugate. The deviations with respect to these averages read

$$\Phi^{\dagger}_{\vec{k}} = \hat{c}^{\dagger}_{\vec{k},\uparrow}\hat{c}^{\dagger}_{-\vec{k},\downarrow} - \left\langle \hat{c}^{\dagger}_{\vec{k},\uparrow}\hat{c}^{\dagger}_{-\vec{k},\downarrow}\right\rangle \tag{3.19a}$$

$$\Phi_{\vec{k}} = \hat{c}_{-\vec{k},\downarrow}\hat{c}_{\vec{k},\uparrow} - \left\langle \hat{c}_{-\vec{k},\downarrow}\hat{c}_{\vec{k},\uparrow}\right\rangle \tag{3.19b}$$

and are assumed to be small compared to the averages themselves. Rewriting the hamiltonian (3.18) in terms of the averages in (3.19a) and neglecting the term $\Phi^{\dagger}_{\vec{k}}\Phi_{\vec{k}}$, the resulting hamiltonian becomes quadratic in the annihilation and creation operators $\left(\hat{c}_{\vec{k},\sigma}, \hat{c}^{\dagger}_{\vec{k},\sigma}\right)$, hence it is diagonalizable. The diagonalization is completed through the Bogoliubov-Valatin unitary transformations, that allow to find the elementary excitations of the BCS ground state and to study finite-temperature properties like the superconducting energy gap $\Delta_{\vec{k}}(T)$ and the pairing temperature T_c. The equation through which we can study finite-temperature properties is the BCS gap equation

$$\Delta_{\vec{k}} = \int \frac{d^3k'}{(2\pi)^3} V_S(\vec{k},\vec{k}')\,\Delta_{\vec{k}'}\,\frac{\tanh\left(\frac{\sqrt{(\xi_{\vec{k}'})^2+\left|\Delta_{\vec{k}'}\right|^2}}{2k_BT}\right)}{2\sqrt{(\xi_{\vec{k}'})^2+\left|\Delta_{\vec{k}'}\right|^2}}. \tag{3.20a}$$

here written for one band. As previously mentioned, $\Delta_{\vec{k}} = \Delta_{\vec{k}}(T)$ is the temperature-dependent energy gap, which opens in the electron density of states $N_0^{el}(\mu+\xi)$) (per spin and per unit volume) around the chemical potential μ during the transition to the superconducting phase, giving a gapped BCS density of states $N_{BCS}(\mu+\xi)$. The chemical potential μ is set by the electronic density n through the density equation

$$n = 2\int_{-\infty}^{\infty} d\xi\, f_{FD}(\xi)\, N_{BCS}(\mu+\xi). \tag{3.20b}$$

Here, $f_{FD}(\xi) = [e^{\xi/k_BT}+1]^{-1}$ is the Fermi-Dirac distribution function. In the standard textbook solution of the BCS model, the gap is momentum-independent, i.e. $\Delta_{\vec{k}} \equiv \Delta$: in this case, the gap has s-wave symmetry. This allows us to rewrite the integral over k' in the gap equation (3.20a), using the BCS interaction (3.17), as an energy integral. We have

$$1 = -V_{BCS}\int_{-\hbar\omega_D}^{\hbar\omega_D} d\xi N_0^{el}(\mu+\xi)\,\frac{\tanh\left(\frac{\sqrt{\xi^2+|\Delta|^2}}{2k_BT}\right)}{2\sqrt{\xi^2+|\Delta|^2}}. \tag{3.21}$$

The generalization of the gap equation (3.21) to many bands is straightforward: each superconducting band α has a gap Δ_α, and equation (3.21) becomes equation (1a) of paper 2. In the following, in chapter 4, and in paper 2, we will only consider the s-wave solution. The mean-field technique gives reliable results for systems in which thermal and quantum fluctuations are negligible with respect to thermodynamic averages. This also depends on the dimensionality of the system: rigidity with respect to fluctuations decreases with decreasing number of spatial dimensions, thereby lowering the accuracy of mean-field solutions. For two-dimensional systems, a pure BCS solution is prevented by fluctuations according to the Mermin-Wagner theorem [87–89], although a superconducting transition is still possible and its difference with respect to mean-field theory can be small, particularly for multiband systems; instead, one-dimensional systems have to be treated with different methods in general [90].

Up to now, we have reviewed how BCS theory models pairing through phonon exchange, starting from the normal-state Fermi sea (1.72). However, we have not yet commented on the electronic eigenstates $\xi_{\vec{k},\sigma}$ entering into the hamiltonian (3.18): we have not described the role of electrons yet, specifically how the normal-state properties influence the superconducting transition. We notice that the electronic quantity entering into the gap equation (3.21) is the density of states $N_0^{el}(\mu+\xi)$ around the chemical potential μ. This quantity represents how many electron states are available for pairing in the system, inside the pairing energy window (3.17) that is set by the cutoff energy $\hbar\omega_D$. Hence, for BCS the paired states reside in the region of the density of states $N_0^{el}(\mu+\xi)$ such that

$$\xi \in (-\hbar\omega_D, \hbar\omega_D) \tag{3.22}$$

Consequently, pairing depends on the density of states $N_0^{el}(\mu+\xi)$ sampled by the pairing window (3.22); the form of the density of states depends on the spatial dimensionality of the system (i.e. 3D, 2D, or quasi-2D configurations that we will consider in the next chapter 4) and on the number of bands (single band or multiband configurations), while the energy position of the pairing window - given a cutoff $\hbar\omega_D$ - depends on the chemical potential μ, which is set by the density through equation (3.20b).

Therefore, spatial dimensionality and electron density have a significant impact on the superconducting properties, and on the BCS solution of equation (3.21). The standard textbook solution of BCS involves one parabolic band at high density, for which $\xi_{\vec{k}} = \frac{\hbar^2 k^2}{2m} - \mu$ and $\mu \gg \hbar\omega_D$: this considerably simplifies the mathematical treatment, in that the energy dependence of $N_0^{el}(\mu+\xi)$ can be neglected. However, in low-density superconductors

where $\mu \ll \hbar\omega_D$, we cannot employ the same approximations as for the high-density solution, hence we have to seek new solutions. Important examples of such systems are bulk $SrTiO_3$, superconducting thin films and interfaces like $LaAlO_3/SrTIO_3$, which we will study in the next chapter. In the next section, we describe the problem that we face when dealing with low-density BCS superconductors, and we set the framework for its solution; the latter is further developed in paper 2 at the end of this chapter.

3.3 BCS theory near the band edge

Section 3.2.2 led us to appreciate the role of dimensionality and electron density on pairing in the BCS model [82]. Among many other insights, these aspects of BCS theory have inspired the search for materials with improved performances: low-dimensional systems, with a different density of states and a modified pairing interaction with respect to the bulk, have been investigated as a possible way to boost superconductivity. However, reducing the dimensionality of BCS superconductors brings out another density-related issue: the carrier density in individual confined subbands can be so low that the standard approximation $\mu \gg \hbar\omega_D$ on the pairing window (3.22) cannot be performed, as we discussed in section 3.2.2. Bulk materials can also inherently be low-density superconductors, as is the case for doped $SrTiO_3$. Therefore, in the regime where the condition $\mu \gg \hbar\omega_D$ is not met, the form of the BCS solution for the critical properties changes. D. M. Eagles already produced pioneering work in this direction half a century ago [91–93], although this has often been overlooked until recently in calculations based on the BCS gap equation. In the following, we will mainly focus on the influence of low density on the pairing temperature T_c.

As mentioned in section 3.2.2, textbook solutions of BCS theory are provided at high density, such that $E_F \gg \hbar\omega_D$: this is the *adiabatic regime* of superconductivity. In this situation, phonon dynamics occurs on a much lower energy (i.e. velocity) scale than electron dynamics, so that electrons are fast enough to follow and adapt to lattice vibrations almost instantaneously [1, 2, 78]. For the BCS model, such situation is schematically depicted in figure 3.3 (a). This means that, in all the pairing window (3.22), we can take the density of states as to be constant and correspondent to the value at the chemical potential $N_0^{el}(\mu+\xi) \approx N_0^{el}(\mu)\ \forall\xi$. Then, linearization of equation (3.20a) and the further assumption $k_B T_c \ll \hbar\omega_D$ leads to the standard expression for the critical temperature $T_c = \frac{2e^\gamma}{\pi}\frac{\hbar\omega_D}{k_B}e^{-\frac{1}{\lambda_{BCS}}}$, where γ is the Euler constant and $\lambda_{BCS} = V_{BCS}N_0^{el}(\mu)$ is the BCS superconducting coupling constant.

The situation is different at low density, where the *antiadiabatic regime* $E_F \ll \hbar\omega_D$

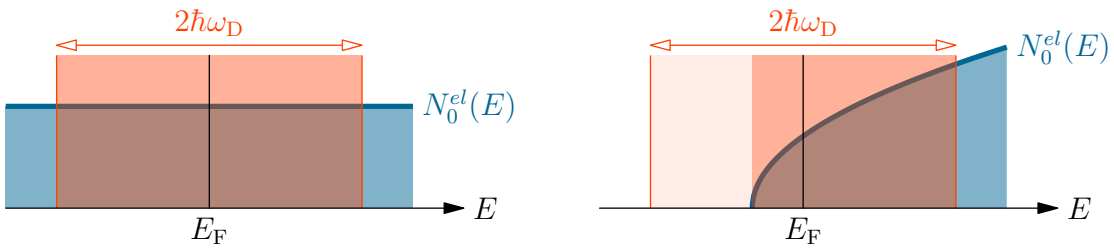

High-density regime

$$E_{\mathrm{F}} \gg \hbar\omega_{\mathrm{D}}, \quad N_0^{el}(E) \approx N_0^{el}(E_{\mathrm{F}})$$

$$T_c \approx \frac{2e^{\gamma}}{\pi k_{\mathrm{B}}} \hbar\omega_{\mathrm{D}} \exp\left(-\frac{1}{V_{BCS} N_0^{el}(E_{\mathrm{F}})}\right)$$

Low-density regime

$$E_{\mathrm{F}} < \hbar\omega_{\mathrm{D}}, \quad N_0^{el}(E) \neq \text{cste}$$

$$T_c = ?$$

Figure 3.3: Schematic representation of the high-density regime and the low-density regime for superconducting pairing. In the former, $\mu \gg \hbar\omega_D$ and the density of states $N_0^{el}(E)$ can be taken constant. In the latter, $E_F \lesssim \hbar\omega_D$, the interaction is cut by the band edge, and the details of $N_0^{el}(E)$ matter. This modifies the pairing temperature T_c with respect to the standard BCS expression.

is realized. In this case, phonon dynamics occurs at higher energies with respect to electron dynamics: lattice vibrations react almost instantaneously to electrons, so that the latter locally polarize the lattice. This means that the screening of phonon clouds surrounding electrons acts faster than electrons themselves, hence phonons dress electrons into polarons [76]. If these new composite objects interact with a residual weak attraction, in principle one can formulate the BCS model in terms of Cooper pairs of polarons [13]. Figure 3.3 (b) illustrates this low-density case in the context of the BCS model, with the chemical potential lying near the bottom of a band: as the chemical potential crosses the edge of a band, there is a regime where the dynamical cutoff of the pairing interaction is controlled by the band edge. This regime is realized in low-density electron liquids: for instance, in doped $SrTiO_3$ the carrier concentration is typically 10^{19} cm^{-3} and the carrier mass is in the range 2–4 electronic masses [94], corresponding to a Fermi temperature of 50–100 K, while the Debye temperature is 513 K [95]. Furthermore, as we see in figure 3.3 (b), the density of states has a non-negligible energy dependence near the band edge, from which it starts to rise from zero: there, the common approximation of taking a constant DOS over the full dynamical range fails to give a good estimate for T_c.

An exact solution of the gap equation (3.20a) requires one to take into account the energy dependence of the DOS, most importantly the cutoff at the band bottom, and the temperature dependence of the chemical potential μ, which is crucial at low-density n. Because n, T_c, and μ all approach zero simultaneously, it is essential to use the exact

relation $\mu(n, T_c)$ in order to capture the correct behavior of T_c for $n \to 0$: equations (3.20a) and (3.20b) have to be solved self-consistently. Furthermore, one should not assume weak coupling and/or assume that T_c is small with respect to μ and $\hbar\omega_D$.

We develop the mean-field approach to the band-edge effect in paper 2, focusing on T_c in the bulk, for one band in different dimensionalities and for multiband configurations. This theory yields a pairing temperature which is in general higher than the temperature of superconducting coherence, especially when the dimensionality and/or the density is low and superconducting fluctuations become important [96–98], as mentioned in section 3.2.2. We ignore these fluctuations and focus on the mean-field equations, refraining from making any approximation when solving them for T_c. This approach has many connections to mean-field studies of the BCS-BEC crossover, where the self-consistency of the temperature-dependent chemical potential at fixed density is required to solve the T_c equation or the gap equation at zero temperature [86, 99, 100]. As we will see, nontrivial consequences of low density are that T_c is a continuous non-analytical function of density and coupling near the band edge, both in 2D and in 3D; the chemical potential at T_c is negative in the low-density limit, in 2D for any coupling and in 3D for couplings larger than a critical value. Moreover, the universal BCS gap to T_c ratio is *not* obeyed in the low-density limit, so this ratio cannot be used to deduce T_c from the zero-temperature gap.

The results here derived will be applied in the next chapter to quantum-confined systems in quasi-2D geometry. There, discretized energy levels - or subbands - are produced along the confined direction, and the chemical potential can be tuned with respect to the quantized eigenstates by altering the confinement parameters, the density, or the pairing interaction: whenever μ crosses the bottom of a discretized subband, we are exactly in the band-edge regime here described, and therefore band-edge effects have to be considered to provide the correct mean-field solution for T_c. This situation models nanostructured BCS superconductors in the form of thin films or interface. However, as previously mentioned, the low-density cutoff of figure 3.3 is also met in bulk systems, with $SrTiO_3$ as one of the most remarkable examples. Due to its characteristics, we will focus on this material, either in the bulk or in quasi-2D geometry, when applying our calculations in the remainder of this thesis.

3.3.1 A low-density superconductor archetype: strontium titanate

Now that we have described the modifications to the pairing temperature when the BCS pairing window (3.22) is inferiorly cut by the band edge, it is interesting to look for

materials in which such conditions may be naturally realized, with the aim of testing our theoretical predictions. Hence, we seek a superconductor with a low carrier density in the conduction bands, which may also be grown in the form of thin films, or may be employed in the construction of artificial heterostructures. Strontium titanate ($SrTiO_3$, named STO hereafter) is an archetype material in this sense, since it has been addressed as "the most dilute superconductor" [101] due to the possibility of chemically dope its conduction bands with carrier densities as low as $n \approx 10^{17}\ cm^{-3}$, while still maintaining a Fermi-liquid character with a low-temperature superconducting ground state. By comparison, ordinary metals like Al, Au or Ag have much larger carrier densities of the order of $n \approx 10^{22}\ cm^{-3}$ [3]. Such properties of STO stem from its peculiar band structure and from many-body interactions, which dress electronic carriers and form polarons [102].

3.3.1.1 Band structure

STO belongs to the crystallographic family of ABO_3 perovskites, where A and B are two cations, the alcaline Sr and the transition metal Ti in the case of STO. In this system, chemical bonding between Sr and TiO_3 has predominantly ionic character [103], whereby the transition metal s electrons are transferred to the oxygen 2p orbitals. In stoichiometric form, STO is a band insulator with an energy gap of $E_g \approx 3.2eV$ between valence and conduction bands: the former are dominated by the 2p oxygen orbitals, while the latter are composed by the 3d levels of titanium, namely $\left\{d_{xy}, d_{xz}, d_{yz}, d_{3z^2-r^2}, d_{x^2-y^2}\right\}$. At high temperatures $T > 105\ K$, STO has a cubic crystal structure with undistorted oxygen octahedra surrounding Ti atoms: figure 3.4 illustrates this geometry in pseudocubic notation, where the Ti atom is at the center of the unit cell and Sr atoms sit on cube corners. The octahedral environment causes a crystal field that acts on the 3d orbitals of Ti, with the result of removing their degeneracy: a low-energy t_{2g} triplet, including the orbitals $\left\{d_{xy}, d_{xz}, d_{yz}\right\}$, is separated from an upper e_g doublet of orbitals $\left\{d_{3z^2-r^2}, d_{x^2-y^2}\right\}$ by an energy splitting $\Delta_{CF} \approx 2\ eV$ [104]. Hence, in the neighborhood of the Brillouin zone center (Γ point), the band structure can be effectively described by a tight-binding model within the t_{2g} manifold of the Ti-3d states, each of which has two directions of strong dispersion - e.g. k_x and k_y for d_{xy} - and one slowly-dispersing direction orthogonal to these - e.g. k_z for d_{xy}. Upon doping, this creates a Fermi surface consisting of three interpenetrating ellipsoids centered at the Γ point, with the ellipsoids oriented along the x, y, and z axes of the reciprocal lattice of the cubic crystal structure. This zone-center degeneracy is lifted by the spin-orbit interaction, which mixes the character of the orbitals in the neighborhood of the Γ point. In the cubic phase, this results in two degenerate spin-orbit doublets at the lowest energy and an additional doublet

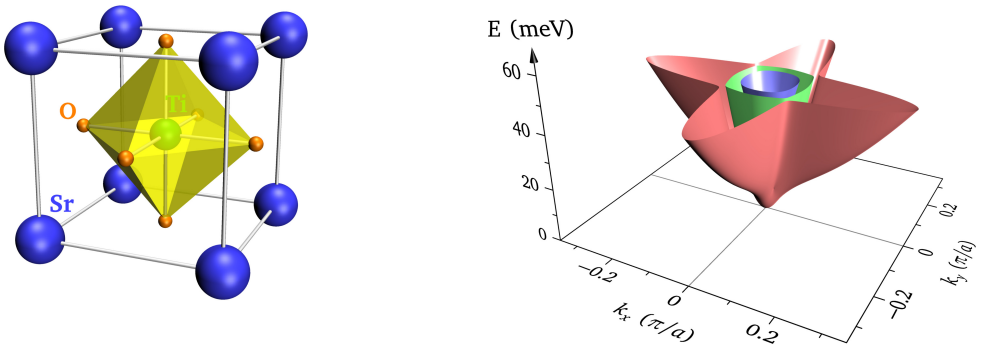

Figure 3.4: Left: the cubic crystal structure of STO in pseudocubic representation. The titanium atom (green) lies at the center of the cell, surrounded by oxygen atoms (orange) in octahedral configuration; strontium atoms (blue) sit at the corners of the unit cell. Right: band energies $E\,[meV]$ of tetragonal STO according to the tight-binding model of reference [13], as a function of k_x and k_y in units of the lattice constant a, for $k_z = 0$. The first, second and third band that are progressively populated with doping are shown in red, green and blue, respectively.

at $\Delta_{SO} = 29.2\ meV$ higher energy [13, 105, 106]. In addition to this, at temperatures $T < 105\ K$ STO undergoes a tetragonal distortion, whereby adjacent oxygen octahedra rotate around the c axis: this removes the degeneracy between the two low-energy doublets by an energy splitting $\Delta_T \approx 3\ meV$ [106, 107]. Including the spin-orbit splitting Δ_{SO} and the tetragonal distortion energy Δ_T into the tight-binding description of the t_{2g} conduction bands, we obtain an effective low-energy hamiltonian for the conduction bands of STO valid at low temperatures [13]. The resulting band structure, obtained from diagonalization of the effective hamiltonian [13] is depicted in the right panel of figure 3.4, as a function of $\left(k_x, k_y\right)$ and for $k_z = 0$. Different colors identify each of the three undegenerate bands of the low-temperature phase.

The lowest conduction band, colored in red in figure 3.4, is a "heavy electron" band consisting of states having angular momentum $m_j = \pm\frac{3}{2}(1-\delta)$, where $\delta = \left(\frac{\Delta_T}{\Delta_{SO}}\right)^2$. While the band disperses upward rather sharply at the Γ point, it is deflected downward at $\left|\vec{k}\right| \approx 0.1/a$ for momentum along the Ti-O bond [13], due to band anticrossing. Hence, the parabolic approximation for this band works well only for momenta below aforementioned downward-deflection value, while above such momentum the Fermi surface of this band elongates into ellipsoid shape along the principal axes, with a starfish shape. The second and third bands, colored in blue and green in figure 3.4, are "light electron" bands, the dispersion of which is to a good approximation an isotropic parabola [13].

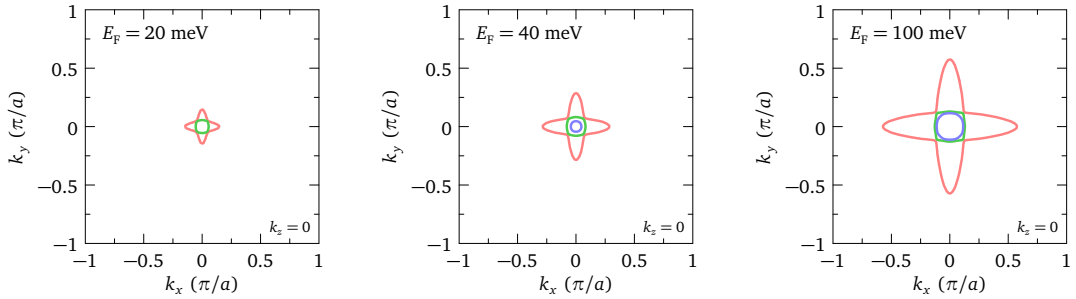

Figure 3.5: Fermi surfaces of tetragonal STO at $T = 0$ according to the tight-binding model of reference [13] at $k_z = 0$, for a Fermi level $E_F = \{20,\ 40,\ 100\}\ meV$. The color code for the bands is the same as in figure 3.4.

3.3.1.2 Doping and Fermi liquid physics

Chemical doping allows one to populate the low-energy t_{2g} manifold of the conduction band: electrons can be introduced by substitution of Sr^{2+} by La^{3+}, or Ti^{4+} by Nb^{5+}. Alternatively, in reduced samples oxygen vacancies produce the same effect, giving $SrTiO_{3-\delta}$ [108]; this can be achieved by reducing STO in oxygen atmosphere at different temperatures [94]. These methods permit to vary the doped carriers concentration in an extensive range $n \approx \left(10^{17} \div 10^{21}\right)\ cm^{-3}$ spanning more than four orders of magnitude. Quantum oscillations studies [60, 94] identified the critical dopings $n_{c1} \approx 7\ 10^{18}\ cm^{-3}$ and $n_{c2} \approx 4.4\ 10^{19}\ cm^{-3}$ at which the second and third t_{2g} bands start being populated, in agreement with band structure calculations and optical measurements [13]: this highlights the multiband character of conduction in STO. Another experimental indication of n_{c2} comes form the observation by Binnig et al. of an additional superconducting gap of smaller size than the main gap for doping concentrations in excess of $5 \cdot 10^{19}\ cm^3$, using tunneling spectroscopy [109]; however, recent high-resolution tunneling spectroscopy [110] and microwave spectroscopy [111] studies observed a single BCS-like superconducting gap in doped STO. Figure 3.5 illustrates the Fermi surface components of STO at $T = 0$, in the $\left(k_x, k_y\right)$ plane with $k_z = 0$, for three values of the Fermi level $E_F = \{20,\ 40,\ 100\}\ meV$. We see that, for $E_F = 20\ meV$, the Fermi surface has two components corresponding to the lowest two bands; further raising the Fermi energy, we start populating the third band as well.

The metallic state of STO shows quadratic temperature dependence of the resistivity $\rho_{el} \propto T^2$ down to the lowest dopings and temperatures [60, 94], and optical data confirms a quadratic frequency dependence of the optical conductivity [102]: as we have seen in chapters 1 and 2 - see specifically equation (2.29) and appendix D - this behaviour indicates a Fermi liquid state. Surprisingly, this Fermi liquid phase persists to the lowest carrier

densities and temperatures, when only the first t_{2g} band is populated, interband scattering could not produce momentum relaxation [13], and the phonon contribution becomes negligible as well; also, Landau quasiparticle scattering alone cannot relax momentum. Hence, as we observed in section 2.4, the precise mechanism at the origin of the Fermi liquid behaviour of STO remains an unresolved conundrum.

3.3.1.3 Electron-phonon coupling and superconductivity

As we have seen in chapter 1, Fermi liquid physics can be understood in terms of Landau electron-hole quasiparticles that are subjected to short-ranged weak interactions; in Landau's hypothesis, this is the net result of interactions dressing bare particles. This allows one to reformulate the problem of the interacting electron liquid in terms of nearly-independent quasielectrons. Interactions between quasielectrons in metals can have intrinsic electronic origin, like Coulomb and exchange processes, and can also stem from the solid-state environment hosting the electron liquid. One of the most prominent sources of interaction in doped STO is provided by the crystalline lattice, which dresses electrons through electron-phonon interaction. Angle-resolved photoemission spectroscopy (ARPES) experiments on Nb-doped STO found evidence for coupling involving longitudinal optical phonons, for doping concentrations $x = \{1,\ 5\}\,\%$ [112], considering only long-range electrostatic interactions; the analysis based on the polar Froelich model extracted three frequencies $\omega_{ph} = \{22,\ 58,\ 99\}\ meV$ for phonon modes at the Γ point, characterized by the electron-phonon coupling constants $\alpha_{e-ph} = \{0.018,\ 0.945,\ 3.090\}$ respectively. Infrared optical spectroscopy on Nb-STO samples at dopings $x = \{0.1,\ 0.2,\ 0.9,\ 2\}\,\%$ [102] showed three transverse phonon absorption peaks, the first of which moving much more in frequency as a function of temperature and doping; at $T = 300\ K$, the reported peak frequencies are $\omega_{ph} = \{11,\ 21.8,\ 67.6\}\ meV$, the first of which measured in the $x = 0.1\%$ sample and decreasing with doping. The associated electron-phonon coupling constants evaluated from the single-polaron model are in the range $3 < \alpha_{e-ph} < 4$. The first temperature- and doping-dependent infrared peak was attributed to the low-energy "ferroelectric" soft phonon, the softening of which causes the dramatic increase of the dielectric constant of STO at low temperatures up to values $\epsilon \approx 10^5$ [113–115]. Indeed, this phenomenon brings STO on the verge of a ferroelectric instability without becoming ferroelectric by itself, so that STO is classified as a *quantum paraelectric*; ferroelectricity is realized at low temperatures by the means of ^{18}O isotope substitution [116], Ca doping [117], electric field effect [118, 119], or mechanical strain [120]. The interplay between ferroelectricity and phonon modes highlights the role of electron-phonon interaction in the physics of STO.

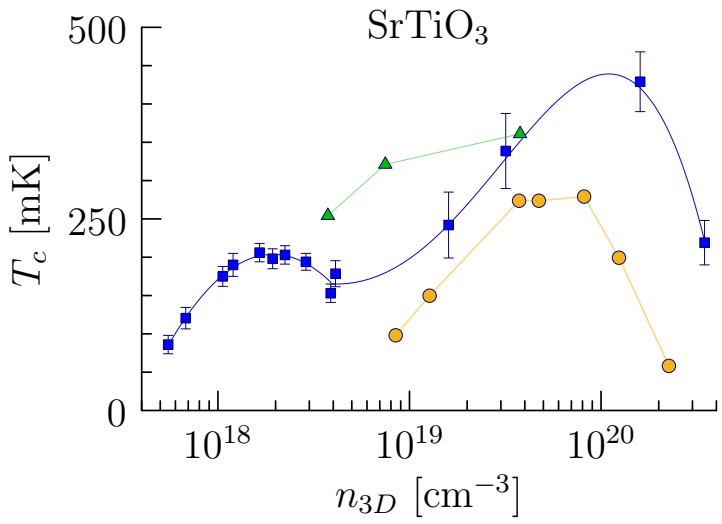

Figure 3.6: Critical temperature T_c $[mK]$ of bulk doped $SrTiO_3$ as a function of 3-dimensional carrier density n_{3D} $\left[cm^{-3}\right]$. Blue square symbols show T_c for oxygen-reduced (first dome) and Nb-doped (second dome) crystals from reference [94]; the blue solid line is a continuous interpolation of T_c [4]. Gold circles correspond to the estimated value of Tc at 50 % of the resistive transition for oxygen-reduced crystals and for Nb-doped crystals respectively, from reference [126]. Green triangles represent T_c estimated at 50 % of the resistive transition for Nb-doped $SrTiO_3$ single crystals measured at the university of Geneva [125, 127].

The main phonons involved in the screening of Coulomb repulsion are the optical ones [13, 102], with the important consequence that their energy exceeds the Fermi energy for the lowest doping levels. In this condition we are effectively into the antiadiabatic regime, discussed in section 3.3 in the context of superconductivity: in particle representation phonons move faster than electrons beacuse the former have higher frequency, and one can regard the electron and phonon ensemble as itinerant electronic quasiparticles which are dressed by the phonon cloud, leaving residual interactions between such composite objects. These objects are called polarons after Landau [121] (for recent reviews, see e.g. [76, 122]). The polaron-polaron interaction can be mediated by optical phonons [13], and in that case the interaction is effectively nonretarded. Indeed, polaronic effects from electron-phonon coupling were observed in the bulk [13, 112] and at the surface of STO [123], as well as for LAO/STO [124]. The effective electron-electron interactions can also lead to the formation of Cooper pairs by overscreening of the Coulomb repulsion, in the same spirit as for our discussion in section 3.2.2. Indeed, doped bulk STO has a superconducting ground state [13, 60, 94, 125] with a dome-shaped critical temperature as a function of carrier density. Various datasets from transport experiments show a finite T_c in both Nb-doped and oxygen-reduced samples, with some examples collected in figure 3.6.

In particular, the transport measurements of reference [94] showed the presence of

a double T_c dome spanning three orders of magnitude in doping, whereby one, two and eventually three bands compose the Fermi surface by increasing the carrier density. The critical dopings n_{c1} and n_{c2} for two- and three-band conduction were experimentally inferred from quantum oscillation frequencies, and found in good agreement with the band structure calculations shown in figures 3.4 and 3.5. This correspondence between the theoretical band structure and the transport measurements led us to focus on the dataset [94] for the analysis of bulk STO in section 4.4. How many bands contribute to superconductivity in the multiband doping regime, and what are the respective coupling constants, are still controversial questions. Tunneling spectroscopy reported a measurement of two superconducting gaps in doped STO [109], pointing towards at least two bands contributing to superconducting pairing.

Numerous proposals for the driving mechanism of Cooper pairing in strontium titanate have been advanced during the last 50 years, with many of them focusing on the previously-described electron-phonon coupling. We mention some of the highlights in this field in the following summary, which remains far from being exhaustive. Eagles considered a model of effective electron-electron interaction via intervalley phonons of energy $\hbar\omega_{ph} = 49.7\ meV$ modified by intervalley Coulomb repulsion, where "intervalley" refers to processes connecting band valleys with minima lying at different points of the Brillouin zone [92]. Soon later, Eagles analyzed the effective masses of carriers in Zr-doped STO as a function of doping, and their connection to superconductivity, in terms of a crossover from large to small polarons [128]. Appel focused on the zone-boundary quasi-acoustic soft phonon associated with the low-temperature tetragonal distortion, and considered this phonon as the source of pairing [129]. Zinamon elaborated on Appel's idea by considering small polarons as the relevant charge carriers [130]. Takada identified plasmons [131,132] and the low-frequency "ferroelectric" soft phonon [113] as concomitant pairing sources. Polaron formation, and its connections to the Fermi-liquid character and superconducting ground state of STO has been investigated both experimentally [13, 102, 133] and theoretically [134].The relative contributions of acoustic and optical phonon branches of STO to superconducting pairing were considered within a dielectric function approach [135]. Quantum critical fluctuations due to the STO "ferroelectric" soft phonon mode were also proposed to explain superconductivity and its connection to quantum paraelectricity [115]. Recent transport experiments combined with optical spectroscopy [127] reported the striking result of a *negative* isotope coefficient for STO, whereby T_c *increases* with ^{18}O isotope substitution in oxygen-doped samples; this result deviates from the standard BCS result $\alpha_O = -\frac{\partial \ln T_c}{\partial \ln M} = \frac{1}{2}$, with M mass of lattice ions [78,82], and has been interpreted in the context of the polaronic model of pairing [127]. All aforementioned proposals underline the interplay of electronic

and lattice degrees of freedom in STO, from which the superconducting domes emerge as a function of doping.

3.3.1.4 Minimal 2-band model for superconducting doped STO

Given the variety of alternative proposals regarding the microscopic pairing mechanism in STO, we now choose to follow an alternative approach which refrains from relying on specific microscopic pairing models. We take a step back and we describe phenomenologically the pairing interaction by fitting the $T_c(n_{3D})$ transport data of reference [94]. In order to estimate the relative contribution of the first two conduction bands to Cooper pairing, we can employ the effective two-band model of section 4.4, which uses the band masses $m_1 = 4m$ and $m_2 = m$ in parabolic approximation, with m free electron mass. The band bottom energies are split by $\Delta E = 2.4\ meV$ [4]. The values of the band masses and splitting are taken such that the resulting density of states in parabolic approximation agrees at best with the one stemming from the tight-binding model [13], and they are further multiplied by a factor 2 due to electron-phonon coupling renormalization [13, 133, 134]. We assume that the pairing interaction $V = V(n_{3D})$, depending on 3D density n_{3D}, is the same for the two bands: physically, this means that the two bands share a common pairing mechanism. The non-parabolicity and anisotropy of the bands are both neglected in this minimal band structure: this approximation is most severe for the first heavy band (red band in figure 3.5), which is strongly anisotropic and non-parabolic for large momentum. Focusing on the low-doping range, we neglect the contribution of the third band to the total density and to superconductivity; however, from the tight-binding model aforementioned band starts to be populated at $n_{c2} \approx 4.4\ 10^{19}\ cm^{-3}$ [13] and may give additional contributions to Cooper pairing. We employ a BCS-like interaction $V(n_{3D})$, that is energy-independent up to a cutoff $\hbar\omega_D = 44.2\ meV$, the latter corresponding to the Debye energy of STO [95]. This way, we fit the theoretical value of $T_c(n_{3D})$ to the experimental data [94], and we extract the doping-dependent value $V(n_{3D})$ of the interaction. From the latter, we calculate the values of the respective coupling constants $\lambda_{11}(\mu)$ and $\lambda_{22}(\mu)$, evaluated at the self-consistent chemical potential μ. The calculation takes into account the proximity to the band edges as discussed in Sec. 3.3. The result is plotted in figure 3.7, at dopings corresponding to the dataset of reference [94], reported in figure 3.6.

The gray points show the adimensional interaction $\frac{V(n_{3D})n_1}{\hbar\omega_D}$, where $n_1 = 2\left(\frac{m\omega_D}{2\pi\hbar}\right)^{\frac{3}{2}}$. The blue and red points are the values of $\lambda_{11}(\mu)$ and $\lambda_{22}(\mu)$, for the first and second band respectively. The decreasing tendency of the interaction $V(n_{3D})$ with n_{3D} is consistent with the analysis on optical [13] and transport data [94], and may reflect the behaviour

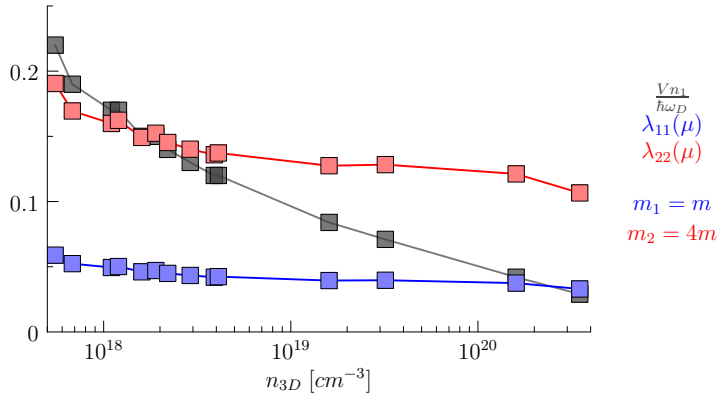

Figure 3.7: Superconducting coupling constants $\lambda_{11}(\mu)$ and $\lambda_{22}(\mu)$ at the chemical potential μ for a two-band BCS model, as a function of 3D carrier density n_{3D}, at the experimental dopings of reference [94]. Blue squares correspond to the light band of mass $m_1 = m$, while red squares refer to the heavy band of mass $m_2 = 4m$, with m free electron mass. The correspondent fitted value of the interaction $\frac{Vn_1}{\hbar\omega_D}$, where $n_1 = 2\left(\frac{m\omega_D}{2\pi\hbar}\right)^{\frac{3}{2}}$, is shown in gray in the background, with $\hbar\omega_D = 44.2\ meV$ Debye energy of STO [95].

of the electron-phonon coupling constant extracted from ARPES measurements on the STO surface quasi-2D electron liquid [136]. The increased dielectric screening of electron-phonon interaction with increasing n_{3D}, which reduces the net polaron-polaron residual interaction, can qualitatively explain this decreasing evolution with density [13, 137]. Moreover, from figure 3.7 we see that the heavy band has much larger coupling than the light band, owing to the larger mass of the former with respect to the latter. Hence, we expect heavy bands to dominate Cooper pairing and to be mainly responsible for superconductivity in strontium titanate, in accordance with the observation of a larger and a smaller gap in tunneling spectroscopy [109]. A phenomenological fit of the pairing interaction, like the one in figure 3.7, cannot tell us the microscopic origin of Cooper pair formation, which ultimately remains an open question. Nevertheless, this parabolic band structure and BCS pairing interaction provides us with a minimal BCS model to describe superconductivity in bulk doped STO. In particular, this model is a simple tool to investigate what happens to the band structure and the pairing interaction when we lower the system dimensionality, by confining one or more spatial directions to microscopic scales: in the next chapter 4, we will see that confinement causes quantization effects for both electron energy levels and the pairing interaction, which deeply affect superconducting properties like the critical temperature. We will apply the quasi-2D model of a superconductor in a square quantum well to the LAO/STO interface (section 4.4) in chapter 4, and we will compare the results to the ones in the bulk.

3.4 Conclusions and perspectives

The critical temperature of a BCS superconductor is modified in low-density systems, where the Fermi energy is lower than the pairing cutoff energy, so that the pairing energy window is inferiorly cut by a band edge. In such conditions, T_c is a continuous non-analytical function of density and coupling near the band edge, both in two and three dimensions. This also affects the evolution of the chemical potential at T_c with density, as well as the ratio of the zero-temperature gap to T_c, which deviates from its universal high-density value. These results show that the effects of band edges on the superconducting properties have to be taken into account in the description of T_c in low-density superconductors, such as bulk doped strontium titanate. Knowing the band structure of the material, this allows one to extract a minimal BCS model for the doping dependence of the pairing interaction from the evolution of T_c with density, like we did for doped STO in section 3.3.1. Further work could be directed to study the zero-temperature gap at any density in different dimensions, and evaluate the gap to T_c ratio at any density in 3D, analogously to the 2D case. Furthermore, one could analyze how fluctuations of the order parameter can modify the critical temperature in the regime where the band edge cuts the pairing window, particularly for two-dimensional systems where a pure BCS solution is prevented, in order to evaluate the accuracy of the mean-field solution as a function of density.

PHYSICAL REVIEW B **94**, 024511 (2016)

BCS superconductivity near the band edge: Exact results for one and several bands

D. Valentinis, D. van der Marel, and C. Berthod*

Department of Quantum Matter Physics (DQMP), University of Geneva, 24 Quai Ernest-Ansermet, CH-1211 Geneva 4, Switzerland

(Received 18 January 2016; published 14 July 2016)

We revisit the problem of a BCS superconductor in the regime where the Fermi energy is smaller than the Debye energy. This regime is relevant for low-density superconductors such as $SrTiO_3$ that are not in the BEC limit, as well as in the problem of "shape resonances" associated with the confinement of a three-dimensional superconductor. While the problem is not new, exact results were lacking in the low-density limit. In two dimensions, we find that the initial rise of the pairing temperature T_c at low density n is nonanalytic and faster than any power of n. In three dimensions, we also find that T_c is nonanalytic, but starts with *zero* slope at weak coupling and infinite slope at strong coupling. Self-consistent treatment of the chemical potential and energy dependence of the density of states are crucial ingredients to obtain these results. We also present exact results for multiband systems and confirm our analytical expressions by numerical simulations.

DOI: 10.1103/PhysRevB.94.024511

I. INTRODUCTION

The Bardeen-Cooper-Schrieffer (BCS) theory [1] remains the only strong microscopic foundation to support our understanding of the fascinating phenomenon of superconductivity. Among many other insights, the theory provides a simple expression for the critical temperature T_c, which continues to inspire the search for materials with improved performances. In particular, it is expected that superconductivity is favored by a low dimensionality due to enhanced density of states (DOS) at the Fermi level [2]. For three-dimensional (3D) materials, an early proposal to use quantum confinement in a thin film [3] has received sustained attention until recently [4]. The confinement-induced two-dimensional (2D) subbands produce discontinuities in the DOS and abrupt changes of T_c as a function of film thickness have been routinely predicted.

The purpose of this study is to explore some consequences of an aspect of the problem, considered by Eagles half a century ago [2,5], but often overlooked in recent calculations based on the BCS gap equation. As the Fermi energy crosses the edge of a band, there is a regime where the dynamical cutoff of the pairing interaction is controlled by the band edge (Fig. 1). This regime is realized in low-density electron gases, when the Fermi energy is smaller than the dynamical range of the interaction. In doped $SrTiO_3$, for instance, the carrier concentration is typically 10^{19}cm^{-3} and the carrier mass is in the range 2–4 electronic masses [6], corresponding to a Fermi temperature of 50–100 K, while the Debye temperature is 513 K [7]. In this situation, the common approximation of taking a constant DOS over the full dynamical range fails to give a good estimate for T_c. The near-band edge regime is also relevant in the quasi-2D problem of shape resonances, since each resonance is due to the Fermi energy crossing a subband edge [8–10]. The pairing in that subband, as well as the intersubband pairing involving that subband, are dominated by the band edge. A synthesis of these two cases is realized in the quasi-2D *and* low-density electron gas at the $LaAlO_3/SrTiO_3$ interface [11–13]. In the present paper we focus on the band-edge effect on T_c in the bulk, emphasizing the generic behaviors in the simple case of an electron gas with parabolic dispersion and a local attraction. We recover the expressions of Eagles [2] in the weak-coupling limit. In the low-density regime, we provide exact relations as a function of the density, which are valid at arbitrary coupling. We also give exact numerical results in 2D and 3D, for one-band and multiband systems. The implications for the problem of quasi-2D shape resonances and the case of $LaAlO_3/SrTiO_3$, will be reported in separate publications.

Our starting point is the mean-field theory for a momentum-independent pairing interaction acting in a limited energy range around the Fermi surface. This theory yields a pairing temperature which is in general higher than the temperature of superconducting coherence, especially when the dimensionality and/or the density is low and superconducting fluctuations become important [14–16]. We ignore these fluctuations and focus on the mean-field equations, refraining from making any approximation when solving them for T_c. This approach is similar to previous mean-field studies of the BCS-BEC crossover where the renormalized chemical potential is solved self-consistently together with the T_c equation or the gap equation at zero temperature [17,18].

An exact solution of the gap equation requires one to take into account the energy dependence of the DOS, most importantly the cutoff at the band bottom, and the temperature dependence of the chemical potential μ, which is crucial at low-density n. Because n, T_c, and μ all approach zero simultaneously, it is essential to use the exact relation $\mu(n,T_c)$ in order to capture the correct behavior of T_c for $n \to 0$. Furthermore, one should not assume weak coupling and/or assume that T_c is small with respect to the Fermi energy and the cutoff for pairing. As a matter of fact, analytical results in this problem are rare. In Ref. [19], rigorous bounds for T_c were obtained for a general interaction. These results are limited to weak coupling and to a positive chemical potential. We will see that the chemical potential at T_c is negative in the low-density limit in 2D for any coupling and in 3D for couplings larger than a critical value. Exact results have also been reported for the zero-temperature gap in 2D [20]. However, since the universal BCS gap to T_c ratio is *not* obeyed in the low-density limit, these results cannot be used to deduce T_c.

*christophe.berthod@unige.ch

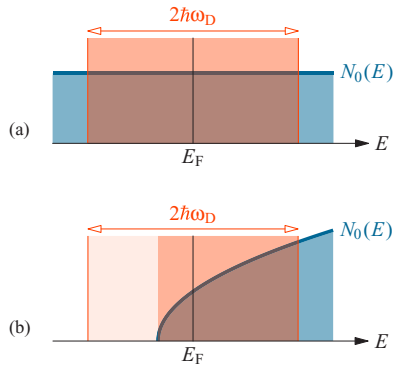

FIG. 1. Schematic representation of (a) the high-density regime and (b) the low-density regime for superconducting pairing. In the former, $E_F \gg \hbar\omega_D$ and the density of states $N_0(E)$ can be taken constant. In the latter, $E_F \lesssim \hbar\omega_D$, the interaction is cut by the band edge, and the details of $N_0(E)$ matter.

This paper is the first in a series and it provides the mathematical foundations for subsequent studies dedicated to shape resonances in thin films and to the $LaAlO_3/SrTiO_3$ interface. It is organized as follows. In Sec. II we recall the basic coupled equations giving n and T_c and we write them in a dimensionless form, for one and several parabolic bands. In Sec. III we present our analytical and numerical results for one band in 2D and 3D, and in Sec. IV we briefly discuss multiband effects.

II. BCS T_c EQUATION FOR MULTIBAND SYSTEMS

A. Dimensionless equations for the pairing temperature

We consider a multiband metal with a local BCS pairing interaction $-V_{\alpha\beta}$ acting between electrons of opposite momenta and spins in bands α and β [21]. We assume that Cooper pairing occurs only for two electrons in the same band, leading below the pairing temperature T_c to an order parameter Δ_α in each band. This includes the possibility of a "proximity" induced gap Δ_β in a band that otherwise feels no pairing potential ($V_{\beta\beta} = 0$), via the nonzero interband interactions $V_{\alpha\beta}$. The mean-field gap equation for Δ_α is

$$\Delta_\alpha = \sum_\beta V_{\alpha\beta}\Delta_\beta \int_{-\hbar\omega_D}^{\hbar\omega_D} d\xi\, N_{0\beta}(\mu+\xi)\, \frac{\tanh\left(\frac{\sqrt{\xi^2+\Delta_\beta^2}}{2k_BT}\right)}{2\sqrt{\xi^2+\Delta_\beta^2}}. \tag{1a}$$

The pairing interaction acts in a range $\pm\hbar\omega_D$ around the chemical potential μ. Although the notation $\hbar\omega_D$ is used here, we envision the problem in its generality and our results do not require phonon-mediated pairing, but apply to any local interaction with a dynamical cutoff. In a lattice version, for instance, the cutoff could be the bandwidth. $N_{0\beta}(E)$ is the DOS per spin and per unit volume for the band β. It is defined on an absolute energy scale, such that $N_{0\beta}(\mu)$ is the DOS at the chemical potential μ, which is common to all bands. The chemical potential must be adjusted to fix the density according to

$$n = 2\int_{-\infty}^{\infty} dE\, f(E)\, N(E). \tag{1b}$$

Here, $f(E) = [e^{(E-\mu)/k_BT}+1]^{-1}$ is the Fermi distribution function and $N(E)$ is the total BCS density of states (per spin) resulting from the opening of the superconducting gaps at the chemical potential in each band.

For the calculation of T_c, it is sufficient to consider the two equations in the limit of vanishing order parameters. For $T = T_c$ we have

$$\Delta_\alpha = \sum_\beta V_{\alpha\beta}\Delta_\beta \int_{-\hbar\omega_D}^{\hbar\omega_D} dE\, N_{0\beta}(\mu+E)\, \frac{\tanh\left(\frac{E}{2k_BT_c}\right)}{2E}, \tag{2a}$$

$$n = 2\int_{-\infty}^{\infty} dE\, f(E) \sum_\beta N_{0\beta}(E). \tag{2b}$$

We now insert explicit formulas for the energy-dependent densities of states and the density and we rewrite the equations (2) in a dimensionless form, which is more convenient for analytical and numerical treatments. The densities of states for a parabolic band in dimensions $d = 2$ and $d = 3$ are given by

$$N_{0\beta}(E) = (d-1)\pi\left(\frac{m_\beta}{2\pi^2\hbar^2}\right)^{\frac{d}{2}} \theta(E-E_{0\beta})(E-E_{0\beta})^{\frac{d}{2}-1}, \tag{3}$$

where m_β is the band mass, $E_{0\beta}$ is the energy of the band minimum, and θ is the Heaviside function. This definition ensures that $N_{0\beta}(\mu)$ is the DOS evaluated at the chemical potential μ common to all bands, consistently with Eq. (1a). The relation between density, chemical potential, and temperature for a parabolic band in arbitrary dimension d is

$$n = -2\left(\frac{mk_BT}{2\pi\hbar^2}\right)^{\frac{d}{2}} \mathrm{Li}_{\frac{d}{2}}\left(-e^{\frac{\mu-E_0}{k_BT}}\right), \tag{4}$$

where $\mathrm{Li}_p(x)$ is the polylogarithm given by the series expansion $\mathrm{Li}_p(x) = \sum_{q=1}^{\infty} x^q/q^p$. This function has the sign of its argument and reduces to a usual logarithm in two dimensions ($p = 1$): $\mathrm{Li}_1(x) = -\ln(1-x)$. We provide a brief derivation of Eq. (4) in Appendix A for the interested reader.

We measure all energies in units of $\hbar\omega_D$, express the density in units of $2[m\omega_D/(2\pi\hbar)]^{d/2}$ where m is a reference mass, and we distinguish the dimensionless variables with tildes, e.g.,

$$\tilde{T}_c = \frac{k_BT_c}{\hbar\omega_D}, \quad \tilde{\mu} = \frac{\mu}{\hbar\omega_D}, \quad \tilde{n} = \frac{n}{2[m\omega_D/(2\pi\hbar)]^{d/2}}, \quad \text{etc.}$$

The coupled equations (2) for T_c become

$$\Delta_\alpha = \sum_\beta \Delta_\beta \bar{\lambda}_{\alpha\beta}\, \psi_d(1+\tilde{\mu}-\tilde{E}_{0\beta}, \tilde{T}_c), \tag{5a}$$

$$\tilde{n} = -\tilde{T}_c^{\frac{d}{2}} \sum_\beta \left(\frac{m_\beta}{m}\right)^{\frac{d}{2}} \mathrm{Li}_{\frac{d}{2}}\left(-e^{\frac{\tilde{\mu}-\tilde{E}_{0\beta}}{\tilde{T}_c}}\right). \tag{5b}$$

We have introduced the dimensionless function,

$$\psi_d(a,b) = \theta(a) \int_{1-\min(a,2)}^{1} dx\, (x+a-1)^{\frac{d}{2}-1} \frac{\tanh\left(\frac{x}{2b}\right)}{2x}, \tag{6}$$

as well as the coupling constants,

$$\bar{\lambda}_{\alpha\beta} = V_{\alpha\beta}(d-1)\pi \left(\frac{m_\beta}{2\pi^2\hbar^2}\right)^{\frac{d}{2}} (\hbar\omega_D)^{\frac{d}{2}-1}. \tag{7}$$

We use a bar to recall that these coupling constants are not evaluated at the Fermi energy like in the common practice, but at an energy $\hbar\omega_D$ above the bottom of each band: $\bar{\lambda}_{\alpha\beta} = V_{\alpha\beta} N_{0\beta}(E_{0\beta} + \hbar\omega_D)$. This choice is natural and leads to the simplest equations. The usual definition $\lambda = V N_0(\mu)$ poses problems when μ lies below the band bottom and more generally because μ is a function of interaction strength and temperature.

In an N-band system, the relations (5) provide $N+1$ equations for the $N+1$ unknowns, which are $\tilde{T}_c$, $\tilde{\mu}$, and the $N-1$ ratios Δ_β/Δ_1. We can assume that $\Delta_1 \neq 0$ without loss of generality, because there is at least one nonzero gap parameter at T_c and we are free to number the bands such that Δ_1 is this one. We now eliminate the $N-1$ gap ratios and reduce the problem to a pair of equations for $\tilde{T}_c$ and $\tilde{\mu}$. With the new definitions $r_\beta = \Delta_\beta/\Delta_1$ and

$$\Lambda_{\alpha\beta}(\tilde{\mu},\tilde{T}_c) = \bar{\lambda}_{\alpha\beta}\psi_d(1+\tilde{\mu}-\tilde{E}_{0\beta},\tilde{T}_c), \tag{8}$$

the set of N equations (5a) becomes the eigenvalue problem $\Lambda \boldsymbol{r} = \boldsymbol{r}$ with $\boldsymbol{r} = (1, r_2, \ldots, r_N)$. This means that, when evaluated at a value of $\tilde{T}_c$ solving Eq. (5a), the matrix Λ has at least one unit eigenvalue. In other words, $\tilde{T}_c$ corresponds to the largest temperature that satisfies the characteristic equation $\det(\mathbb{1} - \Lambda) = 0$. The two coupled dimensionless equations giving n and T_c for N bands are therefore

$$0 = \det[\mathbb{1} - \Lambda(\tilde{\mu},\tilde{T}_c)], \tag{9a}$$

$$\tilde{n} = -\tilde{T}_c^{\frac{d}{2}} \sum_{\alpha=1}^{N} \left(\frac{m_\alpha}{m}\right)^{\frac{d}{2}} \mathrm{Li}_{\frac{d}{2}}\left(-e^{\frac{\tilde{\mu}-\tilde{E}_{0\alpha}}{\tilde{T}_c}}\right). \tag{9b}$$

The existence of a nontrivial solution to Eq. (5a) clearly implies Eq. (9a). The converse is also true: The vanishing of the determinant in Eq. (9a) is sufficient to enforce that the matrix Λ has one unit eigenvalue, which provides a solution to Eq. (5a). The equations (9) have the same structure in 2D and 3D, the quantitative differences stemming mostly from different functions $\psi_d(a,b)$. In the next paragraph we discuss the properties of these functions, which we shall use in the following sections to derive analytical results.

B. Properties of the functions $\psi_d(a,b)$

The functions $\psi_d(a,b)$ are displayed [22] in Fig. 2. The strongest structure develops around $a = 1$, which corresponds physically to having the chemical potential at the bottom of one band. We are mostly interested in the behavior for $b \ll 1$, which is explored in the regime $k_B T_c \ll \hbar\omega_D$ and particularly in the limit $b \to 0$, which is relevant when the density approaches zero. If $a < 1$, $\psi_d(a,b)$ is finite for $b = 0$.

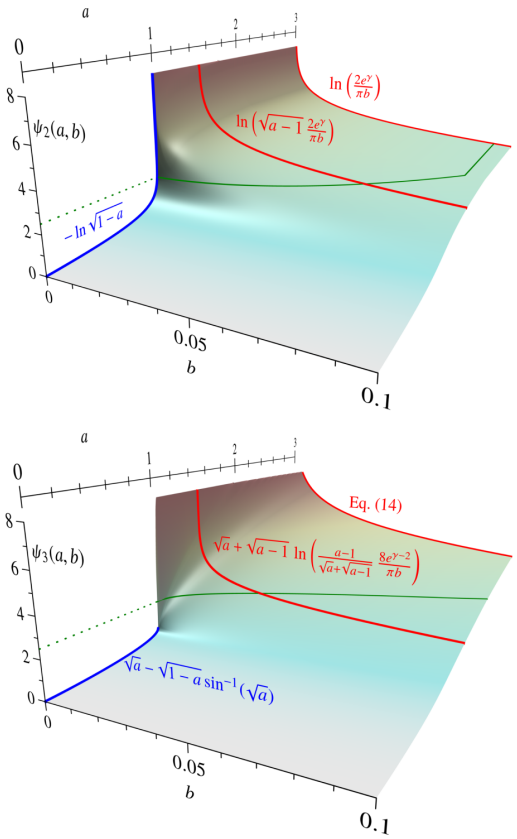

FIG. 2. Representation of the functions $\psi_d(a,b)$ defined in Eq. (6) for dimensions $d = 2$ (top) and $d = 3$ (bottom). Physically, the a axis corresponds to varying μ around the band bottom ($a = 1$) and the b axis is proportional to T_c. The blue lines show the behavior for $b = 0$ and $a < 1$. The two red lines in each graph show the asymptotic b dependencies for $1 < a < 2$ and $a > 2$, respectively. The green lines show cuts at the value $\psi_d(a,b) = 2.5$, which correspond to the path followed in the (a,b) plane by the solution of the BCS equations (9) for one band and for $\bar{\lambda} = 0.4$.

The limiting value is given by

$$\begin{aligned}\psi_d(0 < a < 1, b \to 0) &= \int_{\frac{1-a}{b}}^{\frac{1}{b}} dx\, \frac{(bx+a-1)^{\frac{d}{2}-1}}{2x} \\ &= \begin{cases} -\ln\sqrt{1-a} & (d=2) \\ \sqrt{a} - \sqrt{1-a}\,\sin^{-1}(\sqrt{a}) & (d=3). \end{cases}\end{aligned} \tag{10}$$

These limiting behaviors are indicated on the graphs as blue lines. If $a > 1$, $\psi_d(a,b)$ diverges logarithmically for $b \to 0$, but in different ways in the two ranges $1 < a < 2$ and $a > 2$. The former range corresponds physically to $0 < \mu < \hbar\omega_D$, such that the band edge sets the lower cutoff for the pairing interaction, while the latter range is the usual regime, where the Fermi energy is larger than the Debye energy. In two dimensions, the asymptotic behavior is quite simple: If $a > 2$,

we have the well-known result,

$$\psi_2(a>2,b\to 0)=\int_{-\frac{1}{b}}^{\frac{1}{b}} dx\,\frac{\tanh(x/2)}{2x}=\ln\left(\frac{2e^{\gamma}}{\pi b}\right), \quad (11)$$

with $\gamma\approx 0.577$ the Euler constant. The function is independent of a, because the DOS is constant over the range of integration when $\mu>\hbar\omega_{\rm D}$. If $1<a<2$, we evaluate the function by extending the integral to reproduce the case $a>2$ and subtracting the difference:

$$\psi_2(1<a<2,b\to 0)=\int_{-\frac{1}{b}}^{\frac{1}{b}} dx\,\frac{\tanh(x/2)}{2x}-\int_{-\frac{1}{b}}^{\frac{1-a}{b}} dx\,\frac{-1}{2x}$$
$$=\ln\left(\sqrt{a-1}\,\frac{2e^{\gamma}}{\pi b}\right). \quad (12)$$

Equations (11) and (12) are represented in Fig. 2 (top) as red lines. In order to obtain the exact asymptotic behavior for $b\to 0$ in three dimensions, we introduce the function $t(x)$ as a piece-wise linear approximation of $\tanh(x/2)$—namely, -1 for $x<-2$, $x/2$ for $|x|<2$, and $+1$ for $x>2$—and we calculate analytically the integral with $\tanh(x/2)$ replaced by $t(x)$. The difference between the latter approximation and the exact result is

$$\lim_{b\to 0}\int_{\frac{1-\min(a,2)}{b}}^{\frac{1}{b}} dx\,\sqrt{bx+a-1}\,\frac{\tanh(x/2)-t(x)}{2x}$$
$$=\sqrt{a-1}\ln\left(\frac{4e^{\gamma-1}}{\pi}\right).$$

Expanding the nonsingular terms to leading order in b, we finally get in the regime $0<\mu<\hbar\omega_{\rm D}$:

$$\psi_3(1<a<2,b\to 0)=\sqrt{a}+\sqrt{a-1}$$
$$\times\ln\left(\frac{a-1}{\sqrt{a}+\sqrt{a-1}}\frac{8e^{\gamma-2}}{\pi b}\right), \quad (13)$$

and in the regime $\mu>\hbar\omega_{\rm D}$:

$$\psi_3(a>2,b\to 0)$$
$$=\sqrt{a}+\sqrt{a-2}+\sqrt{a-1}$$
$$\times\ln\left(\frac{a-1}{\sqrt{a}+\sqrt{a-1}}\sqrt{\frac{\sqrt{a-1}-\sqrt{a-2}}{\sqrt{a-1}+\sqrt{a-2}}}\frac{8e^{\gamma-2}}{\pi b}\right). \quad (14)$$

These asymptotic behaviors are indicated in Fig. 2 (bottom) as red lines. Lastly, in the high-density, high-T_c sector $a>2$ and $b\to\infty$, the function reduces simply to $\psi_d(a,b)=(a-1)^{d/2-1}/(2b)$.

Figure 2 also shows a particular cut at the value $\psi_d=2.5$. Since the BCS equation (9a) for one band is simply $\psi_d=1/\bar\lambda$, these cuts show the locus of the solutions $(a,b)=(1+\tilde\mu,\tilde T_c)$ for $\bar\lambda=0.4$. Note that the approximations (11) to (14) shown in red underestimate the function ψ_d at low b; using them instead of the exact functions thus leads to underestimating T_c.

III. ONE PARABOLIC BAND IN 2D AND 3D

A. Analytical results

For a single band, we place the origin of energy at the bottom of the band and we use the band mass as the reference mass. The coupled equations (9) for T_c become simply:

$$1=\bar\lambda\,\psi_d(1+\tilde\mu,\tilde T_c),\quad \tilde n=-\tilde T_c^{\frac{d}{2}}\,\mathrm{Li}_{\frac{d}{2}}(-e^{\tilde\mu/\tilde T_c}). \quad (15)$$

In 2D the relation between $\tilde n$ and $\tilde\mu$ can be trivially inverted and the two equations reduce to a single implicit relation for $\tilde T_c$ as a function of $\tilde n$ and $\bar\lambda$:

$$1=\bar\lambda\,\psi_2(1+\tilde T_c\ln(e^{\tilde n/\tilde T_c}-1),\tilde T_c). \quad (16)$$

At not too low density, we see from the asymptotic expressions indicated in Fig. 2 that the pairing temperature crosses over between two regimes at $\tilde\mu=1$. In 2D we have

$$\tilde T_c\approx\frac{2e^{\gamma}}{\pi}\exp\left(-\frac{1}{\bar\lambda}\right)\times\begin{cases}\sqrt{\tilde\mu} & \tilde\mu\lesssim 1\\ 1 & \tilde\mu>1\end{cases}\quad (d=2). \quad (17)$$

$\tilde T_c$ is independent of $\tilde\mu$ (hence of $\tilde n$) for $\tilde\mu>1$, due to the constant DOS and the conventional BCS expression is recovered. In 3D we find

$$\tilde T_c\approx\frac{8e^{\gamma-2}}{\pi}\sqrt{\tilde\mu}\,\exp\left(-\frac{1}{\bar\lambda\sqrt{\tilde\mu}}\right)\frac{e^{\sqrt{1+1/\tilde\mu}}}{1+\sqrt{1+1/\tilde\mu}}$$
$$\times\begin{cases}1 & \tilde\mu\lesssim 1\\ e^{\sqrt{1-1/\tilde\mu}}\sqrt{\frac{1-\sqrt{1-1/\tilde\mu}}{1+\sqrt{1-1/\tilde\mu}}} & \tilde\mu>1\end{cases}\quad (d=3). \quad (18)$$

The product $\bar\lambda\sqrt{\tilde\mu}$ is the coupling evaluated at the chemical potential, which enters the exponential as expected. Equations (17) and (18) are identical to Eqs. (2) and (3) of Ref. [2] if we admit that $k_{\rm B}T_c=(e^{\gamma}/\pi)\Delta$, which is true in the regime of validity of these expressions, but not in the low-density and/or strong-coupling regimes (see below). We emphasize that these approximations result from expanding the function $\psi_d(a,b)$ in the limit $b\to 0$ for $a>1$ and are therefore accurate only in the limit $T_c\to 0$ at finite positive μ. These equations are *not* accurate in the high-density regime where T_c is large. Our numerical results show that Eqs. (17) and (18) provide a rather poor approximation as soon as T_c reaches a few tenths of $\hbar\omega_{\rm D}$.

We now turn to the low-density region. In 2D any cut of the function $\psi_2(a,b)$ at the value $1/\bar\lambda$ converges at $b=0$ to a value $a<1$, given by the relation $-\ln\sqrt{1-a}=1/\bar\lambda$ (see Fig. 2). Hence the chemical potential converges to a finite negative value $\tilde\mu_{\rm min}=-e^{-2/\bar\lambda}$ when the density approaches zero. This is a conjugated effect of the pairing interaction and the DOS discontinuity: At any finite coupling the momentum distribution is spread and a negative chemical potential leads to a finite density even at zero temperature. The chemical potential at zero density is related to the energy E_b of the two-particle bound state by $\tilde\mu_{\rm min}=\tilde E_b/(2+\tilde E_b)$. Equation (16) for $\tilde T_c\to 0$ becomes $1=-\bar\lambda\ln\sqrt{-\tilde T_c\ln(e^{\tilde n/\tilde T_c}-1)}$, which can be solved for $\tilde n$ as a function of $\tilde T_c$: $\tilde n=\tilde T_c\ln\{1+\exp[-\exp(-2/\bar\lambda)/\tilde T_c]\}$. The latter expression shows that $\tilde n$ is smaller than $\tilde T_c$ when both approach zero, such that in this limit we can replace $\ln(e^{\tilde n/\tilde T_c}-1)$ by $\ln(\tilde n/\tilde T_c)$. We thus find

the solution,

$$\tilde{T}_c = \tilde{n}\,\exp\left[W\left(\frac{e^{-2/\bar{\lambda}}}{\tilde{n}}\right)\right] \qquad (d=2, n\to 0). \tag{19}$$

$W(x)$ is the Lambert function (or "product logarithm"), which gives the principal solution of the equation $x = We^W$. Equation (19) is nonanalytic in both $\bar{\lambda}$ and $\tilde{n}$. It gives a T_c starting with an infinite slope at $n = 0$ and increasing faster than any power of n (in the sense that the running exponent given by the logarithmic derivative approaches zero for $n \to 0$). An approximation of (19) valid to logarithmic accuracy was given earlier [24].

In 3D the function $\psi_3(a < 1,0)$ approaches 1 for $a \to 1$. Therefore we have the same situation as in 2D if $\bar{\lambda} > 1$. In this case the chemical potential approaches a finite negative value given by the solution of $\sqrt{\tilde{\mu}_{\min}+1} - \sqrt{-\tilde{\mu}_{\min}}\sin^{-1}(\sqrt{\tilde{\mu}_{\min}+1}) = 1/\bar{\lambda}$ as the density approaches zero. Since $\tilde{\mu}$ is finite and negative in the limit $\tilde{T}_c \to 0$, we can use the asymptotic expression $-\mathrm{Li}_{3/2}(-e^x) \to e^x$ for $x \to -\infty$ and get the chemical potential $\tilde{\mu} = \tilde{T}_c \ln(\tilde{n}/\tilde{T}_c^{3/2})$. Equation (15) can then be solved for $\tilde{T}_c$ in the relevant regime $-\tilde{\mu} \ll 1$, by making use of Eq. (10) to leading order in $1 - a$. This yields

$$\tilde{T}_c \approx \tilde{n}^{\frac{2}{3}}\,\exp\left[W\left(\frac{8(1/\bar{\lambda}-1)^2}{3\pi^2\tilde{n}^{\frac{2}{3}}}\right)\right] \qquad (d=3, \bar{\lambda}>1, n\to 0). \tag{20}$$

Like in 2D, T_c starts with an infinite slope at $n = 0$ and increases faster than any power of n if $\bar{\lambda} > 1$. If $\bar{\lambda} < 1$ there is no finite solution a to the equation $\psi_3(a,0) = 1/\bar{\lambda}$, meaning that $\mu = 0$ at zero density. As can be seen in Fig. 2, the curvature along the cut for $\psi_3 > 1$ is such that $\tilde{\mu} > \tilde{T}_c$. In the limit $\tilde{T}_c \to 0$ we can use the large-x expansion $-\mathrm{Li}_{3/2}(-e^x) \to 4/(3\sqrt{\pi})x^{3/2}$ and recover $\tilde{\mu} = (3\sqrt{\pi}\tilde{n}/4)^{2/3}$, which is the zero-temperature noninteracting result. Using the asymptotic form (13) we finally obtain

$$\tilde{T}_c = \frac{8e^{\gamma-2}}{\pi}\left(\frac{3\sqrt{\pi}\tilde{n}}{4}\right)^{\frac{2}{3}}\exp\left[-\left(\frac{1}{\bar{\lambda}}-1\right)\left(\frac{4}{3\sqrt{\pi}\tilde{n}}\right)^{\frac{1}{3}}\right], \qquad (d=3, \bar{\lambda}<1, n\to 0). \tag{21}$$

This function starts with *zero* slope at $n = 0$ and increases *slower* than any power of n. It is exactly equivalent to the result [17] $k_B T_c = (8e^{\gamma-2}/\pi)E_F \exp[\pi/(2k_F a_s)]$ if the s-wave scattering length a_s is computed with our interaction potential, namely $4\pi\hbar^2 a_s/m = V/(\bar{\lambda}-1)$. This potential has no bound state for two particles if $\bar{\lambda} < 1$, which explains why $\mu = 0$ at zero density in this case. The change of behavior at $\bar{\lambda} = 1$ is discontinuous according to Eqs. (20) and (21), both functions giving $\tilde{T}_c \propto \tilde{n}^{2/3}$ with different pre-factors.

The analytical expressions (17)–(21) are compared below with the numerical results. Note that if the reference mass is not the band mass m_α, one must replace $\tilde{n}$ by $\tilde{n}(m/m_\alpha)^{d/2}$ in these equations.

As the BCS mean-field theory is not believed to be a useful model in 1D, we have not discussed this case. For completeness, and because it has been argued that the singularity of the 1D DOS could induce large enhancements of T_c in striped quasi-1D superconductors [8], we show in Appendix B that the pairing temperature is also continuous and nonanalytic at the bottom of a 1D band.

Before closing this section, we point out that the solution of the gap equation at $T = 0$ does not generally allow one to deduce T_c. Although the focus of the present paper is on T_c, we give in Appendix C exact results for the zero-temperature gap in 2D at low density, for the purpose of showing that the usual BCS gap to T_c ratio is not obeyed in this limit.

B. Numerical results

The numerical solution of Eq. (16) is shown in Fig. 3. $\tilde{T}_c$ reaches a plateau at high density due to the constant DOS of the band. For $\bar{\lambda}$ of order one, the value $T_{c,\infty}$ on the plateau departs significantly from the approximate solution (17), which becomes worse with increasing $\bar{\lambda}$, while the simple large-T_c result $\tilde{T}_{c,\infty} = \bar{\lambda}/2$ becomes increasingly reliable [inset of Fig. 3(b)]. The density $\tilde{n}_\infty$ at which the plateau is reached corresponds to $\mu - \hbar\omega_D$ coinciding with

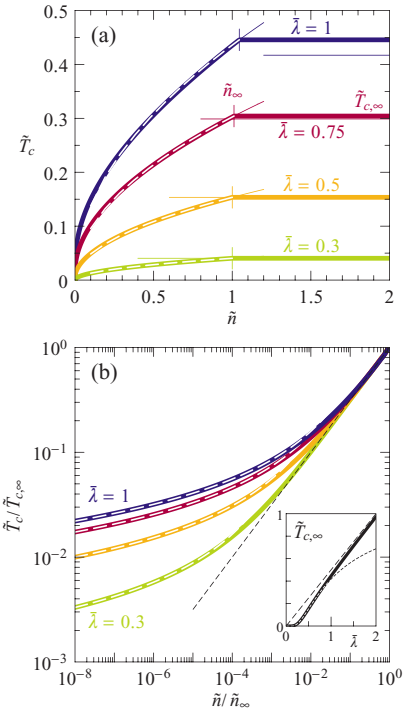

FIG. 3. (a) Pairing temperature as a function of electron density for one parabolic band in two dimensions. T_c is expressed in units of $\hbar\omega_D/k_B$ and n in units of $m\omega_D/(\pi\hbar)$. The thin horizontal lines show the approximate solution (17) for each $\bar{\lambda}$. The vertical bars indicate $\tilde{n}_\infty$ [Eq. (22)]. The dashed lines show the approximate scaling $\tilde{T}_c = \tilde{T}_{c,\infty}(\tilde{n}/\tilde{n}_\infty)^{1/2}$. (b) Same data normalized. The white dashed lines are the prediction of Eq. (19) and the black dashed line indicates the square-root behavior for $\tilde{n} \lesssim \tilde{n}_\infty$. (Inset) Maximum pairing temperature as a function of $\bar{\lambda}$ (solid line), compared with Eq. (17) (dotted) and $\bar{\lambda}/2$ (dashed).

the bottom of the band, which means

$$\tilde{n}_\infty = \tilde{T}_{c,\infty} \ln(e^{1/\tilde{T}_{c,\infty}} + 1). \tag{22}$$

For $\tilde{n} \lesssim \tilde{n}_\infty$, Eq. (17) gives $\tilde{T}_c/\tilde{T}_{c,\infty} \approx \tilde{\mu}^{1/2}$. Since $\tilde{\mu}$ is very close to a linear function of $\tilde{n}$ at intermediate and high densities (see below), we expect to have the universal scaling $\tilde{T}_c/\tilde{T}_{c,\infty} \approx (\tilde{n}/\tilde{n}_\infty)^{1/2}$. This is well obeyed by the data.

Close to $\tilde{n} = 0$ the behavior is nonuniversal, in the sense that the curves do not collapse if $\tilde{n}$ and $\tilde{T}_c$ are rescaled by $\tilde{n}_\infty$ and $\tilde{T}_{c,\infty}$ [Fig. 3(b)]. The numerical data are in perfect agreement with the limiting behavior (19) at all couplings. The flattening of the curves in the log-log plot shows that the running exponent $\eta(n)$ in $T_c \propto n^{\eta(n)}$ approaches zero for $n \to 0$. This is suggestive of a discontinuity in $T_c(n)$ at $n = 0$, reminiscent of the DOS discontinuity. However, since Eq. (19) vanishes continuously for $\tilde{n} \to 0$, the correct picture is that of a T_c tending asymptotically to a discontinuity of size zero with decreasing n.

The numerical results for the 3D case are displayed in Fig. 4. Also shown is the high-density approximation (18), evaluated with $\tilde{\mu}$ replaced by its zero-temperature noninteracting value $\tilde{\mu}_0$. The approximation falls on top of the numerical data for small $\bar{\lambda}$, but deviates significantly for larger coupling. The good agreement at weak coupling is due to a cancellation of errors: the agreement worsens if $\tilde{\mu}$ rather than $\tilde{\mu}_0$ is used in Eq. (18). The reason is that $\mu(T_c) < \mu_0$ and the use of μ_0 always leads to overestimating T_c. This happens to compensate the underestimation of T_c due to the use of Eqs. (13) and (14).

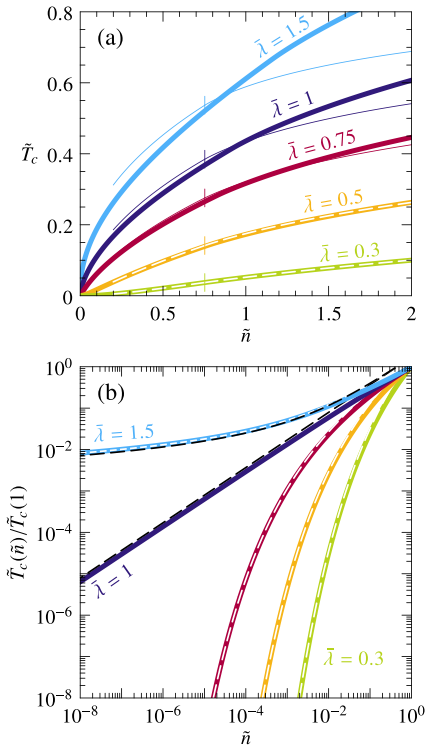

FIG. 4. (a) Pairing temperature as a function of electron density for one parabolic band in three dimensions. T_c is expressed in units of $\hbar\omega_D/k_B$ and n in units of $2[m\omega_D/(2\pi\hbar)]^{3/2}$. The thin and dashed lines show Eq. (18), evaluated using $\tilde{\mu}_0 = (3\sqrt{\pi}\tilde{n}/4)^{2/3}$ for $\tilde{\mu}$. The vertical bars indicate $\tilde{\mu}_0 = 1$. (b) Same data on a log-log scale. The dashed lines show Eqs. (20) and (21). Equation (21) was used for $\bar{\lambda} = 1$. The short-dashed white line for $\bar{\lambda} = 1.5$ is obtained without expanding Eq. (10) around $a = 1$ (see text).

At low density, the change of behavior from a convex increase for $\bar{\lambda} < 1$ to a concave increase for $\bar{\lambda} > 1$ is visible on the log-log plot in Fig. 4(b)—where a convex function has a slope larger than unity. The low-density, low-coupling limit (21) describes the numerical data perfectly. The low-density, high-coupling expression (20) deviates slightly due to the use of Eq. (10) at lowest order in $1 - a$. This small discrepancy disappears if $\tilde{\mu}$ is evaluated without expanding Eq. (10). The value $\bar{\lambda} = 1$ is somewhat peculiar: The numerics shows the expected $\tilde{n}^{2/3}$ scaling, but the pre-factor is neither unity as implied by Eq. (20), nor 0.742 as given by Eq. (21), but ∼0.6.

Figure 5 shows the chemical potential calculated numerically at T_c. In 2D μ converges to a negative value for any coupling, as discussed above. In 3D μ tends to zero at $n = 0$ if $\bar{\lambda} \leqslant 1$. If $\bar{\lambda} > 1$ it converges to a negative value. The density at which $\mu = 0$ is given for $\bar{\lambda} \gtrsim 1$ by $\tilde{n} \approx 0.62(1 - 1/\bar{\lambda})^3$. This coincides with the condition $1/(k_F a_s) \approx 0.68$. The effect of increasing the pairing interaction is mainly to shift the $\mu(n)$ curve downwards. At $n = 0$ this shift is entirely due to the

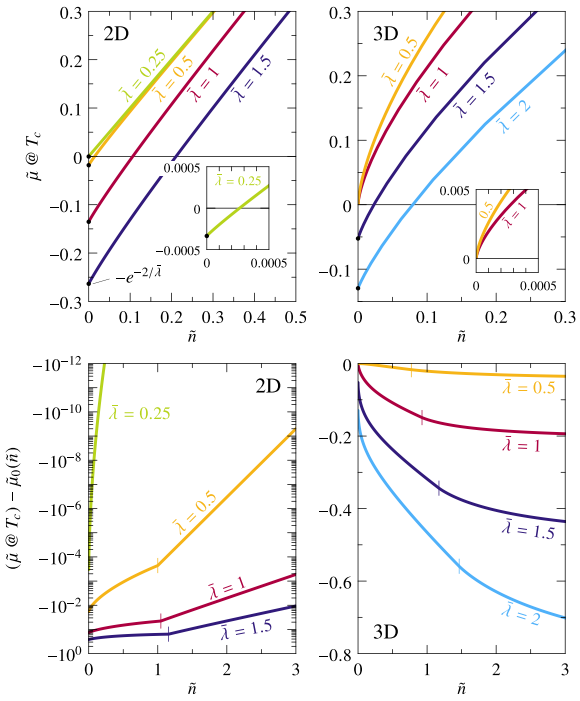

FIG. 5. (Top row) Chemical potential at T_c in the low-density limit. The dots show the solution of $\psi_d(1 + \tilde{\mu}, 0) = 1/\bar{\lambda}$, with $\psi_d(a, 0)$ given by Eq. (10). The insets show that $\mu(n = 0) < 0$ in 2D for all $\bar{\lambda}$, while $\mu(n = 0) = 0$ in 3D for $\bar{\lambda} \leqslant 1$. (Bottom row) Difference between the chemical potential at T_c and the zero-temperature noninteracting value $\tilde{\mu}_0$. The vertical bars indicate $\tilde{\mu} = 1$.

interaction-induced spreading of the momentum distribution. At finite n part of the shift is due to the thermal smearing.

As the density increases, the behavior is qualitatively different in 2D and 3D: while $\tilde{\mu}$ approaches $\tilde{\mu}_0 = \tilde{n}$ in 2D, this does not happen in 3D. In 2D the chemical potential is $\tilde{\mu} = \tilde{T}_c \ln(e^{\tilde{n}/\tilde{T}_c} - 1)$. Since $\tilde{T}_c$ saturates for $\tilde{n} > \tilde{n}_\infty$, we have $\tilde{n} > \tilde{T}_c$ at large $\tilde{n}$ and $\tilde{\mu}$ approaches exponentially the value $\tilde{n}$. This is peculiar to the 2D constant DOS, since both interaction and temperature redistribute states in equal amounts below and above μ_0. In 3D the square-root DOS implies that there are more states added in the tail of the momentum distribution above μ_0, than there are states removed below μ_0. The equilibrium chemical potential must therefore remain below the zero-temperature noninteracting value, by an amount which increases with increasing $\bar{\lambda}$ and also with increasing n.

IV. MULTIBAND EFFECTS

The interest raised by multiband superconductors, in particular MgB_2 and the iron-based family, has triggered many studies over the years [25]. Here we discuss multiband effects that occur near a band edge and are associated with the low density in one of the bands.

It is clear from the previous section that a knowledge of the self-consistent chemical potential is required to understand the behavior of T_c close to a band minimum. This raises the question of the role played by perturbations that affect the chemical potential, such as the presence of a nonsuperconducting band (NB) beneath the superconducting band (SB). In the absence of interband coupling, the NB can only alter the superconducting properties of the SB by changing the chemical potential. In 2D and in 3D for $\bar{\lambda} > 1$, the key observation was that μ is finite and negative at the band bottom, such that the nonanalytic behavior of T_c is not controlled by μ. An NB is therefore not expected in general to change this nonanalytic behavior qualitatively. An exception—confirming the rule—occurs when the bottom of the NB coincides precisely with the energy at which the SB begins to be populated. For this peculiar arrangement, the NB controls the relation between μ and n in the limit $T_c \to 0$ and T_c displays a simple analytic dependence on n, which is linear in 2D and $\propto n^{2/3}$ in 3D. This is illustrated in Fig. 6(a) for the 2D case. Solving the coupled equations (9) for two bands in the appropriate regime, we get a relation between $\tilde{n}$ and $\tilde{T}_c$ which is accurate near the band minimum:

$$\tilde{n} = \tilde{T}_c\left[\frac{m_1}{m}\ln\left(1+e^{\frac{-\exp(-2/\bar{\lambda}_{11})}{\tilde{T}_c}}\right)+\frac{m_2}{m}\ln\left(1+e^{\frac{-\exp(-2/\bar{\lambda}_{11})-\tilde{E}_{02}}{\tilde{T}_c}}\right)\right]. \tag{23}$$

This reproduces the near-band edge behavior as shown in Fig. 6(a) and in particular gives the linear dependence $\tilde{n} = \tilde{T}_c(m_2/m)\ln(2)$ at the transition point where $\tilde{E}_{02} = -\exp(-2/\bar{\lambda}_{11})$.

If $\tilde{E}_{02} < -\exp(-2/\bar{\lambda}_{11})$, the SB is not populated at low density and superconductivity appears at some finite density. In all cases, the $T_c(n)$ curve is "stretched" to higher densities with respect to the one-band result due to the carriers "lost" in the NB. For instance, if the band minima are degenerate, we see from Eq. (9) that the one-band $T_c(n)$ curve is simply modified

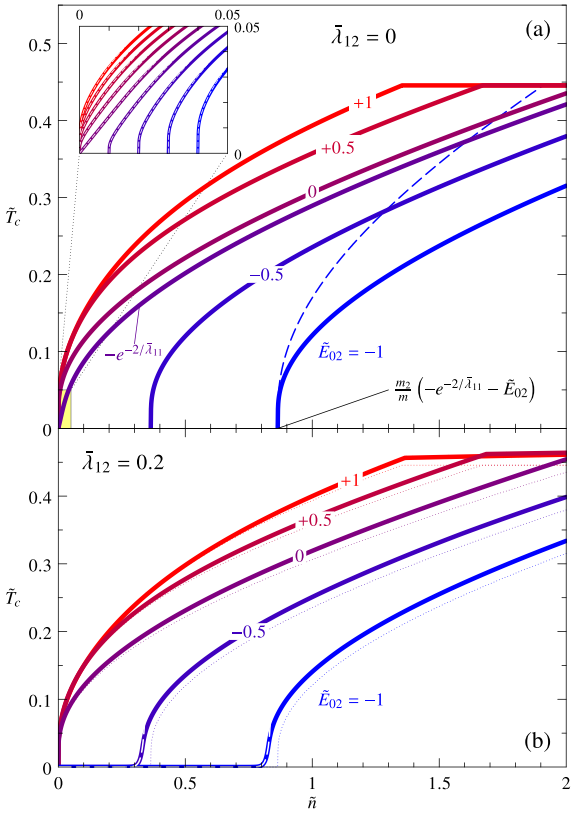

FIG. 6. Pairing temperature for two bands in two dimensions, with couplings $\bar{\lambda}_{11} = 1$, $\bar{\lambda}_{22} = 0$, and (a) $\bar{\lambda}_{12} = 0$, (b) $\bar{\lambda}_{12} = 0.2$. E_{02} is the energy minimum of the second band, measured from the energy minimum of the first. The masses are $m_1 = m_2 = m$. The dashed line in (a) is the one-band result, shifted horizontally for easier comparison. (Inset) Blowup of the transition region. Curves are shown for $\tilde{E}_{02} = -\exp(-2/\bar{\lambda}_{11}) + \delta\tilde{E}$, with $\delta\tilde{E}$ ranging from -0.04 (blue, right) to $+0.04$ (red, left). Note the linear behavior for $\delta\tilde{E} = 0$. The white dashed lines show Eq. (23). In (b), the dotted lines are the result for $\bar{\lambda}_{12} = 0$ and the dashed white lines show Eq. (24).

by a rescaling of the density $n \to n/[1 + (m_1/m_2)^{d/2}]$. This implies that the pairing temperature is necessarily reduced by a nonsuperconducting band, in the absence of interband coupling.

Both attractive and repulsive interband interactions increase T_c for two bands [26,27], as illustrated by the fact that Eq. (9) involve only $\bar{\lambda}_{12}^2$: interband interactions do not induce interband pairing in the present model, but reinforce the intraband pairing by second-order processes involving the other band. If T_c starts at finite density, the interband coupling leads to a tail in the $T_c(n)$ curve. In the regime where the chemical potential is below the SB but well into the NB, we find, for instance, in 2D:

$$\tilde{T}_c = \frac{2e^\gamma}{\pi}\sqrt{\tilde{n}\frac{m}{m_2}}\exp\left\{\frac{1}{\frac{1}{\bar{\lambda}_{12}^2}\left[\bar{\lambda}_{11}+\frac{2}{\ln\left(-\tilde{E}_{02}-\tilde{n}\frac{m}{m_2}\right)}\right]}\right\}. \tag{24}$$

This is compared with the numerical result in Fig. 6(b).

We move on to the case of two superconducting bands and begin with general trends. The observation that T_c is an increasing function of density [28] remains true in the near-band edge regime. It is possible to show that the property $dT_c/dn \geqslant 0$ is guaranteed by Eq. (9) for an arbitrary number of bands and any values of the coupling constants. Reference [6] reports a nonmonotonic dependence of the pairing temperature on carrier concentration in doped $SrTiO_3$: this cannot be interpreted on the basis of Eq. (9) without invoking density-dependent interactions.

A second band can nevertheless lead to a decrease of T_c at fixed density. Specifically, consider a one-band system at some density with coupling $\bar{\lambda}_{11}$ and pairing temperature T_c^0; add a second band at higher energy with coupling $\bar{\lambda}_{22} \leqslant \bar{\lambda}_{11}$ and no interband coupling; then the two-band system with the same density has $T_c \leqslant T_c^0$. This can be rigorously proven by manipulating Eq. (9).

If the second band has a coupling $\bar{\lambda}_{22} > \bar{\lambda}_{11}$, T_c exceeds T_c^0 at high enough density and follows the dependence that would correspond to a nonsuperconducting first band. These various trends are illustrated in Fig. 7 (top panels). Figure 7 (bottom panels) shows the effect of interband interaction, which is generically an increase of T_c.

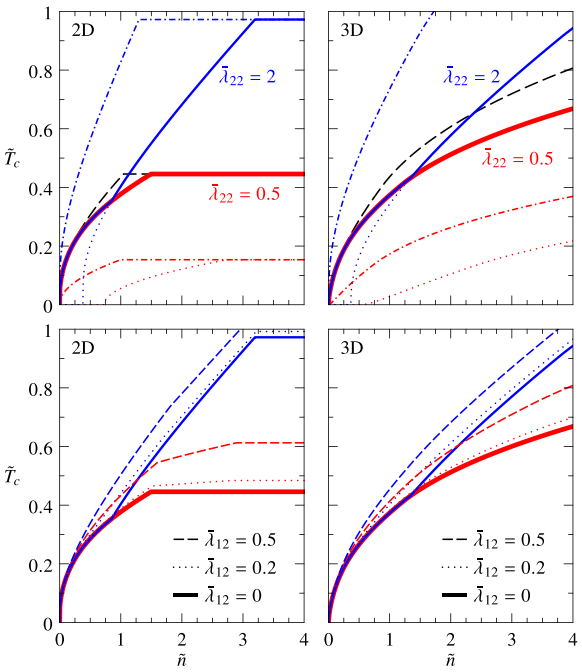

FIG. 7. (Top panels) Change of T_c induced by a second superconducting band in 2D and 3D, without interband coupling. (Dashed black lines) Pairing temperature for a single band with coupling $\bar{\lambda}_{11} = 1$ and mass $m_1/m = 1$. (Solid lines) Pairing temperature for the two-band system with $\tilde{E}_{02} - \tilde{E}_{01} = 0.75$, $m_2 = m_1$, and coupling $\bar{\lambda}_{22} = 0.5$ (red) and $\bar{\lambda}_{22} = 2$ (blue). (Dash-dotted) Case of the second band alone. (Dotted) Case of the two-band system with $\bar{\lambda}_{11} = 0$. (Bottom panels) Increase of T_c by interband coupling. (Solid lines) No interband coupling, same data and coloring as in the top panels. Dotted and dashed lines correspond to interband coupling $\bar{\lambda}_{12} = 0.2$ and 0.5, respectively.

V. CONCLUSION

In summary, in the low-density regime where the dynamical range of the pairing interaction is set by the band edge, the pairing temperature T_c depends on the electron density n in a nonanalytic way. For parabolic bands, we provided exact asymptotic formulas describing this dependency, taking into account the energy variation of the electronic DOS, as well as the variation of the chemical potential with interaction strength and temperature. In one and two dimensions and in three dimensions at strong enough coupling—in other words, when there is a bound solution to the two-particle problem—the chemical potential (at T_c) becomes negative at low density: As a result the $T_c(n)$ curve starts with infinite slope and increases faster than any power of n. Otherwise, i.e., in three dimensions at weak coupling, the chemical potential approaches zero at low density, the $T_c(n)$ curve starts with zero slope, and it increases slower than any power of n.

Our results may be relevant for low-density superconductors. In $SrTiO_3$, oxygen reduction and niobium doping allows one to tune the carrier density [6] in a range such that the dimensionless density $\tilde{n}$ varies typically between 10^{-2} and 10. In the $LaAlO_3/SrTiO_3$ interface, the field-effect induced sheet carrier density can also be tuned [29] such that $\tilde{n}$ varies typically from 10^{-1} to 1. In the low-density range of these domains, our exact formulas differ from the usual formulas valid at higher densities. In the numerical illustrations of the present paper we have used coupling constants $\bar{\lambda}$ of order one, which may appear very large in comparison to the typical values of the order 0.1 reported for $SrTiO_3$. We emphasize that our definition of the coupling constants differs from the usual definition, such that in three dimensions ours are bigger that the usual ones by a factor $(\mu/\hbar\omega_D)^{1/2}$, which is typically three in $SrTiO_3$.

The observation that T_c is a nonanalytic function of n near a band bottom calls for a reconsideration of the problem of shape resonances. These refer to oscillations of T_c in a quasi-two-dimensional superconductor confined in a slab, as a function of the slab thickness. The oscillations arise when the chemical potential crosses the bottom of one of the confinement-induced subbands and were presented in the literature on the subject as discontinuities [4]. Our results show that such discontinuities are artifacts, because T_c vanishes continuously at a band edge in any dimension. The actual dependence of T_c on the slab thickness is therefore a continuous function, which remains to be investigated. A particularly interesting system in this respect is the $LaAlO_3/SrTiO_3$ interface, which cumulates the characteristics of being a low-density superconducting system, confined in a quasi-two-dimensional geometry, and also a multiband system.

ACKNOWLEDGMENTS

We acknowledge fruitful discussions with J.-M. Triscone, S. Gariglio, and M. Grilli. We are grateful to A. V. Chubukov for drawing our attention to a previous approximation of Eq. (19) and to P. Pieri for pointing out the equivalence of

Eq. (21) with a known result in the BEC limit. This work was supported by the Swiss National Science Foundation under Division II.

APPENDIX A: SIMPLE PROOF OF EQ. (4)

The density of a free-electron gas in dimension d is proportional to the volume of the d-dimensional Fermi sphere, smeared by the Fermi function:

$$n = 2\int \frac{d^dk}{(2\pi)^d}\frac{1}{\exp\left(\frac{\hbar^2k^2/2m-\mu}{k_BT}\right)+1}$$
$$= 2\int \frac{d^dk}{(2\pi)^d}\frac{x}{x-\exp\left(\frac{\hbar^2k^2}{2mk_BT}\right)},$$

with $x = -\exp(\mu/k_BT)$. In order to evaluate the integral, we use the expansion $x/(x-a) = -\sum_{q=1}^{\infty} x^q/a^q$ and we write $k^2 = \sum_{i=1}^{d} k_i^2$. This leads to a product of Gaussian integrals:

$$n = -2\sum_{q=1}^{\infty} x^q \prod_{i=1}^{d}\int_{-\infty}^{\infty}\frac{dk_i}{2\pi}\exp\left(-q\frac{\hbar^2k_i^2}{2mk_BT}\right)$$
$$= -2\sum_{q=1}^{\infty} x^q \prod_{i=1}^{d}\sqrt{\frac{mk_BT}{2\pi\hbar^2q}} = -2\left(\frac{mk_BT}{2\pi\hbar^2}\right)^{\frac{d}{2}}\sum_{q=1}^{\infty}\frac{x^q}{q^{d/2}}.$$

Considering the Taylor expansion of the polylogarithm, we see that the q sum in the last expression is $\mathrm{Li}_{d/2}(x)$, which proves Eq. (4).

APPENDIX B: RESULTS FOR ONE PARABOLIC BAND IN 1D

With the proviso that the factor $(d-1)\pi$ in Eqs. (3) and (7) be replaced by 1, Eqs. (2)–(9) are valid for $d = 1$. The asymptotic properties of the function $\psi_1(a,b)$ are

$$\psi_1(0<a<1, b\to 0) = \frac{\sin^{-1}(\sqrt{a})}{\sqrt{1-a}} \approx \frac{\pi/2}{\sqrt{1-a}} - 1,$$
$$\psi_1(1<a<2, b\to 0) = \frac{1}{\sqrt{a-1}}\ln\left(\frac{a-1}{\sqrt{a}+\sqrt{a-1}}\frac{8e^\gamma}{\pi b}\right),$$
$$\psi_1(a>2, b\to 0) = \frac{1}{\sqrt{a-1}}\ln\left(\frac{a-1}{(\sqrt{a}+\sqrt{a-1})(\sqrt{a-1}+\sqrt{a-2})}\frac{8e^\gamma}{\pi b}\right).$$

The corresponding weak-coupling approximations in the regime $\tilde{n} \gtrsim 1$ are

$$\tilde{T}_c \approx \frac{8e^\gamma}{\pi}\exp\left(-\frac{1}{\bar{\lambda}/\sqrt{\tilde{\mu}}}\right)\frac{1}{1+\sqrt{1+1/\tilde{\mu}}}\begin{cases}\sqrt{\tilde{\mu}} & \tilde{\mu}\lesssim 1\\ \frac{1}{1+\sqrt{1-1/\tilde{\mu}}} & \tilde{\mu}>1\end{cases} \qquad (d=1), \tag{B1}$$

in agreement with the result of Ref. [2], where $\bar{\lambda}/\sqrt{\tilde{\mu}}$ is the coupling constant evaluated at the chemical potential. In the low-density limit the chemical potential approaches a finite negative value given by the solution of $1/\bar{\lambda} = \sin^{-1}(\sqrt{1+\tilde{\mu}_{\min}})/\sqrt{-\tilde{\mu}_{\min}} \approx (\pi/2)/\sqrt{-\tilde{\mu}_{\min}} - 1$. We can use the expansion $-\mathrm{Li}_{1/2}(-e^x) \to e^x$ for large negative x and deduce the relation $\tilde{\mu} = \tilde{T}_c\ln(\tilde{n}/\tilde{T}_c^{1/2})$. We find for $\tilde{T}_c$,

$$\tilde{T}_c \approx \tilde{n}^2\exp\left[W\left(\frac{1}{2}\left(\frac{\pi\bar{\lambda}}{1+\bar{\lambda}}\right)^2\frac{1}{\tilde{n}^2}\right)\right] \quad (d=1, n\to 0). \tag{B2}$$

The numerical results are shown in Fig. 8 and compared with the analytical formulas (B1) and (B2). Equation (B1) works well at high density, but severely breaks down at low density, even at weak coupling. The cancellation of errors observed in the 3D case also occurs here to some extent, but the main issue is that Eq. (B1) fails to describe the regime where $\tilde{\mu} < 0$ at low density, while in 3D this regime is absent for $\bar{\lambda} < 1$. Equation (B2) is accurate at weak coupling where $-\tilde{\mu} \ll 1$ and has the small inaccuracy associated with the approximation made in solving for $\tilde{\mu}$ at larger coupling.

APPENDIX C: GAP TO T_c RATIO IN THE LOW-DENSITY LIMIT

We give here the zero-temperature gap explicitly for one band in 2D, as a function of density and coupling. This can be combined with the result (19) in order to obtain the exact gap to T_c ratio in the low-density limit. The expression of the density at $T = 0$ is

$$n = \int_{-\infty}^{\infty} d\xi\, N_0(\mu+\xi)\left(1-\frac{\xi}{\sqrt{\xi^2+\Delta_\xi^2}}\right), \tag{C1}$$

where $N_0(E)$ is the normal-state DOS given by Eq. (3) and $\Delta_\xi = \theta(\hbar\omega_D - |\xi|)\Delta$ with Δ the zero-temperature gap. We set $E_{0\alpha} = 0$ and $m = m_\alpha$ as in Sec. III and move to dimensionless variables. In 2D we have at $T = 0$,

$$\tilde{n} = \begin{cases}0 & \tilde{\mu} < -1\\ \frac{1}{2}(\tilde{\mu}+1+\sqrt{\tilde{\mu}^2+\tilde{\Delta}^2}-\sqrt{1+\tilde{\Delta}^2}) & -1<\tilde{\mu}<1\\ \tilde{\mu} & \tilde{\mu}>1.\end{cases} \tag{C2}$$

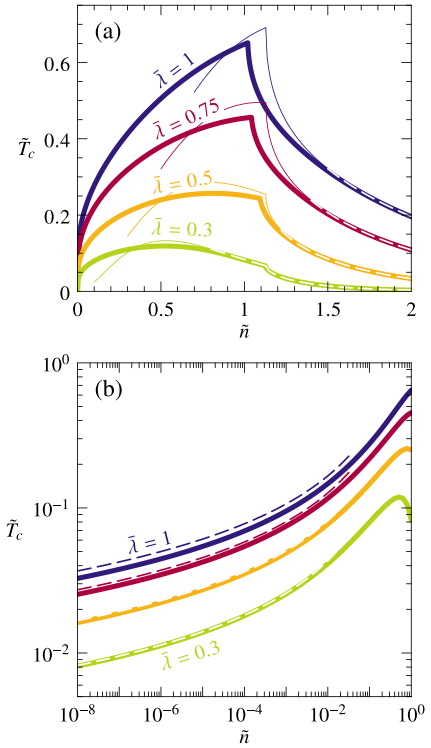

FIG. 8. (a) Pairing temperature as a function of electron density for one parabolic band in one dimension. T_c is expressed in units of $\hbar\omega_D/k_B$ and n in units of $2[m\omega_D/(2\pi\hbar)]^{1/2}$. The thin and dashed lines show Eq. (B1), evaluated using $\tilde{\mu}_0 = (\pi/4)\tilde{n}^2$ for $\tilde{\mu}$. (b) Same data on a log-log scale. The dashed lines show Eq. (B2).

The gap equation is obtained by replacing $\tanh(\cdots)$ by unity in Eq. (1a). For one band in 2D we find

$$1/\bar{\lambda} = \begin{cases} 0 & \tilde{\mu} < -1 \\ \frac{1}{2}\ln\left(\frac{1+\sqrt{1+\tilde{\Delta}^2}}{\sqrt{\tilde{\mu}^2+\tilde{\Delta}^2}-\tilde{\mu}}\right) & -1 < \tilde{\mu} < 1 \\ \ln\left(\frac{1+\sqrt{1+\tilde{\Delta}^2}}{\tilde{\Delta}}\right) & \tilde{\mu} > 1. \end{cases} \qquad \text{(C3)}$$

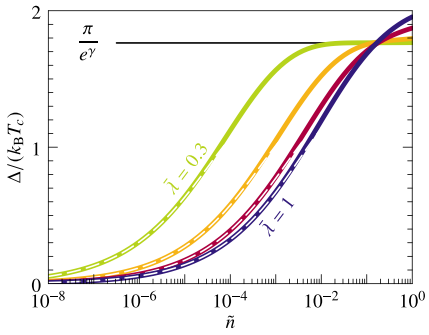

FIG. 9. Zero-temperature gap Δ to T_c ratio calculated numerically for one parabolic band in two dimensions. Curves are drawn as a function of density n expressed in units of $m\omega_D/(\pi\hbar)$ for $\bar{\lambda} = 0.3, 0.5, 0.75$, and 1. The dashed lines show the ratio of Eqs. (C4) and (19). The horizontal line indicates the BCS weak-coupling ratio $\pi/e^\gamma \approx 1.76$.

For $\tilde{\mu} > 1$, the gap is independent of density and given by $\tilde{\Delta} = 1/\sinh(1/\bar{\lambda})$; combined with the weak-coupling result (17), this yields the usual weak-coupling BCS ratio $\Delta/(k_B T_c) = \pi/e^\gamma$. In the low-density regime $\tilde{\mu} < 1$, we eliminate $\tilde{\Delta}$ among Eqs. (C2) and (C3) to find $\tilde{\mu} = \tilde{n} + (\tilde{n}-1)e^{-2/\bar{\lambda}}$. Solving for the gap, we then arrive at

$$\tilde{\Delta} = \frac{\sqrt{\tilde{n} + \tilde{n}(\tilde{n}-1)e^{-2/\bar{\lambda}}}}{\sinh(1/\bar{\lambda})} \qquad (\tilde{n} < 1). \qquad \text{(C4)}$$

Comparing Eqs. (C4) and (19) we see that T_c increases faster than Δ with increasing density. As a result the gap to T_c ratio vanishes for $n \to 0$, as we show in Fig. 9. This result may look surprising in view of the fact that known two-dimensional superconductors tend to have a gap to T_c ratio larger than the BCS value. The suppression shown in Fig. 9 concerns a regime of density which none of these known superconductors has reached until now, to our knowledge.

[1] J. Bardeen, L. N. Cooper, and J. R. Schrieffer, Microscopic theory of superconductivity, Phys. Rev. **108**, 1175 (1957).

[2] D. M. Eagles, Predicted transition temperatures of very thin films and whiskers of superconducting semiconductors—Application to $SrTiO_3$, Phys. Rev. **164**, 489 (1967).

[3] C. J. Thompson and J. M. Blatt, Shape resonances in superconductors–II simplified theory, Phys. Lett. **5**, 6 (1963).

[4] See, e.g., A. Romero-Bermúdez and A. M. García-García, Shape resonances and shell effects in thin-film multiband superconductors, Phys. Rev. B **89**, 024510 (2014).

[5] D. M. Eagles, Effective Masses in Zr-Doped superconducting ceramic $SrTiO_3$, Phys. Rev. **178**, 668 (1969); Possible pairing without superconductivity at low carrier concentrations in bulk and thin-film superconducting semiconductors, **186**, 456 (1969).

[6] X. Lin, G. Bridoux, A. Gourgout, G. Seyfarth, S. Krämer, M. Nardone, B. Fauqué, and K. Behnia, Critical Doping for the Onset of a Two-Band Superconducting Ground State in $SrTiO_{3-\delta}$, Phys. Rev. Lett. **112**, 207002 (2014).

[7] M. Ahrens, R. Merkle, B. Rahmati, and J. Maier, Effective masses of electrons in n-type $SrTiO_3$ determined from low-temperature specific heat capacities, Phys. B: Cond. Mat. **393**, 239 (2007).

[8] A. Perali, A. Bianconi, A. Lanzara, and N. L. Saini, The gap amplification at a shape resonance in a superlattice of quantum stripes: A mechanism for high T_c, Solid State Comm. **100**, 181 (1996).

[9] D. Innocenti, N. Poccia, A. Ricci, A. Valletta, S. Caprara, A. Perali, and A. Bianconi, Resonant and crossover phenomena in a multiband superconductor: Tuning the chemical potential near a band edge, Phys. Rev. B **82**, 184528 (2010); D. Innocenti, S. Caprara, N. Poccia, A. Ricci, A. Valletta, and A. Bianconi, Shape resonance for the anisotropic superconducting gaps near a Lifshitz transition: The effect of electron hopping between layers, Supercond. Sci. Technol. **24**, 015012 (2011).

[10] A. Guidini and A. Perali, Band-edge BCS-BEC crossover in a two-band superconductor: Physical properties and detection parameters, Supercond. Sci. Technol. **27**, 124002 (2014).

[11] P. Zubko, S. Gariglio, M. Gabay, P. Ghosez, and J.-M. Triscone, Interface physics in complex oxide heterostructures, Ann. Rev. Cond. Mat. Phys. **2**, 141 (2011).

[12] R. Pentcheva and W. E. Pickett, Electronic phenomena at complex oxide interfaces: Insights from first principles, J. Phys. Condens. Matter **22**, 043001 (2010).

[13] C. Cancellieri, M. L. Reinle-Schmitt, M. Kobayashi, V. N. Strocov, P. R. Willmott, D. Fontaine, P. Ghosez, A. Filippetti, P. Delugas, and V. Fiorentini, Doping-dependent band structure of $LaAlO_3/SrTiO_3$ interfaces by soft x-ray polarization-controlled resonant angle-resolved photoemission, Phys. Rev. B **89**, 121412 (2014).

[14] V. L. Berezinskiĭ, Destruction of long-range order in one-dimensional and two-dimensional systems having a continuous symmetry group I. Classical systems, Zh. Eksp. Teor. Fiz. **59**, 907 (1970) [Sov. Phys. JETP 32, 493 (1971)].

[15] J. M. Kosterlitz and D. J. Thouless, Ordering, metastability and phase transitions in two-dimensional systems, J. Phys. C: Solid State Phys. **6**, 1181 (1973).

[16] A. Larkin and A. Varlamov, *Theory of Fluctuations in Superconductors*, International Series of Monographs on Physics, Vol. 127 (Oxford University Press, Oxford, 2005).

[17] A. J. Leggett, Diatomic molecules and Cooper pairs, in *Modern Trends in the Theory of Condensed Matter*, Lecture Notes in Physics, Vol. 115, edited by A. Pękalski and J. A. Przystawa (Springer-Verlag, Berlin, 1980), p. 13.

[18] For a recent review, see M. Randeria and E. Taylor, Crossover from Bardeen-Cooper-Schrieffer to Bose-Einstein condensation and the unitary Fermi gas, Ann. Rev. Cond. Mat. Phys. **5**, 209 (2014).

[19] C. Hainzl and R. Seiringer, Critical temperature and energy gap for the BCS equation, Phys. Rev. B **77**, 184517 (2008).

[20] D. van der Marel, Anomalous behavior of the chemical potential in superconductors with a low density of charge carriers, Physica C **165**, 35 (1990).

[21] We pull out a minus sign from the interaction for convenience. $V_{\alpha\beta}$ can be positive (attractive interaction) or negative (repulsive interaction).

[22] The standard numerical integration packages fail to produce an accurate result for Eq. (6), or take a prohibitively long time to converge, especially in the limit $b \to 0$ of interest to us. For a fast and accurate numerical evaluation of Eq. (6) we have used the representation of the Fermi function proposed in Ref. [23]. With 14 Osaki poles and residues, we build a representation of the function $\tanh(x/2)$ which has an accuracy of $\sim 10^{-16}$ for all x, setting the function to ± 1 for $|x| > 16\ln(10)$. With this representation Eq. (6) can be evaluated analytically. This provides a very fast implementation of the functions $\psi_d(a,b)$, with double precision accuracy.

[23] T. Ozaki, Continued fraction representation of the Fermi-Dirac function for large-scale electronic structure calculations, Phys. Rev. B **75**, 035123 (2007).

[24] See A. V. Chubukov, I. Eremin, and D. V. Efremov, Superconductivity versus bound-state formation in a two-band superconductor with small Fermi energy: Applications to Fe-pnictides/chalcogenides and doped $SrTiO_3$, Phys. Rev. B **93**, 174516 (2016).

[25] For a recent review, see M. Zehetmayer, A review of two-band superconductivity: materials and effects on the thermodynamic and reversible mixed-state properties, Supercond. Sci. Tech. **26**, 043001 (2013).

[26] H. Suhl, B. T. Matthias, and L. R. Walker, Bardeen-Cooper-Schrieffer Theory of Superconductivity in the Case of Overlapping Bands, Phys. Rev. Lett. **3**, 552 (1959).

[27] A. Bussmann-Holder, R. Micnas, and A. R. Bishop, Enhancements of the superconducting transition temperature within the two-band model, Eur. Phys. J. B **37**, 345 (2004).

[28] R. M. Fernandes, J. T. Haraldsen, P. Wölfle, and A. V. Balatsky, Two-band superconductivity in doped $SrTiO_3$ films and interfaces, Phys. Rev. B **87**, 014510 (2013).

[29] A. D. Caviglia, S. Gariglio, N. Reyren, D. Jaccard, T. Schneider, M. Gabay, S. Thiel, G. Hammerl, J. Mannhart, and J.-M. Triscone, Electric field control of the $LaAlO_3/SrTiO_3$ interface ground state, Nature (London) **456**, 624 (2008).

Chapter 4

Quantum confinement and superconductivity

Superconducting pairing is influenced by spatial dimensionality and geometry. A primary reason for this influence is that geometry determines both the band structure of the material - for instance, 3D bands in the bulk or quasi-2D bands in thin films - and the pairing interaction between electrons. In turn, the relative position in energy of the electronic bands with respect to the chemical potential μ not only sets the number of occupied bands, according to the total density n, but it also affects deeply the superconducting properties. In particular, as we began considering in chapter 3, the BCS pairing temperature T_c is affected when μ approaches the bottom energy of a band $E_0 \leq \mu$, such that the pairing window for superconductivity is inferiorly cut by the band edge - see figure 3.3. This aspect of the BCS problem is crucial for T_c calculations in quantum-confined systems, like thin films or interfaces, because confinement determines the geometry, and it alters the dimensionality, the energy of quantized subbands and their position relative to the chemical potential. The effect of quantum confinement can be qualitatively sketched as follows: when one or more spatial dimensions of the system are confined to microscopic scales, thereby becoming much smaller than the other dimensions, the *ensemble* starts to show quantum effects in the confined directions. In particular, when we confine one or more dimensions the quantum states start to feel the presence of the system boundaries, and the boundary conditions for eigenfunctions change with respect to the ones of an infinite solid - i.e. periodic (Born-von Karman) boundary conditions [3]. As a consequence, the electronic energy levels $\xi_{\vec{k},\sigma}$ become discretized and form quantized subbands. For example, confining one band $\xi_{\vec{k},\sigma}$ of a 3D system along one direction z into a length $L_z \ll \{L_x, L_y\}$ produces a series of discrete levels ε_p, where $p \in \mathbb{N}^+$ is the subband index stemming from the quantization of

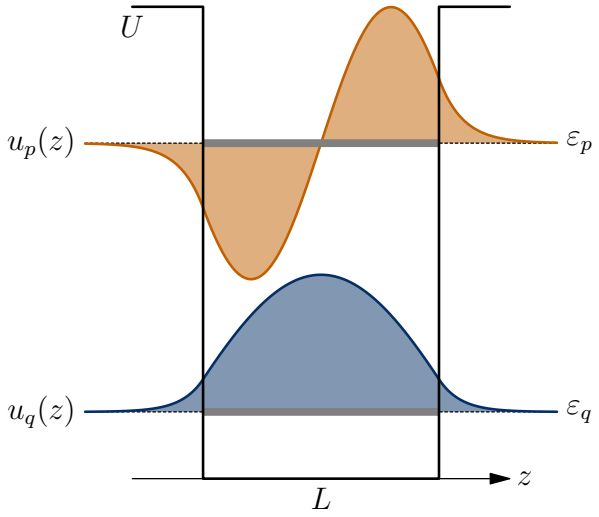

Figure 4.1: Schematic representation of the quantization of subbands due to quantum confinement in a square quantum well of width L and height U. The first two eigenvalues ε_p and ε_q, and the correspondent two eigenfunctions u_p and u_q, are depicted.

the z-component of the bulk wave vector k_z, the latter being no longer a good quantum number [3]. Hence, we can enumerate the eigenfunctions ψ_p associated to the eigenvalues ε_p according to the subband index p - see figure 4.1.

The quantization of eigenvalues ε_p in the confined direction has non-negligible consequences for the density of states (per unit volume and spin) $N_0^{el}(E) = \frac{1}{\mathcal{V}} \sum_{\vec{k}} \delta(E - \xi_{\vec{k}})$: in a quasi-2D geometry, the latter is composed of a series of steps, of absolute height $\frac{m_b}{2\pi\hbar^2} p$ with m_b band mass, which occur at energies corresponding with the quantized eigenvalues ε_p [3]. This situation is depicted in figure 4.2.

In the other two directions $\{L_x, L_y\}$ we have no confinement effects by hypothesis, so that the density of states is composed of 2-dimensional sheets in reciprocal space, enumerated by the subband index p. Therefore, the dimensionality of the system becomes quasi-2D from the initial 3D geometry.

Moreover, the modifications of the eigenfunctions ψ_p has significant consequences for a superconductor: since superconducting pairing for a BCS-like interaction depends on the spatial overlap of the eigenfunctions for paired states, confinement alters the pairing interaction through the changes in ψ_p and their respective overlaps in space. Similar arguments for the density of states and the pairing interaction apply when more than one spatial direction is affected by quantum confinement.

We see that quantization effects can tune the subband eigenvalues ε_p through the confinement parameters, e.g. the thickness L_z for a quasi-2D configuration. On the other hand, the chemical potential is also set by the density according to equation (3.20b). Hence,

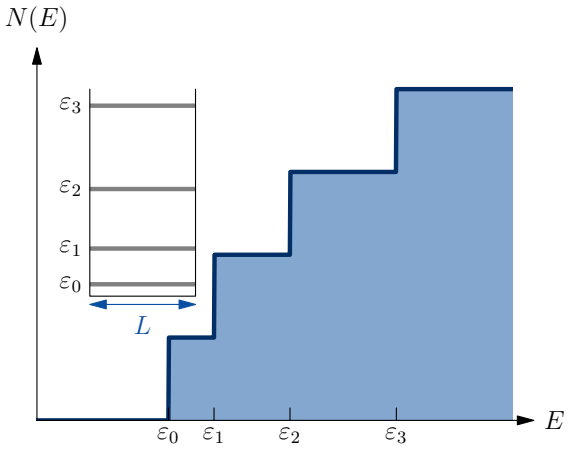

Figure 4.2: Schematic representation of the quasi-2D electronic density of states and the associated subbands ε_p due to quantum confinement, in the specific case of a in infinite square quantum well of width L.

by varying either the confinement parameters or the density, μ successively crosses the edge of different subbands: for a superconductor, this situation corresponds precisely to the regime where BCS pairing is governed by the band edge, as we described in section 3.3. In order to correctly describe the pairing temperature T_c for a confined system, it is necessary to take into account such effects. In this chapter, we will analyze the influence of quantum confinement on a BCS superconductor. For a quasi-2D geometry, we will see that T_c develops a continuous oscillatory evolution as a function of thickness L and density n, determined by the entrance of successive subbands into the pairing window (3.22): such phenomenon is known as shape resonances. Various aspects of this problem are analyzed in paper 3, for a confinement model composed of a single square quantum well of finite width L and depth U. A synthesis of low-density and quantum-confined superconducting system is provided by the quasi-2D interface between lanthanum aluminate and strontium titanate, $LaAlO_3/SrTiO_3$ (LAO/STO). In this case, we expect subband edges to play a relevant role for the critical properties like T_c. Since our formalism allows us to study superconductors in different dimensionality, given a model for confinement, we can ask ourselves whether quantum confinement in quasi-2D geometry, acting on superconducting bulk STO, can explain the doping dependence of T_c in thin films and at the interface. This investigation is pursued in section 4.4, at the end of this chapter. Before dwelling into the details of superconducting shape resonances, we first analyze in the many-body formalism how dimensionality and confinement determine the gap equation of a singlet mean-field superconductor; we then linearize the gap equation at T_c, to find an expression valid in a general single-particle basis for a BCS-like interaction, which can be specialized to different

geometries.

4.1 Gor'kov equations in a basis

4.1.1 Many-body mean-field decoupling

The BCS hamiltonian (3.18) belongs to the general class of condensed-matter hamiltonians composed of a single-particle kinetic term (3.9) and a two-body interaction term (3.10), with the latter providing the source of pairing in a superconductor. In general, we can write these hamiltonians as

$$\hat{H} = \sum_{\alpha\beta} \xi_{\alpha\beta} \hat{a}^\dagger_\alpha \hat{a}_\beta + \frac{1}{2} \sum_{\alpha\beta\nu_1\nu_2} V_{\alpha\beta\nu_1\nu_2} \hat{a}^\dagger_\alpha \hat{a}^\dagger_\beta \hat{a}_{\nu_2} \hat{a}_{\nu_1} \tag{4.1}$$

where $\{\alpha, \beta, \nu_1, \nu_2\}$ are eigenstates of the many-body system with matrix elements $\xi_{\alpha\beta}$, e.g $|\alpha\rangle = \left|\vec{k}, \sigma\right\rangle$ and $\xi_{\vec{k}}$ for electrons with momentum $\vec{k}$ and spin σ. $\left(\hat{a}_\alpha, \hat{a}^\dagger_\alpha\right)$ are the annihilation and creation operators acting on the eigenstate $|\alpha\rangle$.

Our interest is to study the effect of the potential $V_{\alpha\beta\nu_1\nu_2}$ on the single-particle eigenstates, in particular for low-dimensional systems, and specifically for BCS superconductors in this chapter. The equation of motion method for imaginary-time correlation functions is convenient in this case, because it shows transparently how correlations are neglected in the mean-field approximation. We start by defining the Green's matrix

$$\mathscr{G}_{\alpha\beta}(\tau) = -\left\langle \hat{\mathscr{T}}_\tau \hat{a}_\alpha(\tau) \hat{a}^\dagger_\beta(0) \right\rangle, \tag{4.2}$$

which is the correlation function for creation and annihilation operators $\left(\hat{a}_\alpha, \hat{a}^\dagger_\alpha\right)$. We can write the equation of motion for $\mathscr{G}_{\alpha\beta}(\tau)$, that reads [2]

$$-\frac{\partial}{\partial\tau}\mathscr{G}_{\alpha\beta}(\tau) = \delta(\tau)\delta_{\alpha\beta} + \sum_\gamma \xi_{\alpha\gamma}\mathscr{G}_{\gamma\beta}(\tau) + \sum_{\gamma\nu_1\nu_2} V_{\alpha\gamma\nu_1\nu_2} \mathscr{C}_{\left(\hat{a}^\dagger_\gamma \hat{a}_{\nu_2} \hat{a}_{\nu_1}\right)\hat{a}^\dagger_\beta}(\tau) \tag{4.3}$$

The correlation function $\mathscr{C}_{\left(\hat{a}^\dagger_\gamma \hat{a}_{\nu_2} \hat{a}_{\nu_1}\right)\hat{a}^\dagger_\beta}(\tau)$ results from the two-body portion of the hamiltonian (4.1). Equation (4.3) means that the relaxation of single-particle excitations described by $\mathscr{G}_{\alpha\beta}(\tau)$ occurs via the two-body interaction $V_{\alpha\beta\nu_1\nu_2}$ through processes involving the creation of particle-hole pairs. On its turn, the relaxation dynamics depends on the time evolution of $\mathscr{C}_{\left(\hat{a}^\dagger_\gamma \hat{a}_{\nu_2} \hat{a}_{\nu_1}\right)\hat{a}^\dagger_\beta}(\tau)$, which is controlled by higher-order processes in an infinite recursive series of equations of motion, involving an increasing number of ladder operators. [2]. Such an infinite series cannot be solved analytically. If Wick theorem applied,

we could decompose higher-order processes into products of terms involving two field operators at a time, and this way a solution could be obtained in closed form; unfortunately, this is not rigorously valid when two-body correlations are present. Nevertheless, we can obtain a good approximate solution employing mean-field decoupling, that we described in section 3.2.2: introducing the mean value of terms involving two field operators at a time, and neglecting fluctuations with respect to averages - i.e. higher order correlations - we rewrite equation (4.3) using only one-body terms, therefore obtaining an independent-particle approximation for the hamiltonian (4.1). Here we specialize to fermions having annihilation and creation operators $\left(\hat{c}_\alpha,\ \hat{c}_\alpha^\dagger\right)$, since we are going to apply this formalism to electrons. In the many-body formalism, the mean-field approximation yields

$$\mathscr{C}_{\left(\hat{c}_\gamma^\dagger \hat{c}_{\nu_2} \hat{c}_{\nu_1}\right) \hat{c}_\beta^\dagger}(\tau) \approx \left\langle \hat{c}_\gamma^\dagger \hat{c}_{\nu_2} \right\rangle \mathscr{G}_{\nu_1\beta}(\tau) - \left\langle \hat{c}_\gamma^\dagger \hat{c}_{\nu_1} \right\rangle \mathscr{G}_{\nu_2\beta}(\tau) + \left\langle \hat{c}_{\nu_2} \hat{c}_{\nu_1} \right\rangle \mathscr{F}_{\gamma\beta}^\dagger(\tau) \tag{4.4}$$

where we recognize the single-particle Green's function (4.2), as well as a new object $\mathscr{F}_{\gamma\beta}^\dagger(\tau)$. The latter is the *anomalous Green's function*, defined as

$$\mathscr{F}_{\alpha\beta}^\dagger(\tau) = -\left\langle \hat{\mathscr{T}}_\tau \hat{c}_\alpha^\dagger(\tau) \hat{c}_\beta^\dagger(0) \right\rangle \tag{4.5}$$

In the normal state of metals we have $\mathscr{F}_{\alpha\beta}(\tau) = 0$, since the hamiltonian commutes with the number operator. However, we are not going to solve the full hamiltonian (4.1), neither its effective BCS counterpart (3.18), but the mean-field approximation of (3.18), which does not commute with the number operator. In this case, we obtain a nonzero $\mathscr{F}_{\alpha\beta}^\dagger(\tau)$ in the mean-field approximation, which turns out to be proportional to the superconducting energy gap $\Delta_{\alpha\beta}$. This phenomenon is analogous to the appearance of a finite anomalous average $\left\langle \hat{c}_{\vec{k},\uparrow}^\dagger \hat{c}_{-\vec{k},\downarrow}^\dagger \right\rangle$ in the superconducting state, as mentioned in section 3.2.2.

Collecting the equations of motion of $\mathscr{G}_{\alpha\beta}(\tau)$ and $\mathscr{F}_{\alpha\beta}^\dagger(\tau)$, using a matrix notation, and going to the frequency domain, we obtain the two coupled equations known as the Gor'kov equations

$$(i\omega - \hat{K}_0)\mathscr{G}(i\omega) - \Delta\mathscr{F}^\dagger(i\omega) = \mathbb{1} \tag{4.6a}$$

$$(i\omega + \hat{K}_0^*)\mathscr{F}^\dagger(i\omega) + \Delta^*\mathscr{G}(i\omega) = 0 \tag{4.6b}$$

where we introduced the generalized single-particle hamiltonian

$$\hat{K}_0 = \hat{H} + V_H + V_X \tag{4.7}$$

as well as the Hartree and exchange mean fields, which modify the single-particle hamilto-

nian $\hat{H}$ at mean-field approximation

$$[V_H]_{\alpha\beta} = \sum_{\nu_1\nu_2} V_{\alpha\nu_1\beta\nu_2} \left\langle \hat{c}^\dagger_{\nu_1} \hat{c}_{\nu_2} \right\rangle = \sum_{\nu_1\nu_2} V_{\alpha\nu_1\beta\nu_2} lim_{\tau\to 0^-} \mathscr{G}_{\nu_2\nu_1}(\tau) \tag{4.8a}$$

$$[V_X]_{\alpha\beta} = -\sum_{\nu_1\nu_2} V_{\alpha\nu_1\nu_2\beta} \left\langle \hat{c}^\dagger_{\nu_1} \hat{c}_{\nu_2} \right\rangle = -\sum_{\nu_1\nu_2} V_{\alpha\nu_1\nu_2\beta} lim_{\tau\to 0^-} \mathscr{G}_{\nu_2\nu_1}(\tau) \tag{4.8b}$$

If the interaction is taken to be the Coulomb repulsion (3.8), the mean fields (4.8) correspond exactly to the Hartree and exchange mean fields, and the formalism reduces to Hartree-Fock theory; the mean-fields also play a similar role for other types of interaction $V_{\alpha\beta\nu_1\nu_2}$. If the two-body potential $V_{\alpha\beta\nu_1\nu_2}$ is positive (repulsive), then the exchange mean field $V_X < 0$ (attractive). However, this attractive exchange term does not produce any pairing, but it only lowers the energy levels of single-particle eigenstates. The gap equation is

$$[\Delta]_{\alpha\beta} = \sum_{\mu_1\mu_2} V_{\alpha\beta\mu_1\mu_2} \left[\mathscr{F}^\dagger_{\mu_2\mu_1}(\tau = 0^-) \right]^* \tag{4.9}$$

The Gor'kov equations (4.6) are valid for both spin-singlet and spin-triplet pairing.

4.1.2 Spin-singlet pairing

We now specialize equations (4.6) to the most common situation, namely spin-singlet pairing of electrons in a non-magnetic system. These assumptions are retained in the standard formulation of BCS theory. If pairing occurs only in the singlet channel, the gap Δ and the anomalous Green's matrix $\mathscr{F}^\dagger(i\omega)$ do not include any triplet component of the type $\uparrow\uparrow$ or $\downarrow\downarrow$. Furthermore, the assumption of a non-magnetic system implies that the Hamiltonian has no spin-flip term, and that the Green's function is diagonal in the spin indices: this allows to factorize out the spin part from both the hamiltonian and the Green's functions, so that we have

$$(i\omega - K_0)\mathscr{G}(i\omega) - \Delta\mathscr{F}^\dagger_{\uparrow\downarrow}(i\omega) = \mathbb{1} \tag{4.10a}$$

$$(i\omega + K_0^*)\mathscr{F}^\dagger_{\uparrow\downarrow}(i\omega) - \Delta^\dagger\mathscr{G}(i\omega) = 0 \tag{4.10b}$$

where now $\mathscr{G}$ represents the matrix with components $\mathscr{G}_{\alpha\uparrow\beta\uparrow}$ and $\mathscr{F}^\dagger$ has components $\mathscr{F}^\dagger_{\alpha\downarrow\beta\uparrow}$. The gap equation is

$$\Delta_{\alpha\uparrow\beta\downarrow} \equiv \Delta_{\alpha\beta} = \sum_{\mu_1\sigma_1\mu_2\sigma_2} V_{\alpha\uparrow\beta\downarrow\mu_1\sigma_1\mu_2\sigma_2} \left[\mathscr{F}^\dagger_{\mu_2\sigma_2\mu_1\sigma_1}(0^-) \right]^* \tag{4.11}$$

Now the indices α do not contain the spin degrees of freedom anymore, but refer only to the orbital part of the wave functions. If we consider an interaction which acts only between electrons of opposite spins, the gap equation further simplifies. We make this assumption since we often consider a contact interaction, and in this case, the interaction between parallel spins is forbidden by the Pauli principle [3]. For pairing between opposite spin states, we have $V(\vec{r}\sigma,\vec{r}'\sigma') = V(\vec{r},\vec{r}')\delta_{\sigma,-\sigma'}$, therefore the spin part can be separated from equations (4.10). The pairing potential in the basis of the single-particle orbital eigenstates $\varphi_\alpha(\vec{r})$ is

$$V_{\alpha\beta\mu_1\mu_2} = \int d\vec{r}_1 d\vec{r}_2\, \varphi^*_\alpha(\vec{r}_1)\varphi^*_\beta(\vec{r}_2)V(\vec{r}_1,\vec{r}_2)\varphi_{\mu_1}(\vec{r}_1)\varphi_{\mu_2}(\vec{r}_2). \tag{4.12}$$

Inserting the latter into equation (4.11), we find

$$\Delta_{\alpha\beta} = \sum_{\mu_1\mu_2} V_{\alpha\beta\mu_1\mu_2}\left[\mathscr{F}^\dagger_{\mu 2\downarrow\mu_1\uparrow}(0^-)\right]^* \tag{4.13}$$

The gap equation (4.13) is valid in general for a pairing interaction acting between opposite spin states: they show that the gap function $\Delta_{\alpha\beta}$ is proportional to the anomalous Green's function, which is a general feature of mean-field decoupling as previously mentioned. Now, in order to write $\mathscr{F}^\dagger$ explicitly - in terms of the single-particle eigenvalues ξ_α and the gap $\Delta_{\alpha\beta}$ itself - we first have to specify the form of the singlet pairing interaction $V_{\alpha\beta\mu_1\mu_2}$, and then to solve the Gor'kov equations (4.10) for $\mathscr{F}^\dagger$. In the following section we linearize the gap equation (4.13) at T_c in a generic single-particle basis, and then we specialize to the BCS interaction (3.17) with the aim of analyzing the pairing temperature for a BCS superconductor in different geometries.

4.1.2.1 Linearized equations at T_c

Since the anomalous propagator $\mathscr{F}^\dagger$ is proportional to the order parameter $\Delta = \{\Delta_{\alpha\beta}\}$, the linearized Gorkov equations are

$$(i\omega - K_0)\mathscr{G}(i\omega) = \mathbb{1} \tag{4.14}$$

$$(i\omega + K_0^*)\mathscr{F}^\dagger(i\omega) - \Delta^\dagger\mathscr{G}(i\omega) = 0 \tag{4.15}$$

which means that at T_c the electronic Green's function is the normal-state one $\mathscr{G} = \mathscr{G}_0$, in the absence of gap Δ. Hence, we can find the explicit solution for the anomalous term:

$$\mathscr{F}^{\dagger}(i\omega) = (i\omega + K_0^*)^{-1}\Delta^{\dagger}\mathscr{G}_0(i\omega)$$

$$\mathscr{F}^{\dagger}_{\mu_2\downarrow\mu_1\uparrow}(i\omega) = \sum_{\mu_3\mu_4} \underbrace{[(i\omega + K_0^*)^{-1}]_{\mu_2\mu_3}}_{\frac{\delta_{\mu_2\mu_3}}{i\omega+\xi_{\mu_2}}} \underbrace{[\Delta^{\dagger}]_{\mu_3\mu_4}}_{\Delta^*_{\mu_4\mu_3}} \underbrace{[\mathscr{G}_0(i\omega)]_{\mu_4\mu_1}}_{\frac{\delta_{\mu_4\mu_1}}{i\omega-\xi_{\mu_1}}} = \frac{\Delta^*_{\mu_1\mu_2}}{(i\omega-\xi_{\mu_1})(i\omega+\xi_{\mu_2})}.$$

We transform from imaginary frequency to imaginary time, as needed in equation (4.13), using the fact that

$$\frac{1}{\beta}\sum_{i\omega} e^{-i\omega 0^-}\frac{1}{(i\omega-\xi_{\mu_1})(i\omega+\xi_{\mu_2})} = \frac{f_{FD}(\xi_{\mu_1}) - f_{FD}(-\xi_{\mu_2})}{\xi_{\mu_1}+\xi_{\mu_2}}$$

and that, for the Fermi-Dirac distribution $f_{FD}(\xi)$, we have

$$f_{FD}(-\xi) = 1 - f_{FD}(\xi),$$

such that we find the gap equation valid at T_c:

$$\Delta_{\alpha\beta} = \sum_{\mu_1\mu_2} V_{\alpha\beta\mu_1\mu_2}\frac{\Delta_{\mu_1\mu_2}}{\xi_{\mu_1}+\xi_{\mu_2}}\left[f_{FD}(\xi_{\mu_1}) + f_{FD}(\xi_{\mu_2}) - 1\right]. \tag{4.16}$$

Equation (4.16) is written for a generic single-particle basis $\{\alpha\}$: therefore, it can be specialized to a given dimensionality, confinement geometry and type of singlet interaction, to find the pairing temperature T_c.

4.1.2.2 BCS T_c equation in a basis

We now specify the pairing interaction $V_{\alpha\beta\mu_1\mu_2}$ according to the BCS model [82]. This means assuming a local attraction between degenerate time-reversed pairs of states, denoted $(\alpha, \bar{\alpha})$, with a separable energy cutoff. In the homogeneous continuum, momenta $\vec{k}$ provide a good basis and the BCS interaction corresponds to the usual form, given by equation (3.17). In a generic single-particle basis, we have

$$\begin{aligned} V_{\alpha\beta\mu_1\mu_2} &= -V_{BCS}\delta_{\beta\bar{\alpha}}\delta_{\mu_2\bar{\mu}_1}\eta(\xi_\alpha)\eta(\xi_{\mu_1})\int d\vec{r}\,\varphi^*_\alpha(\vec{r})\varphi^*_{\bar{\alpha}}(\vec{r})\varphi_{\mu_1}(\vec{r})\varphi_{\bar{\mu}_1}(\vec{r}) \\ &\equiv -V_{BCS}\delta_{\beta\bar{\alpha}}\delta_{\mu_2\bar{\mu}_1}\eta(\xi_\alpha)\eta(\xi_{\mu_1})O_{\alpha\mu_1}. \end{aligned} \tag{4.17}$$

Notice that equation (4.17) has only one spatial integral over $\vec{r}$, while the generic singlet interaction (4.12) integrates over $\vec{r}_1$ and $\vec{r}_2$: this is because the BCS interaction is local, i.e. it acts only between two electrons at the same coordinate $\vec{r}_1 \equiv \vec{r}_2 = \vec{r}$.

Here we have defined the pairing overlap matrix elements

$$O_{\alpha\beta} = \int d\vec{r}\, \varphi^*_\alpha(\vec{r})\varphi^*_{\bar{\alpha}}(\vec{r})\varphi_\beta(\vec{r})\varphi_{\bar{\beta}}(\vec{r}). \tag{4.18}$$

Equation (4.18) shows that, with a BCS-like separable interaction (4.17), superconducting pairing depends on the overlap in space between paired eigenstates. This stems from the spatial locality of the BCS interaction. Since the eigenstates $\varphi^*_\alpha(\vec{r})$ are modified by quantum confinement, the interaction $V_{\alpha\beta\mu_1\mu_2}$ is altered in confined geometry as well: this is the origin of the so-called *shape resonances*, whereby the pairing interaction is changed by quantum confinement in a quasi-2D geometry.

As previously mentioned, in the homogeneous continuum the time-reversed pairs $(\alpha, \bar{\alpha})$ are the wave-vector states $(\vec{k}, -\vec{k})$, so the interaction is (3.17). Equation (4.16) shows that the order parameter can only pair time-reversed states as well,

$$\Delta_{\alpha\beta} = \delta_{\beta\bar{\alpha}}\eta(\xi_\alpha)\Delta_\alpha$$

and the gap equation becomes

$$\Delta_\alpha = \sum_{\mu_1} \eta^2(\xi_{\mu_1}) V_{BCS} O_{\alpha\mu_1} \frac{\Delta_{\mu_1}}{2\xi_{\mu_1}} \tanh\left(\frac{\xi_{\mu_1}}{2k_B T_c}\right). \tag{4.19}$$

Equation (4.19) gives the pairing temperature T_c for a BCS singlet interaction $-V_{BCS}$ with cutoff $\hbar\omega_D$ in a generic basis of states $\{\mu_1\}$. We will now specialize equation (4.19) to a quasi-2D system, in which one spatial direction is confined, thereby realizing a BCS superconductor in a quantum well. In the case of a finite square well, we obtain the situation depicted in figure 4.1, but many other geometries - e.g. triangular, parabolic, and so on - are possible. In the following, we will focus on a single square quantum well as the confinement model for simplicity: this allows one to write the overlap matrix elements (4.18) in closed form. Later, we will compare the square well solution to other typical confined geometries.

4.1.2.3 Quasi-two dimensional system

We consider a quasi-2D configuration with free particles along the coordinates x and y, and a confinement potential $U(z)$ acting along the z direction: the single-particle hamiltonian $\hat{K}_0$ is then

$$\hat{K}_0 = \frac{p^2}{2m} - \mu + U(z) \tag{4.20}$$

This allows us to factorize the eigenstates into a plane-wave portion $\frac{1}{\sqrt{\mathscr{S}}} e^{i\vec{k}_\parallel \cdot \vec{r}_\parallel}$ in the free direction $\vec{r}_\parallel = x\hat{u}_x + y\hat{u}_y$, with $\hat{u}_x$ and $\hat{u}_y$ unit vectors along x and y, and a confined z-eigenfunction $u_q(z)$ depending on the quantum number $q \in \mathbb{N}^+$. $\mathscr{S}$ is the 2-dimensional surface of the system in the unconfined xy plane. Hence, in real space we have

$$\varphi_\alpha(\vec{r}) \mapsto \varphi_{\vec{k}_\parallel}(\vec{r}_\parallel) u_q(z) = \frac{1}{\sqrt{\mathscr{S}}} e^{i\vec{k}_\parallel \cdot \vec{r}_\parallel} u_q(z) \tag{4.21}$$

The corresponding overlap matrix elements from equation (4.18) are

$$\begin{aligned} O_{\vec{k}_\parallel q \vec{k}'_\parallel q'} &= \int d\vec{r}_\parallel dz \, \frac{1}{\sqrt{\mathscr{S}}} e^{-i\vec{k}_\parallel \cdot \vec{r}_\parallel} u_q^*(z) \frac{1}{\sqrt{\mathscr{S}}} e^{i\vec{k}_\parallel \cdot \vec{r}_\parallel} u_{\bar{q}}^*(z) \frac{1}{\sqrt{\mathscr{S}}} e^{i\vec{k}'_\parallel \cdot \vec{r}_\parallel} u_{q'}(z) \frac{1}{\sqrt{\mathscr{S}}} e^{-i\vec{k}'_\parallel \cdot \vec{r}_\parallel} u_{\bar{q}'}(z) \\ &= \frac{1}{\mathscr{S}} \int dz \, u_q^*(z) u_{\bar{q}}^*(z) u_{q'}(z) u_{\bar{q}'}(z) = \frac{1}{\mathscr{S}} O_{qq'}. \end{aligned} \tag{4.22}$$

where we have defined the overlap matrix elements between paired states in the confined direction z,

$$O_{qq'} = \int dz \, u_q^*(z) u_{\bar{q}}^*(z) u_{q'}(z) u_{\bar{q}'}(z). \tag{4.23}$$

Equations (4.22) and (4.23) show that the overlap matrix elements in the well only depend on the egienfunctions u_q along z, but not on x and y: therefore the gap is independent of the in-plane momentum $\vec{k}_\parallel$. Also, the separable form of the hamiltonian (4.20) means that the eigenvalues are additive in the unconfined $\xi_{\vec{k}_\parallel}$ and confined ε_q directions, according to

$\xi_{\vec{k}_\parallel,q} = \xi_{\vec{k}_\parallel} + \varepsilon_q$. Hence, the gap equation stemming from equations (4.19) and (4.22) reads

$$\begin{aligned}
\Delta_q &= \sum_{\vec{k}_\parallel,q'} \eta^2(\xi_{\vec{k}_\parallel,q'}) V \frac{1}{\mathscr{S}} O_{qq'} \frac{\Delta_{q'}}{2\xi_{\vec{k}_\parallel,q'}} \tanh\left(\frac{\xi_{\vec{k}_\parallel,q'}}{2k_\mathrm{B}T_c}\right) \\
&= \sum_{q'} V O_{qq'} \Delta_{q'} \underbrace{\frac{1}{\mathscr{S}} \sum_{\vec{k}_\parallel} \eta^2(\xi_{\vec{k}_\parallel} + \varepsilon_{q'}) \frac{1}{2(\xi_{\vec{k}_\parallel} + \varepsilon_{q'})} \tanh\left(\frac{\xi_{\vec{k}_\parallel} + \varepsilon_{q'}}{2k_\mathrm{B}T_c}\right)}_{\int dE \underbrace{\frac{1}{\mathscr{S}} \sum_{\vec{k}_\parallel} \delta(E - \xi_{\vec{k}_\parallel} - \varepsilon_{q'})}_{N_{0q'}^{2D}(\mu+E)} \eta^2(E) \frac{1}{2E} \tanh\left(\frac{E}{2k_\mathrm{B}T_c}\right)} \\
&= \sum_{q'} V O_{qq'} \Delta_{q'} \int_{-\hbar\omega_\mathrm{D}}^{\hbar\omega_\mathrm{D}} dE\, N_{0q'}^{2D}(\mu + E) \frac{1}{2E} \tanh\left(\frac{E}{2k_\mathrm{B}T_c}\right). \qquad (4.24)
\end{aligned}$$

In equation (4.24) we transformed the sum over the wave vector $\vec{k}_\parallel$ into an integral over energy E, employing the 2D density of states for the q-th confined subband:

$$N_{0q}^{2D}(\mu + E) = \frac{1}{\mathscr{S}} \sum_{\vec{k}_\parallel} \delta(E - \xi_{\vec{k}_\parallel} - \varepsilon_q). \qquad (4.25)$$

Hence, as anticipated at the beginning of this chapter, we see from equation (4.25) that the effect of quasi-2D confinement on the band structure is to produce a series of 2D sheets in reciprocal space of momenta, labeled by the quantum number q. For a BCS superconductor, the pairing window extending from $\mu - \hbar\omega_D$ to $\mu + \hbar\omega_D$ determines which subbands contribute to Cooper pairing, depending on the relative position of the chemical potential μ with respect to the eigenvalues ε_q. A realistic quantum well has a finite energy barrier $U < +\infty$: states having energy $\varepsilon_q < U$ are *bound* by the potential well, while eigenvalues $\varepsilon_q > U$ belong to unbound states, also named *scattering* or *resonant* states [138]. Hence, we have to take into account this dichotomy of states when we consider a well of finite height. It is useful to imagine the system as composed by the well of width L, inserted into a larger box having dimension $\mathscr{L}$ in the confined z direction - see figure 4.3. In particular, we must split the q' sum in equation (4.24) to separate bound and scattering states. Whenever q and/or q' is a scattering state, the overlap integral $O_{qq'}$ is proportional to $1/\mathscr{L}$, such that we can take this factor away from the definition of the overlap, and use it to convert the sum over scattering states to an integral, assuming that the gap is the same for all scattering states, Δ_s, and likewise the overlap O_{qs}, and assuming moreover that the density of states

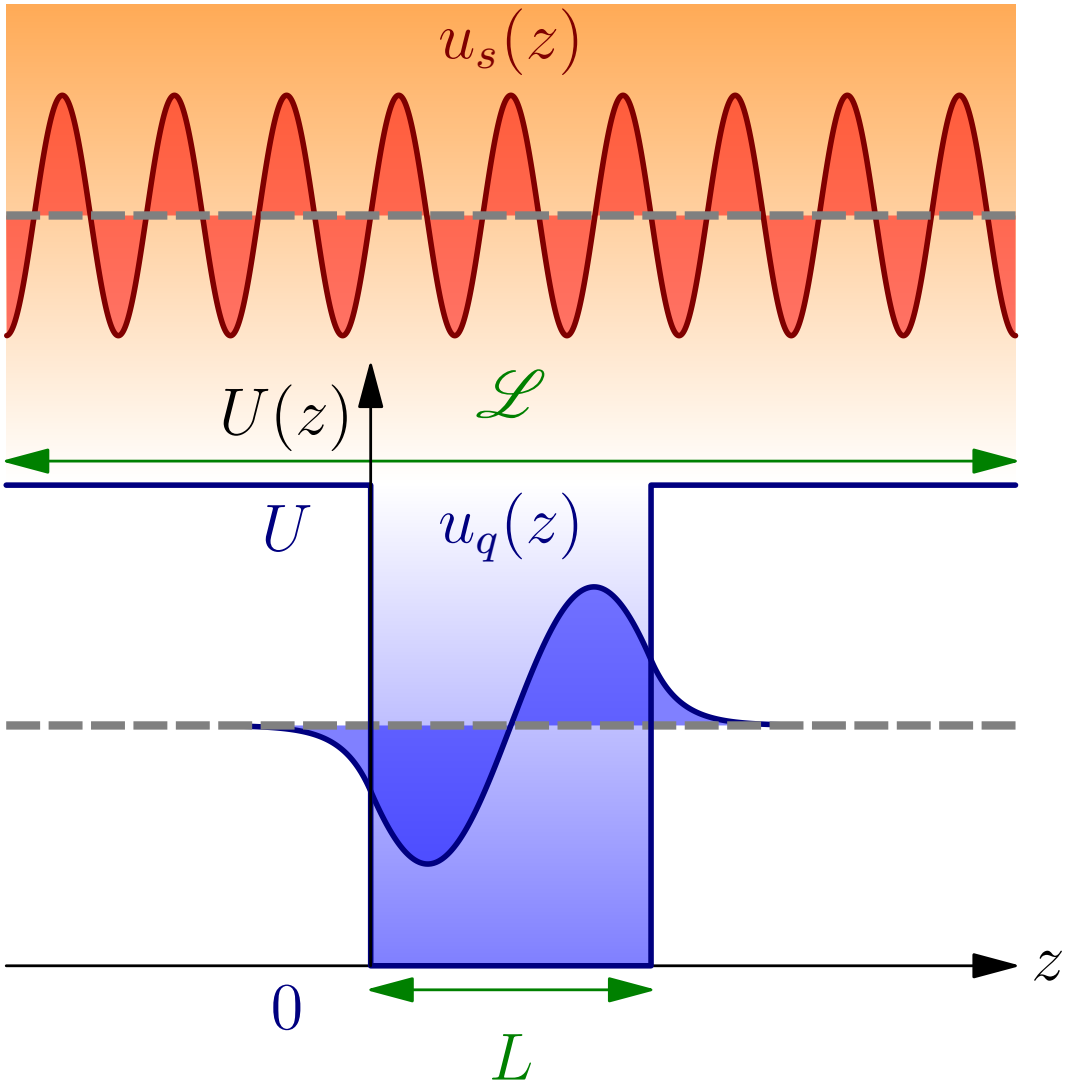

Figure 4.3: Schematic representation of the quasi-2D confinement geometry for the treatment of bound and scattering states, in the case of a rectangular quantum well of finite width L and depth U. The large orange-shaded box has lateral dimension $\mathscr{L}$, while the blue-shaded quantum well has width $L \ll \mathscr{L}$ in the confined z direction (horizontal axis). The confinement profile $U(z)$ (vertical axis) is rectangular, with energy barrier U: scattering states having energy $\varepsilon_s > U$ are unbound, while bound states of the quantum well have energy $\varepsilon_q < U$. One example of unbound eigenfunction $u_s(z)$, subjected to periodic boundary conditions in $\mathscr{L}$, is shown in red; one example of bound eigenfunction $u_q(z)$, obeying the finite-well boundary conditions in L, is shown in blue.

of the scattering state is not modified by the potential. Namely, we can write

$$N_0^{3D}(\mu+E-U)=\frac{1}{\mathscr{L}}\sum_{q'(\text{unbound})}\frac{1}{\mathscr{S}}\sum_{\vec{k}_\parallel}\delta(E-\xi_{\vec{k}_\parallel}-\varepsilon_{q'})\equiv\frac{1}{\mathscr{V}}\sum_{\vec{k}^{3D}}\delta(E-\xi_{\vec{k}^{3D}}-U) \quad (4.26)$$

where the total system volume is $\mathscr{V}=\mathscr{S}\mathscr{L}$. Therefore, for the bound states we have

$$\begin{aligned}\Delta_q &= \sum_{q'(\text{bound})} VO_{qq'}\Delta_{q'}\int_{-\hbar\omega_D}^{\hbar\omega_D} dE\, N_{0q'}^{2D}(\mu+E)\frac{1}{2E}\tanh\left(\frac{E}{2k_BT_c}\right)\\ &\quad+\frac{1}{\mathscr{L}}\sum_{q'(\text{unbound})} V\mathscr{L}O_{qq'}\Delta_{q'}\int_{-\hbar\omega_D}^{\hbar\omega_D} dE\,\frac{1}{\mathscr{S}}\sum_{\vec{k}_\parallel}\delta(E-\xi_{\vec{k}_\parallel}-\varepsilon_{q'})\frac{1}{2E}\tanh\left(\frac{E}{2k_BT_c}\right)\\ &= \sum_{q'(\text{bound})} VO_{qq'}\Delta_{q'}\int_{-\hbar\omega_D}^{\hbar\omega_D} dE\, N_{0q'}^{2D}(\mu+E)\frac{1}{2E}\tanh\left(\frac{E}{2k_BT_c}\right)\\ &\quad+V\mathscr{L}O_{qs}\Delta_s\int_{-\hbar\omega_D}^{\hbar\omega_D} dE\, N_0^{3D}(\mu+E-U)\frac{1}{2E}\tanh\left(\frac{E}{2k_BT_c}\right).\end{aligned}$$

For the scattering states, in principle the small potential well of width L influences the gap Δ_s in the continuum of width $\mathscr{L}\to+\infty$, as there are overlaps $O_{sq'}$ - see figure 4.4 for a finite square well. However, since $O_{sq'}\propto\frac{1}{\mathscr{L}}\to 0$, the presence of the small quantum well below negligibly alters the states in the continuum, and therefore we neglect such alteration of scattering states. The equation is

$$\begin{aligned}\Delta_s &= \underbrace{\sum_{q'(\text{bound})} VO_{sq'}\Delta_{q'}\int_{-\hbar\omega_D}^{\hbar\omega_D} dE\, N_{0q'}^{2D}(\mu+E)\frac{1}{2E}\tanh\left(\frac{E}{2k_BT_c}\right)}_{\to 0}\\ &\quad+V\mathscr{L}O_{ss}\Delta_s\int_{-\hbar\omega_D}^{\hbar\omega_D} dE\, N_0^{3D}(\mu+E-U)\frac{1}{2E}\tanh\left(\frac{E}{2k_BT_c}\right)\end{aligned}$$

which means that, with our approximations, the gap for the scattering states is the same as in the absence of potential. This way, normalizing the gap to that of the lowest bound state, the gap equation at T_c can be put in the form of an eigenvalue problem - see equation (1a) of paper 3, which depends on the couplings among all subbands and on the value of the chemical potential μ. The largest temperature that satisfies the characteristic equation is the pairing temperature T_c of the system. The chemical potential $\mu=\mu(T_c)$ is set at the pairing temperature T_c self-consistently, adjusting itself in accordance with the given 3D density n - see equation (1b) of paper 3. The solution for T_c depends on the specific

confinement geometry $U(z)$, that determines the energies ε_q. In paper 3, we solve the problem for T_c in a square confinement potential of length L, in the case of an infinite and a finite potential barrier U; this case is illustrated in figure 4.3.

There is still one detail to discuss regarding scattering states, i.e. in the case $\varepsilon_q > U$. In principle, the bound states are coupled to the continuum through the overlaps O_{qs}. We have assumed that this overlap, as well as the gap Δ_s, are the same for all scattering states. Hence we have to choose a suitable value for the overlap O_{qs}, which is representative of all scattering states. Moreover, the scattering states contribute to the total density n, and their influence on the density equation (1b) of paper 3 must be considered as well, particularly in the case when a state enters into the well from the continuum, thus becoming bound. In the following section, we present our treatment of aforementioned issues involving scattering states for a square potential well.

4.1.2.4 Treatment of scattering states for a square potential well

For a square potential well of width L and height U, we find that the overlap O_{qs} is a function of the energies ε_q and ε_s. This function approaches unity for all ε_s when ε_q approaches U. For smaller values of ε_q, the function decreases to zero at small ε_s with oscillations depending on L. In paper 3 we have found it convenient to use $\hbar\omega_D$ as the unit of energy, and $n_1 = 2\left(\frac{m\omega_D}{2\pi\hbar}\right)^{\frac{3}{2}}$ as the unit of density in 3D. We take the same convention here. Some examples of the energy evolution of O_{qs} are depicted in figure 4.4, where we show the overlap $\mathscr{L}O_{qs}$ for a bound state having energy $\varepsilon_q = 0.1\hbar\omega_D$, as a function of the scattering state energy ε_s in units of the cutoff energy $\hbar\omega_D$. The well depth is set to $U = \hbar\omega_D$. Blue, red and gold curves correspond to a normalized well thickness $(n_1)^{\frac{1}{3}}L = \{1, 2, 5\}$ respectively.

In line with our assumption that all scattering states share the same gap, we must replace O_{qs} by a single value which is representative for all bound and scattering states. For simplicity we choose the value $O_{qs} = 1$, which is the limit for large ε_s, as we see in figure 4.4. For the overlap of scattering states, we find $O_{ss} = 1$.

The scattering states give a small contribution to the total density. In first approximation, the density contributed by the scattering states is that of a 3D electron gas with chemical potential $\mu - U$. However, when we vary the well thickness L, some scattering states enter the well and become bound at particular values of L. This situation must be handled carefully, because in our approximations the new bound state leads to a discontinuous jump in the density of states. In an exact treatment there would be a deformation of the continuum, such that the evolution of the density of states with L is smooth. We mimic

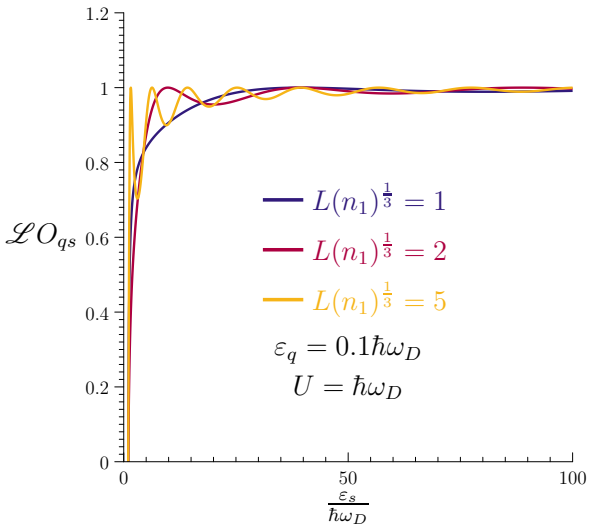

Figure 4.4: Adimensional pairing overlap $\mathscr{L}O_{qs}$ for a bound state having energy $\varepsilon_q = 0.1\hbar\omega_D$, as a function of scattering state energy $\varepsilon_s/(\hbar\omega_D)$ with cutoff energy $\hbar\omega_D$, for a square quantum well of thickness L and depth $U = \hbar\omega_D$. Blue, red and gold curves correspond to a normalized well thickness $(n_1)^{\frac{1}{3}}L = \{1, 2, 5\}$ respectively, with 3D density unit $n_1 = 2\left(\frac{m\omega_D}{2\pi\hbar}\right)^{\frac{3}{2}}$.

this smooth evolution by continuing the localized state into the continuum and taking its contribution into account before it gets localized, on top of the contribution of other scattering states. The details of this model are reported in the appendix of paper 3.

4.2 Superconducting shape resonances

4.2.1 Theory

With the results of section 4.1.2.3 at our disposal, we are now ready to analyze the effect of quasi-2D confinement on T_c for a BCS superconductor: we can solve self-consistently for the pairing temperature T_c to analyze the dependence of the latter on density and confinement parameters. In the following, we focus on the finite square well geometry, for which we have an analytic expression of the pairing overlaps for bound and scattering states, as we have seen in section 4.1.2.4. This geometry is suitable to model a free-standing superconducting thin film of thickness L, with a potential barrier U of the order of the material work function, i.e. the difference between the Fermi level inside the material and vacuum. When analyzing thin films, it is convenient to fix the value of n_{3D}, which corresponds to the intrinsic density of conduction carriers in metals or to the dopant concentration in doped semiconductors. This way, we can look at how T_c varies with film thickness at constant n_{3D}, for a given bulk coupling λ; fixig L and analyzing T_c as a

function of density, one retrieves the non-analytic increasing function of n_{3D} described in paper 2. The result of changing L is to move the relative position of the chemical potential with respect to quantized subbands ε_p: therefore, the BCS pairing window (3.22) moves with μ as well, so that different subbands enter and exit from the pairing window itself. Each time a new subband enters into the window, that subband starts to contribute to superconducting pairing, hence we expect an *increase* of T_c in that condition; then, since the individual subband couplings *decrease* with increasing thickness - see equation (5) of paper 3 - T_c *decreases* until a new subband comes into play. In summary, the pairing temperature displays an oscillatory evolution as a function of film thickness, known as shape resonances. In particular, depending on n_{3D}, λ and U, T_c can be *higher* than the bulk value $T_c^{3D} = lim_{L\to+\infty} T_c(L)$. The sharp steps in the quasi-2D density of states of figure 4.2 would cause abrupt changes in T_c, producing discontinuities at each $\mu = \varepsilon_p$, if the cutoff of the pairing window and the energy dependence of the density of states at subband edges were not considered. Indeed, previous studies [139–149] tracing back to the work of C. J. Thompson and J. M. Blatt [150, 151] neglected the presence of aforementioned subband edges, and obtained discontinuous functions for $T_c(L)$ in an infinite square well, where the oscillation amplitudes are overestimated and the characteristic peak-to-peak periodicity is altered with respect to the full solution comprising subband edges. Hence, we see that the results of paper 2 are essential to provide an exact mean-field calculation of T_c in superconducting thin films; in particular, the consideration of subband edges allows us to discover the presence of a T_c maximum in the low-thickness one-subband regime, which can be studied as a function of density, coupling and confinement barrier. The discrepancies between the exact mean-field solution and the one neglecting subband edges increase as the density is lowered, while the two solutions consistently converge in the high-density limit $n_{3D} \gg n_1$, with 3D density unit $n_1 = 2\left(\frac{m\omega_D}{2\pi\hbar}\right)^{\frac{3}{2}}$, where the standard BCS approximations become increasingly accurate. Moreover, studying T_c as a function of confinement barrier, we see that there is a critical value $U = U^*$ below which T_c is always *lower* than the bulk value at all thicknesses, while for $U > U^*$ T_c *increases* with respect to T_c^{3D}; U^* turns out to be an almost-universal function of the product $\lambda\, n_{3D}$ - see figure 7 of paper 3. The physical meaning of these findings is that, by lowering the confinement barrier, the confined eigenstates u_p are increasingly penetrating outside the barrier, "leaking out" of the well: this weakens pairing inside the well and is detrimental to T_c. Hence, we see that the thin-film pairing temperature can be higher or lower than the bulk value, depending on U: quasi-2D confinement does not always lead to a T_c increase. A higher ratio of the thin-film T_c relative to the bulk value is obtained when we go to low density and low coupling, according to the mean-field treatment. Various aspects of this problem

and the mathematical details are presented in paper 3 at the end of this chapter, for a finite square quantum well.

More elaborate confinement geometries are possible: an asymmetric rectangular well can model a thin film grown on a substrate; a triangular well can describe the confinement profile created by an electric field at polar interfaces; a parabolic well is appropriate for local electrostatic potentials created by Coulomb interaction on charged carriers, and so on. Nevertheless, the quantization of confined states and its impact on the density of states and on the pairing interaction are general features of quasi-2D superconductors, so that we expect the evolution of T_c to be qualitatively similar for different confinement geometries. Additional effects, not considered by the mean-field solution of paper 3, can significantly alter the experimental results with respect to the theoretical predictions. Superconducting fluctuations of amplitude and phase, already mentioned in section 3.2.2, can influence the behaviour of T_c at low density and thickness. Disorder can significantly alter the conduction dynamics both in the normal and in the superconducting state, also leading to superconductor-insulator transitions [152–154]; in appendix E, we sketch how the BCS gap equation (4.19) changes when we introduce a frequency- and momentum-independent scattering rate Γ, in the same spirit as for the normal-state Green's function of section 1.4.1. The band structure of the material is also modified at very low thickness, in a way not captured by simple discretized subbands. Also, retardation effects in electron-phonon interaction and other strong coupling phenomena are not included into the BCS description. The mean-field prediction of continuous T_c oscillations with thickness in superconducting thin films, and the possibility of increasing T_c in the low-thickness regime, calls for possible experimental tests. For this reason, we present a brief review of recent experiments on epitaxial thin films in the following section.

4.2.2 Experiments on epitaxial thin films

The constant progress in thin-film growth technologies during the last decades allows to produce high-quality epitaxial thin films at the nanometric scale for a variety of materials, some of which become superconducting at low temperatures. The control over the film thickness offers viable experimental tests for the shape resonances described in section 4.2.1, with the ultimate aim of improving the superconducting performances. In figure 4.5, we show some selected data on the ratio $\frac{T_c}{T_c^{3D}}$ as a function of film thickness for epitaxial thin films of lead on silicon substrate [155], niobium nitride on magnesium oxyde substrate [156], tin on alumina substrate [157], as well as for $SrTiO_3$/Nb:$SrTiO_3$/$SrTiO_3$ nanostructures [158]. Other references for experiments on superconducting thin films and

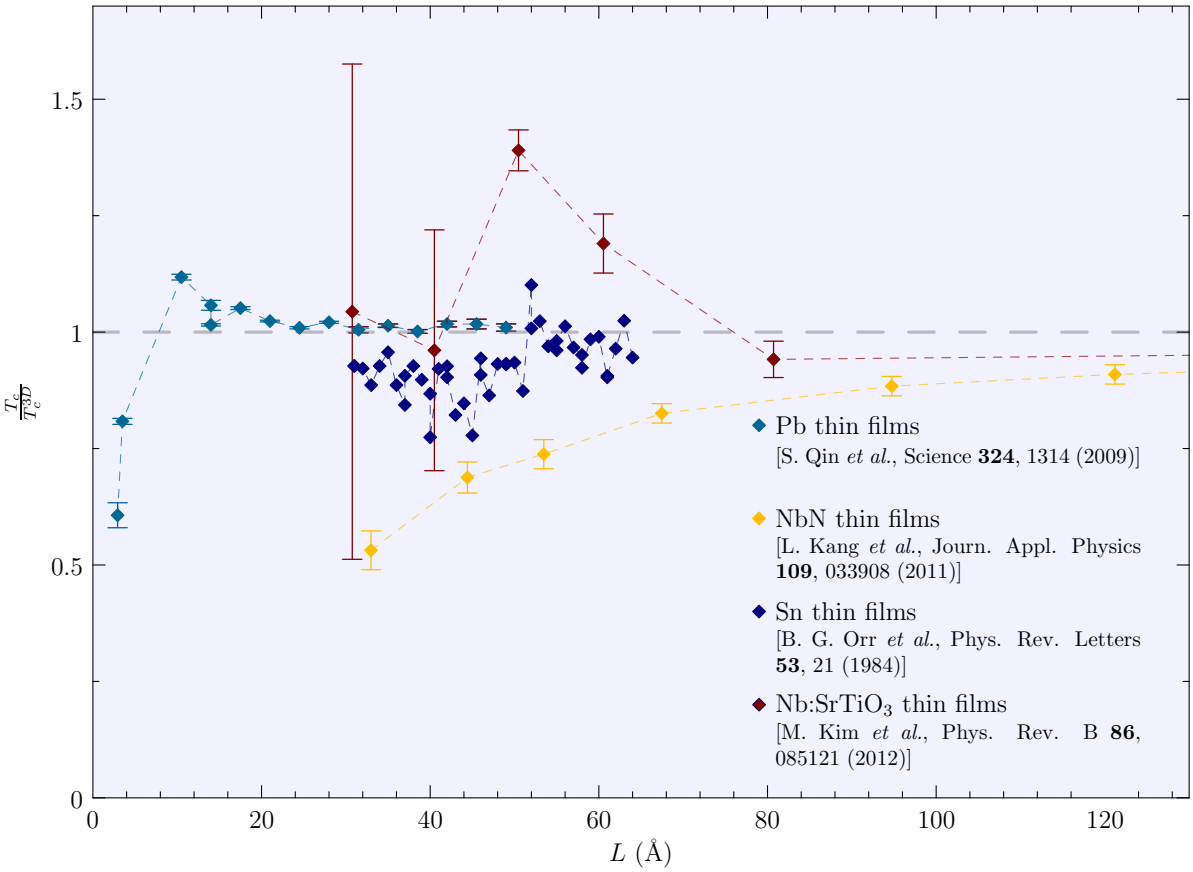

Figure 4.5: Critical temperature $\frac{T_c}{T_c^{3D}}$ divided by the bulk value T_c^{3D} as a function of film thickness L for different datasets. Cyan points: Pb/Si(111) [155]; gold points: NbN/MgO [156]; blue points: Sn/Al_2O_3 [157]; red points: $SrTiO_3/Nb{:}SrTiO_3/SrTiO_3$ nanostructures [158]. Vertical error bars are shown whenever reported in the respective reference.

islands can be retrieved in paper 3.

From figure 4.5, we see that the thin-film T_c can be higher or lower than the measured bulk value, depending on the material. As mentioned in section 4.2.1, one possible factor that contributes to this dichotomy is the confinement barrier U, which may be higher or lower than the critical value U^*. Hence, a systematic estimation of the latter quantity for different materials can help in identifying the best candidates for a T_c enhancement at the nanometric scale. Oscillations of the measured pairing temperature as a function of film thickness are observed in Sn, Pb and $SrTiO_3/Nb{:}SrTiO_3/SrTiO_3$, with T_c exceeding T_c^{3D} in the latter two cases, beyond experimental uncertainty. Continuous improvement on thin film quality can hopefully provide new measurements to investigate quasi-2D confinement of BCS superconductors. We consider specifically the dataset of reference [155] in section VI of paper 3. The case of strontium titanate is particularly interesting for our analysis, since doped $SrTiO_3$ is a low-density Fermi liquid with a superconducting ground state

already in the bulk, as we described in chapter 3. In particular, in section 3.3.1 we have developed a minimal 2-band BCS model to describe superconductivity in bulk doped $SrTiO_3$, including the presence of band edges. Therefore, we can ask ourselves how T_c changes when we confine strontium titanate in quasi-2D geometry. The calculation of T_c as a function of doping in the confined configuration can shed new light on the relation between the superconducting properties of bulk doped STO and of the $LaAlO_3/SrTiO_3$ interface (LAO/STO hereafter). In the next section, we summarize the fundamental properties of LAO/STO which concern our analysis, while the comparison between the bulk and the interface T_c domes within a simple square well potential is presented in section 4.4.

4.3 The LAO/STO interface: a low-density quantum- confined superconductor

Shape resonances in thin films are only one of the possible methods to modify the properties of superconductors by controlling geometry and confinement with experimentally accessible techniques. In fact, the search for superconductors with novel electronic properties has benefited from recent advancements in material engineering: the design and fabrication of epitaxial heterostructures led to the discovery of artificial superconducting systems, with the interface between the band insulators $LaAlO_3$ (LAO) and $SrTiO_3$ (STO) being one of the most known examples [159–161]. The interplay among charge, spin and orbital degrees of freedom at this interface originates quantum confinement [125, 159, 162], superconductivity [163, 164], ferromagnetism [165, 166], spin-orbit coupling [105], all influencing each other to various degrees. From that date, the field of transition metal oxide interfaces has been expanding in different directions: recent developments include the search for topological states [167], spin-polarized electron gases [168] and multiferroic coupling [169, 170].

4.3.1 Charge accumulation

Conduction carriers of LAO/STO reside in a quasi-2D electron liquid (Q2DEL), generated on the STO side of the interface [171] by charge accumulation in a potential well due to quantum confinement. The Q2DEL is formed when LaO and TiO_2 are the atomic planes facing each other at the interface, and when the LAO layer thickness exceeds 3 unit cells [159]. The driving mechanism for the charge accumulation at the interface is still a controversial subject, however the main proposed explanations can be divided into

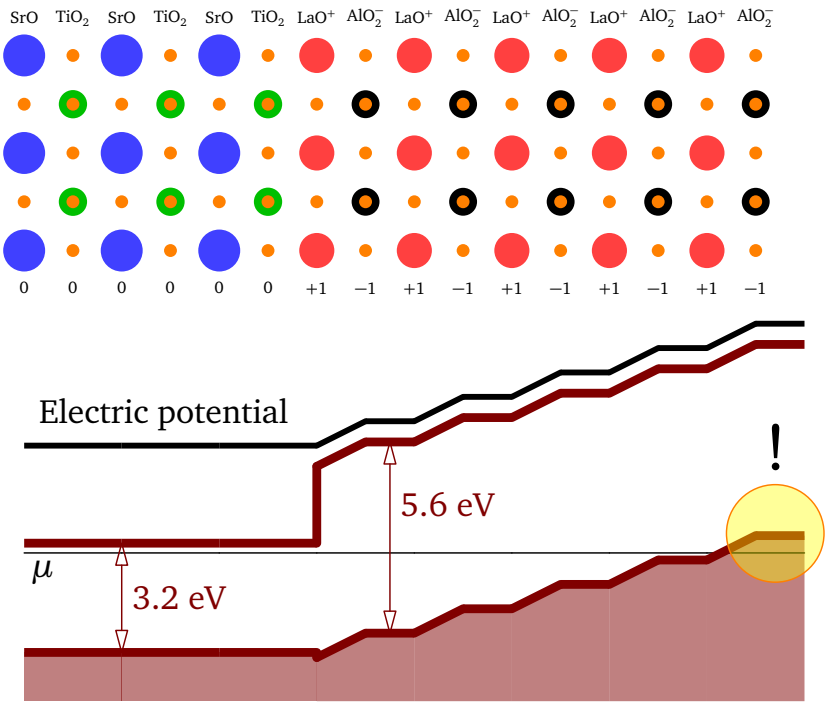

Figure 4.6: Schematic representation of the polar catastrophe scenario for charge accumulation in the q2DEL at the LAO/STO interface. The top part of the figure shows the atomic structure at the interface: LAO grows in a series of atomic planes (LaO) and (AlO_2) carrying a formal +1 and −1 electronic charge, respectively, while STO grows as a set of non-polar planes (SrO) and (TiO_2). The interface band alignment is shown below, with the STO and LAO energy gaps of 3.2 eV and 5.6 eV respectively. The chemical potential μ is common between the two materials in thermodynamic equilibrium. An electric potential (black line) grows with the number of polar LAO monolayers, until the potential reaches the energy gap of STO (see exclamation point) and Zener breakdown occurs, which causes the compensating migration of electrons towards the q2DEL [175].

two categories: *extrinsic* scenarios which refer to the interface stoichiometry, and *intrinsic* scenarios whereby electrons move to the interface because of the interface atomic structure and the polar nature of LAO. According to the extrinsic picture, interface electrons could be at least partly supplied by oxygen vacancies in STO [172] or by cationic intermixing [173, 174]. An alternative, or complementary, intrinsic mechanism links the origin of the carrier density to the polar nature of the LAO layer: along the [001] direction, this material grows as a series of atomic planes (LaO) and (AlO_2) carrying a formal +1 and -1 electronic charge, respectively. On the other hand, STO grows as a set of non-polar planes (SrO) and (TiO_2). Such a structure is schematically illustrated in figure 4.6. The interface band alignment is also shown, with the STO and LAO energy gaps of 3.2 eV and 5.6 eV respectively. The chemical potential μ is common between the two materials in thermodynamic equilibrium.

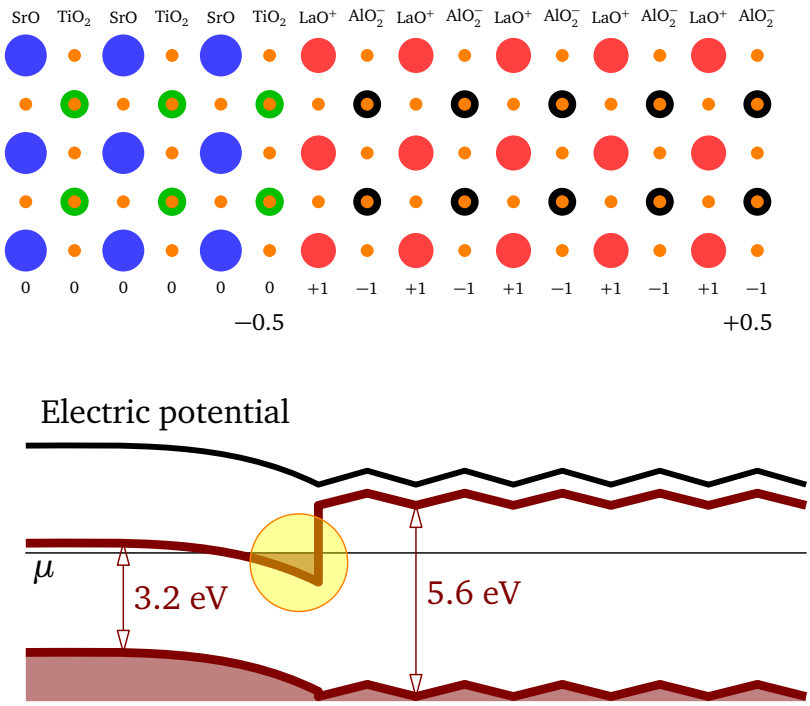

Figure 4.7: Schematic representation of the electrostatically-induced q2DEL at the LAO/STO interface, resulting from the polar catastrophe scenario of figure 4.6. The band bending at the interface forms a potential well for charged carriers, which is highlighted by a yellow circle.

This alternation of LAO polar planes induces a polar discontinuity and an electric potential (black line in figure 4.6) that grows with the LAO layer thickness. When this potential equals the energy gap of STO (see exclamation point in figure 4.6), a Zener breakdown can occur, whereby electrons are transferred from the top of the valence band of LAO to the interface conduction band of STO [171]. The predicted transferred charge amounts to $\frac{1}{2}$ electrons per unit cell, corresponding to a sheet carrier density $n_{2D} = 3.3\ 10^{14}\ cm^{-2}$ [175]. This configuration is sketched in figure 4.7, where the electrostatically-induced potential well hosting the Q2DEL is highlighted by a yellow circle.

The minimum value of 4 LAO unit cells for the occurrence of electron transfer has been predicted by ab-initio calculations [176, 177] and confirmed by transport experiments [163, 178]. Further support for the role of the polar discontinuity has been gained by alloying the LAO layer with STO, which results in a change of the critical LAO thickness for interface conductivity [179]. Nevertheless, there are still problems associated with the intrinsic scenario. Hall effect measures carrier densities that are one order of magnitude lower than the predicted polar catastrophe value, possibly due to charge localization. Moreover, the potential gradient inside the LAO layer and the corresponding hole band arising from the electron transfer have not been seen by spectroscopic measurements

[180–182]. Recent proposals invoke a combination of the extrinsic and intrinsic scenarios; for recent reviews on the growth methods and the charge accumulation mechanisms at the LAO/STO interface, see e.g. references [162, 175]. Regardless of the specific mechanism underlying the formation of the interface Q2DEL, its presence on the STO side highlights the role of quantum confinement on the STO band structure, which is deeply connected to the electronic properties of LAO/STO. Indeed, it is also possible to create Q2DELs in STO (001) single crystals by different means, all giving rise to similar electronic transport phenomena: such techniques include bombardment of Ar^+ ions [183], electrolyte gating [184], hydrogen adsorption [185] or deposition of amorphous [186] and nonperovskite oxides [187]. Furthermore, Q2DELs are known to be produced at other types of interfaces involving a Mott insulator and STO, i.e. $LaTiO_3$/STO (LTO/STO) [188] and $GdTiO_3$/STO (GTO/STO) [189] The LTO/STO heterostructure displays very similar properties to those of LAO/STO; this supports the prominent role of confined STO in the physics of these interfaces.

One key point for our analysis - see section 4.4 - is that in LAO/STO the Hall sheet carrier density is of the order of $n_{2D} \approx 10^{13}\ cm^{-2}$, which translates as a 3D carrier density $n_{3D} = \frac{n_{2D}}{L} \approx 10^{20}\ cm^{-2}$ if we employ the measured thickness $L \approx 10\ nm$ of the Q2DEL [125, 162, 190]. Since n_{3D} is two orders of magnitude lower than the values in standard metals - see e.g. Al in chapter 2 - we realize that LAO/STO is a low-density system, as it is bulk doped STO - see section 3.3.1. Therefore, when analyzing superconductivity at the interface, we have to take into account the presence of subband edges, in the way described in chapter 3. This argument is further reinforced by the presence of interface quantum confinement, which creates subbands and generates shape resonances. We review the essential features of quantum confinement for LAO/STO in the following section.

4.3.2 Quantum confinement

The 2D nature of the Q2DEL, which indicates that carriers are indeed confined on the STO side of the interface, is revealed by various experimental techniques: transport [163, 164, 191], atomic force microscopy [190], infrared ellipsometry [192], X-ray photoelectron spectroscopy [193], all infer an order of magnitude of $1 \div 10\ nm$ for the spatial extension of the gas in the direction perpendicular to the interface, depending on temperature. These findings are in accordance with band structure calculations [162], aimed at investigating the confinement spatial profile and the symmetry and carrier density of individual subbands. As we have seen in figure 4.7, the Q2DEL is quantum-confined due to the interface electric field: the band bending at the interface creates a quantum well of close-to-triangular shape.

This spatial profile can be analyed either by ab initio calculations or model hamiltonians. Ab initio methods reveal that the lowest-energy states at the Γ point, resulting from the Ti 3d levels (see section 3.3.1) have d_{xy} symmetry for the first few TiO_2 planes close to the interface, while farther from the interface the dominant state symmetry changes to d_{xz} /d_{yz} states having higher energies and with eigenfunction tails extending further into STO [194–196]. The d_{xy} states have higher effective mass than d_{xz}/d_{yz} states in the direction perpendicular to the interface, and they might be localized by disorder in practice: this could explain the discrepancy between the polar catastrophe transferred density and Hall measurements [162]. Doping-dependent band structure calculations compared to polarized ARPES experiments have investigated the connection between the Fermi surface shape and the measured carrier density [197]. However, at present ab initio calculations still suffer from finite size effects due to the limited STO layer thickness used in the simulations, which affects the resulting band structure. Furthermore, the strong dependence of the STO dielectric constant with electric field and doping - see also section 3.3.1 - deeply affects the dielectric screening at the interface, in a way not quantitatively reproduced by calculations [184, 198]. Model hamiltonians allow to selectively study some aspects of the confinement problem, such as the effect of an electric field on the STO band structure without spin-orbit coupling and tetragonal distortion [177], the dependence of the LAO/STO subband energies on the transferred carrier density [199], or the role of the STO dielectric constant [200]. Nevertheless, the presence of Rashba-Dresselhaus spin-orbit coupling at the interface [201–203] has yet to be included in the calculations and may have non-negligible consequences for the resulting band structure.

All above considerations highlight the complexity of the LAO/STO band structure: on the theoretical side, the relative contributions of many intertwined degrees of freedom are not precisely known, while direct comparison of subband energies with experiments is complicated by a still limited experimental resolution [162]. However, the electrostatic nature of quantum confinement for the LAO/STO Q2DEL offers another experimental way to investigate the relation between transferred carrier density and band structure: the value of n_{2D} can be tuned by diluting LAO with STO thereby changing the polar discontinuity strength [179], by gating with an electric field on the STO side (back gating [184]) or on LAO (top gating [204]), or combining polar interfaces and field-effect [164, 178]. The mechanism at play can be summarized as follows: an external negative (positive) electric field reduces (increases) the sheet carrier density [164], while simultaneously modifying the spatial profile of confinement, which reacts to the presence of charged carriers in a self-consistent way. This reciprocal feedback of confinement and density has inspired Poisson-Schroedinger calculations of the interface confinement potential, which rely on

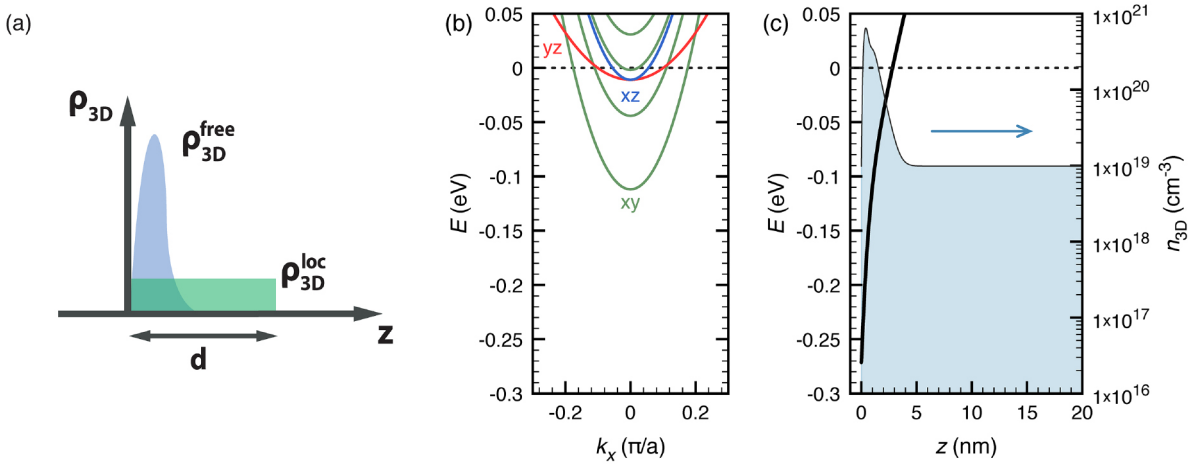

Figure 4.8: (a) Schematic view of the assumed carrier density profile which results from the the sum of the q2DEL mobile charges (ρ_{3D}^{free}, in blue), and localized charges (ρ_{3D}^{loc}, in green). The assumption of localized charges is made to explain the discrepancy between the predicted electron transfer from polar catastrophe and the measured Hall carrier density [162]. (b) Results of Poisson-Schroedinger simulation assuming a total transferred carrier density of 0.25 electrons per unit cell, of which 0.15 electrons per unit cell are trapped, i.e. not mobile. Green: sub-bands with xy symmetry; Red: sub-bands with yz symmetry; Blue: sub-bands with xz symmetry. (c) Confining potential (black) and 3D electron density (light blue) obtained from the Poisson-Schroedinger simulation. From reference [162].

the effective mass and envelope function approximations [162]: given a sheet carrier density n_{2D}, the Schroedinger equation for eigenstates in the orthogonal direction to the interface z, and the Poisson equation determining the local 3D density $n_{3D}(z)$, are solved self-consistently to find the density $n_{3D}(z)$ and confinement $U_{PS}(z)$ profiles. Figure 4.8 reports one example of such calculations for the LAO/STO interface. Similar supercell calculations have been performed for the STO surface electron liquid and compared to ARPES experiments [123, 205], revealing an analogous confinement physics.

In a broad perspective, quantum confinement at the LAO/STO interface may be regarded as an instance of quasi-2D configuration, obtained by confining the bulk bands of STO in a quantum well. From the above discussion, we know that electrons are confined within a distance of the order of $L \approx 10\ nm$. Therefore, at first approximation, we may consider the problem of confining STO into a square quantum well of thickness L, to draw a connection between the band structures in the bulk and at the interface. This can help in identifying similarities and differences between the latter two geometries, especially as far as superconductivity is concerned: we can employ the minimal model for the bulk STO band structure and BCS pairing interaction of section 3.3.1, and then apply quasi-2D confinement as for shape resonances. This approach is developed in section 4.4. As we have discussed in this section, the real confinement profile is not square but rather close-to-triangular, and

the accumulated charge modifies the quantum well shape self-consistently. Therefore, the effective quasi-2D band structure of section 4.4 is only a first approximation. Utilizing a triangular or self-consistent confinement potential could provide a better playground to investigate the couplings among realistic LAO/STO subbands. Nevertheless, if the physics at play is the one of superconducting shape resonances in a thickness $L \approx 10\ nm$, we do not expect qualitative changes for the doping evolution of T_c with respect to the square well solution. A quantitative comparison between shape resonances obtained in different confinement geometries could demonstrate this conjecture. As in bulk doped STO, superconductivity is indeed observed in the gate-tunable LAO/STO Q2DEL. The following section summarizes the essential aspects of this phenomenon and complements the discussion in section 4.4.

4.3.3 Superconductivity

The Q2DEL at the LAO/STO interface shows a superconducting ground state [163] with a maximum critical temperature $T_{c,max} \approx 350\ mK$, comparable to the one of bulk doped STO. Field effect allows one to tune the interface superconductivity, changing the sheet carrier density with gate voltage while simultaneously modifying the confinement potential as described in section 4.3.2. This way, one traces a dome-shaped phase diagram of T_c as a function of n_{2D} [164], reminiscent of the bulk STO domes, while the Q2DEL superconducting thickness remains of the order of $L \approx 10 \div 30\ nm$ throughout the phase diagram [125, 175]. The estimation of this superconducting thickness is extracted from the angular dependence of the critical field [125, 175]. With magnetic field aligned perpendicularly to the interface, one extrapolates the zero-temperature coherence length ξ_0 from $\mu_0 \lim_{T\to 0} H_{c\perp} = \frac{\Phi_0}{2\pi(\xi_0)^2}$, where μ_0 is the vacuum magnetic permeability and $\Phi_0 = \frac{h}{2e}$ is the flux quantum. This coherence length is renormalized into the Pearl length [206] by the superconducting thickness L in perpendicular-field configuration, provided that $\xi_0 \gg L$. In parallel field configuration, this renormalization does not happen and this allows one to extract L from $\mu_0 \lim_{T\to 0} H_{c\parallel} = \frac{\sqrt{3}\Phi_0}{\pi\xi_0 L}$. The experimental in-plane coherence length remains larger than the superconducting thickness at all dopings [125, 162], which is consistent with the 2D character of the superconducting q2DEL.

Transforming the sheet carrier density in a 3D value by $n_{3D} = \frac{n_{2D}}{L}$ [175], we can directly superimpose the doping phase diagrams in the bulk and at the interface, as shown in figure 4.9: the bulk T_c data (blue squares) corresponds to the transport measurements of reference [94], that we have already utilized in section 3.3.1, while the interface T_c (red circles) employs the dataset By A. Fête et al. [175], also utilized in section 4.4.

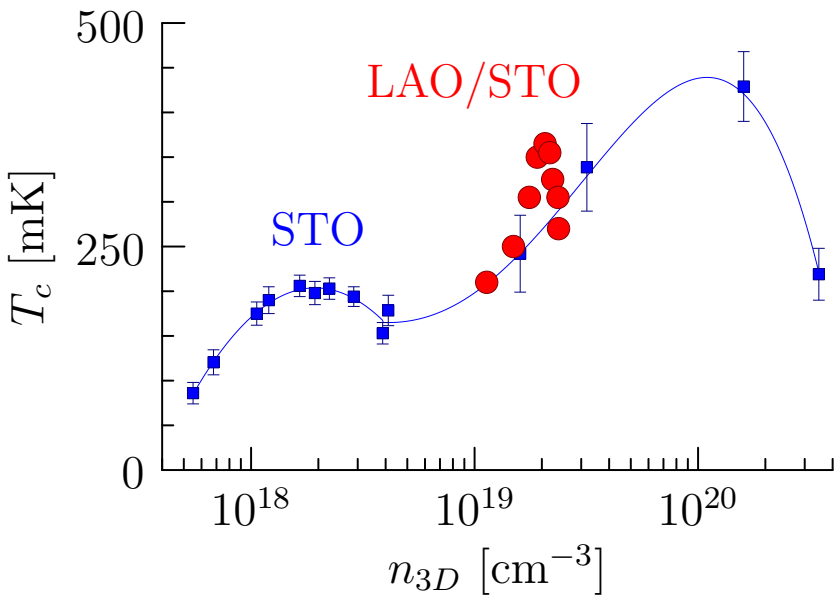

Figure 4.9: Comparison between the experimental T_c domes of doped bulk STO [94] (blue squares) and LAO/STO [175] (red circles), as a function of 3D carrier density n_{3D}. For LAO/STO, the latter has been obtained by $n_{3D} = \frac{n_{2D}}{L}$, where n_{2D} is the sheet carrier density measured by Hall effect [125] and L is the thickness of the superconducting q2DEL extracted from measurements of the angular dependence of the interface critical field [125].

We see that, while the bulk and interface maximum T_c values are similar, the interface dome spans a limited n_{3D} region of doping compared to the bulk domes. Therefore, the LAO/STO dome is not just a copy of the 3D dome. This discrepancy has suggested that the superconductivity of the LAO/STO interface is different from that of bulk STO, although the microscopic nature of either systems is yet to be elucidated [125, 207]. Many speculations for the origin of quasi-2D superconductivity have been proposed. The suppression of T_c on the underdoped side has been linked with superconducting phase fluctuations [87, 97, 208] and the temperature-dependent resistivity was analyzed within BKT theory [164], or a crossover between Ginzburg-Landau fluctuations and BKT regime [209]. The enhancement of Coulomb repulsion due to disorder also affects the resistive transition [152–154, 210]. Another proposed mechanism for superconductivity involves resonances due to multi-subband effects [211]. In the underdoped regime, a pseudogap-like order parameter was observed [207]. The strong interface electric field, leading to Rashba-Dresselhaus spin-orbit coupling, could influence T_c [212, 213] and produce singlet-triplet mixing [214]. Topology can help in distinguishing the symmetry of the order parameter and the associated pairing mechanism [215]; these properties may depend on the crystallographic orientation of the interface [216]. Quantum confinement and Rashba coupling could also produce electronic phase separation at the interface, with percolating paths among superconducting

puddles [217, 218]. The interface dome shape has also been ascribed to onsite Hubbard-type correlations between electrons. [219]. In addition, electron-phonon coupling at the interface generates polarons similarly to bulk STO: polaronic effects have been observed in many STO-based system, comprising the bulk [13, 110, 112] the surface Q2DEL [123], and LAO/STO [124]. Hence, such polaronic effects may contribute in a similar way to Cooper pairing in bulk and quantum-confined STO.

Aside from the open problem of the microscopic origin of pairing in STO and LAO/STO, the comparison of the T_c domes in figure 4.9 calls for a detailed comparison of superconducting STO in 3D and quasi-2D, in order to assess whether the differences between the bulk and interface domes mostly stem from quantum confinement. Taking the minimal two-band model for STO as described in section 3.3.1, confining in a square quantum well of width L as mentioned in section 4.3.2, and calculating the interface T_c as a function of n_{2D} and L, we can explore the possibility that the interface dome results from a shape resonance of quantum-confined STO. Employing the experimental values for n_{2D} and L, in section 4.4 we find a quasi-2D T_c dome, having maximum height of the order of $300 \div 400\, mK$ [175], for any value of the confinement barrier $10\, meV < U < +\infty$. This supports the idea that quantum confinement provides the essential link between bulk and interface superconductivity.

4.4 Surfing the shape resonance at the LAO/STO interface

In this section, we propose an interpretation of the dome in LAO/STO as the result of a shape resonance triggered by the confinement of carriers at the STO surface. We support this scenario by a microscopic calculation reproducing both STO and LAO/STO superconducting domes with the same pairing model, taking into account measurements of the 2DEL thickness and confinement effects for the latter [1]. According to the new interpretation, the differences between the two domes confirm the commonality of the pairing mechanism for the 2D and 3D cases. LAO/STO offers new opportunities to study shape resonances, thanks to a continuously tunable carrier density, in contrast to metallic thin films whose thickness can only be changed in increments of one unit cell. Our modeling furthermore clarifies the roles of the STO light and heavy bands in the LAO/STO superconductivity, showing that T_c is controlled almost exclusively by the heavy one. We first build a minimal model able

[1] This section collects the results in the preprint arXiv:1611.07763, to appear in revised form in Phys. Rev. B.

to capture the density dependence of T_c in bulk STO with a small number of parameters. We then confine this model along one dimension, set the carrier density to the equivalent 3D density for the 2DEL, and obtain a prediction for T_c in the confined geometry. The conversion from the measured 2D density of the 2DEL to a 3D density uses the measured 2DEL superconducting thickness. We will first describe the model we use for bulk STO, next describe recent experimental data on the 2DEL thickness [175], and then present the theoretical results for the 2DEL dome. Focusing on the essential ingredients, we opt for two parabolic bands and a BCS pairing interaction to describe STO. The low-energy sector of the STO conduction band involves three bands with mostly Ti 3d character, split by crystal field and spin-orbit interaction [13, 220]. We discard one band lying 30 meV above the other two and not occupied at the densities considered in this study. The bare masses of the remaining two bands and their splitting at the Γ point are chosen such that the 2D density of states evaluated at $k_z = 0$ with the tight-binding and parabolic dispersions agree at best. We then renormalize both band masses by a factor two representing the effect of electron-phonon coupling and the emergence of large polarons [102, 128, 133]. The resulting band structure is shown in Fig. 4.10(a), where the parameters are indicated as well. The pairing mechanism in STO is still debated [115, 135]. Standard phonon-mediated pairing is questioned because the low density of STO puts it in the anti-adiabatic regime $E_F < \hbar\omega_D$, where E_F and $\hbar\omega_D$ are the Fermi and Debye energies, respectively. Leaving alone the origin of pairing, it is believed that STO is amenable to a BCS description with low coupling constants of the order of 0.1–0.3 [13, 220]. We adopt a local BCS interaction of strength V with a dynamical cutoff $\hbar\omega_D = 44$ meV, consistent with the Debye temperature of STO [95]. The interaction is the same in both bands and we neglect inter-band coupling for simplicity. In this model, for V independent of density n, the critical temperature can only increase with increasing n [221, 222], in contradiction with the observations [94, 126, 223, 224]. To explain the dome, V must drop with increasing n [94]. We fix the n-dependent interaction such that the model reproduces the $T_c(n)$ data of Ref. [94]. This dataset is preferred because it covers a broad range of densities, but this choice does not affect any of our conclusions. The resulting interaction decreases monotonically with increasing n as shown in the inset of Fig. 4.10(b). We interpolate this dependency to get a continuous parametrization $V(n)$. The main panel of Fig. 4.10(b) displays the data of Ref. [94] on top of the continuous $T_c(n)$ curve resulting from that interpolation. The calculation takes full account of the energy-dependent DOS, including the fact that $E_F < \hbar\omega_D$, and uses the self-consistent chemical potential calculated at T_c [222]. With this parametrization the heavy band starts to be populated before the first maximum of the double dome, as shown by quantum oscillations [94]. A glimpse at the band structure and the value of $\hbar\omega_D$ reveals that the

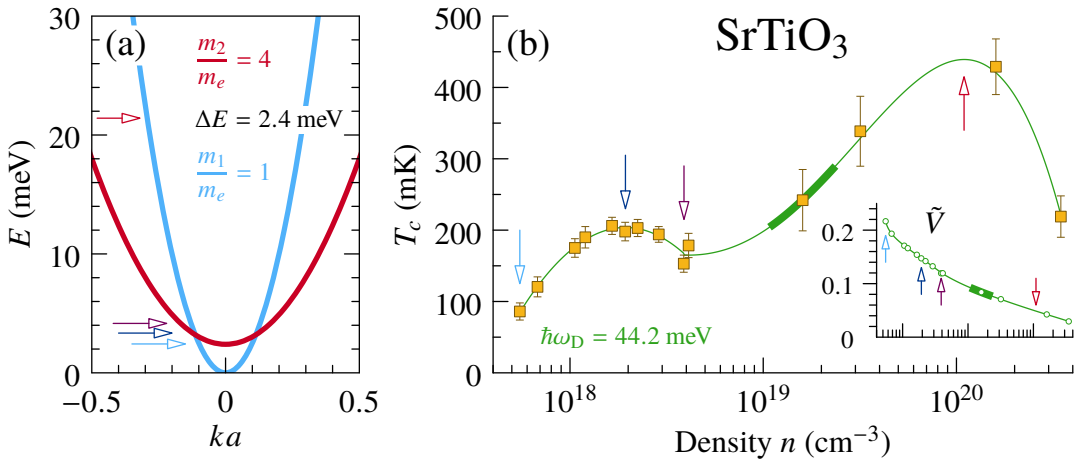

Figure 4.10: Weak-coupling model for the density-dependent superconductivity of $SrTiO_3$. (a) Parabolic approximation for the bottom of the conduction band; ΔE is the band splitting at $k = 0$. (b) Data of Ref. [94] (squares with error bars) and calculated $T_c(n)$ curve (solid line). (Inset) Dimensionless interaction strength [222] $\tilde{V} = 2V[m_e/(2\pi\hbar^2)]^{3/2}\sqrt{\hbar\omega_D}$ reproducing the experimental T_c (circles) and interpolation (solid line). The colored arrows indicate remarkable values of T_c in (b) and the corresponding values of the chemical potential in (a). The thick lines in (b) mark the range of densities visited at the LAO/STO interface.

heavy band contributes to the pairing instability even when it is not populated (see arrows in Fig. 4.10) [2]. Our hypothesis is that the pairing strength at the LAO/STO interface follows the bulk interaction $V(n)$. The carrier density varies across the 2DEL following the profile of the confinement potential, such that the pairing strength would be, strictly speaking, a function of position. As the coherence length is large (50–100 nm) compared with the typical confinement length ($\approx$ 10 nm), which itself is only marginally larger than the Fermi wavelength [225], we use an average V associated with the average carrier density $n = n_{2D}/L$. The density integrated along the confinement direction, $n_{2D} = \int_{-\infty}^{\infty} dz\, n(z)$, has been determined by measuring the Hall sheet conductance [164]. For an estimation of the effective 2DEL thickness L [175], we resort to the analysis of the superconducting transitions measured in magnetic fields [191], applied perpendicular and parallel to the interface [3].

Figure 4.11 displays the thicknesses and critical temperatures measured as a function of the Hall density n_{2D} [175]. The dependence $T_c(n_{2D})$ draws a dome with maximum at 365 mK. The measured thickness is close to 10 nm except at densities above 2.5×10^{13} cm^{-2}

[2] In fact, the contribution of the heavy band is dominant: if the interaction is switched off in the light band the calculated T_c changes by less than a percent, while if the interaction in the heavy band is reduced by 20%, T_c does not exceed 80 mK at all densities.

[3] The angular dependence of the critical field allows the coherence length and the effective thickness of the superconducting 2DEL to be determined. For the samples of Ref. [175], the in-plane coherence length remains larger than the superconducting thickness for all dopings [125, 162], consistently with 2D superconductivity.

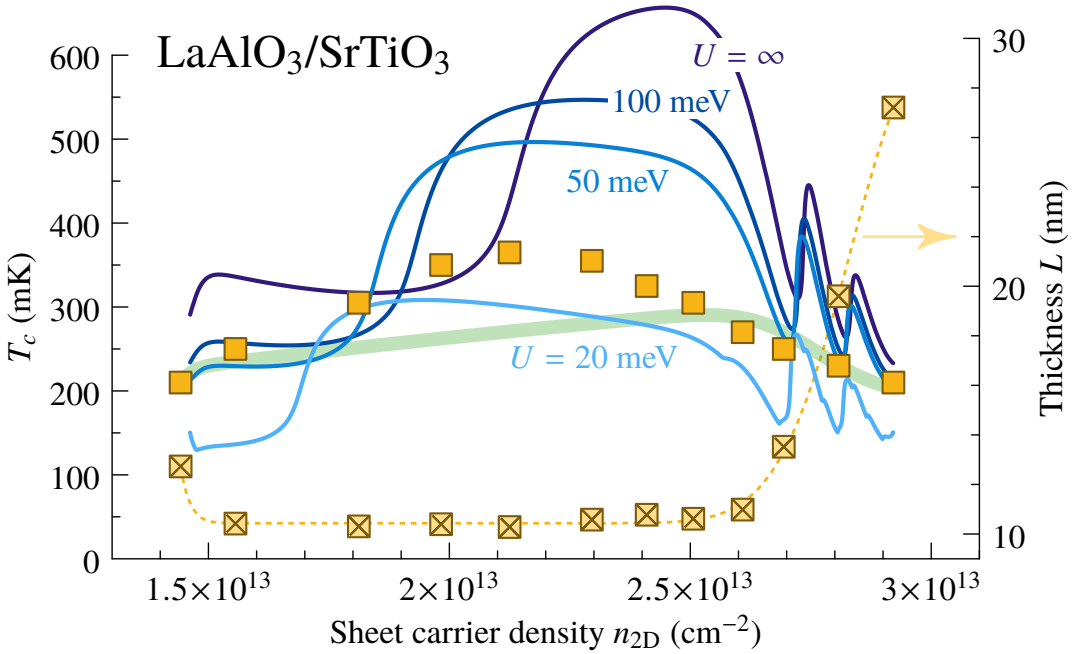

Figure 4.11: 2DEL critical temperature (squares) and thickness (crossed squares, right scale) measured at the LAO/STO interface as a function of sheet carrier density [175]. The solid lines show the calculated T_c obtained by confining the model of Fig. 4.10 in a square potential well of width L and various depths U as indicated. A continuous interpolation of the thickness as a function of density (dotted) was used. For each couple (n_{2D}, L), the pairing interaction is read from the inset of Fig. 4.10(b) at the density $n = n_{2D}/L$. The thick line shows the 3D T_c at density n.

where it increases steadily. Fig. 4.10(b) shows that the field-effect doping at the interface explores a relatively narrow density range (thick line) compared with the chemical doping.

Knowing the equivalent 3D density $n = n_{2D}/L$ for each measured n_{2D}, we can determine the pairing strength $V(n)$ in the 2DEL. We model the confinement by taking the band structure of Fig. 4.10(a) into a square potential well of width L and depth U, following Ref. [226]. This leads to the formation of 2D subbands at energies that depend on L and U. All subbands are coupled by the pairing interaction, which furthermore gets renormalized by the confinement and becomes a function of the band and subband indices via the bound wave functions. The potential well at the LAO/STO interface is certainly not square, but its precise shape is unknown. The formation of 2D bands, interpreted as confinement-induced subbands, is observed experimentally [162, 227, 228], but their occupations and energies are uncertain, preventing us from reconstructing a more realistic potential. We do not expect qualitative changes in our conclusions on going from a square to a triangular or self-consistent confinement potential. The square well moreover has the advantage that the pairing matrix elements are known analytically [226]. The only unknown parameter

of our model is therefore U, whose order of magnitude is estimated from first-principles calculations to be a few tens of meV [177]. Figure 4.11 compares T_c calculated in the square well for various U with the measured T_c of the 2DEL. The calculation yields critical temperatures similar to those measured and a dome-shaped density dependence for all U. This is our main result: localizing STO carriers at a density $\sim 10^{19}$ cm^{-3} into a $\sim$10 nm thick layer leads, owing to quantum confinement effects, to a dome in T_c as a function of sheet carrier density between 1.5 and 3×10^{13} cm^{-2}, with a maximum similar to the maximum T_c of bulk STO. As L becomes large, for $n_{2D} > 2.5 \times 10^{13}$ cm^{-2}, the calculated T_c approaches the 3D value (green line) with rapid oscillations for all U. The measured T_c is also very close to the 3D value in this regime, where T_c drops because n actually *decreases* with increasing n_{2D}. In the range where $L \approx 10$ nm, the 3D T_c raises monotonically like in Fig. 4.10, and one notices a density-dependent critical U, above which the T_c at the interface is higher than in the bulk [226].

We now refine our model to achieve semi-quantitative agreement with the experiment. First, remembering that we mimic a quasi-triangular well by a square one, and also because a systematic error in the experimental determination of L cannot be excluded, we replace the measured 2DEL thickness L_{exp} by $L = \alpha L_{exp}$ when comparing model and experiment. Second, an increase of the splitting ΔE is expected at the interface, since both strain and electric field contribute directly to the 4-fold crystal field. A modified screening also modifies the Hartree shifts of the bands [219]. We adopt the simple dependence $\Delta E = \Delta E_{STO}(1 + \lambda/L)$ with the fit parameter λ, which ensures that the bulk STO splitting is recovered for a thick well. Finally, the confinement potential U is in principle linked with n_{2D} and L via Poisson's equation. The simplest relation results from dimensional analysis as $U = e^2 n_{2D} L/(\epsilon_0 \epsilon)$. The model parameters are adjusted to get the best fit displayed in Fig. 4.12(b), with $\alpha = 0.65$, $\lambda = 30$ nm, and $\epsilon = 630$. The result $\alpha < 1$ is expected, because a square well of width L_{exp} hosts an electron gas thicker than a triangular well of the same width. Moreover the effective thickness $\alpha L_{exp} \approx 7$ nm matches the value measured by AFM [190]. Figure 4.12(a) shows the subband structure with a splitting five times larger than the bulk splitting at a density 2×10^{13} cm^{-2}. We find that two light and two heavy subbands are partly occupied. Photoemission measurements have reported two light subbands lying below the lowest heavy band [197]; our model reproduces this configuration at densities larger than 2.8×10^{13} cm^{-2}. The Hall-coefficient nonlinearity observed in Ref. [229] at 1.6×10^{13} cm^{-2} corresponds in our model to entering the second heavy subband. Finally, the fitted dielectric constant is consistent with the high polarizability of STO: it agrees well with the value $\epsilon = 600$ obtained from the low-temperature field-dependent dielectric function of STO, given approximately by $\epsilon = 1 + \chi_0/(1 + \mathcal{E}/\mathcal{E}_0)$ with

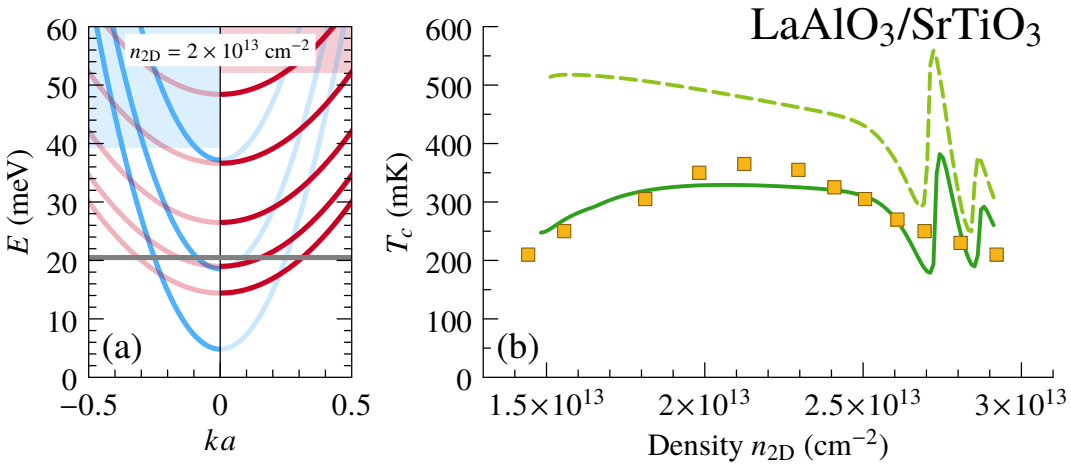

Figure 4.12: (a) Subband structure in a quantum well of width 6.8 nm and depth 39 meV for a band splitting $\Delta E = 12.9$ meV, corresponding to $n_{2D} = 2 \times 10^{13}$ cm^{-2}. The bound light (heavy) subbands with energies below U ($U + \Delta E$) are shown on the left (right). The chemical potential $\mu = 20.5$ meV is also indicated. (b) Measured critical temperature (squares) and calculated T_c (solid line) for a band splitting $\Delta E_{STO}(1 + \lambda/\alpha L_{exp})$ and a potential $U = e^2 n_{2D} \alpha L_{exp}/(\epsilon_0 \epsilon)$ with $\alpha = 0.65$, $\lambda = 30$ nm, and $\epsilon = 630$. The dashed line shows T_c calculated with the same α, $\lambda = 12$ nm, and $\epsilon = 377$.

$\chi_0 = 24000$ and $\mathscr{E}_0 = 110$ kV/m [225, 230], if we substitute for $\mathscr{E}$ the order of magnitude of the interface electric field, e.g., $\mathscr{E} = U/(eL) = 4.3$ mV/nm at $n_{2D} = 1.5 \times 10^{13}$ cm^{-2}.

Although we have until now compared the critical temperature with the mean-field T_c from the calculation, in Fig. 4.12(b) we show that the model is not inconsistent with the pseudogap scenario suggested by tunneling experiments [207], in which the mean-field T_c continues to increase as the density is reduced, while the critical temperature is suppressed by 2D fluctuations.

In a thin-film geometry, the critical temperature of a weak-coupling BCS superconductor is a continuous oscillating function of the film thickness L and electron density n [226]. Pronounced oscillations due to the rapid change in L are visible in Figs. 4.11 and 4.12(b), but not resolved in the experiment. Note that the detailed oscillating behavior is very sensitive to the approximations made for the shape of the potential well. Using our square-well model, we plot in Fig. 4.13 the evolution of T_c as a function of both L and $n_{2D} = nL$ in the domain of thicknesses and densities relevant for the 2DEL. The experimental data are shown for comparison at the rescaled thickness αL_{exp}. The T_c landscape in the (L, n_{2D}) plane is rich and displays three types of structures. To describe the features we start at 5 nm thickness, and follow the doping from zero upwards. At the lowest doping T_c is exponentially small and reaches a first low-T_c step near 8×10^{12} cm^{-2}, before raising steeply to ~400 mK for doping of the order of 10^{13} cm^{-2}. At this thickness and for the doping

range displayed in the figure, superconductivity is entirely in the two heavy subbands (the two lowest red curves in Fig. 4.12). The low-T_c stage corresponds to the first heavy subband, with a T_c suppressed by a shallow confinement potential (see Fig. 4.11 for the effect of U on T_c) [226]. For fixed 2D carrier density, the number of occupied subbands varies with the layer thickness as $(n_{2D}L^2)^{1/3}$. Since T_c passes through a maximum when a new heavy subband becomes occupied, the effect of increasing the thickness results in a succession of T_c maxima; the amplitude of these oscillations decays rapidly with increasing thickness since the layer becomes more and more like a 3D bulk sample with carrier density approaching zero according to $n = n_{2D}/L$. The location of maxima is given approximately by $n_{2D} \approx \frac{\pi}{12}p(p+1)(4p+5)/L^2$ with integer p. The scars running at a small angle with respect to the first maximum are slope changes of T_c occurring when a new heavy subband gets bound in the well as L increases, leading to a slight T_c enhancement. The very faint lines almost parallel to the density axis indicate that a new heavy subband enters the pairing window at $\mu + \hbar\omega_D$. These features reflect that in our calculation we use a BCS-type model interaction with a sharp cutoff at $\hbar\omega_D$. Finally, μ crossing the third light subband gives another faint structure crossing the previous ones and ending at zero density near $L = 20$ nm; other structures associated with the light band are too weak to be visible. Moving up in density for $L = 20$ nm, T_c becomes distinguishable from zero for $n_{2D} = 3.6 \times 10^{12}$ cm^{-2}, and rises in a succession of steps, each corresponding to a new heavy subband becoming occupied. In the limit of infinite thickness the 3D situation depicted in Fig. 4.10 is ultimately obtained. The figure illustrates that many combinations of thickness and doping parameters can result in a dome-like doping or thickness dependence of T_c, however the maximal value of T_c itself is never strongly different from $T_c^{\max}$ observed in optimally doped bulk STO. We believe that this theoretical observation provides the main clue as to why T_c is so similar in bulk and interface superconductivity: The pairing potential is basically the same in all cases. Tuning of the density of states by 2D confinement allows the effective pairing interaction to be varied to a certain extent, but its main effect is to define the subband structure. Optimal T_c is found for small densities, which holds true in bulk 3D and quasi-2D alike, thus leading to very similar values of the optimal T_c in 2D and 3D systems.

In summary, we have explored the hypothesis that the pairing potential responsible for superconductivity is the same in 2D interfaces and 3D bulk $SrTiO_3$. We showed that the superconducting dome in the 2D material corresponds to a much narrower effective doping range than in the 3D material, and the optimal T_c in this case coincides with a shape resonance due to the onset of occupation of one of the subbands created by the 3D confining potential. We have shown that the optimal T_c should be very similar in the

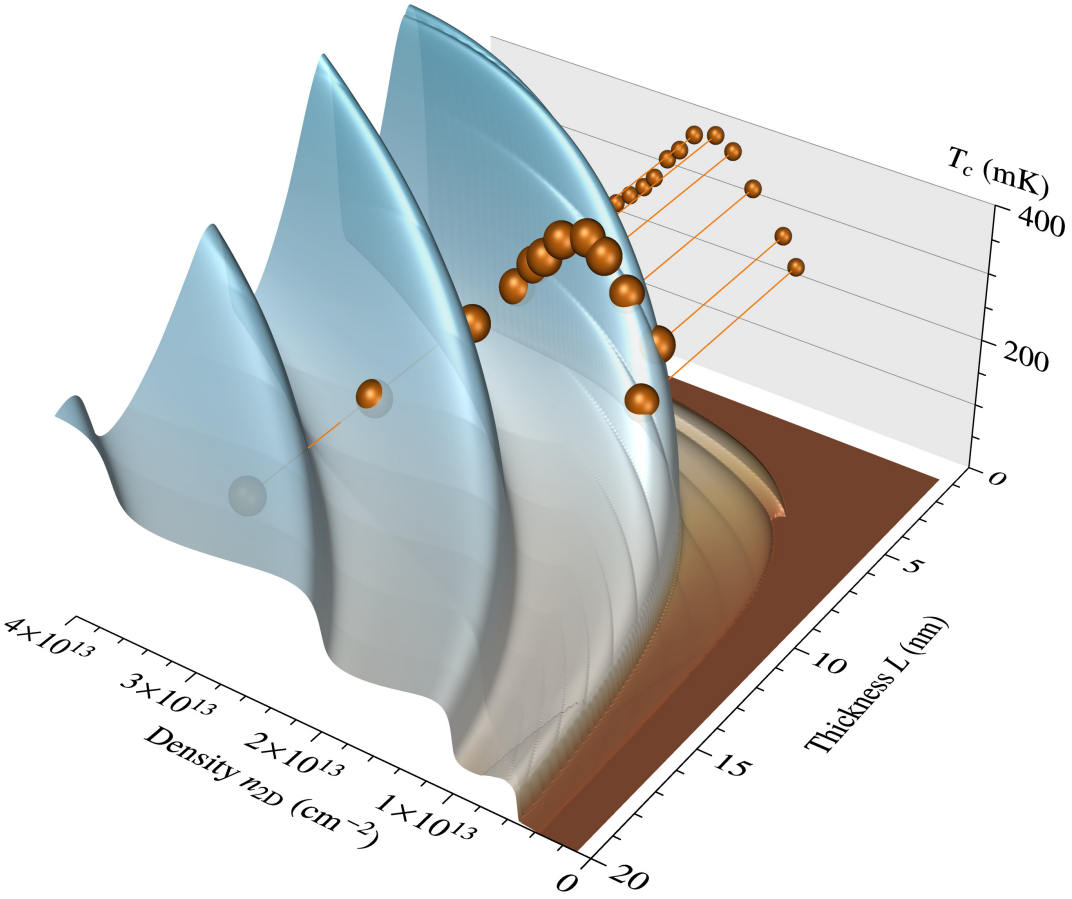

Figure 4.13: Critical temperature as a function of thickness L and sheet carrier density n_{2D}. The spheres show the experimental data of Fig. 4.11 where the thickness has been reduced by a factor $\alpha = 0.65$. The shaded surface shows the T_c calculated with a band splitting $\Delta E_{STO}(1 + \lambda/L)$ in a square well of width L and depth $U = e^2 n_{2D} L/(\epsilon_0 \epsilon)$, with $\lambda = 30$ nm, and $\epsilon = 630$.

2D and 3D cases. Potential for optimization of T_c is offered by tuning the confinement potential U, which in principle allows T_c to be increased up to a factor 3, and by controlled tuning of the thickness parameter L on the 1 nm scale.

4.5 Conclusions and perspectives

Quantum confinement in quasi-2D geometry produces quantized subbands, thus modifying the density of states and the pairing interaction of a BCS superconductor. The chemical potential, and the associated BCS pairing window, move as a function of density as well as of the confinement parameters, like the width L and barrier height U for a

rectangular well. Different subbands enter into the pairing window and contribute to superconductivity for different density and confinement parameters: this influences the pairing temperature. Considering the cutoff of the pairing window near a subband edge and the finite-temperature chemical potential is necessary to obtain the exact solution for T_c in the quasi-2D configuration. In a rectangular well, the pairing temperature shows continuous shape resonances as a function of well width L, and the quasi-2D T_c can be either enhanced or reduced with respect to the bulk value depending on the barrier height U. This rectangular-well geometry provides a simple model for superconducting thin films of thickness L, and it allows to evaluate at mean field how T_c changes in the thin-film geometry with respect to the bulk. The latter evaluation method finds a natural application in the LAO/STO interface, which represents a synthesis of low-density and quantum-confined superconducting system. We interpret the doping evolution of T_c at the interface as a shape resonance due to heavy subbands, created by the confining potential acting on bulk STO. This provides an explanation for the similar value of the optimal T_c in the quasi-2D and 3D cases, and highlights the connections between superconductivity in doped bulk STO and at the LAO/STO interface. Further developments may include a systematic analysis of T_c for different quasi-2D geometries, apart for the rectangular well, to compare the changes in T_c with respect to the bulk value for different confinement models of interest for practical applications. Also, the exact solution for the quasi-2D zero-temperature gap would allow to study the gap shape resonances, and compare them to the ones in the pairing temperature.

PHYSICAL REVIEW B **94**, 054516 (2016)

Rise and fall of shape resonances in thin films of BCS superconductors

D. Valentinis, D. van der Marel, and C. Berthod*
Department of Quantum Matter Physics (DQMP), University of Geneva, 24 quai Ernest-Ansermet, 1211 Geneva 4, Switzerland

(Received 19 January 2016; revised manuscript received 15 July 2016; published 23 August 2016)

The confinement of a superconductor in a thin film changes its Fermi-level density of states and is expected to change its critical temperature T_c. Previous calculations have reported large discontinuities of T_c when the chemical potential coincides with a subband edge. By solving the BCS gap equation exactly, we show that such discontinuities are artifacts and that T_c is a continuous function of the film thickness. We also find that T_c is reduced in thin films compared with the bulk if the confinement potential is lower than a critical value, while for stronger confinement T_c increases with decreasing film thickness, reaches a maximum, and eventually drops to zero. Our numerical results are supported by several exact solutions. We finally interpret experimental data for ultrathin lead thin films in terms of a thickness-dependent effective mass.

DOI: 10.1103/PhysRevB.94.054516

I. INTRODUCTION

The quantum confinement of superconductors has historically attracted considerable interest, as a plausible route to increase the critical temperature through the enhancement of the Fermi-level density of states in reduced dimensions. Among the factors that influence the critical properties, dimensionality and geometry are appealing, being easier to manipulate than the microscopic parameters of the materials. New fascinating phenomena have been predicted to occur in confined geometries: for instance, Thompson and Blatt [1], followed by many others until recently [2–10], predicted large oscillations of the critical temperature T_c in superconducting films, as a function of the film thickness. The oscillations known as "shape resonances" arise when the Fermi level crosses the edge of one of the confinement-induced subbands. Early experimental studies with disordered thin films revealed significant enhancements of T_c in Al and Ga, but little or no enhancement in Sn, In, and Pb [11–14]. Measurements made on epitaxial films and islands showed instead no noticeable change of T_c in Al with respect to the bulk value [15], and a decrease in Bi, In, and Pb [16–19], as well as in NbN [20]. Oscillations of T_c as a function of film thickness were seen in Sn [21], and more recently in Pb [22–25]. Last but not least, a spectacular enhancement of T_c was recently observed in a monolayer of FeSe grown on $SrTiO_3$ [26].

A common trend of these experiments is that oscillations of T_c as a function of film thickness are either below the level of noise or, when they are seen, much smaller than the oscillations typically reported in theoretical studies. The calculations published so far for ideal thin films show discontinuous jumps of T_c with relative amplitudes which can be as large as 100% at low thickness, while the strongest oscillations seen experimentally hardly exceed 15% [21–23]. Such theoretical results are obtained by solving the BCS gap equation approximately, with a thickness-dependent Fermi-level density of states (DOS), which has discontinuities at the edge of each subband. These DOS discontinuities are responsible for the large jumps in T_c. Extrinsic effects such as an interaction with the substrate have been invoked to explain the discrepancy between theory and experiment [9]. In a previous paper (denoted part I hereafter) [27], we have shown that the BCS gap equation predicts a continuous evolution of T_c when the Fermi energy approaches a band minimum. In view of this, discontinuities in T_c are an artifact of replacing the energy-dependent DOS by a DOS which is constant over the full dynamical range of the pairing interaction. This approximation breaks down when the interaction is cut by the band edge. In the BCS theory, the actual dependence of T_c on film thickness must therefore be continuous, and the previously reported large oscillations must be replaced by a smoother evolution. In the present paper, we unveil the precise shape of the $T_c(L)$ curve predicted by the BCS gap equation for ideal thin films of thickness L, and we interpret the numerical results with the help of exact asymptotic formulas derived in part I.

Beside the oscillations, the overall trend of T_c with reducing thickness is of particular interest. Thompson and Blatt [1] found an increase, but their model assumed hard-wall boundary conditions for the wave functions. Yu *et al.* [3] noticed that the leakage of the wave functions outside the film reduces the pairing strength within the film, and they proposed a phenomenological model to account for this effect, which can produce a *decrease* of T_c with decreasing L. This phenomenological description may be improved and challenged by calculating the pairing matrix elements with the exact wave functions of a finite potential well. This program was followed by Bianconi and coworkers in a series of papers [28,29] where they considered a periodic arrangement describing a multilayer. Here we consider a single well as a model for a thin film. We thus find two regimes for the confinement potential. Below a certain critical potential, T_c goes down with reducing L while if the confinement is stronger than the critical value, T_c increases until it reaches a maximum at a parameter-dependent thickness, before dropping rapidly to zero. The existence of a critical confinement potential—below which no enhancement of the critical temperature is to be expected—may help to understand the contrasting experimental results obtained with different thin films.

It was recently found that ultrathin Pb films deposited on Si(111) have a T_c lower than bulk Pb, with a nonmonotonic

*Author to whom correspondence should be addressed: christophe.berthod@unige.ch

dependence on the film thickness [25]. The authors tentatively ascribed this to an interaction with the substrate. Based on our calculations, we propose a semiquantitative interpretation in terms of an effective mass which increases significantly in ultrathin films. Another system of interest is the two-dimensional electron gas at the $LaAlO_3/SrTiO_3$ interface, which enters a superconducting phase at a density-dependent temperature slightly lower than the T_c of bulk $SrTiO_3$ [30]. Whether or not this interface superconductivity has the same origin as in bulk $SrTiO_3$, and whether it can be understood by the confinement of $SrTiO_3$ carriers, remain important open issues [31–33]. The investigation of this case requires to consider a multiband system. We defer it to an upcoming study and focus here on the one-band problem.

In Sec. II, we recall the basic BCS equations for T_c and we give the modified pairing matrix elements in a square potential well. Sections III and IV deal with the $T_c(L)$ curve in infinite and finite potential wells, respectively. A discussion of our main results is proposed in Sec. V. The application to Pb thin films is presented in Sec. VI. Conclusions and perspectives are given in Sec. VII.

II. MODEL AND BASIC EQUATIONS

A. Critical temperature of a one-parabolic band BCS superconductor in a quasi-two dimensional geometry

We consider a one-band three-dimensional (3D) BCS superconductor with parabolic dispersion, and a pairing interaction $-V$ effective in an energy range $\pm\hbar\omega_D$ around the chemical potential μ. The superconductor is confined to a thin film of thickness L, leading to quantization of the energy levels in the direction z perpendicular to the film. This system is equivalent to a two-dimensional (2D) multiband system in which *all* bands are coupled by the pairing interaction. The bands of the 2D system are the subbands of the 3D one associated with the discrete energy levels in the confinement direction, and the intersubband couplings reflect the pairing in 3D between momenta k_z and $-k_z$. In the quasi-2D film geometry, the two coupled equations giving T_c and μ as a function of the density n are (see part I)

$$0 = \det[\mathbb{1} - \Lambda(\tilde{\mu},\tilde{T}_c)], \tag{1a}$$

$$\tilde{n} = \frac{2^{1/3}}{\tilde{L}}\frac{m_b}{m}\tilde{T}_c\sum_q \ln\left(1+e^{\frac{\tilde{\mu}-\tilde{E}_q}{\tilde{T}_c}}\right). \tag{1b}$$

As in part I, tildes indicate dimensionless quantities defined by measuring energies in units of $\hbar\omega_D$ and densities in units of $2(m\omega_D/2\pi\hbar)^{3/2}$, where m is a reference mass, while m_b is the band mass of the material. Thus $\tilde{\mu} = \mu/\hbar\omega_D$, $\tilde{T}_c = k_B T_c/\hbar\omega_D$, $\tilde{n} = n/[2(m\omega_D/2\pi\hbar)^{3/2}]$, and $\tilde{L} = L\times 2^{1/3}(m\omega_D/2\pi\hbar)^{1/2}$. The energies E_q are the discrete levels in the confinement potential, corresponding to the minima of the 2D subbands. Equation (1b) differs by a factor $2^{1/3}/\tilde{L}$ from Eq. (9b) of part I in dimension $d = 2$; this can be understood as follows. The energy levels of the quasi-2D system, $E_{q\boldsymbol{k}} = E_q + \hbar^2k^2/2m_b$, allow one to express the density of states (DOS) per unit volume and per spin as $N_0(E) = (1/L)\sum_q \int d^2k/(2\pi)^2\delta(E - E_q - \hbar^2k^2/2m_b) = (1/L)\sum_q N_0^{2D}(E-E_q)$, where $N_0^{2D}(E)$ is the DOS of a 2D electron gas measured from its band minimum. The factor $1/L$, which becomes $2^{1/3}/\tilde{L}$ once the equation has been turned to dimensionless form, ensures that the density in Eq. (1b) is a 3D density. It is easy to check that Eq. (1b) goes to the correct 3D limit at large L.

$\Lambda(\tilde{\mu},\tilde{T}_c)$ is a matrix in the space of subbands with matrix elements

$$\Lambda_{qp}(\tilde{\mu},\tilde{T}_c) = \bar{\lambda}_{qp}\psi_2(1+\tilde{\mu}-\tilde{E}_p,\tilde{T}_c), \tag{2}$$

$$\psi_2(a,b) = \theta(a)\int_{1-\min(a,2)}^{1}\frac{dx}{2x}\tanh\left(\frac{x}{2b}\right). \tag{3}$$

As the function $\psi_2(a,b)$ vanishes for negative a, the size of the matrix Λ is set by the condition $\tilde{E}_p < \tilde{\mu}+1$, meaning that subbands at energies higher than $\hbar\omega_D$ above the chemical potential do not contribute to T_c. The determinant in Eq. (1a) accounts for the fact that the superconducting gap parameters take different values in all the coupled subbands. We ignore the spatial dependence of the gap parameters [34], which should be irrelevant since all gaps approach zero at T_c. The coupling constants $\bar{\lambda}_{qp}$ characterize the intra- and intersubband pairing interactions. They depend on the 3D Fermi-surface interaction V, as well as on the subband wave functions $u_q(z)$ in the confinement direction. The pairing interaction in the quasi-2D geometry is [1]

$$V_{qp} = V\int_{-\infty}^{\infty} dz\,|u_q(z)u_p(z)|^2.$$

On the other hand, the coupling constants $\bar{\lambda}$ in 3D and $\bar{\lambda}_{qp}$ in 2D are related to the interaction parameters via (see part I):

$$\bar{\lambda} = 2\pi V\left(\frac{m_b}{2\pi^2\hbar^2}\right)^{\frac{3}{2}}(\hbar\omega_D)^{\frac{1}{2}}, \qquad \bar{\lambda}_{qp} = V_{qp}\frac{m_b}{2\pi\hbar^2}.$$

Moving on to dimensionless variables for the wave functions, we are led to the following relation between the coupling constants in 3D and in quasi-2D:

$$\bar{\lambda}_{qp} = \bar{\lambda}\frac{\sqrt{\pi}}{2^{2/3}}\left(\frac{m}{m_b}\right)^{\frac{1}{2}}\int_{-\infty}^{\infty} d\tilde{z}\,|\tilde{u}_q(\tilde{z})\tilde{u}_p(\tilde{z})|^2. \tag{4}$$

Once the shape of the confinement potential is chosen, and the resulting eigenvalues E_q and eigenstates $u_q(z)$ are known, Eqs. (1) to (4) completely determine the value of T_c as a function of n, $\bar{\lambda}$, and L. We shall solve this problem numerically without further approximation, and also take advantage of some analytical results derived in part I.

B. Coupling constants for bound states in a square potential

For a square confinement potential with hard boundaries, the energy levels and the wave functions are $E_q = (\hbar^2/2m_b)(q\pi/L)^2$ and $u_q(z) = (2/L)^{1/2}\sin(q\pi z/L)$, respectively, with q a positive integer. The correction to the pairing matrix element follows [1]:

$$O_{qp} \equiv \int_{-\infty}^{\infty} dz\,|u_q(z)u_p(z)|^2 = \frac{1}{L}\left(1+\frac{1}{2}\delta_{qp}\right). \tag{5}$$

Using the model (5), Thompson and Blatt found a general increase of the critical temperature with decreasing L, and discontinuous jumps of T_c at the subband edges [1]. Similar results were obtained using von Neumann rather than Dirichlet

boundary conditions for the wave functions [2]. These calculations neglected self-consistency in the chemical potential and, more importantly, the suppression of T_c discussed in part I when the chemical potential lies less than $\hbar\omega_D$ above one of the subband minima. We shall see in the next section that taking this suppression into account removes the discontinuities, but preserves the overall increase of T_c in quasi-2D with respect to 3D. The usefulness of the hard-wall model (5) for describing real systems was questioned early on [35], as it violates charge-neutrality conditions at the surface [36]. In an attempt to overcome this difficulty, Yu *et al.* [3] considered hard walls shifted beyond the physical film surfaces, and found a correction factor $(1 - b/L)$ to Eq. (5), with b a length measuring the extension of the wave functions outside the film. By tuning the value of b, the $T_c(L)$ curve can be changed from an increasing to a decreasing function of decreasing L [3,5].

In our calculations the charge neutrality is guaranteed by the self-consistent adjustment of the chemical potential. Nevertheless, for a more realistic confinement model, it is useful to consider a finite-depth potential well. This allows one to put the approach of Ref. [3] on a firmer ground, giving a meaning to the phenomenological parameter b. We shall also find that the correction factors O_{qp} have a richer dependence on L and on the subband indices than the simple model (5) and the extension of Yu *et al.*

For a square well of depth U, the eigenvalues for the even and odd bound states are determined, as is well known, by solving the transcendental equations $\tan(k_q L/2) = s_q$ and $\tan(k_q L/2) = -1/s_q$, respectively, where $k_q^2 = 2m_b E_q/\hbar^2$ and $s_q^2 = U/E_q - 1$. The wave functions for bound states are known as well, and will not be reproduced here. From these wave functions, we calculate the correction to the pairing matrix element and find for the diagonal terms

$$O_{qq} = \frac{1}{L + \frac{2}{k_q s_q}} \left(\frac{3}{2} - \frac{E_q}{U} \frac{1}{2 + k_q s_q L} \right). \tag{6a}$$

This expression reproduces the result $3/(2L)$ of Eq. (5) at large U and gives $3/(2L) \times (1 - b/L)$ in the limits of large L and $E_q \ll U$, as in the approach of Ref. [3], with $b = 2/(2m_b U/\hbar^2)^{1/2}$. For the off-diagonal terms, we find

$$O_{qp} = \frac{1}{\left(L + \frac{2}{k_q s_q}\right)\left(L + \frac{2}{k_p s_p}\right)} \left(L + 2 \frac{\frac{E_q}{U} k_p s_p - \frac{E_p}{U} k_q s_q}{k_q^2 - k_p^2} \right). \tag{6b}$$

This again reproduces the $1/L$ of Eq. (5) and approaches $1/L \times (1 - b/L)$ with the same b as above in the corresponding limits. Except in those particular limits, however, one sees that the coupling constants (4) depend on the subband indices for a finite-depth square well.

III. INFINITE QUANTUM WELL

A. Continuity of $T_c(L)$ curve and suppression of T_c oscillations with respect to Thompson-Blatt model

In a potential well of width L and infinite depth, the subbands have energies proportional to $1/L^2$. The contribution of each subband to the three-dimensional density is proportional to $1/L$. As L is increased, all subbands move down in energy like $1/L^2$: in order to keep the three-dimensional density fixed, the chemical potential must follow with a slower decrease proportional to $1/L$. In the approximate treatment of the BCS gap equation by Thompson and Blatt (TB) [1], the chemical potential μ is calculated at zero temperature and the subbands contribute to the critical temperature if μ lies above their minimum. As soon as μ enters a subband, this subband is treated as if its DOS were extending over the whole pairing window. This abrupt increase of "virtual" states available only for pairing produces a discontinuous jump of the critical temperature to a higher value. The resulting dependence $T_c(L)$ oscillates with discontinuous jumps as illustrated in Fig. 1. After the jump, T_c decreases because the effective couplings behave as $1/L$ [see Eq. (5)]. Consistently, since each new subband contributes with a smaller effective coupling, the amplitude of the jumps decreases with increasing L. In the exact BCS equation (1), a subband begins to enhance T_c when the chemical potential lies $\hbar\omega_D$ *below* its minimum, as it is apparent in Eq. (2). The contribution of this band is exponentially small in its first stages, and gradually increases to reach a plateau when $\mu > E_p + \hbar\omega_D$ (see part I and Fig. 2 below). The resulting $T_c(L)$ curve has no discontinuity, as seen in Fig. 1. The absence of discontinuities in T_c, despite the existence of discontinuous jumps in the quasi-2D DOS, is reminiscent of the continuous vanishing of T_c at the bottom of a single two-dimensional band (part I).

In order to facilitate the comparison of the TB and exact results, the critical temperatures are normalized in Fig. 1 to the corresponding 3D values which are asymptotically reached at large L. The 3D value is slightly larger in the TB approximation, which neglects the energy dependence of the 3D DOS and the self-consistent adjustment of the chemical potential. Overall, the two curves show an enhancement of T_c with reducing film thickness, accompanied by oscillations whose amplitude also increases with decreasing L. The main qualitative difference between the TB and exact results is that

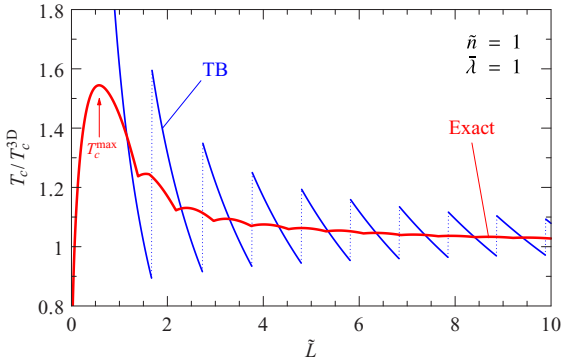

FIG. 1. BCS critical temperature in a thin film, modeled as a square potential of infinite depth, as a function of film thickness L. The Thompson–Blatt approximate result (TB) is compared with the exact result for a dimensionless 3D density $\tilde{n} = 1$ and a coupling $\tilde{\lambda} = 1$. Similar results are obtained for other densities and couplings. The 3D critical temperatures are $k_B T_c^{3D}/\hbar\omega_D = 0.500$ and 0.436 in the TB and exact calculations, respectively. The band mass is used as the reference mass: $\tilde{L} = 2^{1/3}(m_b\omega_D/2\pi\hbar)^{1/2}L$.

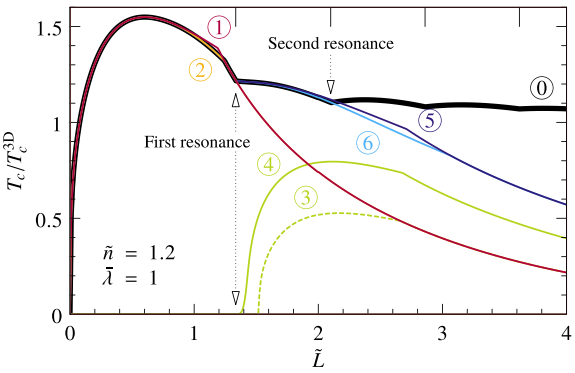

FIG. 2. Relative variation of the critical temperature with varying film thickness (curve 0) and its interpretation (curves 1 to 6); see text. The vertical bars at the top mark the film thicknesses where $\mu = E_q - \hbar\omega_D$ for $q = 2,3,4,5$.

the former is discontinuous while the latter is continuous, as already discussed. Consequently, the exact amplitude of the T_c oscillations is much smaller than the TB approximation would suggest. Using the self-consistent μ rather than its zero-temperature counterpart provides further smoothing of the $T_c(L)$ curve, since there is no sharp structure associated with μ crossing a subband edge. Another qualitative difference is that, thanks to a consistent treatment of the pairing down to the smallest L, the exact T_c vanishes in the limit $L \to 0$, while the TB result diverges. The exact T_c thus presents a striking maximum at small L. Finally, the period of the oscillations as a function of L is shorter in the exact data. We analyze the period, the behavior of T_c at small L, and the properties of the maximum T_c in the subsequent sections. In the remainder of the present section, we provide a step-by-step interpretation of the exact $T_c(L)$ curve, and we study its dependence on coupling and density.

Figure 2 presents a deconstruction of the exact $T_c(L)$ curve. This is achieved by pushing a set of subbands to high energy such that they become irrelevant and by selectively turning on and off the various intra- and intersubband couplings. For the curve labeled "1", all subbands are eliminated except the lowest. This curve matches the exact result labeled "0" in the regime of small L, showing that only the lowest subband contributes to T_c in this regime. The one-subband regime corresponds to a 2D problem with an effective 2D density proportional to nL and an effective coupling proportional to $\bar{\lambda}/L$, as described further in Sec. III C. A comparison with the 2D results of part I therefore allows one to understand curve 1. In 2D, T_c vanishes at low density for arbitrarily large coupling, hence the vanishing of T_c in quasi-2D for $L \to 0$, in spite of the diverging effective coupling. As the density increases, T_c reaches a plateau in 2D when the whole pairing window lies within the band—hence the break close to $\tilde{L} = 1.2$—and then remains constant at a coupling-dependent value—hence the decrease after the break in curve 1, controlled by the decrease of the effective coupling. For the curve labeled "2", only the two lowest subbands are kept but all couplings related to the second subband are set to zero: $\bar{\lambda}_{12} = \bar{\lambda}_{21} = \bar{\lambda}_{22} = 0$. The sole effect of the second subband in this case is to correct (lower) the chemical potential and thus displace the break of curve 1 to a slightly larger value of L, which coincides with the position of the break in curve 0. At larger L, curves 1 and 2 are identical. One sees that the model 2 with only two subbands and only $\bar{\lambda}_{11}$ different from zero explains the exact result up to the first resonance, which is marked by the double arrow in Fig. 2. This resonance is due to the pairing in the second subband. For $\tilde{n} = 1$, the break and the first resonance accidentally occur at nearly the same $\tilde{L}$ (see Fig. 1): this is the reason for taking $\tilde{n} = 1.2$ in Fig. 2.

Curves 3 and 4 illustrate the superconducting properties of the second subband when the first remains normal and all the others are irrelevant. Curve 3 has $\bar{\lambda}_{11} = \bar{\lambda}_{12} = \bar{\lambda}_{21} = 0$, such that the lowest subband accommodates a certain number of electrons but plays no role in pairing. Curve 3 is therefore analogous to curve 1, except for a shift in chemical potential. This explains why both curves are identical at large L. Curve 4 has $\bar{\lambda}_{11} = 0$ but $\bar{\lambda}_{12} = \bar{\lambda}_{21} \neq 0$. The raise of T_c is shifted to a lower value of L as compared to curve 3 due to induced superconductivity in the lowest subband. An analytical expression for the exponential raise of T_c in this situation has been derived in part I. The double arrow indicates that the onset of this "proximity effect" in the lowest subband corresponds to the position of the first resonance in curve 0. In other words, the first resonance occurs when the pairing interaction in the second subband starts to reinforce the superconductivity of the lowest subband. Turning on the pairing in the lowest subband changes curve 4 into curve 5. Specifically, curve 5 is the complete two-subband model with all intra- and intersubband couplings turned on. The break associated with the second subband in curve 5 occurs after the second resonance (see also curves 3 and 4), as opposed to the break in curve 1 which occurs before the first resonance. The second break in curve 5 is shifted to larger L when the lowering of the chemical potential due to the third subband is considered (curve 6), leading to a model accurate up to the second resonance. The second resonance coincides with induced superconductivity from the third subband into the second one, and so on for the other resonances.

One sees that the exact $T_c(L)$ curve has more structure than the TB curve. These structures are of two different types and induce discontinuities in the derivative dT_c/dL. The structures which set the main oscillation pattern correspond to the onset of induced superconductivity from one subband into the subband immediately underneath: they occur when $\mu = E_q - \hbar\omega_D$. At these points dT_c/dL jumps to a higher value producing a cusp, as opposed to the TB case where dT_c/dL jumps to a lower value at each discontinuity. The other structures are weaker and occur when the lower end of the pairing window coincides with the minimum of a subband, i.e., $\mu = E_q + \hbar\omega_D$. At these points dT_c/dL jumps to a lower value producing a break. Two such structures are present in the data of Fig. 2, although only one of them can be seen with the naked eye, just below the first resonance.

In Fig. 3, we plot the evolution of the chemical potential and of the subband energies with increasing L, illustrating graphically their mutual relationship with the features of the $T_c(L)$ curve. Figure 3(a) shows the exact μ and the noninteracting zero-temperature chemical potential μ_0 used in the TB approximation, both measured from the lowest

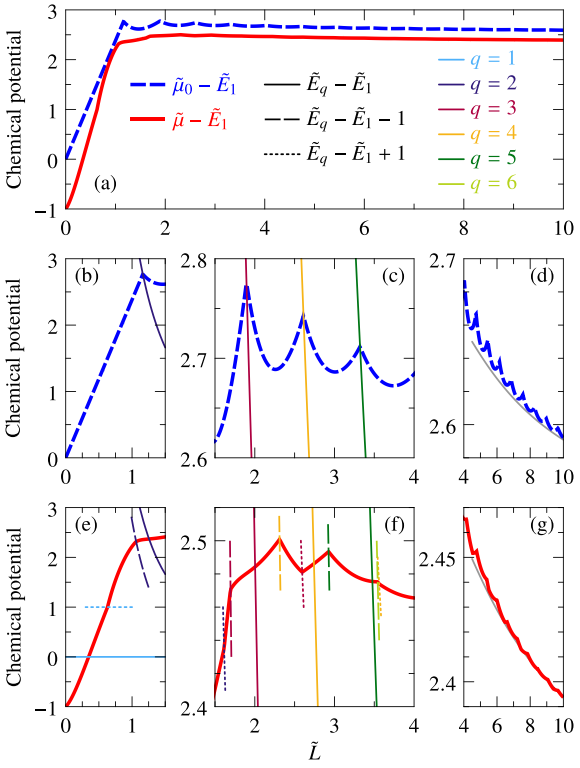

FIG. 3. (a) Evolution of the approximate (dashed-blue) and exact (solid-red) chemical potentials as a function of film thickness. The dimensionless density is $\tilde{n} = 3$, the coupling is $\bar{\lambda} = 1$, and all energies are measured from the lowest subband E_1, and expressed in units of $\hbar\omega_D$. (b)–(g) Chemical potential in different ranges of film thickness and energies E_q (thin solid lines), $E_q - \hbar\omega_D$ (thin dashed), and $E_q + \hbar\omega_D$ (dotted) for $q = 1, \ldots, 6$. In (d) and (g), the gray line shows the $1/L$ behavior at large L. The horizontal axis in all graphs is $\tilde{L} = 2^{1/3}(m_b\omega_D/2\pi\hbar)^{1/2}L$.

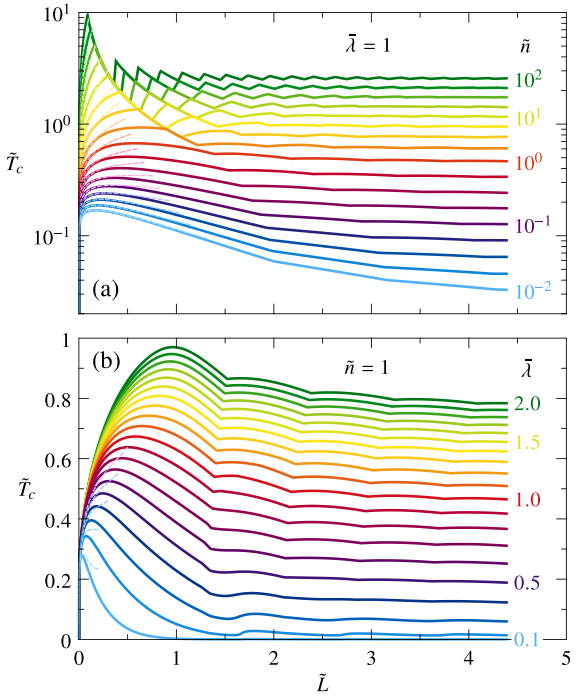

FIG. 4. Critical temperature as a function of film thickness for (a) various densities at fixed coupling and (b) various couplings at fixed density. T_c is expressed in units of $\hbar\omega_D/k_B$ and n in units of $2[m_b\omega_D/(2\pi\hbar)]^{3/2}$. The dashed lines show the asymptotic behavior at low L, Eq. (11).

subband minimum E_1, and expressed in units of $\hbar\omega_D$. We observe that $\mu < \mu_0$, as expected since the chemical potential is a decreasing function of both temperature and coupling. In particular, we see that while μ_0 approaches E_1 for $L \to 0$, the exact μ approches $E_1 - \hbar\omega_D$; this will be further discussed in Sec. III C. Figures 3(b), 3(c), and 3(d) emphasize different parts of the μ_0 variation, while Figs. 3(e), 3(f), and 3(g) do the same for μ. The thin solid lines in panels (b), (c), (e), and (f) correspond to the subband energies measured with respect to E_1, which decrease as $1/L^2$ with increasing L.

Clearly, the singularities of μ_0, hence the discontinuities of $T_c(L)$ in the TB approximation, are given by the condition $\mu_0 = E_q$. There is no singularity at the points $\mu = E_q$ in the exact calculation, however, as seen in panels (e) and (f). Instead, the singularities of the first type discussed above correspond to $\mu = E_q - \hbar\omega_D$ (thin dashed lines), and those of the second type to $\mu = E_q + \hbar\omega_D$ (dotted lines). The density was fixed to $\tilde{n} = 3$ in Fig. 3, in order to reveal several of these singularities. The panels (d) and (g) show that the chemical potential approaches the 3D value at large L from above with a correction of order $1/L$, as argued at the beginning of this section. In the TB case, the large-L behavior is [1] $\tilde{\mu}_0 = (3\sqrt{\pi}\tilde{n}/4)^{2/3} + (3\pi^2\tilde{n}/128)^{1/3}/\tilde{L}$, as indicated by the gray line in panel (d). In the exact case (g), the gray line shows a fit to the form $\mu = \mu^{3D} + A/L$.

In Fig. 4, we illustrate how the $T_c(L)$ curve changes with density and coupling. With increasing density at fixed coupling, the amplitude of the T_c oscillations increases and their period decreases [Fig. 4(a)]. At the same time, the bulk value T_c^{3D} increases (see part I), and so does the maximum critical temperature T_c^{max} observed at low L. One can identify two regimes for the behavior of T_c^{max}. At low density, the maximum occurs before the break and is therefore determined by the smooth evolution of T_c close to the edge of the lowest subband; at high density, the maximum coincides with the break and is determined by the condition $\mu = E_1 + \hbar\omega_D$. We will see in Sec. III D that the position and height of the maximum approach universal functions of the product $\bar{\lambda}\tilde{n}$, and that the transition between two regimes takes place at $\bar{\lambda}\tilde{n} = 1$. Increasing coupling at fixed density, one sees that the position and height of the maximum move up [Fig. 4(b)]. The positions of the resonances are weakly affected, because the coupling influences them only indirectly via its effect on T_c, hence on the self-consistent chemical potential at T_c: increasing the coupling pushes T_c up, μ down, and therefore moves the resonances to larger L. One can finally notice that

the maximum enhancement of the critical temperature due to confinement, $T_c^{\max}/T_c^{3D}$, is close to unity at strong coupling but increases dramatically at weak coupling.

B. Characteristic length of T_c oscillations

An oscillatory evolution of T_c as a function of film thickness is one of the most striking observations made in several experiments performed on metallic thin films [13,21–25]. It is therefore crucial to connect the length ΔL of these oscillations with the microscopic properties of the metal. In the TB model, the length is simply π/k_F as quoted in many papers [1–10], irrespective of the band mass and of the properties of the superconducting pairing. This result follows directly from the condition $\mu_0 = E_q$ which defines the discontinuities of $T_c(L)$ in the TB model. The condition yields unevenly spaced discontinuities at low L, but the spacing becomes constant as the chemical potential depends much less on L with increasing L (see Fig. 3). At large L, the chemical potential approaches the bulk value, which is $\tilde{\mu}_0 = \frac{m}{m_b}(3\sqrt{\pi}\tilde{n}/4)^{2/3}$ in dimensionless form, where we have reintroduced explicitly the band mass. On the other hand, the dimensionless subband energies in an infinite square well are $\tilde{E}_q = \frac{m}{m_b}(\pi/2^{4/3})(q/\tilde{L})^2$. The condition $\tilde{\mu}_0 = \tilde{E}_q$ thus yields equidistant values of $\tilde{L}$ for integer q, separated by the characteristic length

$$\Delta\tilde{L}_0 = \left(\frac{\pi}{3\tilde{n}}\right)^{\frac{1}{3}}. \tag{7}$$

Using $n = k_F^3/(3\pi^2)$, we get the desired result $\Delta L_0 = \pi/k_F$. In the exact BCS equation, however, the period of oscillations is fixed by the condition $\tilde{\mu} = \tilde{E}_q - 1$ as we have seen. It is straightforward to extract from this condition an analytical expression for the characteristic length at large L in the weak coupling limit $\bar{\lambda} \to 0$, where μ can be replaced by μ_0. We obtain

$$\Delta\tilde{L} = \frac{1}{\sqrt{\left(\frac{3\tilde{n}}{\pi}\right)^{2/3} + \frac{2^{4/3}}{\pi}\frac{m_b}{m}}} \qquad (\bar{\lambda} \to 0). \tag{8}$$

In dimensionful form, this gives $\Delta L = \pi/\sqrt{k_F^2 + 2m_b\omega_D/\hbar}$. The exact period of oscillations at weak coupling is shorter than the TB result. Beside the Fermi wavelength, one sees the emergence of a new length scale $\hbar/\sqrt{2m_b\hbar\omega_D}$ associated with the pairing cutoff, which controls the length of the T_c oscillations at low density—or, more specifically, when the Fermi energy is small compared with the Debye energy. The TB result is recovered at high density.

For a finite coupling, the bulk chemical potential can be written as $\mu = \mu_0 - \Delta\mu$. $\Delta\mu$ is a positive function increasing with density and coupling (see part I). Considering this correction, the exact length becomes

$$\Delta\tilde{L} = \frac{1}{\sqrt{\left(\frac{3\tilde{n}}{\pi}\right)^{2/3} + \frac{2^{4/3}}{\pi}\frac{m_b}{m}(1-\Delta\tilde{\mu})}}. \tag{9}$$

This shows that a finite coupling brings the exact length closer to the TB result as compared to Eq. (8), and can even lead to a length *longer* than π/k_F if $\Delta\mu > \hbar\omega_D$, which happens at large coupling and/or high density. The various trends are illustrated in Fig. 5. We have evaluated numerically the length by tracking successive oscillations at $\tilde{L} > 50$. The result (8) is well obeyed for $\bar{\lambda} < 1$. A length longer than the TB value can be seen at high density on the $\bar{\lambda} = 3$ curve.

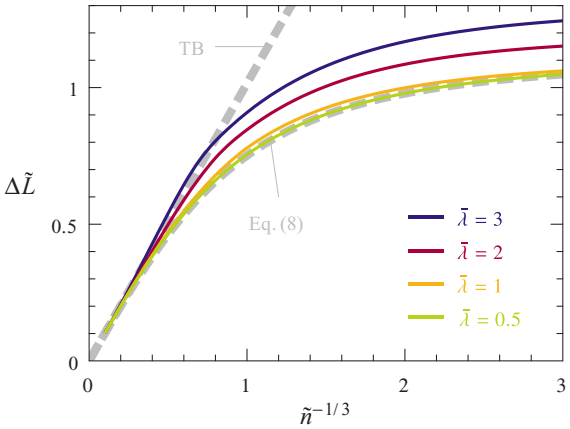

FIG. 5. Characteristic length of the T_c oscillations as a function of density and coupling, calculated numerically at large L. The Thompson–Blatt (TB) expression (7) and weak-coupling expression (8) are shown for comparison. The band mass is used as the reference mass ($m = m_b$), $\tilde{n} = n/[2(m_b\omega_D/2\pi\hbar)^{3/2}]$, and $\Delta\tilde{L} = 2^{1/3}(m_b\omega_D/2\pi\hbar)^{1/2}\Delta L$.

C. Asymptotic behavior for ultrathin films

For ultrathin films the exact BCS T_c approaches zero for all densities and couplings (Fig. 4). This is a regime where only the lowest subband matters. The TB model is unreliable in this limit, as it returns a diverging T_c. The reason for a large T_c is the $1/L$ divergence of the quasi-2D coupling [Eqs. (4) and (5)], combined with the facts that the lowest subband remains occupied all the way down to $L = 0$ ($\mu_0 > E_1$, see Fig. 3) and contributes to T_c like a bulk 2D band. In the self-consistent calculation, the chemical potential at T_c moves below the lowest subband as L approaches zero, and reaches the limit $E_1 - \hbar\omega_D$ at $L = 0$ (Fig. 3). Thus there is no state to pair at $L = 0$ and T_c vanishes. In the one-subband regime, the problem reduces to a 2D problem with effective density and coupling. Indeed, for a single subband, Eq. (1) becomes

$$1 = \bar{\lambda}_{\text{eff}}\,\psi_2(1+\tilde{\mu}', \tilde{T}_c), \quad \tilde{n}_{\text{eff}} = \tilde{T}_c \ln(1 + e^{\tilde{\mu}'/\tilde{T}_c}), \tag{10}$$

with $\tilde{\mu}' = \tilde{\mu} - \tilde{E}_1$. The effective 2D density vanishes linearly with L and reads $\tilde{n}_{\text{eff}} = 2^{-1/3}(m/m_b)\tilde{n}\tilde{L}$, while the effective coupling diverges as $1/L$ and is given by $\bar{\lambda}_{\text{eff}} = (3\sqrt{\pi}/2^{5/3})(m/m_b)^{1/2}\bar{\lambda}/\tilde{L}$. Equation (10) is identical to Eq. (15) of part I in dimension $d = 2$. The exact solution as $\tilde{n}_{\text{eff}}$ approaches zero is

$$\tilde{T}_c = \tilde{n}_{\text{eff}} \exp\left[W\left(\frac{e^{-2/\bar{\lambda}_{\text{eff}}}}{\tilde{n}_{\text{eff}}}\right)\right]. \tag{11}$$

$W(x)$ is the Lambert function. The limiting value of the chemical potential for $\tilde{n}_{\text{eff}} = 0$ is $\tilde{\mu}' = -e^{-2/\bar{\lambda}_{\text{eff}}}$, which gives $\tilde{\mu}' = -1$ at $\tilde{L} = 0$ consistently with Fig. 3. Equation (11) is compared with the full $T_c(L)$ dependency in Fig. 4. For

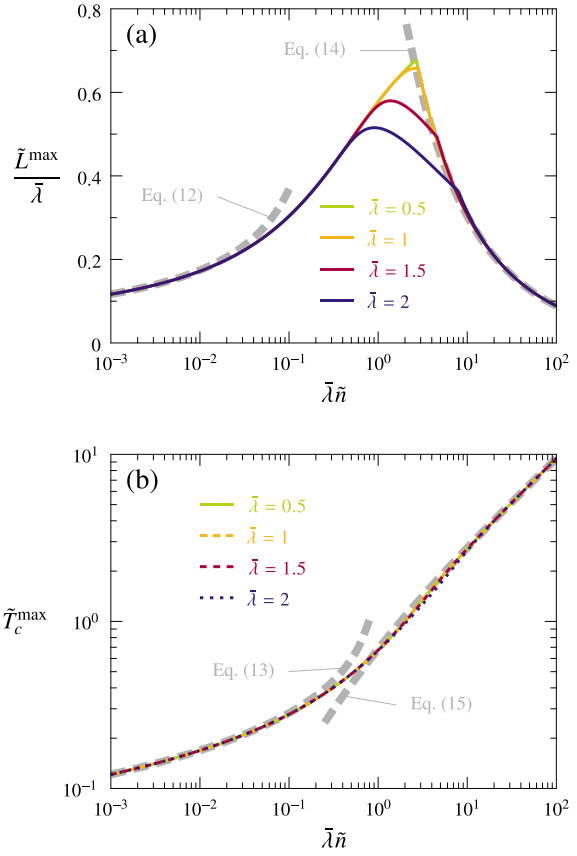

FIG. 6. (a) Thickness $L^{\max}$ leading to the maximum T_c normalized by the coupling $\bar{\lambda}$ and (b) maximum T_c as a function of $\bar{\lambda}\tilde{n}$ for various values of $\bar{\lambda}$. The broken thick lines show the asymptotic formulas in the various regimes.

small values of $\bar{\lambda}\tilde{n}$, the validity of the asymptotic formula extends past the maximum T_c: Eq. (11) is therefore the good starting point for obtaining analytically $T_c^{\max}$ in this limit. In the opposite limit of large $\bar{\lambda}\tilde{n}$, the initial raise of T_c is correctly described, but the maximum is controlled by the break as already pointed out.

D. Maximum T_c in the one-subband regime

A figure of merit of the $T_c(L)$ curve is the maximum critical temperature which can be achieved by varying L. In Fig. 6, we display the thickness $L^{\max}$ at which the maximum occurs as well as $T_c^{\max}$ as a function of the product $\bar{\lambda}\tilde{n}$. It is seen that $L^{\max}/\bar{\lambda}$ and $T_c^{\max}$ approach universal functions at large and small values of $\bar{\lambda}\tilde{n}$. While $L^{\max}/\bar{\lambda}$ shows some dependence on $\bar{\lambda}$ in the transition region $\bar{\lambda}\tilde{n} \sim 1$, $T_c^{\max}$ follows a remarkable scaling law in the whole range of $\bar{\lambda}\tilde{n}$ values, with only tiny dependence on $\bar{\lambda}$ in the transition region.

The asymptotic behavior at small $\bar{\lambda}\tilde{n}$ can be deduced from Eq. (11), because in this limit $\bar{\lambda}$ and/or $\tilde{n}$ can be taken arbitrarily small, such that the position and height of the maximum is exactly captured (see Fig. 4). Differentiating Eq. (11) with respect to $\tilde{L}$, we find the position of the maximum as

$$\frac{\tilde{L}^{\max}}{\bar{\lambda}} = \frac{A}{2B}[-\ln(A\bar{\lambda}\tilde{n}) - \sqrt{\ln^2(A\bar{\lambda}\tilde{n}) - 4}], \qquad (12)$$

where $A = (3\sqrt{\pi}/8)(m/m_b)^{3/2}$ and $B = 2^{-1/3}m/m_b$. This is indeed a function of the product $\bar{\lambda}\tilde{n}$. Substituting this back into Eq. (11) gives the maximum critical temperature. In order to simplify its expression while preserving the correct asymptotic behavior, we replace $\tilde{L}^{\max}/\bar{\lambda}$ in Eq. (12) by the simpler formula $-A/[B\ln(A\bar{\lambda}\tilde{n})]$. $T_c^{\max}$ can then be rearranged in the form

$$\tilde{T}_c^{\max} = \frac{e^{1/\ln(A\bar{\lambda}\tilde{n})}}{W\left(-\frac{\ln(A\bar{\lambda}\tilde{n})}{A\bar{\lambda}\tilde{n}}e^{1/\ln(A\bar{\lambda}\tilde{n})}\right)}. \qquad (13)$$

Equations (12) and (13) capture the universal behavior of the maximum T_c at small $\bar{\lambda}\tilde{n}$, as demonstrated in Fig. 6.

For large $\bar{\lambda}\tilde{n}$, the maximum T_c coincides with the break which occurs when $\mu = E_1 + \hbar\omega_D$. Eq. (22) of part I shows that the following holds at this break: $\tilde{n}_{\rm eff}^{\max} = \tilde{T}_c^{\max}\ln(e^{1/\tilde{T}_c^{\max}} + 1)$. The effective coupling at the maximum is proportional to $\bar{\lambda}/\tilde{L}^{\max}$, which becomes large in the regime considered [Fig. 6(a)]. In this strong-coupling regime, the critical temperature is proportional to the coupling (part I) such that $\tilde{T}_c^{\max} = \bar{\lambda}_{\rm eff}^{\max}/2$. Putting everything together we obtain

$$\bar{\lambda}\tilde{n}\left(\frac{\tilde{L}^{\max}}{\bar{\lambda}}\right)^2 = \frac{A}{B^2}\ln\left(e^{\frac{B}{A}\frac{\tilde{L}^{\max}}{\bar{\lambda}}} + 1\right).$$

This equation yields $\tilde{L}^{\max}/\bar{\lambda}$ as a function of $\bar{\lambda}\tilde{n}$, but admits no closed solution. Since $\tilde{L}^{\max}/\bar{\lambda}$ approaches zero in the limit of interest, we can expand the ln and solve. This gives

$$\frac{\tilde{L}^{\max}}{\bar{\lambda}} = \frac{A}{2B}\frac{1+\sqrt{1+16\ln(2)\,A\bar{\lambda}\tilde{n}}}{2A\bar{\lambda}\tilde{n}}, \qquad (14)$$

$$\tilde{T}_c^{\max} = \frac{\sqrt{1+16\ln(2)\,A\bar{\lambda}\tilde{n}}-1}{4\ln(2)}. \qquad (15)$$

Both expressions are compared with the numerical data in Fig. 6.

IV. FINITE QUANTUM WELL AND CRITICAL POTENTIAL

The infinite-well model has the advantage of its simplicity, permitting exact analytical results in some regimes. However, realistic superconducting films are better described by a finite confinement potential. For a free-standing film, this potential is set by the material's work function, possibly reduced by finite-size effects if the film is very thin; this is usually a large energy scale compared with $\hbar\omega_D$. For films deposited on a substrate or sandwiched between two buffer layers, however, the confinement potential may be weak and comparable with $\hbar\omega_D$. The phenomenological model of Yu *et al.* [3] is appropriate for thick films and large confinement potentials, but breaks down in the opposite limits. In this section, we study numerically the critical temperature for a film confined in a square potential well of width L and depth U. The main changes in the model with respect to the infinite-well case are a modification of the bound-state energies and the replacement of the overlap integral (5) by (6). Since (6) is smaller than (5), a smaller T_c is to be expected in the finite well. An additional

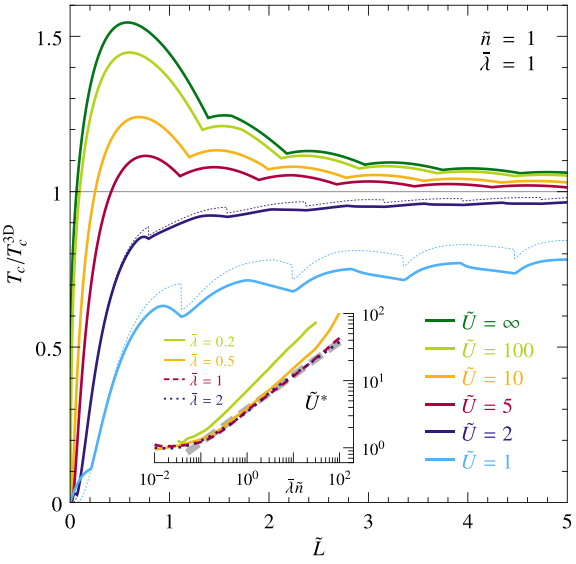

FIG. 7. Relative change of the critical temperature as a function of film thickness for various strengths of the confinement potential. The dotted lines are calculated by neglecting the contribution of scattering states. (Inset) Critical potential as a function of $\bar{\lambda}\tilde{n}$ for various couplings. The thick gray line is the function $4.65\,(A\bar{\lambda}\tilde{n})^{1/2}$ with $A = (3\sqrt{\pi}/8)(m/m_b)^{3/2}$. The confinement potential is measured in units of $\hbar\omega_D$. The band mass is used as the reference mass.

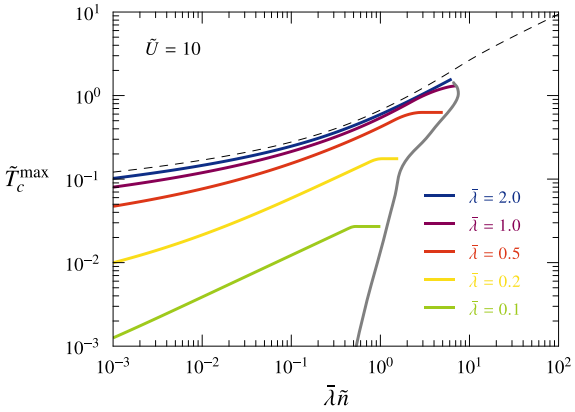

FIG. 8. Maximum T_c as a function of $\bar{\lambda}\tilde{n}$ for a confinement potential $\tilde{U} = 10$. The dashed line is the result for $\tilde{U} = \infty$ and $\bar{\lambda} = 2$ (Fig. 6). The gray line shows the variation of $\tilde{T}_c^{3D}$ with $\bar{\lambda}$ at the critical density.

difficulty appears at small U, because unbound states outside the well feel the pairing interaction and change T_c. If U is small and the density is high enough, we may even reach a regime where the scattering states are occupied. We have found that spurious discontinuities occur in the dependence of T_c on various model parameters if the scattering states are ignored. These discontinuities are removed by including the appropriate corrections in Eq. (1). The details are reported in the Appendix.

Figure 7 illustrates the evolution of T_c with film thickness in a finite well. The critical temperature is lower than in the infinite well as expected. As the well becomes more and more shallow, the energy of the bound states decreases and the resonances move to lower values of L. There are two regimes for the potential U, separated by a critical value U^*. For $U > U^*$, T_c is an increasing function of decreasing L and there is an absolute maximum in T_c at small L, like for the infinite well. For $U < U^*$, T_c decreases as the thickness is reduced and the maximum at low L is lost. The scattering states give a non-negligible contribution in this latter regime as illustrated in Fig. 7. The critical potential U^* decreases with decreasing density and increasing coupling. We find that $\tilde{U}^*$ approaches a universal function of $\bar{\lambda}\tilde{n}$ at strong coupling (inset of Fig. 7). Except at small $\bar{\lambda}\tilde{n}$, this function is well fitted by the power law $\tilde{U}^* \propto (\bar{\lambda}\tilde{n})^{1/2}$.

The maximum in T_c, when it exists, is no longer a universal function of $\bar{\lambda}\tilde{n}$ as illustrated in Fig. 8. T_c^{max} is much more efficiently suppressed in a finite well at weak coupling than at strong coupling, consistent with the fact that U^* is lower at strong coupling. The analysis leading to Eqs. (12)–(15) can be repeated, with the factor $3/(2L)$ appearing in the effective coupling due to Eq. (5) replaced by O_{11} defined in Eq. (6a). Figures 4(b) and 6(a) show that at weak coupling the maximum occurs very close to $L = 0$; this is also where the overlap O_{11} is dominated by the tails of the wave function outside the well and is therefore most strongly suppressed by reducing U. At large $\bar{\lambda}\tilde{n}$, T_c^{max} eventually disappears when the $\tilde{U}^*$ line is crossed at some critical density (see inset of Fig. 7). At this density the maximum T_c corresponds to the 3D value, which is plotted as a gray line in Fig. 8.

V. DISCUSSION OF THE MAIN RESULTS

Our primary result is that the critical temperature of an electron gas with BCS-like pairing interaction varies continuously, unlike the DOS, as a function of thickness when the system is confined into a thin film. While approximate calculations have suggested jumps in T_c when the chemical potential coincides with the bottom of a subband, our calculations show *dips* in T_c when the chemical potential lies $\hbar\omega_D$ *below* the bottom of a subband. This fact changes the characteristic length of T_c oscillations from π/k_F at high density to $\pi\hbar/\sqrt{2m_b\hbar\omega_D}$ at low density. In-between the dips, T_c exhibits maxima which are rather weak, except in the ultrathin limit where only one subband is occupied: there T_c shows a maximum which can be high. The parameter driving the maximum T_c is $A\bar{\lambda}\tilde{n} = 3Vn/(8\hbar\omega_D)$. For a strong confinement, we have

$$k_B T_c^{max} = \hbar\omega_D F\left(\frac{3}{8}\frac{Vn}{\hbar\omega_D}\right), \tag{16}$$

where $F(x)$ is the nearly universal function displayed in Fig. 6(b). Surprisingly, while the critical temperature increases in 3D with increasing the band mass, the largest critical temperature achievable by quantum confinement does not depend on the mass. The function $F(x)$ is proportional to $\sqrt{x}$ at large x and $k_B T_c^{max}$ approaches $0.74\sqrt{\hbar\omega_D Vn}$ for $Vn \gg \hbar\omega_D$. In the opposite limit $Vn \ll \hbar\omega_D$, the expression $k_B T_c^{max} \approx \hbar\omega_D/\ln(6.3\hbar\omega_D/Vn)$ provides a good

approximation. These expressions show that $T_c^{\max}$ is an increasing function of $\hbar\omega_D$, V, and n in all parameter regimes.

Another finding of our study is the existence of a critical confinement potential U^* below which the thin films have a T_c lower than the bulk T_c. This observation may shed a new light on the experimental data available for thin films. At strong to intermediate coupling, the critical potential is well fitted by the power law $U^* \approx 2.85\sqrt{\hbar\omega_D Vn}$. Therefore the larger the density, the stronger the confinement needed in order to observe an enhancement of the critical temperature in thin films. The optimal conditions for observing the T_c enhancement are a low value of U^* and a large value of $T_c^{\max}$. The classical BCS superconductors are in the high-density regime where $T_c^{\max} \sim \sqrt{\hbar\omega_D Vn}$, for they obey the adiabatic condition $\hbar\omega_D \ll E_F$, which implies $\tilde{n} \propto (E_F/\hbar\omega_D)^{3/2} \gg 1$. Since $T_c^{\max}$ and U^* both scale in the same way in this regime, it is unlikely that the optimal conditions be met. For instance, the critical temperature of bulk Al ($T_c = 1.2$ K, nominal valence electron density $n = 6 \times 10^{22}\text{cm}^{-3}$, mass $m_b = m$, Debye energy $\hbar\omega_D = 37$ meV) is reproduced by setting $\bar{\lambda} = 0.0135$. This implies $\bar{\lambda}\tilde{n} = 19$, putting indeed Al in the high density regime. Because $\bar{\lambda}$ is so small, the fit given above underestimates U^*. The exact value is $U^* = 8.3$ eV, that is, 2.7 eV measured from the Fermi energy. This is smaller than the Al work function (4 eV), such that free-standing Al films would be expected to show some T_c enhancement. For ultrathin epitaxial films grown on silicon [15], the confinement is limited by the Si bandgap and a decrease of T_c is predicted. We speculate that the T_c enhancement observed in granular films [11,14,37] is due to stronger confinement effects in the grains [38].

It is interesting to ask whether the spectacular enhancement of T_c recently discovered in FeSe monolayers grown on $SrTiO_3$ (STO) [26] may be, at least partly, ascribed to quantum confinement. Unlike the classical superconductors, FeSe is a low-density system. The four bands forming the Fermi surface have masses between 1.9 and 7.2 electronic masses and similar Fermi energies as low as 3.6 to 18 meV [39]. For simplicity, we envision a one-band system characterized by the average values $m_b/m = 5.5$ and $E_F = 10$ meV for a density equivalent to 0.0091 electron per Fe atom, consistent with the measurements. It is uncertain which value one should use for the cutoff of the pairing interaction, especially for the monolayer where this value may be set by the coupling to the STO substrate. For bulk FeSe, we take as the lower bound the spin resonance at $4.4T_c = 3$ meV [40,41], which would be the characteristic energy in the spin-fluctuation pairing scenario. An upper bound may be the Debye energy of 18 meV in a phonon-mediated scenario [42]. The corresponding range of interaction strength needed to reproduce the bulk T_c of 8 K is given by $Vn = 8.4$–4.2 meV. For the lower cutoff, we have $Vn > \hbar\omega_D$ while for the higher we have $Vn < \hbar\omega_D$. The approximate formulas given above yield $T_c^{\max} \approx 43$–63 K for strong confinement if the bulk cutoff is used for the thin film. The exact values are $T_c^{\max} = 30$–63 K, and these maxima occur for thicknesses $L = 9.2$–2.4 Å, larger than the FeSe interlayer distance (1.46 Å). Exactly at the latter thickness, the predicted critical temperature range is $T_c = 20$–61 K. The critical potential, on the other hand, is low and easily overcome: we find $U^* = 18$–27 meV, in good agreement with the approximate formula given in the previous paragraph. With a finite confinement barrier given by half the STO bandgap (1.6 eV) and for the thickness $L = 1.46$ Å, the calculated T_c varies between 17 and 47 K. Thus the quantum confinement alone can explain an increase of T_c by a factor 2 to 6. We estimate the effect of a possible "boost" from the substrate by raising the cutoff to the energy of the STO optical phonon mode to which the FeSe electrons appear to be strongly coupled (100 meV) [43], while keeping the interaction strength fixed to the bulk FeSe value. The range of critical temperatures for the monolayer skyrockets to 219–173 K. With its low density and relatively high T_c, FeSe appears as an ideal candidate to observe significant confinement effects.

VI. APPLICATION TO LEAD THIN FILMS

There is a large body of experimental literature dedicated to lead thin films [17,19,22–25,44] and islands [18,45,46] deposited on silicon. The thin films generically have a lower T_c than bulk Pb. Oscillations as a function of film thickness showing larger T_c's for films made of an even number of monolayers (ML) were reported [22,23]. These trends can be understood within the Bogoliubov–de Gennes formalism [34,47]. Other theoretical ideas have also been put forward, such as a change of the electron-phonon coupling in the films [48] or a role played by the interaction with the Si substrate [9]. Superconductivity was later shown to persist down to 5 ML [24], 2 ML [25], and even a single ML [19]. A recent first-principles strong-coupling calculation for free-standing films could explain their superconductivity down to 5 ML [49]. We consider more specifically here the data set of Ref. [25] for ultrathin films (2–15 ML) deposited on Si(111), in particular the peculiar behavior of the thinnest films. Qin *et al.* measured by scanning tunneling spectroscopy a 10% enhancement of T_c at 4 ML, followed by an abrupt drop by ~30% at 2 ML. 3-ML films were not stable. The authors argue that the 2-ML films are in the one-subband regime. Two types of these 2-ML films were found, with different T_c values. In the first type with the larger T_c, the in-plane lattice parameter of the film is the same as in bulk Pb, while for the second type with the lower T_c the in-plane parameter is 86% larger than in the bulk, suggesting that the film is pseudomorphically strained to match the Si $\sqrt{3} \times \sqrt{3}$ reconstructed surface.

The maximum at 4 ML and the drop at 2 ML in the one-subband regime are reminiscent of the behavior seen in Fig. 7. This suggests that the model may shed some light on the various trends seen in these data. A direct application seems questionable, because Pb is not a free-electron-like metal and the confinement potential of these films is most probably asymmetric [9]. Nevertheless, we find that the simple model with one parabolic band and a symmetric potential can provide an effective description of the experiment and give hints about the origin of the maximum at 4 ML. We have converted the film thicknesses from ML to length using an interlayer distance of 2.86 Å, except for the strained 2-ML film for which we used 1.54 Å. 2.86 Å corresponds to the distance between (111) planes in bulk Pb, while the value 1.54 Å assumes that the 86% in-plane tensile strain is isochoric, leaving the density unchanged. The interlayer distance of the strained 2-ML film is uncertain, but its value does not influence critically our

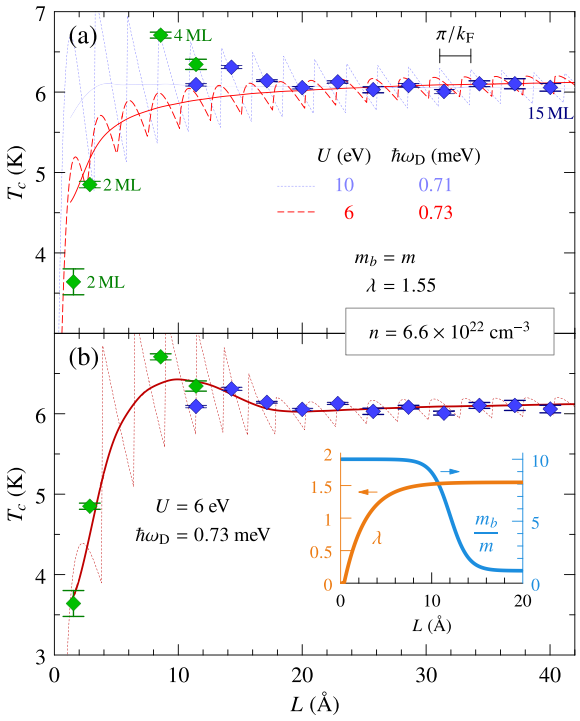

FIG. 9. Superconducting transition temperature of Pb thin films as a function of film thickness L. The diamonds with error bars show the measurements of Ref. [25]; different colors correspond to different data sets. (a) Prediction of the model using parameters of bulk Pb with a strong (dotted line) and weak (dashed line) confinement potential. A running average is shown by the solid lines. (b) Interpretation of the data by means of thickness-dependent coupling parameter and band mass. The L dependence of these quantities is shown in the inset.

analysis. The evolution of the measured T_c with film thickness is shown in Fig. 9 (diamonds with error bars).

Among the five parameters of the model, the ones with best known values are the electron density, the coupling strength on the Fermi surface, and the band mass. The cutoff of the pairing interaction and the confinement potential are less obvious. The nominal Fermi-surface density of lead is $n = 6.6 \times 10^{22}$ cm^{-3}, corresponding to two $6p$ electrons per atom and four atoms per cell in a cubic cell with lattice parameter $a = 4.95$ Å. Although the strain in the films may induce small changes, we will keep the electron density fixed to this nominal value in the following. For the Fermi-surface coupling we use the Allen–Dynes value $\lambda = 1.55$ [50]. Recall that the coupling $\bar{\lambda}$ is evaluated at an energy $\hbar\omega_D$ above the band bottom, not at the Fermi energy, hence we define $\bar{\lambda} = \lambda\sqrt{\hbar\omega_D/E_F}$. We fix the band mass to the free-electron value, as indicated by electronic structure calculations [51]. With this band mass, the linear coefficient of the electronic specific heat is $k_B^2/(3\hbar^2)(1 + \lambda)m_b k_F = 3.03$ mJ mol^{-1} K^{-2}, very close to the experimental value of 3.06 [52]. The resulting Fermi energy is $E_F = 5.95$ eV.

The films are confined on one side by vacuum and on the other side by the Si substrate. An estimate for the potential barrier to vacuum is given by the Pb work function $\phi = 4.14$ eV, corresponding to a confinement potential $U = E_F + \phi = 10$ eV. The barrier to the Si substrate is given by the n-type Schottky barrier which, for bulk Pb on Si(111), is 0.7–0.9 eV [53]. The Schottky barrier is sensitive to the details of the interface atomic and electronic structure: for thin films it may or may not agree with the value for macroscopic contacts. We will consider as an extreme case the limit of a vanishing Schottky barrier by taking a confinement potential $U = 6$ eV. We fix the remaining parameter, $\hbar\omega_D$, by the requirement that the critical temperature for the thickest films is of the order of 6 K like in the experiment. This gives $\hbar\omega_D = 0.71$ and 0.73 meV for $U = 10$ and 6 eV, respectively. These "Debye energies" are roughly ten times smaller than the specific-heat Debye temperature of 105 K [54]. It must be kept in mind that our model is a weak-coupling parametrization of the critical temperature of lead, and that no Coulomb correction is involved. If we insist on identifying $\hbar\omega_D$ with the Debye temperature, the coupling parameter and band mass needed in order to reproduce T_c and the Fermi-level DOS are 0.34 and 1.9 electronic masses, respectively. Both sets of parameters bring us to the same qualitative conclusions; our preference for the former set with $\lambda = 1.55$ and unit mass will be explained below.

The $T_c(L)$ curves calculated with $U = 10$ and 6 eV are plotted in Fig. 9(a). In both cases, there are rapid oscillations of T_c. The period of oscillations is given by the Thompson–Blatt formula, as expected at high density. The experimental data seems to indicate a longer period of ∼2 ML, as would be expected if the density were ten times smaller than the nominal value. Such a big loss of electron density is unlikely, and we tentatively attribute the apparent change of period to the fact that the interlayer distance is incommensurate with the expected period. The amplitude of the oscillations has the correct order of magnitude, though. This amplitude is chiefly controlled by the cutoff $\hbar\omega_D$, and would be more than two times larger with a cutoff equal to the Debye temperature of lead. This is our motivation for favoring low values of $\hbar\omega_D$. The curve for $U = 10$ eV happens to hit the experimental points at 2 and 4 ML. Given the uncertainty about the effective film thickness, this must be viewed as an accident. Without precise information about the effective film thickness, it seems more appropriate to ignore the oscillations and focus on the overall trend of T_c as a function of L. Performing a running average with period π/k_F, we thus find that the weak-barrier model with $U = 6$ eV better captures the low T_c at 2 ML.

Neither model explains the maximum at 4 ML, however. This suggests that at least one of the parameters n, m_b, and λ is changing with decreasing thickness. Changes of n will not produce the desired result. To explain the 4-ML data, an increase of λ up to ∼1.8 would be necessary; with such a coupling, however, the 2-ML data can only be explained if the relative band mass is decreased to ∼0.6. The opposite scenario with an increase of the mass in the ultrathin films seems more likely. A number of photoemission experiments have indeed reported large effective masses for Pb thin films grown on Si(111), with mass enhancements by up to a factor ten [55–57]. Figure 9(b) represents one possible interpretation of the whole experimental data set, by means of an effective mass which decreases from $10m$ to m with increasing film thickness, as plotted in the inset. At the same time, the coupling

must be suppressed at very low L, in order to explain the data at 2 ML. This suppression of coupling with decreasing thickness is supported by *ab initio* calculations based on the Migdal-Eliashberg theory for free-standing Pb films [18,48], and the same decreasing tendency has been deduced from femtosecond laser photoemission spectroscopy measurements [58].

VII. CONCLUSION

By solving exactly the BCS gap equation at T_c, we have shown that the critical temperature of thin films is a continuous function of the film thickness. Previously published discontinuous jumps of T_c are artifacts of approximating the DOS by a constant. This approximation breaks down when the chemical potential is close to the edge of a subband, such that the pairing interaction is cut by the subband bottom. In the extreme case of a hard-wall confinement, T_c increases with reducing thickness until it reaches a maximum before dropping to zero. The value of T_c at the maximum follows a surprising scaling law, which is independent of the electronic band bass. In a symmetric rectangular potential well of finite depth U, the evolution of T_c with thickness changes qualitatively at a parameter-dependent characteristic potential U^*. For $U > U^*$, the behavior is similar to the hard-wall case, while for $U < U^*$ the critical temperature is lower in the film than in the bulk.

Our results provide new guidelines in the endeavor to improve the superconducting properties by quantum confinement. The existence of a maximum in T_c at low thickness is intriguing, but the observation of this maximum requires a strong enough confinement. Quite generally, one expects T_c to be enhanced by a stronger confinement potential. In this respect, small-bandgap semiconductors may not be the ideal substrates. The exploration of different substrates, the use of interface engineering, or ideally the study of free-standing films would allow to challenge this idea. The scaling law for the characteristic potential in the regime $\lambda\sqrt{\hbar\omega_D/E_F} > 1$ reads $U^* \propto \sqrt{\lambda\,\hbar\omega_D E_F}$. This points towards low-density superconductors like $SrTiO_3$ or FeSe as the best candidates for a small U^*, which could be overcome to observe the T_c increase.

One may question the relevance of a continuous free-electron-like weak-coupling model for representing realistic thin films. While the limitations of this model are obvious, we have shown that it provides a description of the evolution of T_c with thickness for thin films of Pb on Si(111) with reasonable parameters. This strengthens our confidence that the model may perhaps be useful for other systems as well.

ACKNOWLEDGMENTS

We thank J. M. Triscone and S. Gariglio for stimulating discussions. We are grateful to A. Bianconi, A. P. Durajski, A. García-García, D. H. Liebenberg, F. Peeters, A. Perali, and D. Roditchev for useful comments and discussions. This work was supported by the Swiss National Science Foundation under Division II.

APPENDIX: INCLUSION OF SCATTERING STATES

To begin with, we consider electrons interacting via a generic two-body interaction $\hat{V} = \frac{1}{2}\sum_{\alpha\beta\gamma\delta} V_{\alpha\beta\gamma\delta} c^\dagger_\alpha c^\dagger_\beta c_\delta c_\gamma$ where the greek letters denote single-particle states with wave functions $\varphi_\alpha(\boldsymbol{r})$, etc. Decoupling this interaction in the usual way, we derive Gor'kov equations which we then linearize at T_c in order to obtain a gap equation expressed in the generic single-particle basis. This gap equation is

$$\Delta_{\alpha\beta} = \sum_{\mu\nu} V_{\alpha\beta\mu\nu} \frac{\Delta_{\mu\nu}}{\xi_\mu + \xi_\nu} [f(\xi_\mu) + f(\xi_\nu) - 1]. \tag{A1}$$

ξ_μ is the single-particle energy measured from the chemical potential and $f(\xi)$ is the Fermi distribution. At this point we specialize to a BCS-like interaction which is local, acts between pairs of time-reversed states denoted $(\alpha,\bar{\alpha})$ with $\xi_\alpha = \xi_{\bar{\alpha}}$, and has a separable energy cutoff:

$$V_{\alpha\beta\mu\nu} = -V\delta_{\beta\bar{\alpha}}\delta_{\nu\bar{\mu}}\eta(\xi_\alpha)\eta(\xi_\mu)O_{\alpha\mu}. \tag{A2}$$

$V > 0$ gives the strength of the local pairing, the function $\eta(\xi)$ implements the energy cutoff, and the overlap integrals are defined as $O_{\alpha\mu} = \int d\boldsymbol{r}\, \varphi^*_\alpha(\boldsymbol{r})\varphi^*_{\bar{\alpha}}(\boldsymbol{r})\varphi_\mu(\boldsymbol{r})\varphi_{\bar{\mu}}(\boldsymbol{r})$. The order parameter is nonzero only for time-reversed pairs, $\Delta_{\alpha\beta} = \delta_{\beta\bar{\alpha}}\eta(\xi_\alpha)\Delta_\alpha$, and the following equation for the gap parameters results from (A1) and (A2):

$$\Delta_\alpha = \sum_\mu \eta^2(\xi_\mu) V O_{\alpha\mu} \frac{\Delta_\mu}{2\xi_\mu} \tanh\left(\frac{\xi_\mu}{2k_B T_c}\right). \tag{A3}$$

We now apply this to a quasi-two-dimensional geometry with translation invariance in the (x,y) plane, and some potential well in the region around $z = 0$. The potential is such that all states with energy larger than U are scattering states. The wave functions can be taken as $\varphi_\alpha(\boldsymbol{r}) \mapsto \frac{1}{\sqrt{\mathscr{S}}} e^{i\boldsymbol{k}\cdot\boldsymbol{r}} u_q(z)$ with $\mathscr{S}$ the system size in the (x,y) plane. If the gap parameter is independent of the in-plane momentum $\boldsymbol{k}$, the in-plane momentum sum in (A3) can be expressed in terms of the 2D DOS, leading to

$$\Delta_q = \sum_p V O_{qp} \Delta_p \int_{-\hbar\omega_D}^{\hbar\omega_D} dE\, N_0^{2D}(\mu + E - E_p) \frac{\tanh\left(\frac{E}{2k_B T_c}\right)}{2E}. \tag{A4}$$

We want to separate the p sum into bound and scattering states. Whenever q and/or p corresponds to a scattering state, the overlap integral O_{qp} is proportional to $1/\mathscr{L}$ where $\mathscr{L}$ is the system size in the z direction. We can take this factor away from the definition of the overlap, and use it to convert the sum over scattering states into an integral. At this stage we assume that the gap parameter is the same for all scattering states, Δ_s, and likewise the overlap O_{qs}; this is not true in general, as discussed further below. We moreover assume that the DOS of the scattering states is not significantly modified by the formation of bound states. Using the letters q and p for bound states, and the letter s for scattering states, Eq. (A4)

becomes

$$\Delta_q = \sum_p V O_{qp} \Delta_p \int_{-\hbar\omega_D}^{\hbar\omega_D} dE\, N_0^{2D}(\mu + E - E_p) \frac{\tanh\left(\frac{E}{2k_B T_c}\right)}{2E}$$
$$+ V \mathscr{L} O_{qs} \Delta_s \int_{-\hbar\omega_D}^{\hbar\omega_D} dE\, N_0^{3D}(\mu + E - U) \frac{\tanh\left(\frac{E}{2k_B T_c}\right)}{2E},$$
$$\Delta_s = V \mathscr{L} O_{ss} \Delta_s \int_{-\hbar\omega_D}^{\hbar\omega_D} dE\, N_0^{3D}(\mu + E - U) \frac{\tanh\left(\frac{E}{2k_B T_c}\right)}{2E}.$$

The sum over scattering states has been recast in terms of the 3D DOS. In the second relation, the coupling between scattering and bound states has disappeared, because the overlap $O_{sp} \sim 1/\mathscr{L}$ is summed over a finite number of bound states, and the resulting contribution drops in the thermodynamic limit. Moving on to dimensionless variables and proceeding like in part I, we find that the equation for T_c in the presence of scattering states is once again of the form $0 = \det[\mathbb{1} - \Lambda(\tilde{\mu}, \tilde{T}_c)]$, but the matrix Λ must be augmented by one line and one column in order to account for scattering states. The matrix elements are

$$\Lambda_{qp}(\tilde{\mu}, \tilde{T}_c) = \bar{\lambda}_{qp} \psi_2(1 + \tilde{\mu} - \tilde{E}_p, \tilde{T}_c), \quad \text{(A5a)}$$
$$\Lambda_{qs}(\tilde{\mu}, \tilde{T}_c) = \bar{\lambda} \mathscr{L} O_{qs} \psi_3(1 + \tilde{\mu} - \tilde{U}, \tilde{T}_c), \quad \text{(A5b)}$$
$$\Lambda_{sq}(\tilde{\mu}, \tilde{T}_c) = 0, \quad \text{(A5c)}$$
$$\Lambda_{ss}(\tilde{\mu}, \tilde{T}_c) = \bar{\lambda} \mathscr{L} O_{ss} \psi_3(1 + \tilde{\mu} - \tilde{U}, \tilde{T}_c). \quad \text{(A5d)}$$

$\bar{\lambda}$ is the 3D coupling and $\bar{\lambda}_{qp}$ is defined in Eq. (4). For a square potential well of width L and depth U, we find that the overlap $\mathscr{L} O_{qs}$ is a function of the energies ε_q and ε_s in the thermodynamic limit. This function approaches unity for all ε_s when ε_q approaches U. For smaller values of ε_q, the function is unity at large ε_s but decreases to zero with L-dependent oscillations at small ε_s. In line with our assumption that all scattering states share the same gap, we must replace $\mathscr{L} O_{qs}$ by a single value which is representative of all bound and scattering states. For simplicity, we choose the value $\mathscr{L} O_{qs} = 1$, which is the limit for large ε_s. For the scattering states, we find $\mathscr{L} O_{ss'} = 1$ for all states.

In addition to changing the equation for T_c, the scattering states also give to the electron density a small contribution which must be considered for the determination of the self-consistent chemical potential. In first approximation, the density contributed by the scattering states is that of a 3D electron gas with chemical potential $\mu - U$. We must, however, handle carefully the situation where a new state comes out of the continuum and localizes into the well, for instance while varying the well thickness L. This process is in principle smooth, but with our approximations, which neglect the distortion of scattering states due to the potential well, it is not: when a new state enters the well, it makes a discontinuous contribution to the density of states such that the self-consistent chemical potential jumps to a lower value in order to keep the total density fixed. To avoid this jump, we continue the localized state into the continuum and take its contribution into account before it gets localized, on top of the contribution of the other scattering states. The correction to the density in Eq. (1b) is therefore $n_{3D}(\mu - U) + n_{2D}(\mu - U - \varepsilon_z)/L$, where $n_{dD}(\mu)$ is the density of a free-electron gas in dimension d with chemical potential μ, and ε_z is the continuation of the bound-state energy in the continuum. This function must start at $+\infty$, decrease as a state approaches the well, and reach zero when the state enters the well. We use

$$\varepsilon_z = \frac{\hbar^2}{2m_b}\left(\frac{\pi}{L}\right)^2 \begin{cases} -\tan\left(\sqrt{\frac{2m_b U}{\hbar^2}} L\right) & -\tan\left(\sqrt{\frac{2m_b U}{\hbar^2}} L\right) > 0 \\ \infty & \text{otherwise} \end{cases}.$$

[1] C. J. Thompson and J. M. Blatt, Shape resonances in superconductors - II simplified theory, Phys. Lett. **5**, 6 (1963); J. M. Blatt and C. J. Thompson, Shape Resonances in Superconducting Thin Films, Phys. Rev. Lett. **10**, 332 (1963).

[2] A. Paskin and A. D. Singh, Boundary conditions and quantum effects in thin superconducting films, Phys. Rev. **140**, A1965 (1965).

[3] M. Yu, M. Strongin, and A. Paskin, Consistent calculation of boundary effects in thin superconducting films, Phys. Rev. B **14**, 996 (1976).

[4] E. H. Hwang, S. Das Sarma, and M. A. Stroscio, Role of confined phonons in thin-film superconductivity, Phys. Rev. B **61**, 8659 (2000).

[5] B. Chen, Z. Zhu, and X. C. Xie, Quantum size effects in thermodynamic superconducting properties of ultrathin films, Phys. Rev. B **74**, 132504 (2006).

[6] K. Szałowski, Critical temperature of MgB_2 ultrathin superconducting films: BCS model calculations in the tight-binding approximation, Phys. Rev. B **74**, 094501 (2006).

[7] A. A. Shanenko, M. D. Croitoru, M. Zgirski, F. M. Peeters, and K. Arutyunov, Size-dependent enhancement of superconductivity in Al and Sn nanowires: Shape-resonance effect, Phys. Rev. B **74**, 052502 (2006); M. D. Croitoru, A. A. Shanenko, and F. M. Peeters, Dependence of superconducting properties on the size and shape of a nanoscale superconductor: From nanowire to film, *ibid.* **76**, 024511 (2007).

[8] M. A. N. Araújo, A. M. García-García, and P. D. Sacramento, Enhancement of the critical temperature in iron pnictide superconductors by finite-size effects, Phys. Rev. B **84**, 172502 (2011).

[9] A. Romero-Bermúdez and A. M. García-García, Size effects in superconducting thin films coupled to a substrate, Phys. Rev. B **89**, 064508 (2014); Shape resonances and shell effects in thin-film multiband superconductors **89**, 024510 (2014).

[10] P. Wójcik and M. Zegrodnik, Interplay between quantum confinement and Fulde-Ferrell-Larkin-Ovchinnikov phase in superconducting nanofilms, Physica E **83**, 442 (2016).

[11] M. Strongin, O. F. Kammerer, and A. Paskin, Superconducting Transition Temperature of Thin Films, Phys. Rev. Lett. **14**, 949 (1965).

[12] B. Abeles, R. W. Cohen, and G. W. Cullen, Enhancement of Superconductivity in Metal Films, Phys. Rev. Lett. **17**, 632 (1966).

[13] Y. F. Komnik, E. I. Bukhshtab, and Man'kovskiĭ, Quantum size effect in superconducting tin films, Sov. Phys. JETP **30**, 807 (1970).

[14] D. H. Liebenberg and L. D. F. Allen, Thin-film superconductors as sensitive thermometers, J. App. Phys. **41**, 4050 (1970).

[15] M. Strongin, O. F. Kammerer, H. H. Farrell, and D. L. Miller, Superconducting Properties of Crystalline Ultrathin Films, Phys. Rev. Lett. **30**, 129 (1973).

[16] D. B. Haviland, Y. Liu, and A. M. Goldman, Onset of Superconductivity in the Two-Dimensional Limit, Phys. Rev. Lett. **62**, 2180 (1989).

[17] O. Pfennigstorf, A. Petkova, H. L. Guenter, and M. Henzler, Conduction mechanism in ultrathin metallic films, Phys. Rev. B **65**, 045412 (2002).

[18] C. Brun, I-Po Hong, F. Patthey, I. Y. Sklyadneva, R. Heid, P. M. Echenique, K. P. Bohnen, E. V. Chulkov, and W.-D. Schneider, Reduction of the Superconducting Gap of Ultrathin Pb Islands Grown on Si(111), Phys. Rev. Lett. **102**, 207002 (2009).

[19] T. Zhang, P. Cheng, W.-J. Li, Y.-J. Sun, G. Wang, X.-G. Zhu, K. He, L. Wang, X. Ma, X. Chen, Y. Wang, Y. Liu, H.-Q. Lin, J.-F. Jia, and Q.-K. Xue, Superconductivity in one-atomic-layer metal films grown on Si(111), Nat. Phys. **6**, 104 (2010).

[20] L. Kang, B. B. Jin, X. Y. Liu, X. Q. Jia, J. Chen, Z. M. Ji, W. W. Xu, P. H. Wu, S. B. Mi, A. Pimenov, Y. J. Wu, and B. G. Wang, Suppression of superconductivity in epitaxial NbN ultrathin films, J. Appl. Phys. **109**, 033908 (2011).

[21] B. G. Orr, H. M. Jaeger, and A. M. Goldman, Transition-Temperature Oscillations in Thin Superconducting Films, Phys. Rev. Lett. **53**, 2046 (1984).

[22] Y. Guo, Y.-F. Zhang, X.-Y. Bao, T.-Z. Han, Z. Tang, L.-X. Zhang, W.-G. Zhu, E. G. Wang, Q. Niu, Z. Q. Qiu, J.-F. Jia, Z.-X. Zhao, and Q.-K. Xue, Superconductivity modulated by quantum size effects, Science **306**, 1915 (2004).

[23] X.-Y. Bao, Y.-F. Zhang, Y. Wang, J.-F. Jia, Q.-K. Xue, X. C. Xie, and Z.-X. Zhao, Quantum Size Effects on the Perpendicular Upper Critical Field in Ultrathin Lead Films, Phys. Rev. Lett. **95**, 247005 (2005).

[24] D. Eom, S. Qin, M.-Y. Chou, and C. K. Shih, Persistent Superconductivity in Ultrathin Pb Films: A Scanning Tunneling Spectroscopy Study, Phys. Rev. Lett. **96**, 027005 (2006).

[25] S. Qin, J. Kim, Q. Niu, and C.-K. Shih, Superconductivity at the two-dimensional limit, Science **324**, 1314 (2009).

[26] J.-F. Ge, Z.-L. Liu, C. Liu, C.-L. Gao, D. Qian, Q.-K. Xue, Y. Liu, and J.-F. Jia, Superconductivity above 100 K in single-layer FeSe films on doped $SrTiO_3$, Nat. Mater. **14**, 285 (2015).

[27] D. Valentinis, D. van der Marel, and C. Berthod, BCS superconductivity near the band edge: Exact results for one and several bands, Phys. Rev. B **94**, 024511 (2016).

[28] D. Innocenti, N. Poccia, A. Ricci, A. Valletta, S. Caprara, A. Perali, and A. Bianconi, Resonant and crossover phenomena in a multiband superconductor: Tuning the chemical potential near a band edge, Phys. Rev. B **82**, 184528 (2010); D. Innocenti, S. Caprara, N. Poccia, A. Ricci, A. Valletta, and A. Bianconi, Shape resonance for the anisotropic superconducting gaps near a Lifshitz transition: The effect of electron hopping between layers, Supercond. Sci. Technol. **24**, 015012 (2011).

[29] A. Bianconi, D. Innocenti, A. Valletta, and A. Perali, Shape Resonances in superconducting gaps in a 2DEG at oxide-oxide interface, J. Phys.: Conf. Ser. **529**, 012007 (2014).

[30] S. Gariglio, M. Gabay, J. Mannhart, and J.-M. Triscone, Interface superconductivity, Physica C **514**, 189 (2015).

[31] S. N. Klimin, J. Tempere, J. T. Devreese, and D. van der Marel, Interface superconductivity in $LaAlO_3-SrTiO_3$ heterostructures, Phys. Rev. B **89**, 184514 (2014).

[32] R. M. Fernandes, J. T. Haraldsen, P. Wölfle, and A. V. Balatsky, Two-band superconductivity in doped $SrTiO_3$ films and interfaces, Phys. Rev. B **87**, 014510 (2013).

[33] Y. Nakamura and Y. Yanase, Multi-orbital superconductivity in $SrTiO_3/LaAlO_3$ interface and $SrTiO_3$ surface, J. Phys. Soc. Jpn **82**, 083705 (2013).

[34] See e.g., A. A. Shanenko, M. D. Croitoru, and F. M. Peeters, Oscillations of the superconducting temperature induced by quantum well states in thin metallic films: Numerical solution of the Bogoliubov–de Gennes equations, Phys. Rev. B **75**, 014519 (2007).

[35] R. E. Allen, Superconducting transition temperature and other properties of thin metallic films, Phys. Rev. B **12**, 3650 (1975).

[36] J. Appelbaum and E. Blount, Sum rule for crystalline metal surfaces, Phys. Rev. B **8**, 483 (1973).

[37] U. S. Pracht, N. Bachar, L. Benfatto, G. Deutscher, E. Farber, M. Dressel, and M. Scheffler, Enhanced Cooper pairing versus suppressed phase coherence shaping the superconducting dome in coupled aluminum nanograins, Phys. Rev. B **93**, 100503 (2016).

[38] N. Y. Ovchinnikov and Z. V. Kresin, Giant strengthening of superconducting pairing in metallic nanoclusters, Eur. Phys. J. B **45**, 5 (2005); Strong pair correlation in small metallic nanoclusters: the energy spectrum, *ibid.* **47**, 333 (2005); V. Z. Kresin and Y. N. Ovchinnikov, Shell structure and strengthening of superconducting pair correlation in nanoclusters, Phys. Rev. B **74**, 024514 (2006).

[39] T. Terashima, N. Kikugawa, A. Kiswandhi, E.-S. Choi, J. S. Brooks, S. Kasahara, T. Watashige, H. Ikeda, T. Shibauchi, Y. Matsuda, T. Wolf, A. E. Böhmer, F. Hardy, C. Meingast, H. v. Löhneysen, M.-T. Suzuki, R. Arita, and S. Uji, Anomalous Fermi surface in FeSe seen by Shubnikov–de Haas oscillation measurements, Phys. Rev. B **90**, 144517 (2014).

[40] Z. Wang, H. Yang, D. Fang, B. Shen, Q.-H. Wang, L. Shan, C. Zhang, P. Dai, and H.-H. Wen, Close relationship between superconductivity and the bosonic mode in $Ba_{0.6}K_{0.4}Fe_2As_2$ and $Na(Fe_{0.975}Co_{0.025})As$, Nat. Phys. **9**, 42 (2013).

[41] D. S. Inosov, Spin fluctuations in iron pnictides and chalcogenides: From antiferromagnetism to superconductivity, C. R. Physique **17**, 60 (2015).

[42] J.-Y. Lin, Y. S. Hsieh, D. A. Chareev, A. N. Vasiliev, Y. Parsons, and H. D. Yang, Coexistence of isotropic and extended s-wave order parameters in FeSe as revealed by low-temperature specific heat, Phys. Rev. B **84**, 220507 (2011).

[43] J. J. Lee, F. T. Schmitt, R. G. Moore, S. Johnston, Y.-T. Cui, W. Li, M. Yi, Z. K. Liu, M. Hashimoto, Y. Zhang, D. H. Lu, T. P. Devereaux, D.-H. Lee, and Z.-X. Shen, Interfacial mode coupling as the origin of the enhancement of T_c in FeSe films on $SrTiO_3$, Nature (London) **515**, 245 (2014).

[44] M. M. Özer, J. R. Thompson, and H. H. Weitering, Hard superconductivity of a soft metal in the quantum regime, Nat. Phys. **2**, 173 (2006).

[45] C. Brun, T. Cren, V. Cherkez, F. Debontridder, S. Pons, D. Fokin, M. C. Tringides, S. Bozhko, L. B. Ioffe, B. L. Altshuler, and D. Roditchev, Remarkable effects of disorder on superconductivity of single atomic layers of lead on silicon, Nat. Phys. **10**, 444 (2014).

[46] D. Roditchev, C. Brun, L. Serrier-Garcia, J. C. Cuevas, V. H. L. Bessa, M. V. Milosevic, F. Debontridder, V. Stolyarov, and T. Cren, Direct observation of Josephson vortex cores, Nat. Phys. **11**, 332 (2014).

[47] Y. Chen, A. A. Shanenko, and F. M. Peeters, Superconducting transition temperature of Pb nanofilms: Impact of thickness-dependent oscillations of the phonon-mediated electron-electron coupling, Phys. Rev. B **85**, 224517 (2012).

[48] J. Noffsinger and M. L. Cohen, First-principles calculation of the electron-phonon coupling in ultrathin Pb superconductors: Suppression of the transition temperature by surface phonons, Phys. Rev. B **81**, 214519 (2010).

[49] A. P. Durajski, Effect of layer thickness on the superconducting properties in ultrathin Pb films, Supercond. Sci. Technol. **28**, 095011 (2015).

[50] P. B. Allen and R. C. Dynes, Transition temperature of strong-coupled superconductors reanalyzed, Phys. Rev. B **12**, 905 (1975).

[51] A. D. Zdetsis, E. N. Economou, and D. A. Papaconstantopoulos, *Ab initio* bandstructure of lead, J. Phys. F: Met. Phys. **10**, 1149 (1990).

[52] B. J. C. van der Hoeven and P. H. Keesom, Specific heat of lead and lead alloys between 0.4 and 4.2 K, Phys. Rev. **137**, A103 (1965).

[53] D. R. Heslinga, H. H. Weitering, D. P. van der Werf, T. M. Klapwijk, and T. Hibma, Atomic-Structure-Dependent Schottky Barrier at Epitaxial Pb/Si(111) Interfaces, Phys. Rev. Lett. **64**, 1589 (1990).

[54] G. R. Stewart, Measurement of low-temperature specific heat, Rev. Sci. Instrum. **54**, 1 (1983).

[55] A. Mans, J. H. Dil, A. R. H. F. Ettema, and H. H. Weitering, Quantum electronic stability and spectroscopy of ultrathin Pb films on Si(111)7 $\times$ 7, Phys. Rev. B **66**, 195410 (2002).

[56] M. H. Upton, T. Miller, and T.-C. Chiang, Unusual band dispersion in Pb films on Si(111), Phys. Rev. B **71**, 033403 (2005).

[57] J. H. Dil, J. W. Kim, T. Kampen, K. Horn, and A. R. H. F. Ettema, Electron localization in metallic quantum wells: Pb versus In on Si(111), Phys. Rev. B **73**, 161308 (2006).

[58] M. Ligges, M. Sandhofer, I. Sklyadneva, R. Heid, K.-P. Bohnen, S. Freutel, L. Rettig, P. Zhou, P. M. Echenique, E. V. Chulkov, and U. Bovensiepen, Electron-phonon coupling in quantum-well states of the Pb/Si(111) system, J. Phys.: Condens. Matter **26**, 352001 (2014).

Appendices

Appendix A

Kinetic equation for soundlike collective excitations in Fermi liquids

Starting from the hamiltonian (1.73), we linearize the changes in the quasiparticle energies $E_n\left[\vec{p}+e\vec{A}(\vec{r},t),\sigma\right]$ and in the distribution function $\delta \mathtt{N}_{\vec{p}',\sigma'}(\vec{r},t)$, with respect to the vector potential $\vec{A}(\vec{r},t)$, as in

$$\begin{aligned}\delta \mathtt{N}_{\vec{p},\sigma}(\vec{r},t) &= \mathtt{N}_{\vec{p}}(\vec{r},t) - \mathtt{N}_0\left(E_n\left[\vec{p}+e\vec{A}(\vec{r},t),\sigma\right]\right) \\ &\approx \mathtt{N}_{\vec{p}}(\vec{r},t) - \mathtt{N}_0\left(E_n\left[\vec{p}\right]\right) - \frac{d\mathtt{N}_0\left(E_n\left[\vec{p}\right]\right)}{dE_n(\vec{p},\sigma)}\frac{\vec{p}\cdot\vec{A}(\vec{r},t)}{m^*}\end{aligned} \tag{A.1}$$

The nonequilibrium quasiparticle distribution function $\mathtt{N}_{\vec{p}}(\vec{r},t)$ descends directly from Liouville's equation, for a classical flow characterized by volume-conserving evolution in phase space. Therefore, we can write a quasi-classical mean-field kinetic equation for $\mathtt{N}_{\vec{p}}(\vec{r},t)$, which is

$$\frac{\partial \mathtt{N}_{\vec{p},\sigma}(\vec{r},t)}{\partial t} + \frac{1}{\hbar}\frac{\partial \hat{H}_{qp}(\vec{r},\vec{p},\sigma)}{\partial \vec{p}}\frac{\partial \mathtt{N}_{\vec{p},\sigma}(\vec{r},t)}{\partial \vec{r}} - \frac{1}{\hbar}\frac{\partial \hat{H}_{qp}(\vec{r},\vec{p},\sigma)}{\partial \vec{r}}\frac{\partial \mathtt{N}_{\vec{p},\sigma}(\vec{r},t)}{\partial \vec{p}} = \left[\frac{\partial \mathtt{N}_{\vec{p},\sigma}(\vec{r},t)}{\partial t}\right]_{coll} \tag{A.2}$$

In equation (A.1), the collisional term $\left[\frac{\partial \mathtt{N}_{\vec{p},\sigma}(\vec{r},t)}{\partial t}\right]_{coll}$ describes damping by collision processes that are not included into the mean field hamiltonian $\hat{H}_{qp}(\vec{r},\vec{p},\sigma)$. In fact, the Fermi liquid phenomenology relies on the existence of low-energy nearly-independent quasiparticles, which do not collide, and additional damping must be introduced by an external collision term. This collisional integral makes quasielectrons and quasiholes acquire a finite lifetime, $\tau_{qel} < +\infty$ and $\tau_{qh} < +\infty$ respectively: as common in quantum mechanics, we are treating a time-dependent problem with the eigenstates of a stationary configuration, in

this case the one for free fermions, but including time-dependent scattering as a finite lifetime for the stationary states. For the *true* thermodynamic equilibrium, we know that the distribution function is the Fermi-Dirac statistics $f_{FD}[E_n(\vec{p},\sigma)]$ [3]: since this is the configuration for global thermodynamic equilibrium, it is a stationary state and we must have a vanishing collison term $\left[\frac{\partial f_{FD}[E_n(\vec{p},\sigma)]}{\partial t}\right]_{coll}=0$, which specifies the relation between the lifetimes τ_{qel} and τ_{qh}. The nonequilibrium distribution function $\mathtt{N}_{\vec{p},\sigma}(\vec{r},t)$ can be written as a deviation with respect to the true Fermi-Dirac global equilibrium, as $\mathtt{N}_{\vec{p},\sigma}(\vec{r},t)=f_{FD}[E_n(\vec{p},\sigma)]+\Xi_{\vec{k},\sigma}(\vec{r},t)$. Inserting the latter into equation (A.1), we arrive at

$$\frac{\partial \Xi_{\vec{k},\sigma}(\vec{r},t)}{\partial t}+\vec{v}_{\vec{k},\sigma}\cdot\frac{\partial \Xi_{\vec{k},\sigma}(\vec{r},t)}{\partial \vec{r}}+\vec{v}_{\vec{k},\sigma}\cdot\vec{F}_{\sigma}(\vec{r},t)\delta[E_n(\vec{p},\sigma)-\mu]=\left[\frac{\partial \Xi_{\vec{k},\sigma}(\vec{r},t)}{\partial t}\right]_{coll} \tag{A.3}$$

In equation (A.3), we have defined the total quasi-classical force acting on the individual quasiparticles

$$\vec{F}_{\sigma}(\vec{r},t)=-\nabla_{\vec{r}}\left[-e\phi_{\sigma}(\vec{r},t)+\sum_{\vec{k}',\sigma'}f_{\vec{k},\sigma,\vec{k}',\sigma'}\Xi_{\vec{k},\sigma}(\vec{r},t)+\frac{\hbar\vec{k}}{m}\cdot e\vec{A}(\vec{r},t)\right] \tag{A.4}$$

The linearized kinetic equation (A.3) is manifestly gauge-invariant, and it satisfies the continuity equation for the flow of quasiparticles [7]: this is the starting point for many applications of Landau phenomenology of Fermi liquids, for example the study of collective modes in the absence of perturbations.

Now, we concentrate on stable density-density collective modes in the Fermi liquid. Hence, we neglect collisions between quasiparticles according to $\left[\frac{\partial \Xi_{\vec{k},\sigma}(\vec{r},t)}{\partial t}\right]_{coll}\approx 0$. Stable collective modes propagate even in the absence of perturbations, so we set the electromagnetic potentials to zero as $\phi_{\sigma}(\vec{r},t)=0$, $\vec{A}(\vec{r},t)=0$. Collective modes have wave-like evolution, therefore the deviation of the distribution function with respect to global equilibrium will be periodic in space and time, i.e. $\Xi_{\vec{k},\sigma}(\vec{r},t)\propto e^{i(\vec{q}\cdot\vec{r}-\omega t)}$, with $\vec{q}$ transferred wave vector for the excitation. Inserting this wave-like form in equation (A.3), without electromagnetic potentials and collisions, leads to

$$\left(\vec{q}\cdot v_{\vec{k},\sigma}-\omega\right)\Xi_{\vec{k},\sigma}(\vec{r},t)+\vec{q}\cdot v_{\vec{k},\sigma}\delta\left[E_n\left(\vec{k},\sigma\right)-\mu\right]\sum_{\vec{k}',\sigma'}f_{\vec{k},\sigma,\vec{k}',\sigma'}\Xi_{\vec{k},\sigma}(\vec{r},t)=0 \tag{A.5}$$

We assume small deviations with respect to thermodynamic equilibrium: physically, we consider changes in the distribution function at first order in the quasiparticle energies, with

respect to the Fermi-Dirac distribution at global equilibrium. In principle, excitations can alter the quasiparticle energies $E_n\left(\vec{k},\sigma\right)$ either by changing the wave vector $\vec{k}$ *or* by flipping the spin σ; in the following, having in mind sound-like collective modes, we assume that alterations of $E_n\left(\vec{k},\sigma\right)$ stem from variations in the quasiparticle momentum $\vec{k}$. Under these hypothesis, expanding the distribution deviations to first order in the energies $E_n\left(\vec{q},\sigma\right)$, we have $\Xi_{\vec{k},\sigma}(\vec{q},\omega) = \epsilon_{\vec{k}}(\vec{q},\omega)\frac{\partial f_{FD}\left[E_n\left(\vec{k},\sigma\right)\right]}{\partial E_n\left(\vec{k},\sigma\right)}_{\mu}$, with $\frac{\partial f_{FD}\left[E_n\left(\vec{k},\sigma\right)\right]}{\partial E_n\left(\vec{k},\sigma\right)}_{\mu} \equiv -\delta\left[E_n\left(\vec{k},\sigma\right)-\mu\right]$ for the Fermi-Dirac distribution [2,3]. If we had wanted to analyze magnetic modes in the Fermi liquid, like spin waves, we could also have assumed a distribution function change of the kind $\Xi_{\vec{k},\sigma}(\vec{q},\omega) = s_\sigma(\vec{q},\omega)\sigma\frac{\partial f_{FD}\left[E_n\left(\vec{k},\sigma\right)\right]}{\partial E_n\left(\vec{k},\sigma\right)}_{\mu} = s_\sigma(\vec{q},\omega)\sigma\,\delta\left[E_n\left(\vec{k},\sigma\right)-\mu\right]$, with the quasiparticle energies modified by spin rotations [7]. Finally, let us note that a Taylor series expansion at first order of the change in the distribution function selects quasiparticles at the chemical potential μ: essentially only excitations around μ contribute to collective modes, since states at $E << \mu$ deep down into the Fermi sea are occupied and blocked by Pauli exclusion principle.

This way, the kinetic equation (A.5) in local equilibrium, written in reciprocal space of momenta $\vec{q}$ and frequency ω, becomes

$$\left(\vec{q}\cdot\vec{v}_{\vec{k},\sigma}-\omega\right)\epsilon_{\vec{k}}(\vec{q},\omega)+\vec{q}\cdot\vec{v}_{\vec{k},\sigma}\,\delta\left[E\left(\vec{k},\sigma\right)-\mu\right]\left\{\sum_{\vec{k}',\sigma'} f_{\vec{k},\sigma,\vec{k}',\sigma'}\epsilon_{\vec{k}'}(\vec{q},\omega)\delta\left[E_n(\vec{k}',\sigma')-\mu\right]\right\} = 0 \tag{A.6}$$

As previously mentioned, the delta functions $\delta\left[E_n(\vec{k},\sigma)-\mu\right]$ and $\delta\left[E_n(\vec{k}',\sigma')-\mu\right]$ fix the value of k and k', respectively: therefore, the character of the collective mode, including its polarization direction, will be determined by the respective orientation of the excitation wave vector $\vec{q}$ with respect to $\vec{k}$ and $\vec{k}'$.

For long wavelengths $q \to 0$, we expect sound waves with acoustic dispersion $\omega_\lambda(\vec{q}) = v_{S,FL}q$, with $v_{S,FL}$ sound velocity for the Fermi liquid. Setting the latter relation into equation (A.6), we have in scalar form

$$\left(v_{\vec{k},\sigma}\cos\theta - v_{S,FL}\right)\epsilon_{\vec{k}}(\vec{q},\omega)+v_{\vec{k},\sigma}\cos\theta\,\delta\left[E\left(\vec{k},\sigma\right)-\mu\right]\left\{\sum_{\vec{k}',\sigma'} f_{\vec{k},\sigma,\vec{k}',\sigma'}\epsilon_{\vec{k}'}(\vec{q},\omega)\delta\left[E_n(\vec{k}',\sigma')-\mu\right]\right\} = 0 \tag{A.7}$$

where $\theta = \frac{arccos\left(\vec{q}\cdot\vec{v}_{\vec{k},\sigma}\right)}{|\vec{q}\cdot\vec{v}_{\vec{k},\sigma}|}$ is the angle between the wave vector $\vec{q}$ and the quasiparticle velocity $v_{\vec{k},\sigma}$.

To continue, we need to expand the angular dependence of the interaction matrix elements $f_{\vec{k},\sigma,\vec{k}',\sigma'}$, which determines the spatial polarization of the perturbation. Being an

angular distribution in 3-dimensional space, a suitable expansion basis for $f_{\vec{k},\sigma,\vec{k}',\sigma'}$ is given by spherical harmonics, in terms of Legendre polynomials [7,8]. We recall that Legendre polynomials are $\wp_n(x) = \frac{1}{2^n n!}\frac{d^n}{dx^n}\left[(x^2-1)^n\right]$, and the associated Legendre polynomials satisfy $P_l^m(x) = (-1)^m(1-x^2)^{\frac{m}{2}}\frac{d^m}{dx^m}[\wp_l(x)]$. The latter are used in the definition of spherical harmonics $Y_{l,m}(\theta,\phi) = \sqrt{\frac{(2l+1)(l-m)!}{4\pi(l+m)!}}P_l^m(\cos\theta)e^{im\phi}$, $-l \leq m \leq l.$, which often intervene in physical problems where spherical symmetry is involved [138]. The Fermi liquid expansion of the interaction matrix elements is usually done in terms of Landau parameters F_n^α, $n \in \mathbb{N}$, $\alpha = \{S,A\}$ [7,8], which represent the respective magnitudes of quasiparticle interactions for each possible angular pattern of the collective mode at the Fermi surface, i.e. for all spherical harmonics. First, we observe that, having selected quasiparticle energies at the Fermi surface at first order, the interaction matrix elements will be at the Fermi surface FS: $f_{\vec{k},\sigma,\vec{k}',\sigma'} \equiv f^{FS}_{\sigma,\sigma'}\delta\left[E_n(\vec{k},\sigma)-\mu\right]\delta\left[E_n(\vec{k}',\sigma')-\mu\right]$. The Fermi liquid Landau parameters in $d \in \mathbb{N}^+$ dimensions are defined as

$$F_l^{S,A} = \frac{N_0^*(0)}{2}\int\frac{d\Omega}{4\pi}\left[f^{FS}_{\uparrow,\uparrow}(\cos\theta) \pm f^{FS}_{\uparrow,\downarrow}(\cos\theta)\right]\frac{\wp_l(\cos\theta)}{2l+1},\ d=3 \tag{A.8}$$

$$F_l^{S,A} = \frac{N_0^*(0)}{2}\int\frac{d\Omega}{2\pi}\left[f^{FS}_{\uparrow,\uparrow}(\cos\theta) \pm f^{FS}_{\uparrow,\downarrow}(\cos\theta)\right]\frac{\cos(l\theta)(1+\delta_{l0})}{2},\ d=2 \tag{A.9}$$

In equations (A.8) and (A.9), the superscript S or A refers to the additive or subtractive combination of $f^{FS}_{\uparrow,\uparrow}(\cos\theta) \pm f^{FS}_{\uparrow,\downarrow}(\cos\theta)$, which distinguishes between symmetric and anti-symmetric Landau parameters. The former kind is associated to the charge density-density perturbations, while the latter deals with the magnetic spin-spin response. The density of states per unit volume $N_0^*(0)$ includes renormalization effects due to quasiparticle residual interactions, and therefore differs from the free fermions one $N_0^{el}(0)$. We concentrate on the problem in 3 dimensions, and write the inverse relation of (A.8), which is

$$f^{FS}_{\uparrow,\uparrow}(\cos\theta) \pm f^{FS}_{\uparrow,\downarrow}(\cos\theta) = \frac{2}{N_0^*(0)}\sum_{l=0}^{+\infty}F_l^{S,A}\wp_l(\cos\theta) \tag{A.10}$$

With these definitions, we can act on the term between curly brackets in equation (A.6). The delta function $\delta\left[E_n(\vec{k}',\sigma')-\mu\right]$ inside the sum over $\vec{k}'$ and σ' effectively counts how many states at the chemical potential we have, which is the definition of the density of states $N_0^*(0)$. All remains of the sum is an integration over angular variables, which depends on the angles between the wave vectors $\vec{k}$ and $\vec{k}'$. With a factor $\frac{1}{2}$ to avoid double counting

of interactions for $\vec{k}$ with $\vec{k}^{'}$ and viceversa, we have

$$\sum_{\vec{k}^{'},\sigma^{'}} f_{\vec{k},\sigma,\vec{k}^{'},\sigma^{'}} \epsilon_{\vec{k}^{'}}(\vec{q},\omega)\delta\left[E_n(\vec{k}^{'},\sigma^{'})-\mu\right] \equiv \frac{1}{2}\sum_{\vec{k}^{'},\sigma^{'}} \delta\left[E_n(\vec{k}^{'},\sigma^{'})-\mu\right]\int \frac{d\Omega^{'}}{4\pi}\sum_{\sigma^{'}} f^{FS}_{\sigma,\sigma^{'}}\epsilon_{\vec{k}^{'}}(\vec{q},\omega)$$
$$= \frac{N_0^*(0)}{2}\int \frac{d\Omega^{'}}{4\pi}\sum_{\sigma^{'}} f^{FS}_{\sigma,\sigma^{'}}\epsilon_{\vec{k}^{'}}(\vec{q},\omega)$$

Equation (A.6) becomes

$$\left(\vec{q}\cdot\vec{v}_{\vec{k},\sigma}-\omega\right)\epsilon_{\vec{k}}(\vec{q},\omega)+\vec{q}\cdot\vec{v}_{\vec{k},\sigma}\frac{N_0^*(0)}{2}\int\frac{d\Omega^{'}}{4\pi}\sum_{\sigma^{'}} f^{FS}_{\sigma,\sigma^{'}}\epsilon_{\vec{k}^{'}}(\vec{q},\omega)=0 \tag{A.11}$$

Employing the Landau parameter expansion (A.10) of the interaction matrix elements leads to

$$\left(qv_{\vec{k},\sigma}\cos\theta-\omega\right)\epsilon_{\vec{k}}(\vec{q},\omega)+qv_{\vec{k},\sigma}\cos\theta\int\frac{d\Omega^{'}}{4\pi}\sum_{l=0}^{+\infty}F_l^{S,A}\wp_l(\cos\theta^{'})\epsilon_{\vec{k}^{'}}(\vec{q},\omega)=0 \tag{A.12}$$

which is equation (1.74) quoted in the main text of section 1.5.1.

Appendix B

General form of collective excitations in 3D Fermi liquids

Following the work of Abrikosov and Khalatnikov [7], we present the general solution in 3 dimensions for sound-like collective excitations in a Fermi liquid, at any order of spherical harmonics expansion $l \in \mathbb{N}$. The kinetic equation to solve is always (1.74), with the interaction matrix elements expanded in terms of symmetric Landau parameters F_l^S as in equation (A.10). The quasiparticle distribution change is also expanded in spherical harmonics as in equation (1.75). In the latter, the associated Legendre polynomials $P_l^m(z) = P_l^{-m}(z)$ appear, while the interaction matrix elements are expanded in terms of Legendre polynomials $\wp_l(z)$. It is convenient to write everything in terms of associated polynomials $P_l^m(z)$, utilizing the combination theorem

$$\wp_l(z) = \sum_{m=-l}^{l} P_l^m(\theta) P_l^m(\theta') e^{im(\phi-\phi')} \frac{(n-|m|)!}{(n+|m|)!} \tag{B.1}$$

Introducing the notation

$$\Phi_{lm} = F_l^S \frac{(n-|m|)!}{(n+|m|)!} \int \frac{d\Omega'}{4\pi} P_l^m(\theta') e^{-im\phi'} \varepsilon_{\theta',\phi'} \tag{B.2}$$

the kinetic equation (1.74) becomes

$$(q v_{\vec{k},\sigma} \cos\theta - \omega)\varepsilon_{\theta,\phi} + q v_{\vec{k},\sigma} \cos\theta P_l^m(\theta) e^{im\phi} \Phi_{lm} = 0 \tag{B.3}$$

From (B.3), the distribution function change $\varepsilon_{\theta,\phi}$ is explicitly

$$\varepsilon_{\theta,\phi} = -\frac{q v_{\vec{k},\sigma} \cos\theta}{q v_{\vec{k},\sigma} \cos\theta - \omega} P_l^m(\theta) e^{im\phi} \Phi_{lm} \tag{B.4}$$

Substituting back equation (B.4) into equation (B.2) and integrating with respect to ϕ', we have

$$-F_l^S \frac{(n-|m|)!}{(n+|m|)!} \int \frac{d\Omega'}{4\pi} \sum_n P_l^m(\theta') \frac{q v_{\vec{k},\sigma} \cos\theta'}{q v_{\vec{k},\sigma} \cos\theta' - \omega} P_n^m(\theta') \Phi_{nm} = \sum_n \Phi_{nm} \delta_{nl} \tag{B.5}$$

Thus we have obtained a system of homogeneous equations which determine the quantities Φ_{lm} [7]. The system separates into independent sub-systems corresponding to various values of m. Equation (B.5) shows that oscillations of several different kinds can propagate in a Fermi liquid at absolute zero temperature, and that they are characterized by a different dependence of the amplitude on the angles θ' and ϕ'. The class $m = 0$ corresponds to oscillations for which the distribution change $\varepsilon_{\theta,\phi}$ is isotropic in a plane perpendicular to the wave vector $\vec{k}$, while for $m > 0$ the oscillations are polarized in a definite way in this plane. The number of types of oscillations is determined by the possible values of $m \ : \ |m| \leq l$. The propagation velocity $v_{S,L} = \frac{\omega}{q}$ of the oscillations is found from the condition that the determinant of the corresponding system should be null,

$$\left\| \delta_{nl} F_l^S \Omega_{nl}^m(v_{S,L}) \right\| = 0 \tag{B.6}$$

$$\Omega_{nl}^m(v_{S,L}) = \frac{(n-|m|)!}{(n+|m|)!} \int \frac{d\Omega'}{4\pi} P_n^m(\theta') \frac{v_{\vec{k},\sigma} \cos\theta'}{v_{\vec{k},\sigma} \cos\theta' - v_{S,L}} P_l^m(\theta')$$

Since $P_l^m(z) = P_l^{-m}(z)$ from the properties of associated Legendre polynomials, the coefficients of the determinant (B.6) do not depend on the sign of m, and therefore oscillations which differ only in the sign of m propagate with the same velocity. Equation (B.6) shows that the equations for the velocity are transcendental. In the general case, they do not always have real roots, but cases are possible in which there are several. This corresponds to several types of self-sustained oscillations, having identical polarization in a plane perpendicular to the wave vector $\vec{k}$.

Appendix C

Can we transmit only one mode through an interface?

The refractive indexes of the two degenerate electromagnetic modes in the presence of viscosity are given by equation (2.2) Then, the transmission coefficients for the two modes $\{t_1, t_2\}$ are

$$t_\alpha = \frac{2(n_\beta - 1)}{(n_\alpha + 1)(n_\beta - n_\alpha)} \frac{1 - n_\beta i\lambda_s k}{1 + (1 - n_\beta - n_\alpha) i\lambda_s k} \tag{C.1}$$

where $k = \frac{\omega}{c}$ is the wavenumber in vacuum. From equation (C.1) we see that the transmission coefficient t_α would be null if two conditions were satisfied: either $n_\beta = 1$, or $n_\beta i\lambda_s k = 1$. We take the second mode t_2, as it is the most interesting one that undergoes negative refraction for $\nu_c \tau_{\vec{k}} (\omega_p)^2 > 1$, and we want all the intensity to feed this mode, i.e. $t_1 = 0$. Considering $n_1 = 1$, and solving with equation (2.2), this becomes equivalent to $\frac{4(\omega_p)^2}{\omega^3 c} = 0$; therefore, we would have $t_1 = 0$ only in the limit of infinite frequency $\omega \to +\infty$. However, we also know that viscosity disappears in the high-frequency collisionless limit as $\nu(\omega) \propto \frac{1}{1 - i\omega\bar{\tau}}$, with $\bar{\tau} \propto \tau_{\vec{k}}$, so that, even in this limit, the mode $n_2(\omega)$ is completely suppressed for all frequencies.

The other condition, $n_2 i\lambda_s k = 1$, leads to an equation which can never be satisfied for a real and positive frequency $\omega > 0$. Since the treatment for the mode n_1 is completely equivalent by interchanging the labels $\{1, 2\}$, we conclude that it is not possible to completely separate one viscous optical mode from the other at an interface, but the two modes always come together; this is reasonable, since outside the viscous material only the coherent sum of the electric fields from the two modes matters [12].

Appendix D

Derivation of Landau quasiparticle scattering time

In a Fermi liquid, short-range quasiparticle residual interactions at the Fermi surface are usually expressed in terms of symmetric and antisymmetric Landau parameters F_l^j, $j = \{A, S\}$, as described at the beginning of section 1.5.1 and in appendix A. These quantities parameterize the bare interactions among quasiparticles. The many-body polarization of the medium renormalizes these interactions, produces renormalized Landau parameters [13, 23]

$$A_l^j = \frac{F_l^j}{1 + \frac{F_l^j}{2l+1}} \tag{D.1}$$

The quantities (D.1) represent the scattering amplitudes between quasiparticles and can mediate Cooper pairing in superconducting materials [13]. The parameters A_l^j enter into the Fermi liquid collision time, due to phase-space limitation of quasiparticle scattering [1, 13, 23], according to

$$\frac{1}{\tau_c} = \frac{(m^*)^3 \Delta_u}{12\pi^2\hbar^3}\left[(\hbar\omega)^2 + (\pi k_B T)^2\right]\left\langle \frac{W(\theta,\phi)}{\cos\frac{\theta}{2}} \right\rangle \tag{D.2}$$

where $W(\theta, \phi)$ is the transition probability governing inelastic scattering at the Fermi surface, and $\{\theta, \phi\}$ are the angles between the Fermi momentum $\vec{k}_F$ and the excitation momentum $\vec{q}$ in 3-dimensional space. The brackets $\langle\rangle$ represent an average over the solid angle in momentum space. In s-p approximation [1, 13], we consider short-range quasiparticle interactions only in the angular channels $l = \{0, 1\}$, comprising both symmetric and antysimmetric parts. Then, the angular average in equation (D.2) is performed on the

transition probability

$$W(\theta,\phi) = \frac{\pi}{4\hbar}\left[A_S(\theta,\phi) + A_t(\theta,\phi)\right]^2 + \frac{\pi}{2\hbar}\left[A_t(\theta,\phi)\right]^2 \tag{D.3}$$

where $A_S(\theta,\phi) = \frac{1}{N_0^{el}(0)}\left[(A_0^S - 3A_0^A) + (A_1^S - 3A_1^A\cos\theta)\right]$ and $A_t(\theta,\phi) = \frac{1}{N_0^{el}(0)}\left[(A_0^S + A_0^A) + (A_1^S + A_1^A\cos\theta)\right]\cos\phi$ are the scattering amplitudes for singlet and triplet state, respectively [1, 13]. Averaging over the angular coordinates θ and ϕ gives

$$\left\langle \frac{W(\theta,\phi)}{\cos\frac{\theta}{2}} \right\rangle = \int \frac{\sin\theta d\theta d\phi}{4\pi}\frac{W(\theta,\phi)}{\cos\frac{\theta}{2}} = 12(\lambda_t)^2\frac{\pi^5\hbar^5}{(m^*)^3E_F^*} \tag{D.4}$$

where $12(\lambda_t)^2$ contains contributions from the Landau interaction parameters $\left\{A_0^S, A_0^A, A_1^S, A_1^A\right\}$ with numerical coefficients, in accordance with equation (B.7) of reference [13]. Inserting equation (D.4) into equation (D.2) finally yields equation (2.29) quoted in the main text.

Appendix E

Gor'kov equations with a scattering rate

We derive the BCS gap equation in a basis, in the presence of an energy- and momentum-independent scattering rate Γ - see also section 1.4.1. The linearized equations at T_c become

$$(i\omega + i\Gamma - K_0)\mathscr{G}(i\omega) = \mathbb{1}$$
$$(i\omega + i\Gamma + K_0^*)\mathscr{F}^\dagger(i\omega) - \Delta^\dagger\mathscr{G}(i\omega) = 0$$

and the anomalous function is

$$\mathscr{F}^\dagger_{\mu_2\mu_1}(i\omega) = \frac{\Delta^*_{\mu_1\mu_2}}{(i\omega + i\Gamma - \xi_{\mu_1})(i\omega + i\Gamma + \xi_{\mu_2})}.$$

In order to perform the Fourier transform we note that

$$\begin{aligned}
\frac{1}{\beta}\sum_{i\omega} e^{-i\omega 0^-}\frac{1}{(i\omega+i\Gamma-\xi_{\mu_1})(i\omega+i\Gamma+\xi_{\mu_2})} = \\
&\frac{i}{2\pi}\frac{1}{\xi_{\mu_1}+\xi_{\mu_2}}\sum_{n=-\infty}^{\infty}\left[\frac{1}{n+\frac{1}{2}+\frac{\beta}{2\pi i}(\xi_{\mu_2}+i\Gamma)}-\frac{1}{n+\frac{1}{2}-\frac{\beta}{2\pi i}(\xi_{\mu_1}-i\Gamma)}\right] \\
&=\frac{i}{2\pi}\frac{1}{\xi_{\mu_1}+\xi_{\mu_2}}\left\{\sum_{n=0}^{\infty}\left[\frac{1}{n+\frac{1}{2}+\frac{\beta}{2\pi i}(\xi_{\mu_2}+i\Gamma)}-\frac{1}{n+\frac{1}{2}-\frac{\beta}{2\pi i}(\xi_{\mu_1}-i\Gamma)}\right]\right. \\
&\qquad+\frac{1}{-n+\frac{1}{2}+\frac{\beta}{2\pi i}(\xi_{\mu_2}+i\Gamma)}-\frac{1}{-n+\frac{1}{2}-\frac{\beta}{2\pi i}(\xi_{\mu_1}-i\Gamma)} \\
&\qquad\left.-\frac{1}{\frac{1}{2}+\frac{\beta}{2\pi i}(\xi_{\mu_2}+i\Gamma)}+\frac{1}{\frac{1}{2}-\frac{\beta}{2\pi i}(\xi_{\mu_1}-i\Gamma)}\right\} \\
&=\frac{i}{2\pi}\frac{1}{\xi_{\mu_1}+\xi_{\mu_2}}\left[-\psi\left(\frac{1}{2}+\frac{\beta}{2\pi i}(\xi_{\mu_2}+i\Gamma)\right)+\psi\left(\frac{1}{2}-\frac{\beta}{2\pi i}(\xi_{\mu_1}-i\Gamma)\right)\right. \\
&\qquad+\psi\left(-\frac{1}{2}-\frac{\beta}{2\pi i}(\xi_{\mu_2}+i\Gamma)\right)-\psi\left(-\frac{1}{2}+\frac{\beta}{2\pi i}(\xi_{\mu_1}-i\Gamma)\right) \\
&\qquad\left.-\frac{1}{\frac{1}{2}+\frac{\beta}{2\pi i}(\xi_{\mu_2}+i\Gamma)}+\frac{1}{\frac{1}{2}-\frac{\beta}{2\pi i}(\xi_{\mu_1}-i\Gamma)}\right]. \qquad \text{(E.1)}
\end{aligned}$$

In equation (E.1), we have utilized the digamma function $\psi(z)=\lim_{M\to+\infty}\left(\ln M-\sum_{n=0}^{M}\frac{1}{n+z}\right)$. Now we use the property of the digamma function

$$\psi(-x)=\frac{1}{x}+\pi\cot(\pi x)+\psi(x)$$

to get

$$\begin{aligned}
\mathscr{F}_{\mu_2\mu_1}(0^-) &= \Delta^*_{\mu_1\mu_2}\frac{i}{2}\frac{1}{\xi_{\mu_1}+\xi_{\mu_2}}\left[\cot\left(\frac{\pi}{2}+\frac{\beta}{2i}(\xi_{\mu_2}+i\Gamma)\right)-\cot\left(\frac{\pi}{2}-\frac{\beta}{2i}(\xi_{\mu_1}-i\Gamma)\right)\right] \\
&= \Delta^*_{\mu_1\mu_2}\frac{i}{2}\frac{1}{\xi_{\mu_1}+\xi_{\mu_2}}\left[-\tan\left(\frac{\beta}{2i}(\xi_{\mu_2}+i\Gamma)\right)+\tan\left(-\frac{\beta}{2i}(\xi_{\mu_1}-i\Gamma)\right)\right] \\
&= -\Delta^*_{\mu_1\mu_2}\frac{1}{\xi_{\mu_1}+\xi_{\mu_2}}\frac{1}{2}\left[\tanh\left(\frac{\xi_{\mu_1}-i\Gamma}{2k_{\mathrm{B}}T_c}\right)+\tanh\left(\frac{\xi_{\mu_2}+i\Gamma}{2k_{\mathrm{B}}T_c}\right)\right].
\end{aligned}$$

The gap equation becomes

$$\Delta_{\alpha\beta}=-\sum_{\mu_1\mu_2}V_{\alpha\beta\mu_1\mu_2}\frac{\Delta_{\mu_1\mu_2}}{\xi_{\mu_1}+\xi_{\mu_2}}\frac{1}{2}\left[\tanh\left(\frac{\xi_{\mu_1}+i\Gamma}{2k_{\mathrm{B}}T_c}\right)+\tanh\left(\frac{\xi_{\mu_2}-i\Gamma}{2k_{\mathrm{B}}T_c}\right)\right].$$

or, with the BCS interaction (3.17):

$$\Delta_\alpha = \sum_{\mu_1} \eta^2(\xi_{\mu_1}) V_{BCS} O_{\alpha\mu_1} \frac{\Delta_{\mu_1}}{2\xi_{\mu_1}} \text{Re tanh}\left(\frac{\xi_{\mu_1} + i\Gamma}{2k_B T_c}\right).$$

Hence, the effect of the scattering rate Γ is to add an imaginary part to the hyperbolic tangent function $\tanh\left(\frac{\xi_{\mu_1}+i\Gamma}{2k_B T_c}\right)$, with respect to the clean case (4.19), thus reducing T_c.

Bibliography

[1] G. D. Mahan, *Many-particle physics*. New York: Kluwer Academic/Plenum, 2000.

[2] C. Berthod, *Applications of the Many-Body Formalism in Condensed-Matter Physics*. 2014.

[3] N. W. Ashcroft and N. D. Mermin, *Solid State Physics*. Fort Worth: Harcourt, 1976.

[4] J. D. Jackson, *Classical Electrodynamics*. New York: John Wiley and Sons, 1962.

[5] M. Dressel and G. Grï£ıner, *Electrodynamics of Solids*. Cambridge: Cambridge University Press, 2002.

[6] G. Giuliani and G. Vignale, *Quantum Theory of the Electron Liquid*. Cambridge: Cambridge University Press, 2005.

[7] A. A. Abrikosov and I. M. Khalatnikov, "The theory of a Fermi liquid (the properties of liquid ^{3}He at low temperatures)," *Reports on Progress in Physics*, vol. 22, no. 1, p. 329, 1959.

[8] L. Landau and E. Lifshitz, *Statistical Physics*. No. v. 5, Elsevier Science, 2013.

[9] H. Bruus and K. Flensberg, *Many-body quantum theory in condensed matter physics: an introduction*. Oxford University Press, 2004.

[10] M. J. Lea, A. R. Birks, P. M. Lee, and E. R. Dobbs, "The dispersion of transverse zero sound in liquid helium 3," *Journal of Physics C: Solid State Physics*, vol. 6, no. 11, p. L226, 1973.

[11] P. R. Roach and J. B. Ketterson, "Observation of transverse zero sound in normal ^{3}He," *Phys. Rev. Lett.*, vol. 36, pp. 736–740, Mar 1976.

[12] D. Forcella, J. Zaanen, D. Valentinis, and D. van der Marel, "Electromagnetic properties of viscous charged fluids," *Phys. Rev. B*, vol. 90, no. 035143, p. 456, 2014.

[13] D. van der Marel, J. L. M. van Mechelen, and I. I. Mazin, "Common fermi-liquid origin of T^2 resistivity and superconductivity in n-type $SrTiO_3$," *Phys. Rev. B*, vol. 84, p. 205111, Nov 2011.

[14] D. van der Marel, *Electronic properties of solids*. 2011.

[15] C. P. Enz, "Two-fluid hydrodynamic description of ordered systems," *Rev. Mod. Phys.*, vol. 46, pp. 705–753, Oct 1974.

[16] D. Forcella, A. Mezzalira, and D. Musso, "Electromagnetic response of strongly coupled plasmas," *Journal of High Energy Physics*, vol. 2014, no. 11, pp. 1–26, 2014.

[17] A. J. Beekman, J. Nissinen, K. Wu, K. Liu, R.-J. Slager, Z. Nussinov, V. Cvetkovic, and J. Zaanen, "Dual gauge field theory of quantum liquid crystals in two dimensions," *arXiv:1603.04254*, 2016.

[18] A. vom Felde, J. Sprösser-Prou, and J. Fink, "Valence-electron excitations in the alkali metals," *Phys. Rev. B*, vol. 40, pp. 10181–10193, Nov 1989.

[19] S. Conti and G. Vignale, "Elasticity of an electron liquid," *Phys. Rev. B*, vol. 60, pp. 7966–7980, Sep 1999.

[20] S. Gasiorowicz, *Quantum physics*. John Wiley & Sons, 2007.

[21] A. A. Abrikosov, L. P. Gorkov, and I. E. Dzyaloshinski, *Methods of quantum field theory in statistical physics*. Courier Corporation, 2012.

[22] P. Nozieres and D. Pines, *Theory Of Quantum Liquids*. Advanced Books Classics Series, Westview Press, 1999.

[23] P. Coleman, *Introduction to many-body physics*. Cambridge University Press, 2015.

[24] D. Forcella, C. Prada, and R. Carminati, "Causality, non-locality and negative refraction," *arXiv:1610.04126*, 2016.

[25] C. Berthod, J. Mravlje, X. Deng, R. Žitko, D. van der Marel, and A. Georges, "Non-Drude universal scaling laws for the optical response of local Fermi liquids," *Phys. Rev. B*, vol. 87, p. 115109, Mar 2013.

[26] D. Van Der Marel, "Optical spectroscopy of plasmons and excitons in cuprate superconductors," *Journ. supercond. nov. magn.*, vol. 17, no. 5, pp. 559–575, 2004.

[27] T. A. Litovitz and C. M. Davis, "5 - structural and shear relaxation in liquids," in *Properties of Gases, Liquids, and Solutions - Physical Acoustics* (W. P. Mason, ed.), vol. 2, Part A of *Physical Acoustics*, pp. 281 – 349, Academic Press, 1965.

[28] J. P. R. Bolton in *Proceedings of the XIV Int. Conf. on low-temp. Phys.*, vol. 1, p. 115, American Elsevier, 1975.

[29] S. Sachdev, *Quantum phase transitions*. Wiley Online Library, 2007.

[30] J. Zaanen, "Superconductivity: Why the temperature is high," *Nature*, vol. 430, no. 6999, pp. 512–513, 2004.

[31] M. Müller, J. Schmalian, and L. Fritz, "Graphene: A nearly perfect fluid," *Phys. Rev. Lett.*, vol. 103, p. 025301, Jul 2009.

[32] G. Policastro, D. T. Son, and A. O. Starinets, "Shear viscosity of strongly coupled $n = 4$ supersymmetric Yang-Mills plasma," *Phys. Rev. Lett.*, vol. 87, p. 081601, Aug 2001.

[33] A. Rebhan and D. Steineder, "Violation of the holographic viscosity bound in a strongly coupled anisotropic plasma," *Phys. Rev. Lett.*, vol. 108, p. 021601, Jan 2012.

[34] L. Luo and J. E. Thomas, "Thermodynamic measurements in a strongly interacting fermi gas," *Journal of Low Temperature Physics*, vol. 154, no. 1, pp. 1–29, 2009.

[35] R. A. Davison, K. Schalm, and J. Zaanen, "Holographic duality and the resistivity of strange metals," *Phys. Rev. B*, vol. 89, p. 245116, Jun 2014.

[36] S. A. Hartnoll, R. Mahajan, M. Punk, and S. Sachdev, "Transport near the Ising-nematic quantum critical point of metals in two dimensions," *Phys. Rev. B*, vol. 89, p. 155130, Apr 2014.

[37] A. Lucas, S. Sachdev, and K. Schalm, "Scale-invariant hyperscaling-violating holographic theories and the resistivity of strange metals with random-field disorder," *Phys. Rev. D*, vol. 89, p. 066018, Mar 2014.

[38] V. P. Silin, "Theory of a degenerate electron liquid," *Soviet Phys. JETP*, vol. 6, p. 387, 1958.

[39] V. Silin, "On the theory of the anomalous skin effect in metals," *Soviet Phys. JETP*, vol. 6, 1958.

[40] L. Landau, E. Lifshitz, A. Kosevich, and L. Pitaevskiĭ, *Theory of Elasticity*. Course of theoretical physics, Butterworth-Heinemann, 1986.

[41] L. D. Landau and L. M. Lifshitz, *Fluid Mechanics*. Oxford: Pergamon Press, 1987.

[42] A. V. Andreev, S. A. Kivelson, and B. Spivak, "Hydrodynamic description of transport in strongly correlated electron systems," *Phys. Rev. Lett.*, vol. 106, p. 256804, Jun 2011.

[43] L. Levitov and G. Falkovich, "Electron viscosity, current vortices and negative nonlocal resistance in graphene," *Nature Physics*, 2016.

[44] V. G. Veselago, "The electrodynamics of substances with simultaneously negative values of ϵ and μ," *Sov. Phys. Uspekhi*, vol. 10, no. 4, p. 509, 1968.

[45] V. Veselago, L. Braginsky, V. Shklover, and C. Hafner, "Negative refractive index materials," *J. Comput. Theor. Nanos.*, vol. 3, no. 2, pp. 189–218, 2006.

[46] L. Bocquet and J.-L. Barrat, "Flow boundary conditions from nano- to micro-scales," *Soft Matter*, vol. 3, pp. 685–693, 2007.

[47] J. Feenstra, *Low-Energy Electrodynamics of High-Tc Superconductors*. Groningen: Ph. D. Thesis, University of Groningen, 1997.

[48] P. U. Jepsen, D. G. Cooke, and M. Koch, "Terahertz spectroscopy and imaging–modern techniques and applications," *Laser & Photonics Reviews*, vol. 5, no. 1, pp. 124–166, 2011.

[49] S. L. Dexheimer, *Terahertz spectroscopy: principles and applications*. CRC press, 2007.

[50] G. E. H. Reuter and E. H. Sondheimer, "The theory of the anomalous skin effect in metals," *Proc. R. Soc. A*, vol. 195, no. 336, 1948.

[51] E. H. Sondheimer, "The anomalous skin effect and the optical properties of metals," *Advances in Physics*, vol. 50, no. 499, 2001.

[52] A. B. Pippard, "The surface impedance of superconductors and normal metals at high frequencies. i. resistance of superconducting tin and mercury at 1200 mcyc./sec.," *Proc. Roy. Soc. A*, vol. 191, 1947.

[53] A. B. Pippard, "The surface impedance of superconductors and normal metals at high frequencies. ii. the anomalous skin effect in normal metals," *Proceedings of the Royal Society of*

London A: Mathematical, Physical and Engineering Sciences, vol. 191, no. 1026, pp. 385–399, 1947.

[54] A. B. Pippard, "The surface impedance of superconductors and normal metals at high frequencies. iii. the relation between impedance and superconducting penetration depth," *Proceedings of the Royal Society of London A: Mathematical, Physical and Engineering Sciences*, vol. 191, no. 1026, pp. 399–415, 1947.

[55] R. G. Chambers, "The anomalous skin effect," *Proc. Roy. Soc. A*, vol. 215, 1952.

[56] O. Svelto, *Principles of Lasers*. Berlin: Springer, 2010.

[57] Y. Maeno, H. Hashimoto, K. Yoshida, S. Nishizaki, T. Fujita, J. Bednorz, and F. Lichtenberg, "Superconductivity in a layered perovskite without copper," *Nature*, vol. 372, no. 6506, pp. 532–534, 1994.

[58] A. P. Mackenzie and Y. Maeno, "The superconductivity of Sr_2RuO_4 and the physics of spin-triplet pairing," *Rev. Mod. Phys.*, vol. 75, pp. 657–712, May 2003.

[59] D. Stricker, J. Mravlje, C. Berthod, R. Fittipaldi, A. Vecchione, A. Georges, and D. van der Marel, "Optical response of Sr_2RuO_4 reveals universal Fermi-liquid scaling and quasiparticles beyond Landau theory," *Phys. Rev. Lett.*, vol. 113, p. 087404, Aug 2014.

[60] X. Lin, B. Fauqué, and K. Behnia, "Scalable T^2 resistivity in a small single-component Fermi surface," *Science*, vol. 349, no. 6251, pp. 945–948, 2015.

[61] A. H. Thompson, "Electron-electron scattering in TiS_2," *Phys. Rev. Lett.*, vol. 35, pp. 1786–1789, Dec 1975.

[62] K. Kadowaki and S. Woods, "Universal relationship of the resistivity and specific heat in heavy-fermion compounds," *Solid State Communications*, vol. 58, no. 8, pp. 507 – 509, 1986.

[63] S. I. Mirzaei, D. Stricker, J. N. Hancock, C. Berthod, A. Georges, E. van Heumen, M. K. Chan, X. Zhao, Y. Li, M. Greven, N. Barišic, and D. van der Marel, "Spectroscopic evidence for Fermi liquid-like energy and temperature dependence of the relaxation rate in the pseudogap phase of the cuprates," *Proceedings of the National Academy of Sciences*, vol. 110, no. 15, pp. 5774–5778, 2013.

[64] L. D. Landau, "Oscillations in a fermi liquid," *Soviet Phys. JETP*, vol. 5, no. 1, pp. 101–108, 1957.

[65] W. E. Lawrence and J. W. Wilkins, "Electron-electron scattering in the transport coefficients of simple metals," *Phys. Rev. B*, vol. 7, pp. 2317–2332, Mar 1973.

[66] W. G. Baber, "The contribution to the electrical resistance of metals from collisions between electrons," *Proceedings of the Royal Society of London A: Mathematical, Physical and Engineering Sciences*, vol. 158, no. 894, pp. 383–396, 1937.

[67] H. Pal, V. Yudson, and D. Maslov, "Resistivity of non-galilean-invariant Fermi- and non-Fermi liquids," *Lithuanian Journal of Physics*, vol. 52, no. 2, 2012.

[68] M. J. M. de Jong and L. W. Molenkamp, "Hydrodynamic electron flow in high-mobility wires," *Phys. Rev. B*, vol. 51, pp. 13389–13402, May 1995.

[69] J. M. Ziman, *Electrons and phonons: the theory of transport phenomena in solids*. Oxford University Press, 1960.

[70] G. W. C. Kaye and T. H. Laby, *Tables of physical and chemical constants: and some mathematical functions*. Longmans, Green and Company, 1921.

[71] D. J. Scalapino, "Possible antiferromagnetic paramagnon pairing mechanism," in *Proceedings of symposium S at the 1987 Spring meeting of the MRS on high temperature superconductors (Extended Abstracts)*, 1987.

[72] D. J. Scalapino and S. R. White, "Superconducting condensation energy and an antiferromagnetic exchange-based pairing mechanism," *Phys. Rev. B*, vol. 58, pp. 8222–8224, Oct 1998.

[73] M. R. Norman, *High-temperature Superconductivity - Magnetic Mechanisms*. John Wiley and Sons, Ltd, 2007.

[74] W. Kohn and J. M. Luttinger, "New mechanism for superconductivity," *Phys. Rev. Lett.*, vol. 15, pp. 524–526, Sep 1965.

[75] M. Y. Kagan, D. V. Efremov, M. S. Mar'enko, and V. V. Val'kov, "Kohn-Luttinger effect and anomalous pairing in repulsive Fermi-systems at low density," *Low Temperature Physics*, vol. 38, no. 9, pp. 874–879, 2012.

[76] J. T. Devreese and A. S. Alexandrov, "Frï£ihlich polaron and bipolaron: recent developments," *Reports on Progress in Physics*, vol. 72, no. 6, p. 066501, 2009.

[77] R. P. Feynman, "Slow electrons in a polar crystal," *Phys. Rev.*, vol. 97, pp. 660–665, Feb 1955.

[78] J. R. Schrieffer, "Theory of superconductivity," 1963.

[79] A. Altland and B. D. Simons, *Condensed matter field theory*. Cambridge University Press, 2010.

[80] Y. Maeno, T. M. Rice, and M. Sigrist, "The intriguing superconductivity of strontium ruthenate," *Physics Today*, vol. 54, no. 1, pp. 42–47, 2001.

[81] T. M. Rice and M. Sigrist, "Sr_2RuO_4 : an electronic analogue of ^{3}He?," *J. Phys. Cond. Mat.*, vol. 7, no. 47, p. L643, 1995.

[82] J. Bardeen, L. N. Cooper, and J. R. Schrieffer, "Theory of superconductivity," *Phys. Rev.*, vol. 108, pp. 1175–1204, Dec 1957.

[83] G. M. Eliashberg, "Interactions between electrons and lattice vibrations in a superconductor," *Sov. Phys. JETP*, vol. 11, no. 3, 1960.

[84] W. L. McMillan, "Transition temperature of strong-coupled superconductors," *Physical Review*, vol. 167, no. 2, p. 331, 1968.

[85] P. Nozières and S. Schmitt-Rink, "Bose condensation in an attractive fermion gas: From weak to strong coupling superconductivity," *J. Low. Temp. Phys.*, vol. 59, no. 3/4, p. 195, 1985.

[86] M. Y. Kagan, *Bose–Einstein Condensation and Feshbach Resonance in Ultracold Quantum Gases and Mixtures*, pp. 153–180. Dordrecht: Springer Netherlands, 2013.

[87] N. D. Mermin and H. Wagner, "Absence of ferromagnetism or antiferromagnetism in one- or two-dimensional isotropic Heisenberg models," *Phys. Rev. Lett.*, vol. 17, pp. 1133–1136, Nov 1966.

[88] N. D. Mermin and H. Wagner, "Absence of ferromagnetism or antiferromagnetism in one- or two-dimensional isotropic Heisenberg models - erratum," *Phys. Rev. Lett.*, vol. 17, pp. 1307–1307, Dec 1966.

[89] N. D. Mermin, "Absence of ordering in certain classical systems," *Journal of Mathematical Physics*, vol. 8, no. 5, pp. 1061–1064, 1967.

[90] T. Giamarchi, *Quantum physics in one dimension*. Oxford university press, 2004.

[91] D. M. Eagles, "Predicted transition temperatures of very thin films and whiskers of superconducting semiconductors—application to $SrTiO_3$," *Phys. Rev.*, vol. 164, no. 2, p. 489, 1967.

[92] D. M. Eagles, "Effective masses in zr-doped superconducting ceramic $SrTiO_3$," *Phys. Rev.*, vol. 178, no. 2, p. 668, 1969.

[93] D. M. Eagles, "Possible pairing without superconductivity at low carrier concentrations in bulk and thin-film superconducting semiconductors," *Phys. Rev.*, vol. 186, no. 2, p. 456, 1969.

[94] X. Lin, G. Bridoux, A. Gourgout, G. Seyfarth, S. Krämer, M. Nardone, B. Fauqué, and K. Behnia, "Critical doping for the onset of a two-band superconducting ground state in $srtio_{3-\delta}$," *Phys. Rev. Lett.*, vol. 112, no. 20, p. 207002, 2014.

[95] M. Ahrens, R. Merkle, B. Rahmati, and J. Maier, "Effective masses of electrons in *n*-type $SrTiO_3$ determined from low-temperature specific heat capacities," *Physica B: Cond. Mat.*, vol. 393, no. 1–2, p. 239, 2007.

[96] V. L. Berezinskiĭ, "Destruction of long-range order in one-dimensional and two-dimensional systems having a continuous symmetry group i. classical systems," *Zh. Eksp. Teor. Fiz.*, vol. 59, p. 907, 1970.

[97] J. M. Kosterlitz and D. J. Thouless, "Ordering, metastability and phase transitions in two-dimensional systems," *J. Phys. C: Solid State Phys.*, vol. 6, no. 7, p. 1181, 1973.

[98] A. Larkin and A. Varlamov, *Theory of Fluctuations in Superconductors*, vol. 127 of *International Series of Monographs on Physics*. Oxford University Press, 2005.

[99] A. J. Leggett, *Diatomic Molecules and Cooper Pairs*, vol. 115 of *Lecture Notes in Physics*, p. 13. Berlin: Springer-Verlag, 1980.

[100] M. Randeria and E. Taylor, "Crossover from Bardeen-Cooper-Schrieffer to Bose-Einstein condensation and the unitary Fermi gas," *Ann. Rev. Cond. Mat. Phys.*, vol. 5, no. 1, p. 209, 2014.

[101] X. Lin, Z. Zhu, B. Fauqué, and K. Behnia, "Fermi surface of the most dilute superconductor," *Phys. Rev. X*, vol. 3, p. 021002, Apr 2013.

[102] J. L. M. van Mechelen, D. van der Marel, C. Grimaldi, A. B. Kuzmenko, N. P. Armitage, N. Reyren, H. Hagemann, and I. I. Mazin, "Electron-phonon interaction and charge carrier mass enhancement in $SrTiO_3$," *Phys. Rev. Lett.*, vol. 100, p. 226403, June 2008.

[103] S. Saha, T. P. Sinha, and A. Mookerjee, "Structural and optical properties of paraelectric $SrTiO_3$," *Journal of Physics: Condensed Matter*, vol. 12, no. 14, p. 3325, 2000.

[104] A. Janotti, D. Steiauf, and C. G. Van de Walle, "Strain effects on the electronic structure of $SrTiO_3$: Toward high electron mobilities," *Phys. Rev. B*, vol. 84, p. 201304, Nov 2011.

[105] Z. Zhong, A. Tóth, and K. Held, "Theory of spin-orbit coupling at $LaAlO_3/SrTiO_3$ interfaces and $SrTiO_3$ surfaces," *Phys. Rev. B*, vol. 87, p. 161102, Apr 2013.

[106] F. El-Mellouhi, E. N. Brothers, M. J. Lucero, I. W. Bulik, and G. E. Scuseria, "Structural phase transitions of the metal oxide perovskites $SrTiO_3$, $LaAlO_3$, and $LaTiO_3$ studied with a screened hybrid functional," *Phys. Rev. B*, vol. 87, p. 035107, Jan 2013.

[107] H. Uwe, R. Yoshizaki, T. Sakudo, A. Izumi, and T. Uzumaki, "Conduction band structure of srtio 3," *Japanese Journal of Applied Physics*, vol. 24, no. S2, p. 335, 1985.

[108] A. Spinelli, M. A. Torija, C. Liu, C. Jan, and C. Leighton, "Electronic transport in doped $SrTiO_3$: Conduction mechanisms and potential applications," *Phys. Rev. B*, vol. 81, p. 155110, Apr 2010.

[109] G. Binnig, A. Baratoff, H. E. Hoenig, and J. G. Bednorz, "Two-band superconductivity in Nb-doped $SrTiO_3$," *Phys. Rev. Lett.*, vol. 45, pp. 1352–1355, Oct 1980.

[110] A. G. Swartz, H. Inoue, T. A. Merz, Y. Hikita, S. Raghu, T. P. Devereaux, S. Johnston, and H. Y. Hwang, "Strong polaronic behavior in a weak coupling superconductor," *arXiv:1608.05621*, 2016.

[111] M. Thiemann, M. H. Beutel, M. Dressel, N. R. Lee-Hone, D. M. Broun, E. Fillis-Tsirakis, H. Boschker, J. Mannhart, and M. Scheffler, "Single gap superconductivity in doped srtio3," *arXiv:1703.04716*, 2017.

[112] W. Meevasana, X. J. Zhou, B. Moritz, C.-C. Chen, R. H. He, S.-I. Fujimori, D. H. Lu, S.-K. Mo, R. G. Moore, F. Baumberger, T. P. Devereaux, D. van der Marel, N. Nagaosa, J. Zaanen, and Z.-X. Shen, "Strong energy-momentum dispersion of phonon-dressed carriers in the lightly doped band insulator $SrTiO_3$," *New J. Phys.*, vol. 12, no. 2, p. 023004, 2010.

[113] K. A. Müller and H. Burkard, "$SrTiO_3$: An intrinsic quantum paraelectric below 4 K," *Phys. Rev. B*, vol. 19, pp. 3593–3602, Apr 1979.

[114] M. A. Saifi and L. E. Cross, "Dielectric properties of strontium titanate at low temperature," *Phys. Rev. B*, vol. 2, pp. 677–684, Aug 1970.

[115] J. M. Edge, Y. Kedem, U. Aschauer, N. A. Spaldin, and A. V. Balatsky, "Quantum critical origin of the superconducting dome in $SrTiO_3$," *Phys. Rev. Lett.*, vol. 115, p. 247002, Dec 2015.

[116] M. Itoh, R. Wang, Y. Inaguma, T. Yamaguchi, Y.-J. Shan, and T. Nakamura, "Ferroelectricity induced by oxygen isotope exchange in strontium titanate perovskite," *Phys. Rev. Lett.*, vol. 82, pp. 3540–3543, Apr 1999.

[117] T. Mitsui and W. B. Westphal, "Dielectric and x-ray studies of $Ca_xBa_{1-x}TiO_3$ and $Ca_xSr_{1-x}TiO_3$," *Phys. Rev.*, vol. 124, pp. 1354–1359, Dec 1961.

[118] J. H. Barrett, "Dielectric constant in perovskite type crystals," *Phys. Rev.*, vol. 86, pp. 118–120, Apr 1952.

[119] P. A. Fleury and J. M. Worlock, "Electric-field-induced raman scattering in $SrTiO_3$ and $KTaO_3$," *Phys. Rev.*, vol. 174, pp. 613–623, Oct 1968.

[120] W. Burke and R. Pressley, "Stress-induced ferroelectricity in $SrTiO_3$," *Solid State Communications*, vol. 9, no. 3, pp. 191 – 195, 1971.

[121] L. Landau, "On the motion of electrons in a crystal lattice," *Phys. Z. Sowjetunion*, vol. 3, pp. 664–665, 1933.

[122] A. S. Alexandrov and J. T. Devreese, "Polarons and bipolarons in advanced materials," in *Advances in Polaron Physics*, pp. 135–143, Springer, 2010.

[123] P. D. C. King, S. McKeown Walker, A. Tamai, A. de la Torre, T. Eknapakul, P. Buaphet, S.-K. Mo, W. Meevasana, M. S. Bahramy, and F. Baumberger, "Quasiparticle dynamics and spin-orbital texture of the $SrTiO_3$ two-dimensional electron gas," *Nat. Commun.*, vol. 5, p. 3414, 2014.

[124] C. Cancellieri, A. S. Mishchenko, U. Aschauer, A. Filippetti, C. Faber, O. S. Barišsic, V. A. Rogalev, T. Schmitt, N. Nagaosa, and V. N. Strocov, "Polaronic metal state at the $LaAlO_3/SrTiO_3$ interface," *Nature Communications*, vol. 10386, 2016.

[125] S. Gariglio, M. Gabay, J. Mannhart, and J.-M. Triscone, "Interface superconductivity," *Physica C*, vol. 514, pp. 189–198, 2015.

[126] C. S. Koonce, M. L. Cohen, J. F. Schooley, W. R. Hosler, and E. R. Pfeiffer, "Superconducting transition temperatures of semiconducting $srtio_3$," *Phys. Rev.*, vol. 163, pp. 380–390, Nov 1967.

[127] A. Stucky, G. Scheerer, Z. Ren, D. Jaccard, J.-M. Poumirol, C. Barreteau, E. Giannini, and D. van der Marel, "Isotope effect in superconducting n-doped $SrTiO_3$," *Scientific Reports*, vol. 6, 2016.

[128] D. M. Eagles, "Theory of transitions from large to nearly-small polarons, with application to Zr-doped superconducting $SrTiO_3$," *Phys. Rev.*, vol. 181, pp. 1278–1290, May 1969.

[129] J. Appel, "Soft-mode superconductivity in $SrTiO_{3-x}$," *Phys. Rev.*, vol. 180, pp. 508–516, Apr 1969.

[130] Z. Zinamon, "Superconductivity by small polarons," *Philosophical Magazine*, vol. 21, no. 170, pp. 347–356, 1970.

[131] Y. Takada, "Theory of superconductivity in polar semiconductors and its application to n-type semiconducting srtio3," *Journal of the Physical Society of Japan*, vol. 49, no. 4, pp. 1267–1275, 1980.

[132] J. Ruhman and P. A. Lee, "Superconductivity at very low density: The case of strontium titanate," *Phys. Rev. B*, vol. 94, p. 224515, Dec 2016.

[133] J. T. Devreese, S. N. Klimin, J. L. M. van Mechelen, and D. van der Marel, "Many-body large polaron optical conductivity in $SrTi_{1-x}Nb_xO_3$," *Phys. Rev. B*, vol. 81, p. 125119, Mar 2010.

[134] S. N. Klimin, J. Tempere, D. van der Marel, and J. T. Devreese, "Microscopic mechanisms for the Fermi-liquid behavior of Nb-doped strontium titanate," *Phys. Rev. B*, vol. 86, p. 045113, Jul 2012.

[135] S. N. Klimin, J. Tempere, J. T. Devreese, and D. van der Marel, "Interface superconductivity in $LaAlO_3$-$SrTiO_3$ heterostructures," *Phys. Rev. B*, vol. 89, no. 18, p. 184514, 2014.

[136] Z. Wang, S. M. Walker, A. Tamai, Y. Wang, Z. Ristic, F. Bruno, A. de la Torre, S. Riccò, N. Plumb, M. Shi, *et al.*, "Tailoring the nature and strength of electron-phonon interactions in the srtio3 (001) 2d electron liquid," *Nature materials*, 2016.

[137] L. P. Gor'kov, "Phonon mechanism in the most dilute superconductor n-type $SrTiO_3$," *Proceedings of the National Academy of Sciences*, vol. 113, no. 17, pp. 4646–4651, 2016.

[138] R. Eisberg and R. Resnick, *Quantum physics*. John Wiley New York, 1974.

[139] A. Paskin and A. D. Singh, "Boundary conditions and quantum effects in thin superconducting films," *Phys. Rev.*, vol. 140, no. 6A, p. A1965, 1965.

[140] M. Yu, M. Strongin, and A. Paskin, "Consistent calculation of boundary effects in thin superconducting films," *Phys. Rev. B*, vol. 14, no. 3, p. 996, 1976.

[141] E. H. Hwang, S. Das Sarma, and M. A. Stroscio, "Role of confined phonons in thin-film superconductivity," *Phys. Rev. B*, vol. 61, no. 13, p. 8659, 2000.

[142] B. Chen, Z. Zhu, and X. C. Xie, "Quantum size effects in thermodynamic superconducting properties of ultrathin films," *Phys. Rev. B*, vol. 74, no. 13, p. 132504, 2006.

[143] K. Szałowski, "Critical temperature of MgB_2 ultrathin superconducting films: BCS model calculations in the tight-binding approximation," *Phys. Rev. B*, vol. 74, no. 9, p. 094501, 2006.

[144] A. A. Shanenko, M. D. Croitoru, M. Zgirski, F. M. Peeters, and K. Arutyunov, "Size-dependent enhancement of superconductivity in Al and Sn nanowires: Shape-resonance effect," *Phys. Rev. B*, vol. 74, no. 5, p. 052502, 2006.

[145] M. D. Croitoru, A. A. Shanenko, and F. M. Peeters, "Dependence of superconducting properties on the size and shape of a nanoscale superconductor: From nanowire to film," *Phys. Rev. B*, vol. 76, no. 2, p. 024511, 2007.

[146] M. A. N. Araújo, A. M. García-García, and P. D. Sacramento, "Enhancement of the critical temperature in iron pnictide superconductors by finite-size effects," *Phys. Rev. B*, vol. 84, no. 17, p. 172502, 2011.

[147] A. Romero-Bermúdez and A. M. García-García, "Size effects in superconducting thin films coupled to a substrate," *Phys. Rev. B*, vol. 89, no. 6, p. 064508, 2014.

[148] A. Romero-Bermúdez and A. M. García-García, "Shape resonances and shell effects in thin-film multiband superconductors," *Phys. Rev. B*, vol. 89, no. 2, p. 024510, 2014.

[149] P. Wójcik and M. Zegrodnik, "Interplay between quantum confinement and Fulde-Ferrell-Larkin-Ovchinnikov phase in superconducting nanofilms," *Physica E*, vol. 83, p. 442, 2016.

[150] C. J. Thompson and J. M. Blatt, "Shape resonances in superconductors - ii simplified theory," *Phys. Lett.*, vol. 5, no. 1, p. 6, 1963.

[151] J. M. Blatt and C. J. Thompson, "Shape resonances in superconducting thin films," *Phys. Rev. Lett.*, vol. 10, no. 8, p. 332, 1963.

[152] A. Finkel'stein, "Suppression of superconductivity in homogeneously disordered systems," *Physica B: Condensed Matter*, vol. 197, no. 1, pp. 636 – 648, 1994.

[153] M. P. A. Fisher, G. Grinstein, and S. M. Girvin, "Presence of quantum diffusion in two dimensions: Universal resistance at the superconductor-insulator transition," *Phys. Rev. Lett.*, vol. 64, pp. 587–590, Jan 1990.

[154] M. P. A. Fisher, "Quantum phase transitions in disordered two-dimensional superconductors," *Phys. Rev. Lett.*, vol. 65, pp. 923–926, Aug 1990.

[155] S. Qin, J. Kim, Q. Niu, and C.-K. Shih, "Superconductivity at the two-dimensional limit," *Science*, vol. 324, no. 5932, p. 1314, 2009.

[156] L. Kang, B. B. Jin, X. Y. Liu, X. Q. Jia, J. Chen, Z. M. Ji, W. W. Xu, P. H. Wu, S. B. Mi, A. Pimenov, Y. J. Wu, and B. G. Wang, "Suppression of superconductivity in epitaxial NbN ultrathin films," *J. Appl. Phys.*, vol. 109, no. 3, p. 033908, 2011.

[157] B. G. Orr, H. M. Jaeger, and A. M. Goldman, "Transition-temperature oscillations in thin superconducting films," *Phys. Rev. Lett.*, vol. 53, no. 21, p. 2046, 1984.

[158] M. Kim, Y. Kozuka, C. Bell, Y. Hikita, and H. Y. Hwang, "Intrinsic spin-orbit coupling in superconducting δ-doped $SrTiO_3$ heterostructures," *Phys. Rev. B*, vol. 86, p. 085121, Aug 2012.

[159] A. Ohtomo and H. Y. Hwang, "A high-mobility electron gas at the $LaAlO_3/SrTiO_3$ heterointerface.," *Nature*, vol. 427, pp. 423–6, 2004.

[160] P. Zubko, S. Gariglio, M. Gabay, P. Ghosez, and J.-M. Triscone, "Interface Physics in Complex Oxide Heterostructures," *Annu. Rev. Condens. Matter Phys.*, vol. 2, pp. 141–165, 2011.

[161] H. Y. Hwang, Y. Iwasa, M. Kawasaki, B. Keimer, N. Nagaosa, and Y. Tokura, "Emergent phenomena at oxide interfaces," *Nat. Mater.*, vol. 11, pp. 103–113, 2012.

[162] S. Gariglio, A. Fête, and J.-M. Triscone, "Electron confinement at the $LaAlO_3/SrTiO_3$ interface," *J. Phys.: Condens. Mat.*, vol. 27, no. 28, p. 283201, 2015.

[163] N. Reyren, S. Thiel, A. D. Caviglia, L. F. Kourkoutis, G. Hammerl, C. Richter, C. W. Schneider, T. Kopp, A.-S. Rüetschi, D. Jaccard, M. Gabay, D. A. Muller, J.-M. Triscone, and J. Mannhart, "Superconducting interfaces between insulating oxides," *Science*, vol. 317, p. 1196, 2007.

[164] A. D. Caviglia, S. Gariglio, N. Reyren, D. Jaccard, T. Schneider, M. Gabay, S. Thiel, G. Hammerl, J. Mannhart, and J.-M. Triscone, "Electric field control of the $LaAlO_3/SrTiO_3$ interface ground state," *Nature*, vol. 456, pp. 624–627, 2008.

[165] J. A. Bert, B. Kalisky, C. Bell, M. Kim, Y. Hikita, H. Y. Hwang, and K. A. Moler, "Direct imaging of the coexistence of ferromagnetism and superconductivity at the $LaAlO_3/SrTiO_3$ interface," *Nature physics*, vol. 7, no. 10, pp. 767–771, 2011.

[166] L. Li, C. Richter, J. Mannhart, and R. Ashoori, "Coexistence of magnetic order and two-dimensional superconductivity at $LaAlO_3/SrTiO_3$ interfaces," *Nature physics*, vol. 7, no. 10, pp. 762–766, 2011.

[167] D. Xiao, W. Zhu, Y. Ran, N. Nagaosa, and S. Okamoto, "Interface engineering of quantum hall effects in digital transition metal oxide heterostructures," *Nature Communications*, vol. 2, p. 596, 2011.

[168] M. Verissimo-Alves, P. García-Fernández, D. I. Bilc, P. Ghosez, and J. Junquera, "Highly confined spin-polarized two-dimensional electron gas in $SrTiO_3/SrRuO_3$ superlattices," *Phys. Rev. Lett.*, vol. 108, p. 107003, Mar 2012.

[169] J. P. Velev, S. S. Jaswal, and E. Y. Tsymbal, "Multi-ferroic and magnetoelectric materials and interfaces," *Philosophical Transactions of the Royal Society of London A: Mathematical, Physical and Engineering Sciences*, vol. 369, no. 1948, pp. 3069–3097, 2011.

[170] C. A. F. Vaz, "Electric field control of magnetism in multiferroic heterostructures," *Journal of Physics: Condensed Matter*, vol. 24, no. 33, p. 333201, 2012.

[171] N. Nakagawa, H. Y. Hwang, and D. A. Muller, "Why some interfaces cannot be sharp," *Nature materials*, vol. 5, no. 3, pp. 204–209, 2006.

[172] G. Herranz, M. Basletić, M. Bibes, C. Carrétéro, E. Tafra, E. Jacquet, K. Bouzehouane, C. Deranlot, A. Hamzić, J.-M. Broto, A. Barthélémy, and A. Fert, "High mobility in $LaAlO_3/SrTiO_3$ heterostructures: Origin, dimensionality, and perspectives," *Phys. Rev. Lett.*, vol. 98, p. 216803, May 2007.

[173] P. R. Willmott, S. A. Pauli, R. Herger, C. M. Schlepütz, D. Martoccia, B. D. Patterson, B. Delley, R. Clarke, D. Kumah, C. Cionca, and Y. Yacoby, "Structural basis for the conducting interface between $LaAlO_3$ and $SrTiO_3$," *Phys. Rev. Lett.*, vol. 99, p. 155502, Oct 2007.

[174] M. Salluzzo, S. Gariglio, X. Torrelles, Z. Ristic, R. Di Capua, J. Drnec, M. M. Sala, G. Ghiringhelli, R. Felici, and N. B. Brookes, "Structural and electronic reconstructions at the $LaAlO_3/SrTiO_3$ interface," *Advanced Materials*, vol. 25, no. 16, pp. 2333–2338, 2013.

[175] S. Gariglio, M. Gabay, and J.-M. Triscone, "Research update: Conductivity and beyond at the $LaAlO_3/SrTiO_3$ interface," *APL Mater.*, vol. 4, no. 6, p. 060701, 2016.

[176] C. Cancellieri, D. Fontaine, S. Gariglio, N. Reyren, A. D. Caviglia, A. Fête, S. J. Leake, S. A. Pauli, P. R. Willmott, M. Stengel, P. Ghosez, and J.-M. Triscone, "Electrostriction at the $LaAlO_3/SrTiO_3$ interface," *Phys. Rev. Lett.*, vol. 107, p. 056102, Jul 2011.

[177] M. Stengel, "First-principles modeling of electrostatically doped perovskite systems," *Phys. Rev. Lett.*, vol. 106, p. 136803, Mar 2011.

[178] S. Thiel, G. Hammerl, A. Schmehl, C. Schneider, and J. Mannhart, "Tunable quasi-two-dimensional electron gases in oxide heterostructures," *Science*, vol. 313, no. 5795, pp. 1942–1945, 2006.

[179] M. Reinle-Schmitt, C. Cancellieri, D. Li, D. Fontaine, M. Medarde, E. Pomjakushina, C. Schneider, S. Gariglio, P. Ghosez, J.-M. Triscone, *et al.*, "Tunable conductivity threshold at polar oxide interfaces," *Nature communications*, vol. 3, p. 932, 2012.

[180] Y. Segal, J. H. Ngai, J. W. Reiner, F. J. Walker, and C. H. Ahn, "X-ray photoemission studies of the metal-insulator transition in $LaAlO_3/SrTiO_3$ structures grown by molecular beam epitaxy," *Phys. Rev. B*, vol. 80, p. 241107, Dec 2009.

[181] E. Slooten, Z. Zhong, H. J. A. Molegraaf, P. D. Eerkes, S. de Jong, F. Massee, E. van Heumen, M. K. Kruize, S. Wenderich, J. E. Kleibeuker, M. Gorgoi, H. Hilgenkamp, A. Brinkman, M. Huijben, G. Rijnders, D. H. A. Blank, G. Koster, P. J. Kelly, and M. S. Golden, "Hard x-ray photoemission and density functional theory study of the internal electric field in $SrTiO_3/LaAlO_3$ oxide heterostructures," *Phys. Rev. B*, vol. 87, p. 085128, Feb 2013.

[182] G. Berner, M. Sing, H. Fujiwara, A. Yasui, Y. Saitoh, A. Yamasaki, Y. Nishitani, A. Sekiyama, N. Pavlenko, T. Kopp, C. Richter, J. Mannhart, S. Suga, and R. Claessen, "Direct k-space mapping of the electronic structure in an oxide-oxide interface," *Phys. Rev. Lett.*, vol. 110, p. 247601, Jun 2013.

[183] D. W. Reagor and V. Y. Butko, "Highly conductive nanolayers on strontium titanate produced by preferential ion-beam etching," *Nature Materials*, vol. 4, no. 8, pp. 593–596, 2005.

[184] K. Ueno, S. Nakamura, H. Shimotani, A. Ohtomo, N. Kimura, T. Nojima, H. Aoki, Y. Iwasa, and M. Kawasaki, "Electric-field-induced superconductivity in an insulator," *Nature materials*, vol. 7, no. 11, pp. 855–858, 2008.

[185] M. D'Angelo, R. Yukawa, K. Ozawa, S. Yamamoto, T. Hirahara, S. Hasegawa, M. G. Silly, F. Sirotti, and I. Matsuda, "Hydrogen-induced surface metallization of $SrTiO_3(001)$," *Phys. Rev. Lett.*, vol. 108, p. 116802, Mar 2012.

[186] Y. Chen, N. Pryds, J. E. Kleibeuker, G. Koster, J. Sun, E. Stamate, B. Shen, G. Rijnders, and S. Linderoth, "Metallic and insulating interfaces of amorphous srtio3-based oxide heterostructures," *Nano Letters*, vol. 11, no. 9, pp. 3774–3778, 2011.

[187] Y. Chen, N. Bovet, F. Trier, D. Christensen, F. Qu, N. Andersen, T. Kasama, W. Zhang, R. Giraud, J. Dufouleur, *et al.*, "A high-mobility two-dimensional electron gas at the spinel/perovskite interface of γ-$Al_2O_3/SrTiO_3$," *Nature communications*, vol. 4, p. 1371, 2013.

[188] J. Biscaras, N. Bergeal, A. Kushwaha, T. Wolf, A. Rastogi, R. Budhani, and J. Lesueur, "Two-dimensional superconductivity at a mott insulator/band insulator interface $LaTiO_3/SrTiO_3$," *Nature communications*, vol. 1, pp. 89–89, 2009.

[189] P. Moetakef, T. A. Cain, D. G. Ouellette, J. Y. Zhang, D. O. Klenov, A. Janotti, C. G. Van de Walle, S. Rajan, S. J. Allen, and S. Stemmer, "Electrostatic carrier doping of $GdTiO_3/SrTiO_3$ interfaces," *Applied Physics Letters*, vol. 99, no. 23, p. 232116, 2011.

[190] M. Basletic, J. L. Maurice, C. Carretero, G. Herranz, O. Copie, M. Bibes, E. Jacquet, K. Bouzehouane, S. Fusil, and A. Barthelemy, "Mapping the spatial distribution of charge carriers in $LaAlO_3/SrTiO_3$ heterostructures," *Nat. Mater.*, vol. 7, pp. 621–625, 2008.

[191] N. Reyren, S. Gariglio, A. D. Caviglia, D. Jaccard, T. Schneider, and J.-M. Triscone, "Anisotropy of the superconducting transport properties of the $LaAlO_3/SrTiO_3$ interface," *Appl. Phys. Lett.*, vol. 94, no. 11, p. 112506, 2009.

[192] A. Dubroka, M. Rössle, K. W. Kim, V. K. Malik, L. Schultz, S. Thiel, C. W. Schneider, J. Mannhart, G. Herranz, O. Copie, M. Bibes, A. Barthélémy, and C. Bernhard, "Dynamical response and confinement of the electrons at the $laalo_3/srtio_3$ interface," *Phys. Rev. Lett.*, vol. 104, p. 156807, Apr 2010.

[193] M. Sing, G. Berner, K. Goß, A. Müller, A. Ruff, A. Wetscherek, S. Thiel, J. Mannhart, S. A. Pauli, C. W. Schneider, P. R. Willmott, M. Gorgoi, F. Schäfers, and R. Claessen, "Profiling the interface electron gas of $LaAlO_3/SrTiO_3$ heterostructures with hard x-ray photoelectron spectroscopy," *Phys. Rev. Lett.*, vol. 102, p. 176805, Apr 2009.

[194] Z. S. Popović, S. Satpathy, and R. M. Martin, "Origin of the two-dimensional electron gas carrier density at the $LaAlO_3$ on $SrTiO_3$ interface," *Phys. Rev. Lett.*, vol. 101, p. 256801, Dec 2008.

[195] W.-j. Son, E. Cho, B. Lee, J. Lee, and S. Han, "Density and spatial distribution of charge carriers in the intrinsic n-type $LaAlO_3$-$SrTiO_3$ interface," *Phys. Rev. B*, vol. 79, p. 245411, Jun 2009.

[196] P. Delugas, A. Filippetti, V. Fiorentini, D. I. Bilc, D. Fontaine, and P. Ghosez, "Spontaneous 2-dimensional carrier confinement at the n-type $SrTiO_3/LaAlO_3$ interface," *Phys. Rev. Lett.*, vol. 106, p. 166807, Apr 2011.

[197] C. Cancellieri, M. L. Reinle-Schmitt, M. Kobayashi, V. N. Strocov, P. R. Willmott, D. Fontaine, P. Ghosez, A. Filippetti, P. Delugas, and V. Fiorentini, "Doping-dependent band structure of $LaAlO_3/SrTiO_3$ interfaces by soft x-ray polarization-controlled resonant angle-resolved photoemission," *Phys. Rev. B*, vol. 89, p. 121412, Mar 2014.

[198] D. Matthey, S. Gariglio, and J.-M. Triscone, "Field-effect experiments in $NdBa_2Cu_3O_{7-\delta}$ ultrathin films using a $SrTiO_3$ single-crystal gate insulator," *Applied Physics Letters*, vol. 83, no. 18, pp. 3758–3760, 2003.

[199] G. Khalsa and A. H. MacDonald, "Theory of the $SrTiO_3$ surface state two-dimensional electron gas," *Phys. Rev. B*, vol. 86, p. 125121, Sep 2012.

[200] A. Raslan, P. Lafleur, and W. A. Atkinson, "Temperature-dependent band structure of $SrTiO_3$ interfaces," *arXiv:1609.07223*, 2017.

[201] A. D. Caviglia, M. Gabay, S. Gariglio, N. Reyren, C. Cancellieri, and J.-M. Triscone, "Tunable Rashba spin-orbit interaction at oxide interfaces," *Phys. Rev. Lett.*, vol. 104, p. 126803, Mar 2010.

[202] M. Ben Shalom, M. Sachs, D. Rakhmilevitch, A. Palevski, and Y. Dagan, "Tuning spin-orbit coupling and superconductivity at the $SrTiO_3/LaAlO_3$ interface: A magnetotransport study," *Phys. Rev. Lett.*, vol. 104, p. 126802, Mar 2010.

[203] A. Fête, S. Gariglio, A. D. Caviglia, J.-M. Triscone, and M. Gabay, "Rashba induced magnetoconductance oscillations in the $LaAlO_3$-$SrTiO_3$ heterostructure," *Phys. Rev. B*, vol. 86, p. 201105, Nov 2012.

[204] P. D. Eerkes, W. G. van der Wiel, and H. Hilgenkamp, "Modulation of conductance and superconductivity by top-gating in $LaAlO_3/SrTiO_3$ 2-dimensional electron systems," *Applied Physics Letters*, vol. 103, no. 20, p. 201603, 2013.

[205] S. McKeown Walker, *Two dimensional electron liquids at oxide surfaces studied by angle resolved photoemission spectroscopy*. PhD thesis, University of Geneva, 2016.

[206] M. Tinkham, *Introduction to superconductivity*. Courier Corporation, 1996.

[207] C. Richter, H. Boschker, W. Dietsche, E. Fillis-Tsirakis, R. Jany, F. Loder, L. F. Kourkoutis, D. a. Muller, J. R. Kirtley, C. W. Schneider, and J. Mannhart, "Interface superconductor with gap behaviour like a high-temperature superconductor.," *Nature*, vol. 502, pp. 528–31, 2013.

[208] D. R. Nelson and J. M. Kosterlitz, "Universal jump in the superfluid density of two-dimensional superfluids," *Phys. Rev. Lett.*, vol. 39, pp. 1201–1205, Nov 1977.

[209] L. Benfatto, C. Castellani, and T. Giamarchi, "Broadening of the Berezinskii-Kosterlitz-Thouless superconducting transition by inhomogeneity and finite-size effects," *Phys. Rev. B*, vol. 80, p. 214506, Dec 2009.

[210] A. M. Finkelstein, "Superconducting transition temperature in amorphous films," *JETP Letters*, vol. 45, no. 1, p. 46, 1987.

[211] A. Bianconi, D. Innocenti, A. Valletta, and A. Perali, "Shape resonances in superconducting gaps in a 2DEG at oxide-oxide interface," *J. Phys.: Conf. Ser.*, vol. 529, no. 1, p. 012007, 2014.

[212] S. J. Papadakis, E. P. De Poortere, H. C. Manoharan, M. Shayegan, and R. Winkler, "The effect of spin splitting on the metallic behavior of a two-dimensional system," *Science*, vol. 283, no. 5410, pp. 2056–2058, 1999.

[213] V. M. Edelstein, "Magnetoelectric effect in polar superconductors," *Phys. Rev. Lett.*, vol. 75, pp. 2004–2007, Sep 1995.

[214] L. P. Gor'kov and E. I. Rashba, "Superconducting 2d system with lifted spin degeneracy: Mixed singlet-triplet state," *Phys. Rev. Lett.*, vol. 87, p. 037004, Jul 2001.

[215] M. S. Scheurer and J. Schmalian, "Topological superconductivity and unconventional pairing in oxide interfaces," *Nat. Comm.*, vol. 6, p. 6005, Jan 2015.

[216] M. S. Scheurer and J. Schmalian, "Selection rules for Cooper pairing in two-dimensional interfaces and sheets," *arXiv:1503.03646v2*, 2016.

[217] S. Caprara, F. Peronaci, and M. Grilli, "Intrinsic instability of electronic interfaces with strong Rashba coupling," *Phys. Rev. Lett.*, vol. 109, p. 196401, November 2012.

[218] S. Caprara, J. Biscaras, N. Bergeal, D. Bucheli, S. Hurand, C. Feuillet-Palma, A. Rastogi, R. C. Budhani, J. Lesueur, and M. Grilli, "Multiband superconductivity and nanoscale inhomogeneity at oxide interfaces," *Phys. Rev. B*, vol. 88, no. 2, p. 020504, 2013.

[219] E. Maniv, M. Ben Shalom, A. Ron, M. Mograbi, A. Palevski, M. Goldstein, and Y. Dagan, "Strong correlations elucidate the electronic structure and phase diagram of $LaAlO_3/SrTiO_3$ interface," *Nat. Comm.*, vol. 6, p. 8239, 2015.

[220] S. J. Allen, B. Jalan, S. Lee, D. G. Ouellette, G. Khalsa, J. Jaroszynski, S. Stemmer, and A. H. MacDonald, "Conduction-band edge and Shubnikov–de Haas effect in low-electron-density $SrTiO_3$," *Phys. Rev. B*, vol. 88, p. 045114, Jul 2013.

[221] R. M. Fernandes, J. T. Haraldsen, P. Wölfle, and A. V. Balatsky, "Two-band superconductivity in doped $SrTiO_3$ films and interfaces," *Phys. Rev. B*, vol. 87, no. 1, p. 014510, 2013.

[222] D. Valentinis, D. van der Marel, and C. Berthod, "BCS superconductivity near the band edge: Exact results for one and several bands," *Phys. Rev. B*, vol. 94, p. 024511, 2016.

[223] J. F. Schooley, W. R. Hosler, and M. L. Cohen, "Superconductivity in semiconducting $SrTiO_3$," *Phys. Rev. Lett.*, vol. 12, p. 474, 1964.

[224] J. Schooley, W. Hosler, E. Ambler, J. Becker, M. Cohen, and C. Koonce, "Dependence of the superconducting transition temperature on carrier concentration in semiconducting $SrTiO_3$," *Phys. Rev. Lett.*, vol. 14, p. 305, 1965.

[225] O. Copie, V. Garcia, C. Bödefeld, C. Carrétéro, M. Bibes, G. Herranz, E. Jacquet, J.-L. Maurice, B. Vinter, S. Fusil, K. Bouzehouane, H. Jaffrès, and A. Barthélémy, "Towards two-dimensional metallic behavior at $LaAlO_3/SrTiO_3$ interfaces," *Phys. Rev. Lett.*, vol. 102, p. 216804, 2009.

[226] D. Valentinis, D. van der Marel, and C. Berthod, "Rise and fall of shape resonances in thin films of BCS superconductors," *Phys. Rev. B*, vol. 94, p. 054516, 2016.

[227] M. Ben Shalom, A. Ron, A. Palevski, and Y. Dagan, "Shubnikov–De Haas oscillations in $SrTiO_3/LaAlO_3$ interface," *Phys. Rev. Lett.*, vol. 105, p. 206401, 2010.

[228] A. Fête, S. Gariglio, C. Berthod, D. Li, D. Stornaiuolo, M. Gabay, and J.-M. Triscone, "Large modulation of the Shubnikov-de Haas oscillations by the Rashba interaction at the $LaAlO_3/SrTiO_3$ interface," *New J. Phys.*, vol. 16, p. 112002, 2014.

[229] A. Joshua, S. Pecker, J. Ruhman, E. Altman, and S. Ilani, "A universal critical density underlying the physics of electrons at the $LaAlO_3/SrTiO_3$ interface," *Nat. Comm.*, vol. 3, p. 1129, Oct. 2012.

[230] H.-M. Christen, J. Mannhart, E. J. Williams, and C. Gerber, "Dielectric properties of sputtered $SrTiO_3$ films," *Phys. Rev. B*, vol. 49, p. 12095, 1994.

Publication list

[1] D. Forcella, J. Zaanen, D. Valentinis and D. van der Marel, "Electromagnetic properties of viscous charged fluids", *Phys. Rev. B*, vol. 90, p. 035143, July 2014.

[2] D. Valentinis, D. van der Marel and C. Berthod, "BCS superconductivity near the band edge: Exact results for one and several bands", *Phys. Rev. B*, vol. 94, p. 024511, July 2016.

[3] D. Valentinis, D. van der Marel and C. Berthod, "Rise and fall of shape resonances in thin films of BCS superconductors", *Phys. Rev. B*, vol. 94, p. 054516, August 2016.

[4] D. Valentinis, S. Gariglio, A. Fête, J.-M. Triscone, C. Berthod and D. van der Marel, "Modulation of the superconducting critical temperature due to quantum confinement at the $LaAlO_3/SrTiO_3$ interface", *arXiv:1611.07763*, accepted by Phys. Rev. B, November 2016.

List of Figures